Measurement of Strong Coupling Constant using Radiative Hadronic Events in e^+e^- Collision at LEP

by
Daisuke Toya

A dissertation submitted in partial fulfillment
of the requirements for the degree of
Doctor of Philosophy
in The University of Tokyo
2003

Abstract

The strong coupling constant α_s at effective center-of-mass energies ranging from 24GeV to 78GeV and at center-of-mass energies ranging from 189GeV to 205GeV are measured using the OPAL detector at LEP collider.

LEP runs at $E_{\mathrm{CM}} = 91$GeV from year 1992 to 1995. The dataset corresponds to the integrated luminosity 103pb^{-1}. The radiative multi-hadronic events (i.e. $\mathrm{e^+e^-} \to \gamma +$ hadrons) in the dataset are used for the measurement of α_s at effective center of mass energies spanning from 24GeV to 78GeV.

For the measurement of α_s at the center of mass energies spanning from 189GeV to 205GeV, non-radiative hadronic events in data taken in year 1998, 1999 and 2000 at LEP running at $E_{\mathrm{CM}} > M_{\mathrm{Z}}$.

In order to determine the α_s, $\mathcal{O}(\alpha_s^2)$ + NLLA QCD calculations are fitted to the corrected data distributions. Since the calculation is done with partons, the correction of hadronization effect is applied to the theoretical prediction before the fitting.

The measurement is performed for six event shape variables. The result of the fitting are shown with the statistical error and the systematic uncertainties including the experimental uncertainties, hadronization model uncertainties and renormalization scale uncertainty.

The constant $\Lambda_{\overline{MS}}^{(5)}$ is determined by fitting the solution of the renormalization group equation at NNLO to α_s determined at various effective center-of-mass energies. The energy dependence of combined α_s for all event shape variables gives

$$\Lambda_{\overline{MS}}^{(5)} = 0.2242 \pm 0.031(\mathrm{stat.} + \mathrm{expt.} + \mathrm{hadr.})^{+0.072}_{-0.048}(\mathrm{scale.})\ \mathrm{GeV}.$$

This result is consistent with the average by PDG, $\Lambda_{\overline{MS}}^{(5)} = 0.216^{+0.025}_{-0.024}$GeV.

The values of α_s for all event shape variables are combined into one value for each center-of-mass energy. The combined values for each center-of-mass energy are combined into one value. The combined value of all values of α_s which are obtained in this study is

$$\alpha_s(M_{\mathrm{Z}}) = 0.1193 \pm 0.0017(\mathrm{stat.})^{+0.0055}_{-0.0046}(\mathrm{syst.}). \tag{1}$$

It is consistent with the PDG world average.

This study includes the first α_s measurement using radiative hadronic events presented by OPAL collaboration. α_s is measured in wide energy range by this method. The values of α_s measured in same conditions (selections, systematic uncertainties ...) can be used for study of the energy dependence of α_s. The measurement of α_s at the center of mass energies 189GeV to 205GeV is the measurement at highest energy $\mathrm{e^+e^-}$ collisions. The values have an important role as lever arm for the accurate measurement on Z^0 pole to know energy scale dependence.

Contents

List of Figures

List of Tables

Chapter 1

Introduction

In the Standard Model (SM) of elementary particle physics, the fundamental building blocks of matter are the quark and lepton which have a spin of 1/2 in units of $\hbar$. The quark consists of three doublets; (u,d),(c,s) and (t,b). There are three charged leptons; electron, muon and tau. Three neutral leptons which are called neutrinos partner the three charged leptons.

The SM consists of theories which describe three of four fundamental interactions; electromagnetic interaction, weak interaction and strong interaction. The electromagnetic interaction and the weak interaction are described in one model as electro-weak interaction. The electro-weak interaction is mediated by four gauge bosons, Z^0 W^+, W^- and γ.

Quantum chromo dynamics (QCD) is a gauge theory describing the strong interaction. This is a extension of quantum electro dynamics (QED) to non-Abelian (i.e. generators of the symmetry group are non-commutative) gauge field theory. Such a theory was originally introduced by Yang and Mills [4], 't Hooft [5], Gross and Wilczek [6] and Politzer [7]. The massless gauge boson called gluon mediates the interaction between quarks.

It is pointed by Bjorken [8] that structure functions of nucleon in the deep inelastic region depend only on the ratio q^2/ν rather than on two independent variables momentum transfer squared, q^2, and energy transfer, ν. This is called Bjorken scaling and recognized by assuming that the electron scatters off almost free point-like constituents inside nucleons which are called "partons". It means that the strong interaction becomes weak at short distance or equivalently at large momentum transfer. This property has to be satisfied by the theory which describes the strong interaction. QCD has the desired property "asymptotic freedom". According to this property, perturbation theory can be used to discuss short-distance reactions.

Asymptotic freedom is directly confirmed by measurements of the strong coupling constant, α_s at various energy scales of reaction. The measurement of α_s by event shape variables, which are variables on the event topology of hadronic final state is frequently used at electron-positron collider experiments. It is determined by experiments at CESR($E_{CM} = 10.53$) [9], PEP collider(29GeV) [10,11], PETRA(22,35,44GeV) [12,13], TRISTAN(58GeV) [14], SLC(91GeV) [15,16] and LEP(91GeV [17–24], 133$\sim$189GeV [25–34]).

In this thesis, we present a study of the strong coupling constant in the energy range between 24 GeV and 209 GeV using e+e- collision data collected by the OPAL detector at LEP.

LEP operates at $E_{\text{CM}} = 91\text{GeV}$ from year 1992 to 1995. It is called "LEP1". The dataset corresponds to the integrated luminosity 103pb^{-1}. The radiative events in the dataset are used for the measurement of α_s at the effective center of mass energies spanning from 2 4GeV to 78GeV. The "radiative events" means hadronic events with photons before or immediately after the Z^0 production.

LEP increased the center-of-mass energy to around and above the threshold of W^+W^- production during the period of 1996-2000. The LEP running is called "LEP2". For the measurement of α_s at the center of mass energies spanning from 189GeV to 205GeV, non-radiative hadronic events in data taken in year 1998, 1999 and 2000 are used. The "non-radiative" means hadronic events without high energy photons. The dataset corresponds to the integrated luminosity 182pb^{-1}, 29pb^{-1},72pb^{-1},75pb^{-1},38pb^{-1} and 206pb^{-1} for E_{cm}=189,192,196,200,202 and 206GeV, respectively.

In Chapter 2, the properties of QCD and the strong coupling constant which are necessary for reading this thesis is summarized. For the measurements using radiative hadronic events using LEP1 data, the photon radiation at $\text{e}^+\text{e}^- \rightarrow$ hadrons reaction is explained in Chapter 3. The LEP collider and the OPAL detector are described in Chapter 4. The measurements using radiative hadronic events in LEP1 data is described in Chapter 5. The measurements with non-radiative hadronic events with LEP2 data is described in Chapter 6. The energy dependence of α_s is studied with values of α_s obtained by the analyses. In order to compare the result of this study with the results from other experiments and the world average, all values of α_s are combined into one value α_s at the energy scale of M_{Z}. Results of the combination are explained in Chapter 7. In Chapter 8 the result of this study is compared with the results from other α_s measurements using event shape variables. Finally, this study is summarized in Chapter 9.

Chapter 2

Theoretical Background

The quantum chromo dynamics (QCD) is a quantum field theory which describes reactions caused by the strong interaction. Massless gauge bosons called gluons mediate the interaction between quarks. Unlike QED, the gauge boson has color charge by itself. Since QCD has the property called "confinement", quarks and gluons can not exist in states other than color singlet.

In case of QCD, the coupling constant, α_s, tends to decrease at small distance or high energy scale. It is called "asymptotic freedom". Asymptotic freedom is a property of non-Abelian gauge theories. It is considered to be perturbatively calculable at high energy scale because of asymptotic freedom. Since the coupling constant is large at low energy scale, it is difficult to calculate perturbatively physical quantities at low energy scale.

When quarks and gluons separate from each other, each parton transforms into many hadrons along an orientation of an momentum vector of the parton. The hadrons are called a "jet". The transformation into hadrons is called the fragmentation or the hadronization. The hadronization is treated by phenomenological models inspired by QCD in analyses of experimental data.

As shown in Figure 2.1, a $q\bar{q}$ pair is produced in the e^+e^- collision at the energy of LEP. The quarks radiate gluons and the gluons split into gluons or quarks (perturbative QCD phase). After the energies of quarks and gluons are reduced to around a few GeV, these quarks and gluons form hadrons (hadronization/fragmentation phase). Hadrons are identified by detectors after decaying into stabler hadrons (Hadron decay phase). In Section 2.1, the calculation methods used for the perturbative phase are explained briefly. The phenomenological models which are used to treat the fragmentaion phase are described in Section 2.2. The topics about the coupling constant α_s are written in Section 2.3.

2.1 Perturbative QCD Phase

Calculations by the perturbative QCD are categorized into order by order calculation of matrix elements and probabilistic approach with parton shower model which is based on the leading logarithm approximation (LLA).

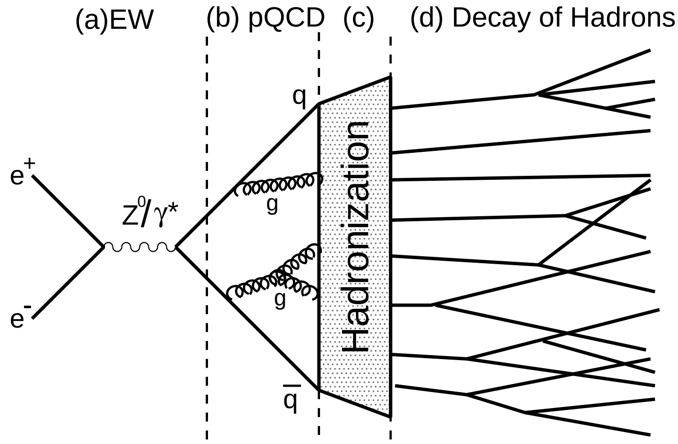

Figure 2.1: Schematic illustration of an $e^+e^- \to$ hadrons event. (a) A quark-antiquark pair is produced after an e^+e^- annihilation. (b) Gluons are radiated from quarks and split into gluons or quarks. (c) Gluons and quarks are transformed into hadrons. (d) Unstable hadrons decay into stable particles.

2.1.1 Matrix Elements

Feynman diagrams are calculated order by order in the matrix element approach. Although the calculation of matrix elements is a preferable approach and can take a correct interference and helicity into account, the increase of the order of α_s makes the calculation of matrix elements difficult. In practice, QCD cross-sections to leading order (LO) or to next-to-leading order (NLO, $\mathcal{O}(\alpha_s^2)$), or in some cases, to next-to-next-to-leading order (NNLO, $\mathcal{O}(\alpha_s^3)$) are known.

The $\mathcal{O}(\alpha_s^2)$ matrix element is unsuccessful in describing the back-to-back two-jet region of phase space. Multiple emissions of soft gluons may be expected to be important in this region. An alternative approach may be taken to the QCD calculations of hadronic final states in the e^+e^- annihilations, based on the resummation of leading logarithms which arise from soft and collinear singularities in gluon emissions. The consequence is that the effective expansion parameter is not simply α_s, but $\alpha_s L^2$ (to leading order L), where $L = \ln(1/y)$ and y is some generic observable which tends to zero in the two jet region. At small y the value of $\alpha_s L^2$ is not small, and therefore these terms must be summed to all orders in α_s in order to provide a satisfactory calculation. For certain observables it has proved possible to sum both the leading and next-to-leading logarithms. They are referred as the Next-to-Leading Log Approximation (NLLA). NLLA calculations are available for eight observables which describe the final state in the process $e^+e^- \to$ hadrons: thrust [35], heavy jet mass [35], two measures of jet broadening [36, 37], energy-energy correlations [38–42][1], two-jet rates [44,45], average jet multiplicities [46], C-parameter [35]. The NLLA and $\mathcal{O}(\alpha_s^2)$ calculation of these observables is described in Section 2.3.4.

[1] There are large disagreement among theoretical calculations. Since the disagreement is larger than uncertainties on the experimental effect and the hadronization models, the energy-energy correlation is not used in this study. [43]

2.1.2 Parton Showers

Parton shower approach is the method based on the approximation to take the leading order term in the perturbative expansion in power of $\ln Q^2$, where Q is energy scale. The approximation is called LLA(Leading Log Approximation)). Compared to the matrix element approach available for up to four jets processes, this approach can treat an arbitrary number of jets because a splitting of gluons is treated probabilistically and repetitively. Owing to these properties, the parton shower approach is used in Monte Carlo simulation.

Virtuality of quarks just after their production is thought to be large and is reduced in splittings like q $\rightarrow$ qg, g $\rightarrow$ gg, g $\rightarrow$ q$\bar{\text{q}}$. In the parton shower approach, an evolution parameter $t(=\ln(Q^2_{\text{evol}}/\Lambda^2))$ represents the virtuality, where Q_{evol} is an energy scale of the evolution, Λ is the fundamental constant of QCD which is described in Section 2.3.2. The probability to cause a splitting a $\rightarrow$ bc when the evolution parameter changes in dt is obtained by the Altarelli-Parisi equation [47]:

$$\frac{d\mathcal{P}_{a\rightarrow bc}}{dt} = \int dz \frac{\alpha_s(Q^2)}{2\pi} P_{a\rightarrow bc}(z), \tag{2.1}$$

where Q is the energy scale of α_s. $P_{a\rightarrow bc}(z)$ is called an Altarelli-Parisi splitting kernel and is known to be:

$$P_{q\rightarrow qg}(z) = C_F \frac{1+z^2}{1-z} \tag{2.2}$$

$$P_{g\rightarrow gg}(z) = N_C \frac{(1-z(1-z))^2}{z(1-z)} \tag{2.3}$$

$$P_{g\rightarrow q\bar{q}}(z) = T_R(z^2-(1-z)^2). \tag{2.4}$$

where C_F is 4/3, N_C is 3,T_R is equivalent to $n_f/2$. n_f is the number of flavors which have mass smaller than the energy scale of the reaction. z is the fraction of momentum to be taken away by a splitting parton. The daughter b takes fraction z and the daughter c takes fraction $1-z$. It is not necessary that the the Q agrees with Q_{evol}.

When the parton shower process start with $t = t_{\text{max}}$ and ends with $t = t_{\text{min}}$, the probability that a splitting will not happen when the evolution parameter changed from t_{max} to t, $\mathcal{P}_{\text{no}-\text{emission}}(t_{max}, t)$, is:

$$\mathcal{P}_{\text{no}-\text{emission}}(t_{max}, t) = S_a(t_{\text{max}})/S_a(t), \tag{2.5}$$

where $S_a(t)$ is the Sudakov form factor:

$$S_a(t) = \exp\left(-\int_{t_{min}}^{t} dt' \frac{d\mathcal{P}_{a\rightarrow bc}}{dt'}\right). \tag{2.6}$$

A splitting will happened at t which satisfies the condition $\mathcal{P}_{\text{no}-\text{emission}}(t_{max}, t) = R$, where R is a random number which is distributed between 0 and 1.

Calculation in Monte Carlo Event Generators

In this study, `JETSET` [48], `HERWIG` [49] and `ARIADNE` [50] are used to simulate multi-hadronic processes. The parton shower approach is used together with matrix elements in the Monte Carlo simulations. The differences between implementations of the parton shower models are explained briefly here.

The largest difference of parton shower approach used in the Monte Carlo generators is in the definition or interpretation of evolution parameter t, energy scale Q^2 and momentum fraction z.

There are definitions of z with different combinations of momentum,p, and energy,E, like $E+p_L$ and $E+|p|$ in addition to E. The difference of the definition affects the region of integration in the Equation 2.1. The effect is small for large z.

JETSET In `JETSET`, the scale of evolution, $Q_{\rm evol}$, in `JETSET` is same as the mass of a virtual parent parton. The evolution continue until $Q_{\rm evol}$ decreases to Q_0, which is set to 1GeV by default. the Q_0 corresponds to the sum of effective masses of the daughter partons.

The energy fraction z is a ratio of daughter parton's energy E_b to mother parton's energy E_a in the center-of-mass system. The lower and upper limits $z_\pm$ given by kinematical conditions are:

$$z_\pm = \frac{1}{2}\left\{1 \pm \frac{|\mathbf{P}_a|}{E_a}\theta(m_a - m_{min,a})\right\} \qquad (m_{min,\mathrm{q}} = Q_0) \tag{2.7}$$

HERWIG `HERWIG` employs the formalism of Sudakov form factors for parton shower branching. The evolution parameter, ζ_i, for a parton branching $i \to j+k$ is defined by

$$\zeta_i = E_i\sqrt{\xi_{jk}} \qquad \xi_{jk} = \frac{p_j p_k}{E_j E_k} \tag{2.8}$$

where p_j and p_k are the daughter 4-momenta and E_j and E_k are their respective energies. The E_i is the energy of the parent parton i. When daughter partons have much smaller mass than their energy, ξ_{jk} is approximately equal to $(1-\cos\theta_{jk})$. Therefore, the ordering of evolution parameter ζ_i is equivalent to the ordering of the angle between daughter partons. By using ζ as evolution parameters, the angular ordering which is the result of the destructive interference of soft gluon emissions is introduced naturally.

ARIADNE The perturbative QCD cascade is formulated in terms of color dipoles in `ARIADNE`. A Color dipole is stretched between a quark and an anti quark, between a quark and a gluon or between two gluons. Gluons are emitted from the color dipole. The color dipole is splitting into two color dipoles after emitting the gluon. The cross-sections for a gluon emission from each type of color dipole are:

$$\frac{d\sigma_{q\bar{q}}}{dx_1 dx_3} = \frac{2\alpha_s}{3\pi}\frac{x_1^2 + x_3^2}{(1-x_1)(1-x_3)}, \tag{2.9}$$

$$\frac{d\sigma_{qg}}{dx_1 dx_3} = \frac{3\alpha_s}{4\pi}\frac{x_1^3 + x_3^2}{(1-x_1)(1-x_3)}, \tag{2.10}$$

$$\frac{d\sigma_{gg}}{dx_1 dx_3} = \frac{3\alpha_s}{4\pi}\frac{x_1^3 + x_3^3}{(1-x_1)(1-x_3)}, \tag{2.11}$$

where the index 1 and 3 indicate partons at ends of color dipole and x_i is the final state energy fractions $(= 2E_i/\sqrt{S_{dip}})$ of a parton i. S_{dip} is the dipole mass. The emission of quarks is done by splitting a gluon into a quark-antiquark pair with Altarelli-Parisi splitting functions.

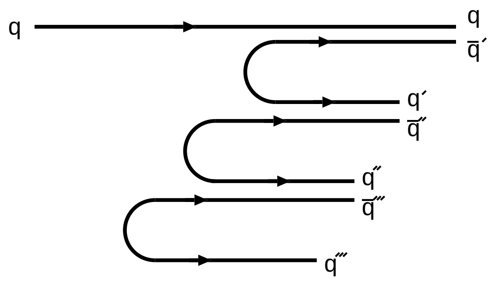

Figure 2.2: Schematic view of the independent fragmentation. Mesons are formed from quarks pairs independently.

2.2 Fragmentation Phase

Many hadrons are produced from the state of quarks and gluons in the fragmentation phase. Although it is better to treat this phase by QCD, phenomenological models which are inspired by QCD are used for usual analysis. Most famous fragmentation models are Independent fragmentation (IF), String Fragmentation (SF) and Cluster Fragmentation (CF). These fragmentation models are explained briefly in the following sections.

2.2.1 Independent Fragmentaion

The independent fragmentation (IF) model is the oldest approach among these fragmentation models. `COJETS` [51] and `EURODEC` [52] are the generators which use the independent fragmentation model. Although `COJETS` is studied in OPAL α_s measurements, the difference between `COJETS` and other generators used in the analyses is larger by 1 figure than the difference in the generators in our previous analyses [53, 54].

Each step of fragmentation is performed independently between partons in the independent fragmentation (Figure 2.2). After producing quark pair $\mathrm{q}'\bar{\mathrm{q}}'$, a meson is formed by combining parent quarks q and $\bar{\mathrm{q}}'$. Since it is known experientially that the scaling law holds for the longitudinal component of meson momentum, the longitudinal momentum is obtained probabilistically from the fragmentation function $f(z)$ ($z = (E_h + P_{L,h})/(E_q + P_{L,q})$). A transverse momentum is obtained by the Gaussian distribution known empirically

$$\exp\left(-\frac{P_T^2}{2\sigma_q}\right), \ (\sigma_q^2 \sim 0.3\mathrm{GeV}). \tag{2.12}$$

This procedure is repeated with q' as a mother parton for the next step.

The following fragmentation functions are used for the independent fragmentation model.

- Field-Feynman parameterization,

$$f(z) = 1 - a + 3a(1-z)^2, \tag{2.13}$$

  with default value $a = 0.77$, is frequently used for ordinary hadrons.

- It is known from experiments that the peak position of fragmentation function shifts to higher value of z for heavy flavors like a charm quark or a bottom quark. The

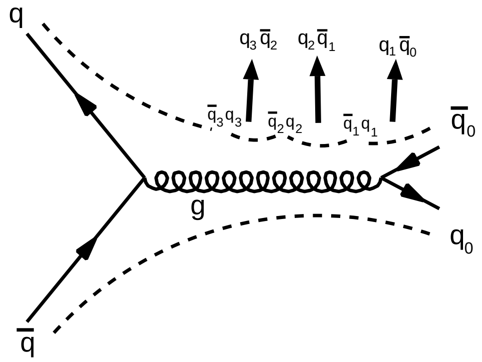

Figure 2.3: Schematic view of the string fragmentation. Mesons are formed from quarks pairs after breaking a string.

Peterson function

$$f(z) \propto \left[z \left(1 - \frac{1}{z} - \frac{\epsilon_Q}{1-z} \right)^2 \right]^{-1} \tag{2.14}$$

is used for this case. ϵ_Q in the above equation is a free parameter and is expected to be proportional to $1/m_Q^2$.

The independent fragmentation model doesn't distinguish a flavor of quark to be taken from vacuum in forming a meson. The flavor is selected according to the ratio $u : d : s : c : b = 1 : 1 : 0.3 : 0 : 0$.

There is no definitive treatment for gluons in independent fragmentation. It is possible to fragment gluons with the same fragmentation function as quarks. The method to fragment gluons after splitting into quark pair with Altarelli-Parisi equation is often used.

2.2.2 String Fragmentaion

String fragmentation is the model originally proposed by Artru and Menessier [55]. It is implemented in `JETSET` and called Lund model now. The feature of this method is that the concept of linear confinement of QCD is employed. A quark pair is regarded as a one dimensional string oscillating by the initial momentum. Mesons are considered to be produced by breaking the string. After stretching a string between quarks, the string is broken from the end of string and mesons are produced(Figure 2.3). If there is not enough energy to produce a meson, the fragmentation is stopped.

The view of tunnelling effect is taken about the generation of a quark pair. The function of a transverse momentum distribution and the composition of flavor which are given empirically in the independent fragmentation model is automatically deduced.

Fragmentation Function An arbitrary fragmentation function can be used for string fragmentation model like independent fragmentation model. If it is required that the fragmentation process as a whole should look the same, irrespectively of whether the iterative procedure is performed from a quark end or a anti-quark end(q or $\bar{q}_0$ in Figure 2.3), the choice of the function is essentially unique. The function is,

$$f(z) \propto \frac{1}{z} z^{a_\alpha} (\frac{1-z}{z})^{a_\beta} \exp\left(\frac{-bm_T^2}{z} \right), \tag{2.15}$$

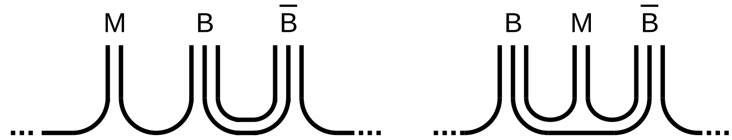

Figure 2.4: A schematic of baryon production in the diquark model (left) and 'popcorn' model (right) leading to $\mathrm{MB\overline{B}}$ and $\mathrm{BM\overline{B}}$ configurations respectively.

where m_T^2 is a transverse mass of the quark. α is the old flavor and β is the new flavor in each iteration process. The meaning of "new" and "old" is explained by Figure 2.3. When the fragmentation proceeds from $\bar{\mathrm{q}}_0$ to q and the quark pair $\mathrm{q}_2\bar{\mathrm{q}}_2$ is produced, a flavor of q_1 is the "old" flavor, and a flavor of q_2 is the "new" flavor. This fragmentation function is called 'Lund left-right symmetric model'. Usually, the function is simplified by assuming that a is equivalent to b. The simplified function is

$$f(z) \propto \frac{1}{z}(1-z)^a \exp\left(\frac{-bm_T^2}{z}\right) \tag{2.16}$$

is used. Since the explicit mass dependence in $f(z)$ implies a harder fragmentation function for heavier hadrons, there is a merit that the similar function as Peterson function is automatically deduced. [2]

It is possible to produce baryons by similar procedure as mesons in the string fragmentation model. Baryons can be formed by producing a pair of di-quark and anti-diquark instead of $q\bar{q}$ (Figure 2.4). But, correlations between baryon and anti-baryon in phase space is stronger than it is actually measured. The baryon production model used in the current version `JETSET` is called "Popcorn model" [56]. As seen in Figure 2.4, three $q\bar{q}$ pairs form baryon, anti-baryon and meson. Since quarks shared by the baryon and the anti-baryon are reduced, the correlation is weakened and the measurement is reproduced.

Fragmentation of Gluon Gluon is represented as a kink of string in the string fragmentation model. When gluon is radiated between quarks, strings are stretched between gluon and quark. Therefore, multiplicity of hadrons between quark jets is expected to be fewer than between gluon and quark jets on this picture.

2.2.3 Cluster Fragmentaion

The cluster model was used first in the simulation program `CALTECH` [57, 58]. `HERWIG` currently is the most famous program which uses the cluster model.

The fragmentation by the cluster model is shown in Figure 2.5. After splitting gluons into quark pairs, quarks are rearranged into color singlet cluster to minimize invariant mass. If a formed cluster has large mass (> 5GeV), hadrons are emitted isotropically in center-of-mass system of the cluster. The emission depends on their phase space and spin. If the mass of the cluster is small, the cluster becomes a hadron.

[2] In the version of `JETSET` which is used in this analysis, Bowler function

$$f(z) \propto \frac{1}{z^{1+r_Q bm_Q^2}} z^{a_\alpha} \left(\frac{1-z}{z}\right)^{a_\beta} \exp\left(-\frac{bm_T^2}{z}\right) \tag{2.17}$$

is used for heavy flavor.

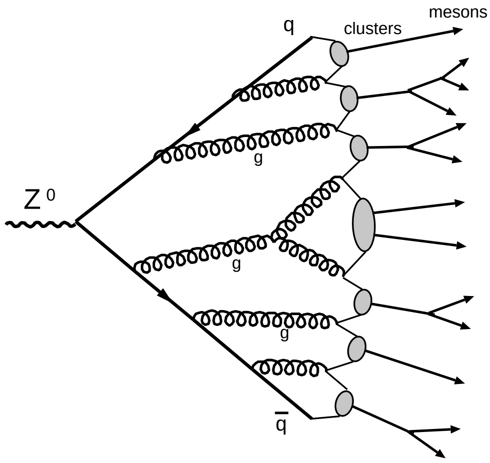

Figure 2.5: Schematic view of the cluster fragmentation. Mesons are formed from quarks pairs after breaking a cluster.

The feature is that the transverse momentum distribution can be deduced. Although heavy hadrons are suppressed automatically like the string model, the cluster model does not reproduce the data so well as the string model. In addition, there is a problem in suppression of production of heavy hadrons of heavy cluster origin.

2.3 The Strong Couping Constant α_s

In this section, properties of the strong coupling constant, α_s, are explained at first. After reviewing the determination of the α_s briefly, event shape variables which are used to determine α_s in this study are explained.

2.3.1 Renormalization

In the quantum field theories like QCD and QED, dimensionless physical quantities $\mathcal{R}$ can be expressed by a perturbation series in powers of the coupling parameter α_s or α, respectively. $\mathcal{R}$ is considered to depend on α_s and a single energy scale Q. When calculating $\mathcal{R}$ as perturbation series in α_s, ultraviolet divergences occur. Because $\mathcal{R}$ must retain a physical value, these divergences are removed by a procedure called "renormalization". This introduces a second mass or energy scale, μ, which represents the point at which the subtraction to remove the ultraviolet divergences is actually performed. As a consequence of this procedure, $\mathcal{R}$ and α_s become functions of the renormalization scale μ. Since $\mathcal{R}$ is dimensionless, it is assumed that $\mathcal{R}$ depends on the ratio Q^2/μ^2 and on the renormalized coupling $\alpha_s(\mu^2)$:

$$\mathcal{R} \equiv \mathcal{R}(Q^2/\mu^2, \alpha_s); \qquad \alpha_s \equiv \alpha_s(\mu^2) \tag{2.18}$$

Because the choice of μ is arbitrary, however, R can not depend on μ, for a fixed value of the coupling, such that

$$\mu^2 \frac{d}{d\mu^2}\mathcal{R}(Q^2/\mu^2, \alpha_s) = \left(\mu^2 \frac{\partial}{\partial \mu^2} + \mu^2 \frac{\partial \alpha_s}{\partial \mu^2}\frac{\partial}{\partial \alpha_s}\right)\mathcal{R} = 0, \tag{2.19}$$

where the convention of multiplying the whole equation with μ^2 is applied in order to keep the expression dimensionless. Equation 2.19 implies that any explicit dependence of $\mathcal{R}$ on μ must be canceled by an appropriate μ dependence of α_s. Therefore, it would be natural to identify the renormalization scale with the physical energy scale of the process, $\mu^2 = Q^2$, eliminating the uncomfortable presence of a second and unspecified scale. In this case, α_s transforms to the "running coupling constant" $\alpha_s(Q^2)$, and the energy dependence of $\mathcal{R}$ enters only through the energy dependence of $\alpha_s(Q^2)$. However, since only matrix elements up to the second order of α_s are obtained from perturbative QCD calculations, the dependence on Q^2/μ^2 remains in the calculations. The effect of the dependence on α_s measurements are estimated by changing μ/Q by factor 2 in this study.

2.3.2 Running of α_s and Definition of Fundamental Constant Λ

Energy dependence of α_s on the renormalization parameter, μ, is given by following differential equations.

$$\mu\frac{\partial\alpha_s}{\partial\mu} = 2\beta(\alpha_s) = -\frac{\beta_0}{2\pi}\alpha_s^2 - \frac{\beta_1}{4\pi}\alpha_s^3 - \frac{\beta_2}{64\pi}\alpha_s^4 + \mathcal{O}(\alpha_s^5) \tag{2.20}$$

$$\beta_0 = 11 - \frac{2}{3}n_f \quad \beta_1 = 51 - \frac{19}{3}n_f \quad \beta_2 = 2857 - \frac{5033}{9}n_f - \frac{325}{27}n_f^2 \tag{2.21}$$

where n_f is the number of flavors which have mass smaller than μ. It is necessary to introduce at least one constant of integration to the differential equation. The certain energy scale is used as the constant in general. It is standard to set the scale to the mass of Z boson, M_{Z}. The parameter Λ which provides a parametrization of the μ dependence of α_s is frequently used also. Λ is defined by:

$$\int_{\alpha_s(\mu)}^{\infty}\frac{d\alpha_s}{\beta(\alpha_s)} \equiv \ln\left(\frac{\Lambda^2}{\mu^2}\right). \tag{2.22}$$

So to speak, Λ is the energy scale at which α_s diverges to infinity.

The solution of Equation 2.20 in the approximation where the first term of function $\beta(\alpha_s)$ is taken is:

$$\alpha_s(\mu) = \frac{4\pi}{\beta_0\ln(\mu^2/\Lambda^2)}. \tag{2.23}$$

In approximation to take the second term, the solution is given by the following equation.

$$\frac{1}{\alpha_s} + \frac{\beta_1}{2\pi\beta_0}\ln\left(\frac{\frac{\beta_1}{2\pi\beta_0}\alpha_s}{1+\frac{\beta_1}{2\pi\beta_0}\alpha_s}\right) = \frac{4\pi}{\beta_0}\ln\left(\frac{\mu^2}{\Lambda^2}\right) \tag{2.24}$$

$\alpha_s(\mu)$ can be obtained by expanding Equation 2.24 in inverse powers of $\ln(\mu^2)$.

$$\alpha_s(\mu) = \frac{4\pi}{\beta_0\ln(Q^2/\Lambda^2)}\left[1 - \frac{2\beta_1\ln(\ln(\mu^2/\Lambda^2))}{\beta_0\ln(\mu^2/\Lambda^2)}\right] \tag{2.25}$$

After solving Equation 2.20 in approximation to take the third term, $\alpha_s(\mu)$ can be obtained by expanding in inverse powers of $\ln(\mu^2)$ like Equation 2.25.

$$\alpha_s(\mu) = \frac{4\pi}{\beta_0 \ln(\mu^2/\Lambda^2)}\left[1 - \frac{2\beta_1}{\beta_0}\frac{\ln\ln(\mu^2/\Lambda^2)}{\ln(\mu^2/\Lambda^2)} + \frac{4\beta_1^2}{\beta_0^4 \ln^2(\mu^2/\Lambda^2)} \times \left(\left(\ln\ln(\mu^2/\Lambda^2) - \frac{1}{2}\right)^2 + \frac{\beta_2\beta_0}{8\beta_1^2} = \frac{5}{4}\right)\right] \tag{2.26}$$

Coefficients of the function β include a number of flavors, n_f, in each equation. Besides this, coefficients for higher terms than β_2 are depend on the prescription of renormalization. Therefore, the definition of Λ is dependent on number of flavor and prescription of renormalization. When the value of Λ is given, this information should be given with the value. Λ in five flavors and $\overline{MS}$ scheme, $\Lambda^{(5)}_{\overline{MS}}$, is shown in this analysis. In Figure 2.6, the values of α_s at LO, NLO and NNLO are shown with their ratio. Λ is set to 0.216GeV and the number of flavors are five. The variation of α_s between LO and NLO is around 20%. The variation between NLO and NNLO is reduced to $1 \sim 2\%$, which is close to the precision of the world average of $\alpha_s(M_Z)$ [59, 60]. Therefore, it is better to use NNLO calculation of the α_s.

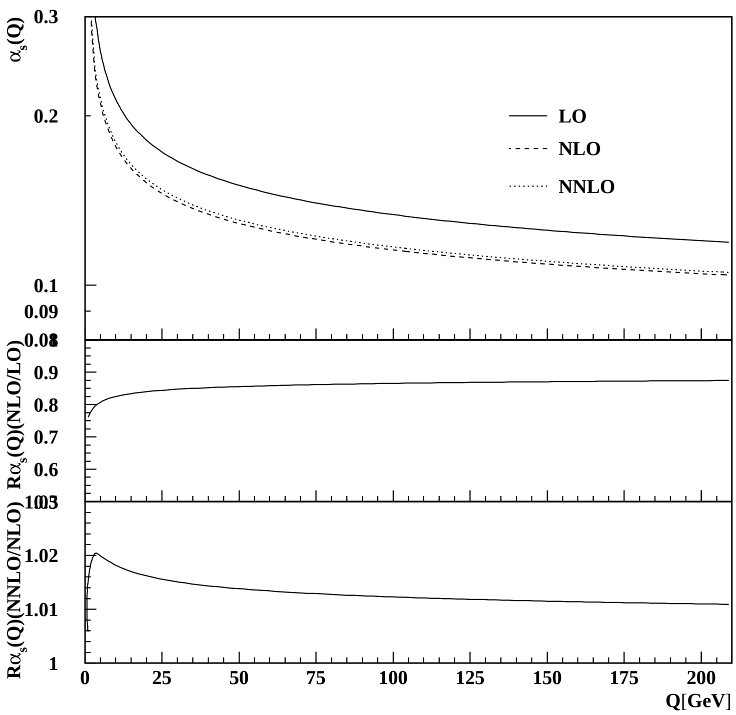

Figure 2.6: The evolution of α_s at LO,NLO and NNLO. Middle and lower plot show the ratios of α_s at NLO to LO and at NNLO to NLO, respectively.

2.3.3 Determination of α_s

α_s is measured using various reactions at energy scale of a few GeV to around 500GeV. For example, the following processes and methods have been used to extract the α_s.

- Total hadronic cross-section [61].

- e^+e^-/ep event shapes. The fitting of variables describe of the event topology (event shape variables) gives α_s value.

- Scaling violations in fragmentation function [62, 63]. α_s is extracted from the fragmentation function $d_i(z, E)$, which is the probability that a hadron of type i is produced with energy zE in e^+e^- collisions at $\sqrt{s} = 2E$.

- Z width. The α_s is extracted from the ratio of hadronic decay width of Z^0, $R_Z = \Gamma(Z^0 \to \text{hadrons})/\Gamma(Z^0 \to \text{leptons})$.

- Deep inelastic scattering(DIS) [64–68]. α_s is obtained from a fitting of structure functions. The Gross-Llewellyn Smith sum rule for deep inelastic neutrino scattering and the Bjorken sum rule are used for extracting α_s.

- Polarized DIS [69–73]. The spin-dependent structure functions which are measured in polarized lepton-nucleon scattering are used to determine α_s.

- τ decays [74, 75]. α_s at a small energy scale of m_τ is extracted from the normalized semi-leptonic branching ratio of τ

$$R_\tau = \frac{\Gamma(\tau \to \text{hadrons} + \nu_\tau)}{\Gamma(\tau \to e\nu_e\nu_\tau)}. \tag{2.27}$$

- Lattice QCD [76–81]. α_s is extracted by comparing lattice QCD calculation of the mass difference of Υ, Υ' ,Υ'' and χ_b or the charmonium system with the results from experiments.

- Υ decay [82]. α_s at the heavy quark mass scale is extracted from the ratio of partial decay widths of Υ into hadrons and $\mu^+\mu^-$.

The values of α_s obtained by these methods are combined into one value in by Particle Data Group (PDG) group. [59]. The values obtained by these methods and the combined value given in [59] are shown in Figure 2.7. The combined value is

$$\alpha_s(M_Z) = 0.1171 \pm 0.0014\ . \tag{2.28}$$

The combined value,$\alpha_s(M_Z) = 0.1183 \pm 0.0027$, was obtained by S.Bethke [60] also. In the combination, the most significant determinations of α_s, based on complete NNLO QCD calculations [74, 75, 83–89] are used. According to [60], small systematic differences between DIS and e^+e^- results and between those obtained from low and from high energy data are seen. These may well be accidental or may be caused, for example, by different methods of treating renormalization and factorization scales.

2.3.4 Event Shape Variables

The six event shape variables among variables which NLLA and $\mathcal{O}(\alpha_s^2)$ calculation are available are used in this analysis. They are defined in the following part.

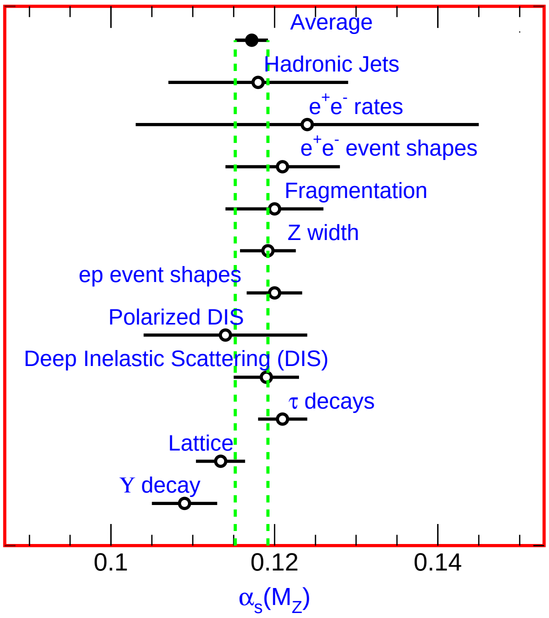

Figure 2.7: Summary of the values of α_s used in the combination by PDG. The values of α_s extrapolated up to $\mu = M_Z$. The errors are the *total* errors including theoretical uncertainties.

Thrust The thrust T is defined [35] by

$$T = \max_{\vec{n}} \left(\frac{\sum_i |\vec{p}_i \cdot \vec{n}|}{\sum_i |\vec{p}_i|} \right) \quad . \tag{2.29}$$

where i runs over all the final state particles, and the axis $\vec{n}$ is chosen to maximize the value of the expression in parenthesis; this axis $\vec{n}$ is referred to as the thrust axis. In this analysis, the observable $(1 - T)$ is used, which tends to zero in the two-jet region like other observables.

Heavy Jet Mass This variable has been proposed in [35]. The particles in an event are formed into two groups by the plane orthogonal to the thrust axis, $\vec{n}$, and the invariant mass of each group is computed. The heavier mass is defined as M_H. For the determination of α_s the scaled variable $M_H/\sqrt{s}$ is used, where s is the square of the center-of-mass energy. In this thesis, M_H means the scaled heavy jet mass. To first order in α_s the heavy jet mass and thrust are related by $(1 - T) = M_H^2/s$.

Jet Broadening measures These observables have been suggested in [36, 37]. The particles in an event is divided into two hemispheres, $S_\pm$, by the plane orthogonal to the thrust axis , $\vec{n}$. In each hemisphere, the quantity:

$$B_\pm = \left(\frac{\sum_{i \in S_\pm} |\vec{p}_i \times \vec{n}_T|}{2 \sum_i |\vec{p}_i|} \right) \tag{2.30}$$

is computed, where the sum in the denominator runs over all particles, while that in the numerator runs over one hemisphere. The observables used for the study of α_s are

$$B_T = B_+ + B_- \quad \text{and} \quad B_W = \max(B_+, B_-) \tag{2.31}$$

referred to as the "total jet broadening" and "wide jet broadening" respectively. To leading order in α_s, $B_T = B_W$. Both B_T and B_W tend to zero in the two-jet region. These variables are sensitive to the transverse structure of jets, and may therefore be complementary to $(1-T)$ and $M_H/\sqrt{s}$, which depend on the longitudinal momenta.

C-parameter The C-parameter was initially defined as [90, 91]

$$C = 3(\lambda_1\lambda_2 + \lambda_2\lambda_3 + \lambda_3\lambda_1) \tag{2.32}$$

where λ_α $(0 \leq \lambda_\alpha \leq 1, \sum_\alpha \lambda_\alpha = 1)$ are the eigenvalues of the linearized momentum tensor

$$\Theta^{\alpha\beta} = \frac{\sum_i \vec{p}_i^{\,\alpha}\vec{p}_i^{\,\beta}/|\vec{p}_i|}{\sum_j |\vec{p}_j|} \tag{2.33}$$

The sums runs over all final-state particle. The kinematic range is $0 \leq C \leq 1$, with $C = 0$ for a perfectly two-jet-like final state and 1 for an isotropic and acoplanar distribution of final-state momenta.

Jet Rates The jet rates through the "Durham" scheme are defined as follows [45,92,93]. The jet resolution variable y_{ij} is defined for each pair of particles i and j by

$$y_{ij} = \frac{2\min(E_i^2, E_j^2)(1-\cos\theta_{ij})}{E_{vis}^2} \tag{2.34}$$

where E_i and E_j are energies of two particles or jets i and j, θ_{ij} is the angle between them and E_{vis} is again the sum over the energies of all particles in the event. If the smallest value of y_{ij} is smaller than some cutoff y_{cut} then particles i and j are replaced by the sum of their four-momenta. After all pairs satisfying $y_{ij} > y_{cut}$, the particles are called as "jets". QCD calculations are available for two-jet rates $R_2(y_{cut}) = \sigma_{2-jet}(y_{cut})/\sigma_{tot}$. A fitting to data is performed with the differential jet rate $D_2(y_{cut}) \equiv dR_2(y_{cut})/dy_{cut}$ instead of $R_2(y_{cut})$. In this document, y_{23}^D indicate the differential jet rate through the "Durham" scheme.

2.4 Resummed and Fix Order QCD calculation

The NLLA and $\mathcal{O}(\alpha_s^2)$ calculations have to be combined before they are fitted to data. There are a number of different schemes to combine them. Four schemes are explained here. They are referred as 'ln(R)-matching', 'R-matching', 'modified R-matching' and 'modified ln(R)-matching', through not all schemes are applicable to all seven observables. All matching schemes embody the full $\mathcal{O}(\alpha_s^2)$ result, together with the resummation of leading and next-to-leading logarithms, but they they differ in higher orders.

For all event shape variables considered in this thesis, the cumulative cross-section for event shape y is written in the general form:

$$R(y) \equiv \int_0^y \frac{1}{\sigma}\frac{d\sigma}{dy}dy = C(\alpha_s)\exp G(\alpha_s, L) + D(\alpha_s, y) \tag{2.35}$$

where y is $(1-T)$, M_H^2/s,B_T,B_W and C in the case of event shapes and $y_{\rm cut}$ for jet rates, and $L \equiv \ln(1/y)$. $D(\alpha_s, y)$ is a remainder function which should vanish as

$y \to 0$. The general structure of the cross-section in powers of α_s and of large logarithms is indicated in Table 2.1. The functions C and G may be written:

$$C(\alpha_s) = 1 + \sum_{n=1}^{\infty} C_n \overline{\alpha}_s^n \tag{2.36}$$

and

$$G(\alpha_s, L) = \sum_{n=1}^{\infty} \sum_{m=1}^{n+1} \equiv Lg_1(\alpha_s, L) + g_2(\alpha_s, L) + \alpha_s^2 g_4(\alpha_s, L) \cdots , \tag{2.37}$$

where for brevity we write $\overline{\alpha}_s$ for $(\alpha_s/2\pi)$. The functions $Lg_1(\alpha_s, L)$ and $g_2(\alpha_s, L)$ represent the sums for the leading and next-to-leading logarithms respectively, to all orders in α_s (see Table 2.1). The NLLA calculations give an approximate expression for $R(y)$ in the form:

$$R_{NLLA}(y) = (1 + C_1\overline{\alpha}_s + C_2\overline{\alpha}_s^2) \exp[Lg_1(\alpha_s, L) + g_2(\alpha_s, L)]. \tag{2.38}$$

The functions g_1 and g_2 are given by the NLLA calculations; the coefficient C_1 is known exactly from the $\mathcal{O}(\alpha_s)$ matrix elements and C_2 is known from numerical integration of the $\mathcal{O}(\alpha_s^2)$ matrix elements; their values are summarized in Table 2.2, Table 2.3 and Table 2.4. The full $\mathcal{O}(\alpha_s^2)$ calculation yields an approximate expression for $R(y)$ of the form:

$$R_{\mathcal{O}(\alpha_s^2)}(y) = 1 + \mathcal{A}(y)\overline{\alpha}_s + \mathcal{B}(y)\overline{\alpha}_s^2. \tag{2.39}$$

The coefficients $\mathcal{A}(y)$ and $\mathcal{B}(y)$ are obtained from program `EVENT` in case of this analysis.

The theoretical prediction of six event shape variables which are used in this analysis are shown in Figure 2.8. The predictions by Monte Carlo (`JETSET` is used as a representative) are shown in the figures also. The $\mathcal{O}(\alpha_s)$ calculation predicts large cross-section in the region where the event shape become zero. The cross-section is suppressed in this region in the $\mathcal{O}(\alpha_s^2)$ calculation and increases in the region with larger event shape value. On the other hand, the LLA and NLLA predict smaller cross-section at the region than $\mathcal{O}(\alpha_s)$ or $\mathcal{O}(\alpha_s^2)$. The cross-sections don't drop in the region with much larger event shape variable in NLLA or LLA. In $\mathcal{O}(\alpha_s^2)$ + NLLA calculation, the cross-section is similar to NLLA in the small event shape region and is similar to $\mathcal{O}(\alpha_s^2)$ in large event shape region. The prediction by Monte Carlo is close to the $\mathcal{O}(\alpha_s^2)$ + NLLA calculation.

2.4.1 Matching Schemes

The simplest matching scheme involves taking the logarithm of Equation 2.39 and expanding as a power series, yielding:

$$\ln R_{\mathcal{O}(\alpha_s^2)}(y) = \mathcal{A}(y)\overline{\alpha}_s + \left[\mathcal{B}(y) - \frac{1}{2}\mathcal{A}(y)^2\right]\overline{\alpha}_s^2 + \mathcal{O}(\alpha_s^3), \tag{2.40}$$

and similarly rewriting Equation 2.38 as:

$$\ln R_{NLLA}(y) = Lg_1(\alpha_s, L) + g_2(\alpha_s, L) + C_1\overline{\alpha}_s + \left[C_2 - \frac{1}{2}C_1^2\right]\overline{\alpha}_s^2 + \mathcal{O}(\alpha_s^3). \tag{2.41}$$

Removing the terms to $\mathcal{O}(\alpha_s^2)$ in the NLLA expression (Equation 2.41), replacing them by the $\mathcal{O}(\alpha_s^2)$ terms from Equation 2.40 and neglecting non-logarithmic terms of higher order yields:

$$\begin{aligned}\ln R(y) &= Lg_1(\alpha_s, L) + g_2(\alpha_s, L) - (G_{11}L + G_{12}L^2)\overline{\alpha}_s - (G_{22}L^2 + G_{23}L^3)\overline{\alpha}_s^2 \\ &\quad + \mathcal{A}(y)\overline{\alpha}_s + \left[\mathcal{B}(y) - \frac{1}{2}\mathcal{A}(y)^2\right]\overline{\alpha}_s^2. \end{aligned} \tag{2.42}$$

This procedure will be referred to as 'ln(R)-matching'. Alternatively the analogous procedure may be carried out for the functions $R(y)$ instead of $\ln(R(y))$, yielding:

$$\begin{aligned}R(y) &= (1 + C_1\overline{\alpha}_s + C_2\overline{\alpha}_s^2)\exp Lg_1(\alpha_s, L) + g_2(\alpha_s, L) - (C_1 + G_{11}L + G_{12}L^2)\overline{\alpha}_s \\ &\quad - \left[C_2 + G_{22}L^2 + G_{23}L^3 + (G_{11} + G_{12}L^2)(C_1 + \frac{1}{2}(G_{11} + G_{12}L^2))\right]\overline{\alpha}_s^2 \\ &\quad + \mathcal{A}(y)\overline{\alpha}_s + \mathcal{B}(y)\overline{\alpha}_s^2. \end{aligned} \tag{2.43}$$

This procedure will be refereed to as 'R-matching'. It would be expected that R-matching would be less reliable than the ln(R)-scheme, because sub-leading term $G_{21}\overline{\alpha}_s^2 L$, which does not vanish as $y \to 0$, is not exponentiated in Equation 2.43, whereas it is exponentiated in Equation 2.42 because it is implicitly included in the $\mathcal{B}(y)$ coefficient. This leads one to consider a modified from of Equation 2.43 in which the $G_{21}\overline{\alpha}_s^2 L$ term is included in the argument of the exponential, and subtracted after exponentiation. This is referred as 'modified R-matching' scheme here. The coefficient G_{21} is not known analytically, but may be inferred approximately from numerical integration of the $\mathcal{O}(\alpha_s^2)$ matrix elements. The relevant G_{nm} coefficients insofar as they are known, are given in Table 2.2, Table 2.3 and Table 2.4, based on [94] for $(1-T)$ and M_H, [37] for B_T and B_W, [95] for C and [46] for jet rate. A further problem is that the NLLA calculations are not guaranteed to satisfy the necessary constraints, $R(y) \to 1$ and $dR(y)/dy \to 0$, at kinematic limit, y_{max}, corresponding to the region of hard gluon emission. In consequence the combined NLLA+$\mathcal{O}(\alpha_s^2)$ calculation may fit data less well than the $\mathcal{O}(\alpha_s^2)$ expression in the hard region. It has been proposed [94, 96] that this difficulty could be overcome in the ln(R)-matching scheme by replacing L in the NLLA part of Equation 2.42 by $L' = \ln(y^{-1} - y_{max}^{-}1 + 1)$. This is referred as 'modified ln(R)-matching'.

	Leading logs	Next-to-Leading logs	Sub-leading logs	Non-logarithmic terms	
$\ln R(y) =$	$G_{12}\overline{\alpha}_s L^2$	$+G_{11}\overline{\alpha}_s L$		$+\alpha_s\mathcal{O}(1)$	$= \mathcal{A}(y)\overline{\alpha}_s$
	$+G_{23}\overline{\alpha}_s^2 L^3$	$+G_{22}\overline{\alpha}_s^2 L^2$	$+G_{21}\overline{\alpha}_s^2 L$	$+\alpha_s^2\mathcal{O}(1)$	$= (\mathcal{B}(y) - \frac{1}{2}\mathcal{A}(y)^2)\overline{\alpha}_s^2$
	$+G_{34}\overline{\alpha}_s^3 L^4$	$+G_{33}\overline{\alpha}_s^3 L^3$	$G_{32}\overline{\alpha}_s^3 L^2$	$+\cdots$	$\mathcal{O}(\alpha_s^3)$
	$+G_{45}\overline{\alpha}_s^4 L^5$	$+G_{44}\overline{\alpha}_s^4 L^4$	$G_{43}\overline{\alpha}_s^4 L^3$	$+\cdots$	$\mathcal{O}(\alpha_s^4)$
	$+\cdots$	$+\cdots$	$+\cdots$	$+\cdots$	
$=$	$Lg_1(\alpha_s L)$	$+g_2(\alpha_s L)$	$+\cdots$	$+\cdots$	$\overline{\alpha_s} \equiv \frac{\alpha_s}{2\pi}$

Table 2.1: Decomposition of the cumulative cross-section.

Variable	C_1	C_2
$(1-T)$	$(-\frac{5}{2}+\frac{\pi^2}{3})C_F$	-42 ± 22
M_H	$(-\frac{5}{2}+\frac{\pi^2}{3})C_F$	-48 ± 20
B_T	$(-\frac{17}{2}+\pi^2)C_F$	14.6 ± 1.6
B_W	$(-\frac{17}{2}+\pi^2)C_F$	18.5 ± 1.6
C	$(-\frac{5}{2}+\frac{2\pi^2}{3})C_F$	76.5 ± 2.9
y_{23}	$(-\frac{5}{2}+\frac{\pi^2}{6}-6\ln 2)C_F$	$-$

Table 2.2: Coefficients used in the matching of the $\mathcal{O}(\alpha_s^2)$ and NLLA QCD calculation.

Variable	G_{12}	G_{11}	G_{23}
$(1-T)$	$-2C_F$	$3C_F$	$-\frac{11}{3}C_FC_A+\frac{2}{3}C_Fn_f$
M_H	$-2C_F$	$3C_F$	$-\frac{11}{3}C_FC_A+\frac{2}{3}C_Fn_f$
B_T	$-4C_F$	$6C_F$	$-\frac{88}{9}C_FC_A+\frac{16}{9}C_Fn_f$
B_W	$-4C_F$	$6C_F$	$-\frac{88}{9}C_FC_A+\frac{16}{9}C_Fn_f$
C	$-2C_F$	$3C_F$	$-\frac{11}{3}C_FC_A+\frac{2}{3}C_Fn_f$
y_{23}	$-C_F$	$3C_F$	$-\frac{11}{9}C_FC_A+\frac{2}{9}C_Fn_f$

Table 2.3: Coefficients used in the matching of the $\mathcal{O}(\alpha_s^2)$ and NLLA QCD calculation.

Variable	G_{22}	G_{21}
$(1-T)$	$-\frac{4}{3}\pi^2C_F^2+(\frac{\pi^2}{3}-\frac{169}{36})C_FC_A+\frac{11}{18}C_Fn_f$	$+30\pm 8$
M_H	$-\frac{2}{3}\pi^2C_F^2+(\frac{\pi^2}{3}-\frac{169}{36})C_FC_A+\frac{11}{18}C_Fn_f$	$+36\pm 11$
B_T	$-(32\ln^2 2+\frac{8}{3}\pi^2)C_F^2+(\frac{2\pi^2}{3}-\frac{35}{9})C_FC_A+\frac{2}{9}C_Fn_f$	$+12.5\pm 1.6$
B_W	$-(32\ln^2 2)C_F^2+(\frac{2\pi^2}{3}-\frac{35}{9})C_FC_A+\frac{2}{9}C_Fn_f$	$+11.7\pm 1.6$
C	$-\frac{4}{3}\pi^2C_F^2+(\frac{\pi^2}{3}-\frac{169}{36})C_FC_A+\frac{11}{18}C_Fn_f$	$+63.4\pm 6.0$
y_{23}	$(-\frac{35}{36}+\frac{\pi^2}{6})C_FC_A-\frac{1}{18}C_Fn_f$	$-$

Table 2.4: Coefficients used in the matching of the $\mathcal{O}(\alpha_s^2)$ and NLLA QCD calculations.

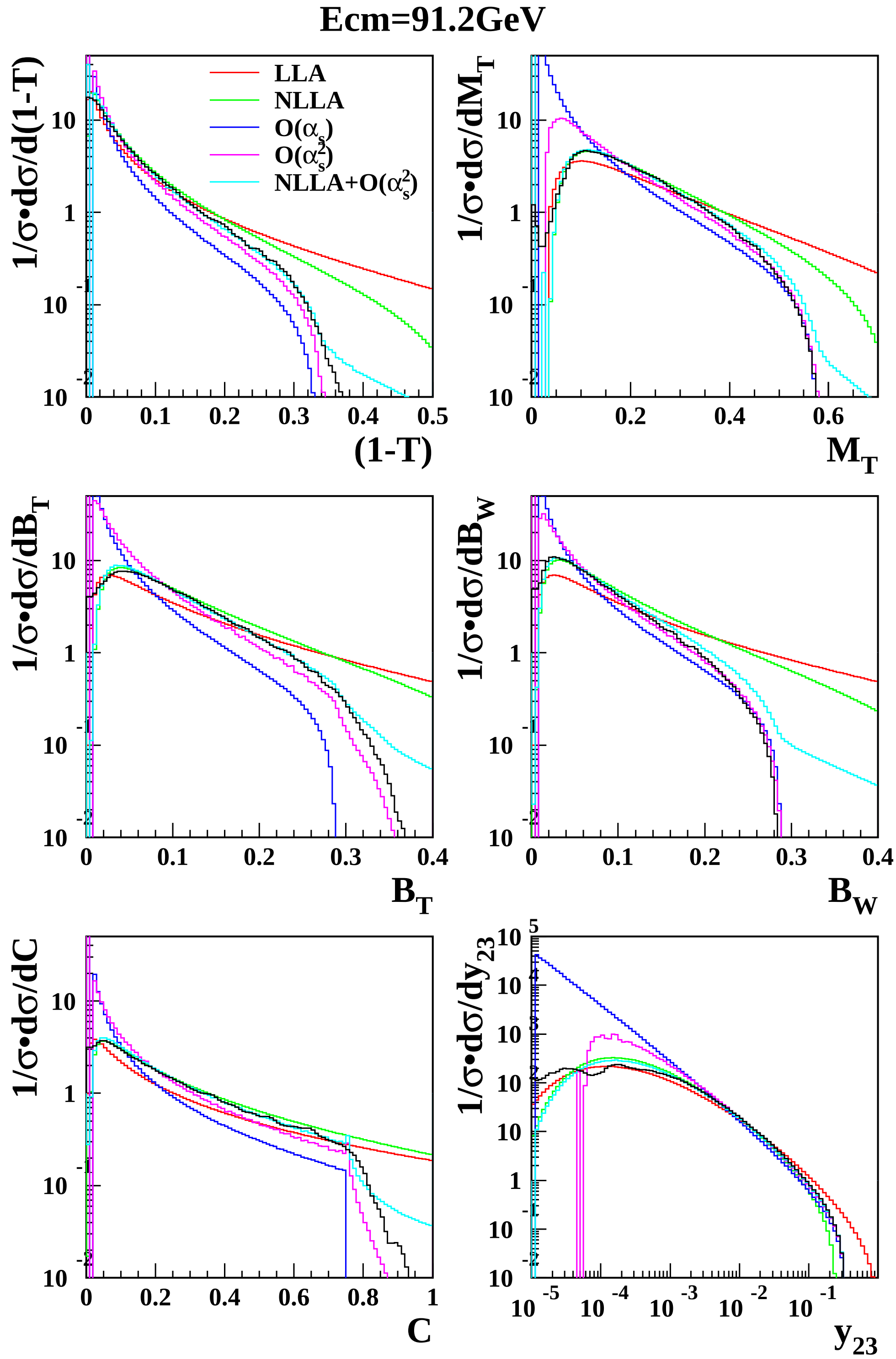

Figure 2.8: Theoretical prediction of event shape variables.

Chapter 3

Photon Radiation in Hadronic Events

It has been recognized that direct photon production with large angle to quarks can be used to explore the properties and interactions of quarks and gluons at short distance [97, 98]. Since the photons leave the short distance regime without further interactions in contrast to quarks and gluons, they allow a direct view of the physics at short distance. In this analysis, we measure the strong coupling constant with radiative hadronic events selected from LEP1 data. After a brief summary of theoretical calculations of cross-sections of radiative hadronic events, we explain the relation between this measurements and usual measurements using non-radiative hadronic events.

3.1 Matrix Element Calculation

The partial width of the decay of Z^0 with final state photon radiation in e^+e^- annihilation is calculated up to $\mathcal{O}(\alpha\alpha_s)$ by G. Kramer and B. Lampe in 1991 [99]. It can be obtained by replacing one of gluons by a photon in their calculation of jet cross sections up to $\mathrm{O}(\alpha_s^2)$ [100].

The partial width of the Z^0 into a photon and n jets, $\Gamma(\mathrm{Z}^0 \to \gamma + n\mathrm{jets})$, is represented by the ratio to the hadronic Z^0 width $\Gamma_{\mathrm{had}} = \Gamma(\mathrm{Z}^0 \to \mathrm{X})$, where X stands for all hadronic final state.

$$\frac{\Gamma(\mathrm{Z}^0 \to +n\mathrm{jets})}{\Gamma_{\mathrm{had}}} = \frac{(\frac{8}{9}c_{\mathrm{u}} + \frac{1}{3}c_{\mathrm{d}})(\alpha/2\pi)g_n(y)}{(2c_{\mathrm{u}} + 3c_{\mathrm{d}})\left[1 + \alpha_s/\pi + 1.42(\alpha_s/\pi)^2\right]}, \tag{3.1}$$

where c_{u} and c_{d} are overall couplings of the Z^0 to up and down type quarks, and $c_{\mathrm{f}} = v_{\mathrm{f}}^2 + a_{\mathrm{f}}^2$. g_n is a function of the resolution cut y, which is lower cut value of a minimum invariant mass of two jets defined by

$$y_{ij} = (p_i + p_j)^2/s, \tag{3.2}$$

where $p_i(p_j)$ is the momentum of i'th (j'th) jet and s is the invariant mass squared of the

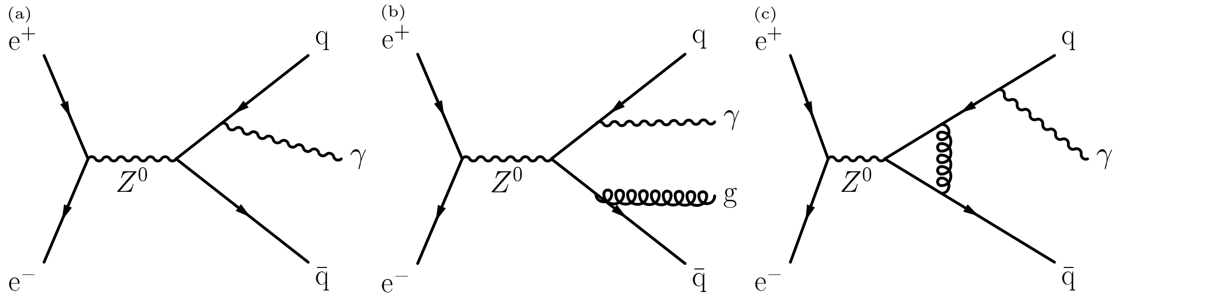

Figure 3.1: Examples of Feynman diagrams contributing to the (a) leading order, (b) next-to-leading order real, and (c) next-to-leading order virtual terms in the $q\bar{q}\gamma$ matrix element calculation.

system. In case of $\mathcal{O}(\alpha_s^2)$, $g_1(y)$, $g_2(y)$ and $g_3(y)$ are given in the following form;

$$g_1(y) = g_1^{(0)} + \frac{\alpha_s}{2\pi} g_1^{(1)}(y), \tag{3.3}$$

$$g_2(y) = g_2^{(0)} + \frac{\alpha_s}{2\pi} g_2^{(1)}(y), \tag{3.4}$$

$$g_3(y) = \frac{\alpha_s}{2\pi} g_3^{(1)}(y), \tag{3.5}$$

where $g_1^{(0)}$, $g_1^{(1)}$, $g_2^{(0)}$, $g_2^{(1)}$ and $g_3^{(1)}$ are given in the form of tables in [99].

Some of the Feynman diagrams contributing at the leading order and the next-to-leading order are shown in Figure 3.1. The diagram (a) in Figure 3.1 contributes to $g_1^{(0)}$ and $g_2^{(0)}$. The three parton final state diagram (b) contributes to $g_1^{(0)}$, $g_2^{(0)}$ and $g_3^{(1)}$. The diagram (c) contributes to $g_1^{(1)}$ and $g_2^{(1)}$.

Since a photon has a hadronic component, the inclusive photon production cross section is described by the convolution with the fragmentation function of photons. The fragmentation function contains non-perturbative origin singularities. To get a well defined cross section in perturbative QCD, the singularities are subtracted and absorbed into the photon fragmentation function (factorization theorem).

In measurement of the cross-section, it is required for photon candidates to be isolated from hadrons originated in quarks and gluons to reduce huge π^0 backgrounds. In perturbative QCD, the isolation condition causes a problem. The photon can not be completely isolated from gluons without breaking cancellation of soft gluon singularity between virtual and real gluons. The cancellation of infrared divergence is crucial in order to get a sensible cross-section. The cone approach [101–106] and the democratic approach [107, 108] have been used for theoretical calculation and analysis of experimental data. In the cone approach, the energy deposit inside the cone around a photon is required to be small. In the democratic approach, jets are reconstructed from all partons (or clusters and tracks) including photons. If the ratio of the hadronic energy over total energy of a jet is smaller than some threshold (usually 10%), the jet is identified as a photon. The former approach is simple and widely used in experimental data analyses (including the analyses in this thesis). the latter approach is more preferable to extract the non-perturbative parton to photon fragmentation function from data.

For the cone approach, it is pointed out that a small fraction of hadronic energy inside the cone gives rise to large logarithms of the fraction. It is associated with soft gluon emission into the isolation cone. A new approach was suggested by S. Frixione [109]. The isolation is refined by allowing less hadronic energy around the photon in the approach. It has been used in studies for prompt photon production at RHIC and LHC.

3.2 Mechanism of Photon Radiation in Monte Carlo Simulation

Detailed discussions on the implementation of photon radiation in event generator are reviewed by authors in [110–113].

JETSET,HERWIG Final state photons are emitted by using basically the same algorithm of parton shower evolution as gluon radiation in these Monte Carlo generators. e_q^2 and α_{em} are used in the photon radiation instead of C_F and α_s. Photons are assumed to be massless in JETSET. Therefore, processes like $\gamma \to q\bar{q}$ and $\gamma \to l\bar{l}$ are not implemented. α_{em} is fixed to 1/137 and has no energy scale dependence.

ARIADNE The differential cross section for radiating a photon from a $\mathrm{q\bar{q}}$ dipole is given by;

$$\frac{d\sigma_\gamma}{dx_1 dx_3} = \frac{\alpha_{EM}}{2\pi} e_q^2 \frac{x_1^2 + x_3^2}{(1-x_1)(1-x_3)} \tag{3.6}$$

where $x_i = 2E_i/\sqrt{S_{dip}}$ are the energy fractions after emission with the two quarks denoted 1 and 3. S_{dip} is the dipole mass. The equation is obtained by appropriately replacing factors of the first equation in Equation 2.9. The probability of emitting a photon is equal at phase space the naive cross section for photon emission at this point times the probability of not having any emissions of photons or gluons at a higher p_T^2.

3.3 Status of Measurement of Isolated Photon Rate

As mentioned in Section 3.1, the isolated photon rate in the process $\mathrm{e^+e^-} \to$ hadrons can be predicted with the quark-to-photon fragmentation function [114, 115]. The prediction of inclusive prompt photon energy spectra are found to be in agreement with measured data [1, 116]. The energy spectrum of prompt photons is shown in Figure 3.2 with the predictions from various parameterizations and extensions of [114, 115].

The huge amount of neutral pions coming from jets becomes the dominant background in analyses using high energy photons. In the OPAL analysis [1], the fraction of the background is obtained by fitting the cluster shape fit variable which is described in Section 5.2.3. Although the energy spectrum of prompt photons which is obtained by using the purity agrees with the theoretical prediction, the underestimation of the prompt photon rate by Monte Carlo simulation is reported in [2, 3, 18, 117].

ALEPH shows that JETSET predicts 20-30% lower cross-section than data in [117]. DELPHI shows that there is an excess of data by $18 \pm 7\%$ in the region of the photon spectrum below 15GeV [2](Figure 3.3). OPAL find photon candidates by the democratic approach described in Section 3.1 [18]. The cross-section predicted by JETSET is $25-30\%$ lower than measured crosssections in the $y_{\rm cut}$ range from 0.002 to 0.100. In addition to the

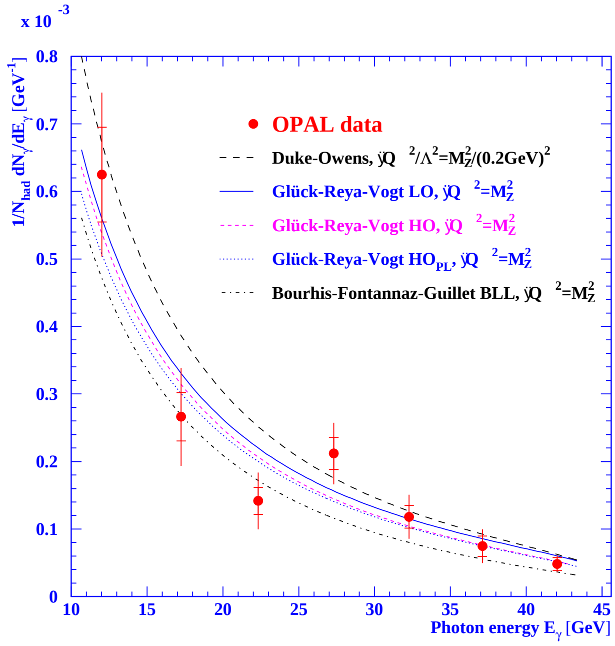

Figure 3.2: The energy spectrum of prompt photons measured in hadronic Z^0 decays and various theoretical predictions. [1]

use of different jet finding algorithm, the uncertainty on the π^0 background rate makes the comparison difficult, since the opening angle of photons which are decayed from a π^0 is small for a high energy π^0. The reconstruction of π^0 is difficult for the photon energy around 15GeV.

L3 addressed the problem in the study on isolated hard photon emission in Z^0 decays [3]. The normalization of the background Monte Carlo distribution is decided by fitting the cluster shape distribution which is predicted by `JETSET` to the distribution which is obtained from data. When the normalization is used, a discrepancy is found in low cluster energy region (Figure 3.4). L3 pushed the study with more data statistics and with different methods for estimation of neutral hadron background [118]. They reconstruct π^0 with energy smaller than 8GeV and estimate background rate by employing a artificial neural net for photon candidates with larger energy. They report that, when the energy deposit inside the cone with opening angle of 10° is restricted to be smaller than 50MeV, `JETSET` reproduce the π^0 rate. But, when the opening angle is set to 25°, `JETSET` underestimates obviously the rate for π^0 with a smaller energy than 8GeV. For larger energy π^0, the data is about a factor 2 larger than the prediction over full energy range. The discrepancy increases for tighter isolation cuts. `HERWIG` tends to give a slightly better description but still underestimates the rate. More recently, L3 reported yet another analysis on the isolated photon emission in Z^0 decays [119]. The analysis uses the new method for background estimation with a reduced dependence on Monte Carlo input. The method is based on the event activity around vectors placed in event locations topologically similar to the selected photon candidates. The discrepancy of the energy spectrum between data and `JETSET` is seen in this analysis also. But `HERWIG` reproduces the spectrum.

The status of the problem at LEP is summarized in the report of LEP2 workshop [120]. Since the problem has not been resolved yet, the Monte Carlo is not used for the estimation of background rates as much as possible in this study.

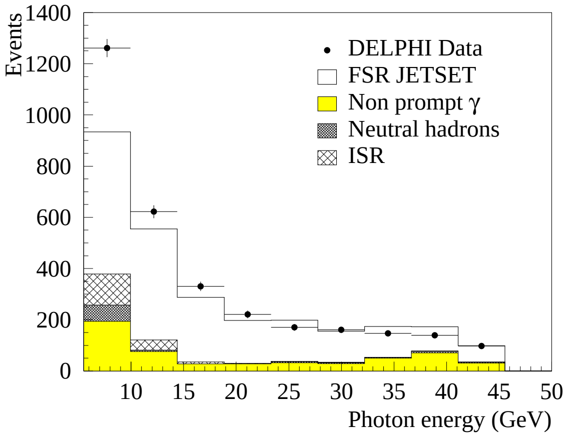

Figure 3.3: The energy spectrum of isolated final state photons observed in the data and predicted by `JETSET` 7.4 PS. [2]

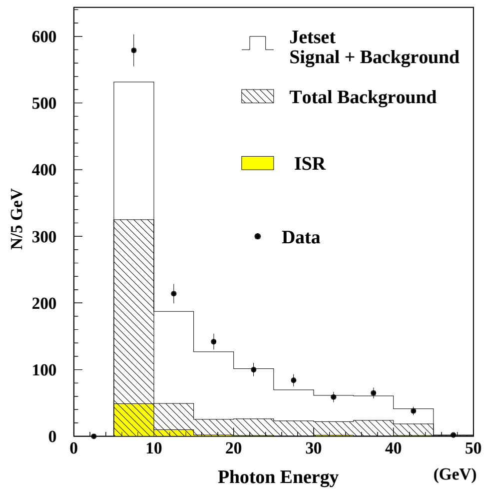

Figure 3.4: Photon energy distribution in [3]. The Monte Carlo distributions are the `JETSET` predictions for the signal, the total background and the initial state radiation background.

3.4 Effect of photon radiation on Event Shape Variables

In a naive picture, if FSR is emitted sufficiently earlier than gluon emissions, it is natural to regard the invariant mass of quark system after the photon emission as the energy scale which is used in the gluon radiation. In parton shower models, a state with a few partons of high virtuality is evolved to a larger number of lower virtuality partons. As described in Section 2.1.2, m^2, opening angle and k_T are used as virtuality in `JETSET`, `HERWIG` and `ARIADNE`, respectively. If a photon is emitted with high energy and large opening angle to a quark, the emission should be done in the early stage of the evolution. However, it does not mean that a photon is always emitted before gluon radiation. The size of the effect of photons which are emitted after gluon radiation should be checked.

It is checked by comparing the mean value of event shapes for the non-radiative events and the radiative hadronic events in Monte Carlo generators. The center-of-mass energies are ranging from 15GeV to 80GeV. The mean values in `JETSET`, `HERWIG` and `ARIADNE` are shown in Figure 3.5, Figure 3.6 and Figure 3.7. The open squares show the mean values of event shapes which are obtained from 500k non-radiative events at each center-of-mass energy. The filled squares show the mean values which are obtained from 375k radiative events. The radiative events are boosted back to the center-of-mass system of hadrons. The effective center-of-mass energy $\sqrt{s'}$ for the radiative events is calculated from momenta of hadrons of the system.

The mean value for radiative events shows similar dependence as the mean value for non-radiative events. They agree well with each other in case of `ARIADNE`. In `JETSET`, the slope of mean values of $(1-T)$,M_H and B_T for radiative events is steeper than that for non-radiative events. Agreements of mean value between radiative events and non-radiative events for HERWIG at low $\sqrt{s'}$ is worst among these three models. The dependence is changed at $\sqrt{s'} = 35$GeV. Although there are some discrepancy for HERWIG and JETSET, the similar energy dependence in the mean values between the radiative events and the non-radiative events is shown by this check.

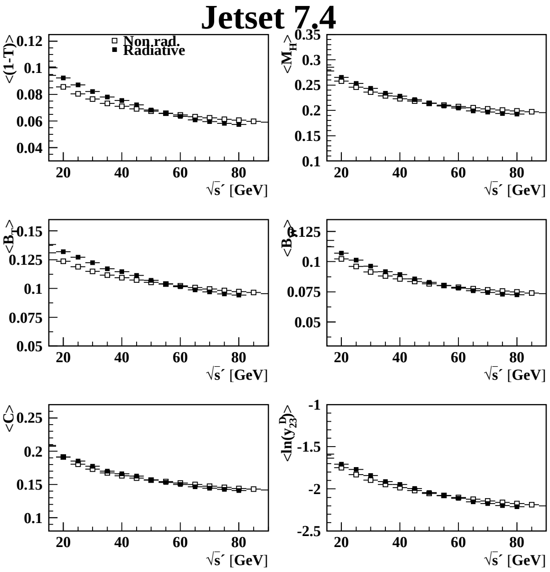

Figure 3.5: The mean value of event shape variables for radiative and non-radiative hadronic events which are obtained by JETSET 7.4.

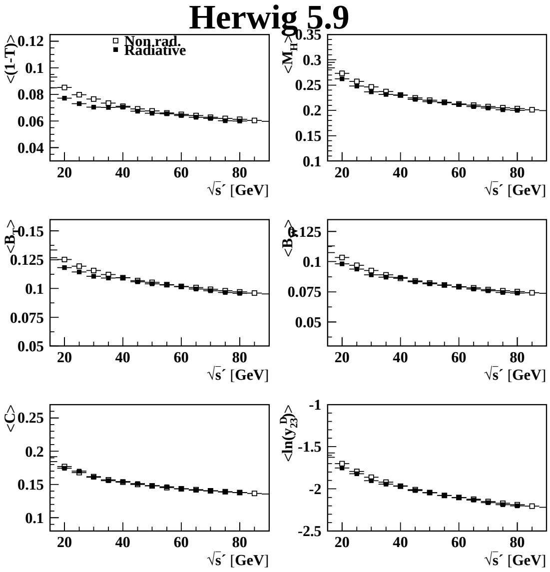

Figure 3.6: The mean value of event shape variables for radiative and non-radiative hadronic events which are obtained by HERWIG 5.9

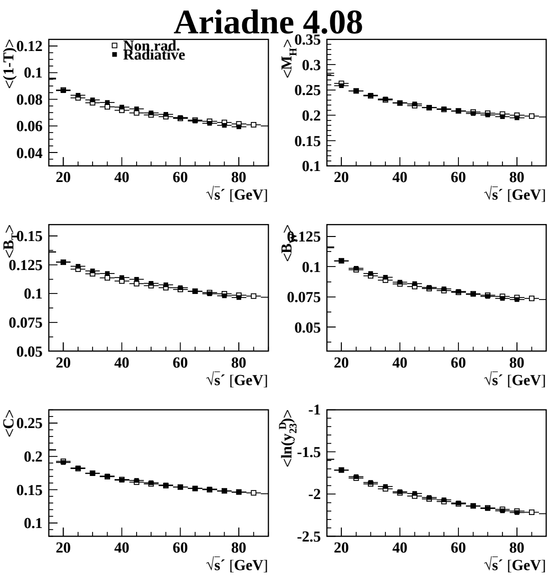

Figure 3.7: The mean value of event shape variables for radiative and non-radiative hadronic events which are obtained by ARIADNE 4.08

Chapter 4

The Experiment

4.1 The LEP Collider

The Large Electron-Positron collider (LEP) at CERN was commissioned on August 13, 1989, after 13 years of design work and construction. The LEP ring is 26.67 km in circumference and lies between 40 and 150m below the surface. The LEP ring consists of eight arcs and straight sections. The arcs contain magnetic cells to guide the beams around the ring. Each magnetic cell is comprised of a defocussing quadrupole, a vertical orbit corrector, a group of six bending dipoles, a focusing sextuple. The total length of a cell is 79.11m and each arc contains 31 of these cells. Acceleration of the beams occurs in the straight sections. The beams collide at interaction points situated at the center of four of eight straight sections. Four large detectors OPAL, ALEPH, DELPHI and L3, measure the products of these high energy collisions. Since its commissioning, LEP operated at at beam energies within a narrow range around 46 GeV to study of the Z resonance. Since the latter part of 1995, the beam energy has been increased continuously. This second phase of study is called as LEP2. In year 2000, the last year of LEP, the beam energy reached around 104 GeV. The integrated luminosities against the number of weeks between 1991 and 2000 are shown in Figure 4.2.

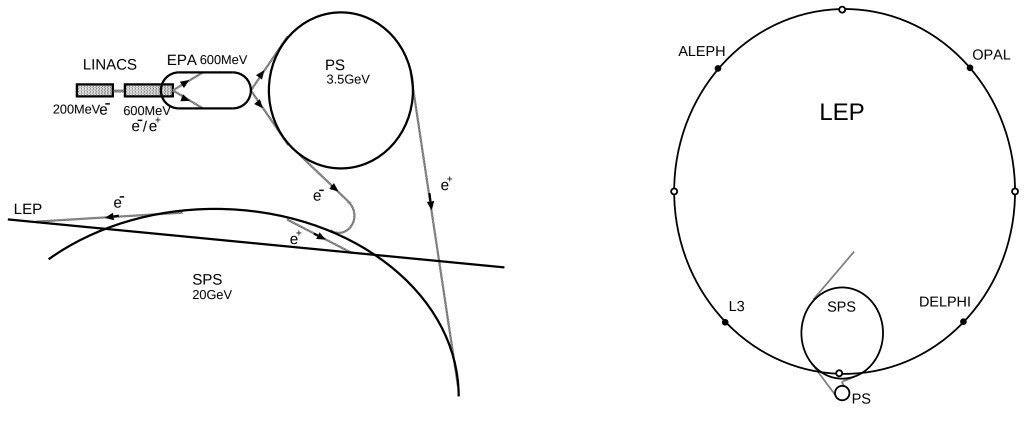

Figure 4.1: The LEP storage ring

The LEP ring is actually the last component of a five-step acceleration process that begins with a pair of 200 MeV and 600 MeV linear accelerators (LINACS), as depicted in Figure 4.1. These LINACS provide the initial beam particles which are then injected into the Electron-Positron Accumulator ring (EPA). The EPA collects these particles into bunches and transfers them into the 28 GeV Proton Synchrotron (PS), which has been modified to accelerate the electron and positron beams from 600MeV to 3.5GeV. Similarly, the 450 GeV Super Proton Synchrotron (SPS) has been altered to enable it to receive these 3.5 GeV beams, accelerate them to 20 GeV and inject them into LEP. Once 20 GeV beams have been extracted from the SPS, they are accelerated to the working beam energy in LEP by a system of 128 radio frequency (RF) copper cavities located in two of the straight section of the ring. In addition, a superconducting quadrupole is located on either side of each of the four experiments in order to give maximum reduction of the beam's transverse dimensions at the collision points. The cross-sectional profile of the beam spot at collision is typically about 10 μm in the vertical direction and 250 μm in the horizontal direction.

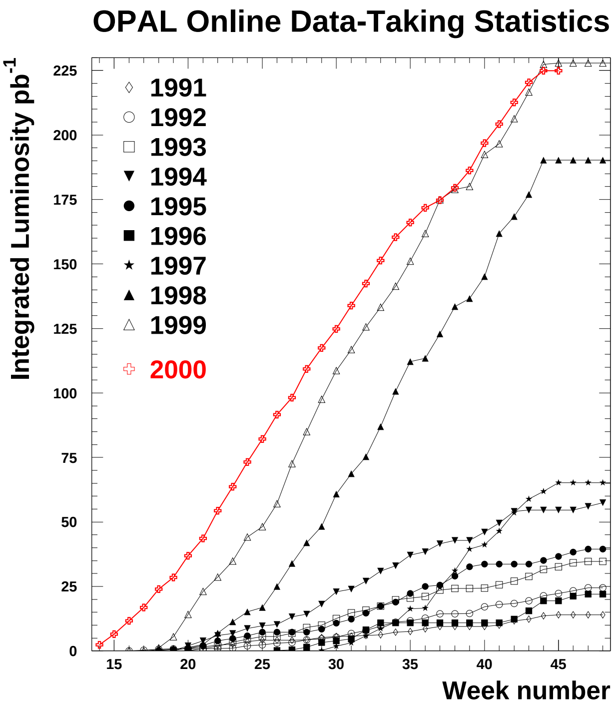

Figure 4.2: The LEP integrated luminosity

4.2 The OPAL detector

The OPAL(Omni-Purpose Apparatus for LEP) detector [121] operated at the LEP e^+e^- collider at CERN. It is a multipurpose apparatus designed to reconstruct all types of events occurring in e^+e^- collisions efficiently and accurately. The OPAL detector consists of a central tracking system, time-of-flight system, electromagnetic calorimeter system, hadron calorimeter system, muon detector and forward detectors (Figure 4.3). In the following sections these detector elements and their trigger and online system are briefly described.

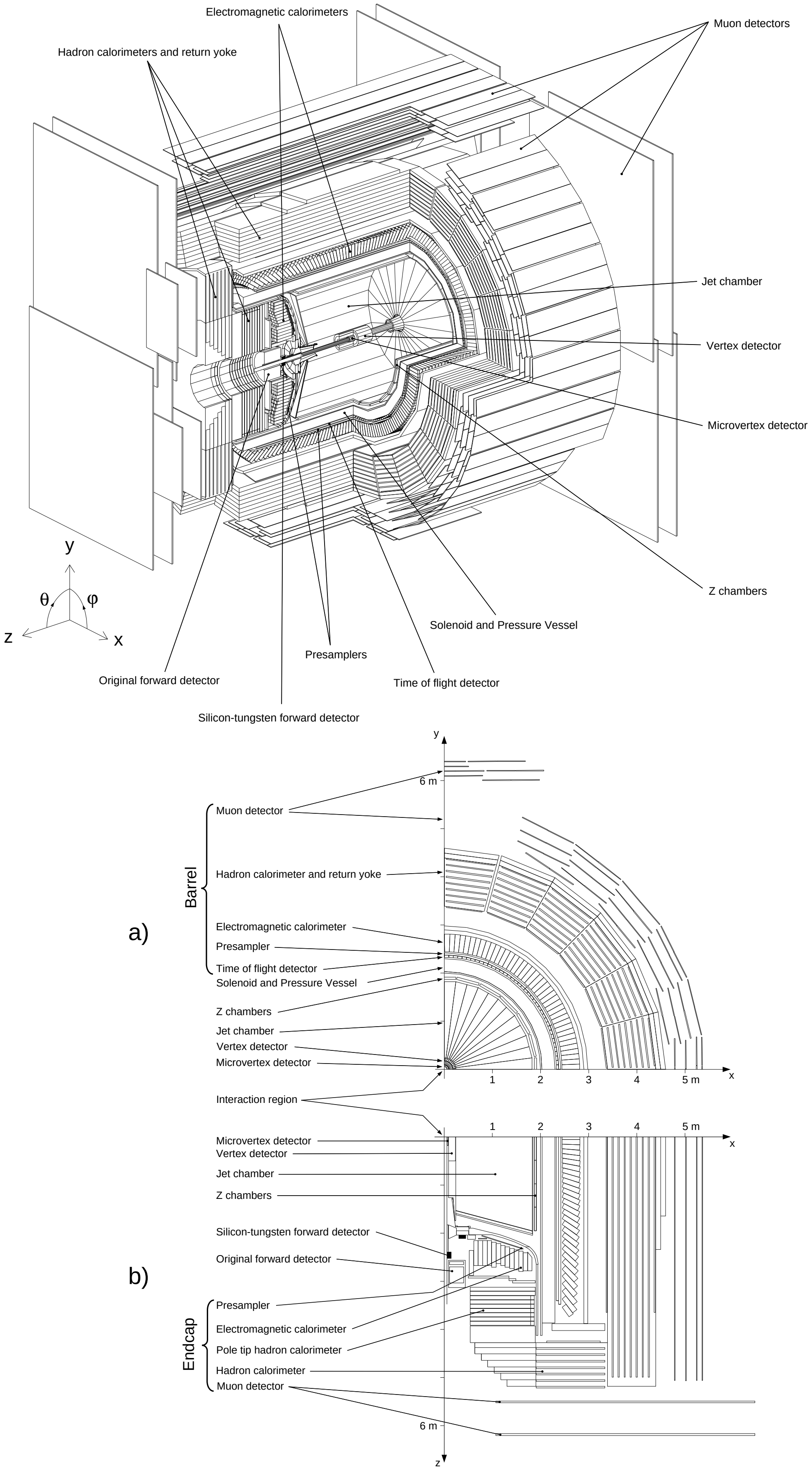

Figure 4.3: The OPAL detector

Central Tracking System

The central tracking system consists of a Silicon Microvertex detector and three drift chambers situated inside a pressure vessel holding a pressure of 4 bar. The central tracking system is inside a solenoid supplying a uniform axial magnetic field of 0.435T.

Silicon Microvertex Detector

The Silicon Microvertex Detector consists of two barrels of single sided Silicon Microstrip Detectors at radii of 6 and 7.5cm. The inner layer consists of 11 ladders and the outer of 14. Each ladder is 18 cm long and consists of 3 silicon wafers daisy chained together. There are 629 strips per detector at 25μm pitch and every other strip is read out at 50μm pitch. The number of ladders was increased to 12 and 15 and the ladders are tilted to close ϕ gaps. The outer layer was also extended from 3 to 5 wafers by addition of a layer of 2 wafer ladders at the -z end. The interaction points was still at the center of the 3 ladder wafer plus 2 wafer ladders with interaction point in the center of the five wafers.

Vertex Detector

The vertex detector is a high precision cylindrical jet drift chamber. It is 100 cm long with a radius of 23.5cm and consists of two layers of 36 sectors each. The inner layer contains the axial sectors, each containing a plane of 12 sense wires strung parallel to the beam direction. The wires range radially from 10.3 to 16.2 cm with a spacing of 0.583 cm. The outer layer contains the stereo sectors each containing a plane of 6 sense wires inclined at a stereo angle of $\sim 4°$. The stereo wires lie between the radii 18.8 and 21.3 cm with a spacing of 0.5cm.

A precise measurement of the drift time on to the axial sector sense wires allows the $r - \phi$ position to be calculated. Measuring the time difference between signals at either end of the sense wires allows a fast but relatively coarse z coordinate that used by the OPAL track trigger and in pattern recognition. A more precise z measurement is then made by combining axial and stereo drift time information offline. Multiple hits on a wire can be recorded. On each wire the hit nearest to the wire is known as the 'first hist' and others as 'second hits'.

Jet Chamber

The jet chamber is a cylindrical drift chamber of length 400 cm with an outer radius of 185cm and inner radius of 25cm. The chamber consists 24 identical sectors each containing a sense wire plane of 159 wires strung parallel to the beam direction. The end of planes are conical and can be described by $|z| = 147 + 0.268 \times R$. The coordinates of wire hits in the r-ϕ plane are determined from a measurement of drift time. The z coordinate is measured using a charge division technique and by summing the charges received at each end of a wire allow the energy loss, dE/dx to be calculated.

Z-Chamber

The Z-chambers provide a precise measurement of the z coordinate of tracks as they leave the jet chamber. They consist of a layer 24 drift chambers 400 cm long, 50 cm wide and 5.9 cm thick covering 94% of azimuthal angle and the polar angle range $|\cos\theta| < 0.72$.

Each chmber is divided in z into 8 cells of 50cm×50cm, with every cell containing 6 sense wires spaced at 0.4 cm.

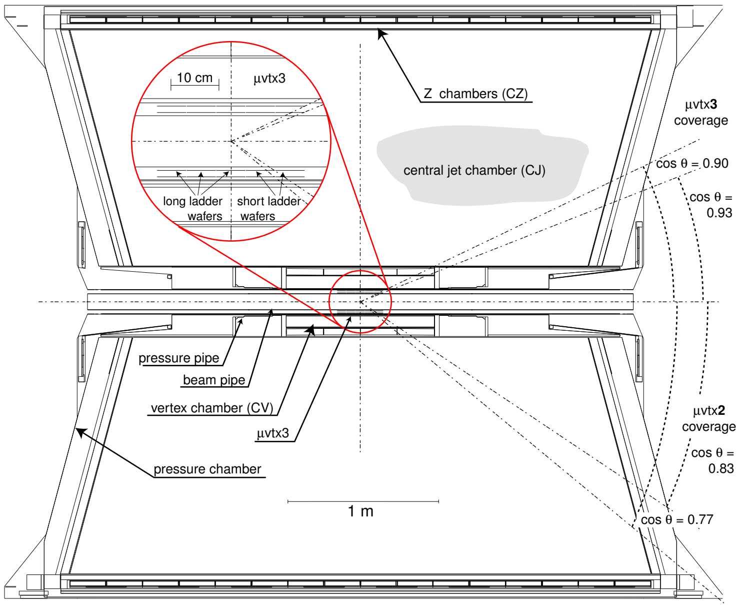

Figure 4.4: The central tracking system

Time-of-Flight System

The Time-of-Flight system provides charged particle identification in the range 0.6 to 2.5 GeV, fast triggering information and an effective rejection of cosmic rays. In the barrel region, it consists of 160 scintillation counters forming a barrel layer 684 cm long at a mean radius of 236 cm surrounding the OPAL coil covering the polar angle range $|\cos\theta| < 0.82$. In the endcap region, it consists of a 10mm thick scintillator layer, between the endcap presampler and the endcap electromagnetic calorimeter, divided into tiles and read out using embedded wavelength-shifting fibers.

Electromagnetic Calorimeter

The function of the electromagnetic calorimeter (ECAL) is to detect and identify electrons and photons. It consists of a lead glass total absorption calorimeter split into a barrel and two end cap arrays. This arrangement together with two forward lead scintillator calorimeters of the forward detector makes the OPAL acceptance for electron detection almost 99% of the solid angle.

The presence of ~ 2 radiation lengths of material in front of the calorimeter (mostly due to the solenoid and pressure vessel), results in most electromagnetic showers initiating before reaching the lead glass. Presampling devices are therefore installed in front of lead glass in the barrel and endcap regions to measure the position and energy of showers to improve overall spatial and energy resolution and give additional γ/π^0 and electron/hadron discrimination. In front of the Barrel Presampler is the Time of Flight Detector.

Electromagnetic Presampler

The barrel electromagnetic presampler consists of 16 chambers forming a cylinder of radius 239 cm and length 662 cm covering the polar angle range $|\cos\theta| < 0.81$. Each chamber consists of two layers of drift tubes operated in the limited streamer mode with the anode wires running parallel to the beam direction. Each layer of tubes contains 1 cm wide cathode strips in conjunction with a measurement of the charge collected at each end of the wires to give a z coordinate by charge division. The hit multiplicity is approximately proportional to the energy deposited in the material in front of the presampler allowing the calorimeter shower energy to be corrected with a corresponding improvement in resolution.

The endcap presampler is a multi-wire proportional counter located in the region between the pressure bell and the endcap lead glass detector. The device consists of 32 chambers arranged in 16 sectors covering all ϕ and the polar angle range $0.83 < |\cos\theta| < 0.95$.

Lead Glass Calorimeter

The barrel lead glass calorimeter consists of a cylindrical array of 9440 lead glass blocks at a radius of 246 cm covering the polar angle range $|\cos\theta| < 0.81$. Each block is 24.6 radiation lengths, 37 cm in depth and $\sim 10 \times 10\text{cm}^2$. In order to maximize detection efficiency the longitudinal axis of each block is angled to point at the interaction region. The focus of this pointing geometry is slightly offset from the e^+e^- collision point in order to reduce particle losses in the gaps between blocks.

Čerenkov light from the passage of relativistic charged particles through the lead glass is detected by 3 inch diameter phototubes at the base of each block.

The endcap electromagnetic calorimeter consists of two dome-shaped arrays of 1132 lead glass blocks located in the region between the pressure bell and the pole tip hadron calorimeter. It has acceptance coverage of the full azimuthal angle and 0.81¡$|\cos\theta|$¡0.98. As opposed to the barrel calorimeter, the endcap lead glass blocks follow a non-pointing geometry being mounted coaxial with the beam line. The lead glass blocks provide typically 22 radiation lengths of material and come in three lengths (38,42 and 52 cm) to form the domed structure following the external contours of the pressure bell.

Hadron Calorimeter

The hadron calorimeter is built in three sections - the barrel, the endcaps and the pole-tips. By positioning detectors between the layers of the magnets return yoke a sampling calorimeter is formed covering a solid angle of 97% of 4π and offering at least 4 interaction lengths of iron absorber to particles emerging from the electromagnetic calorimeter. Essentially all hadrons are absorbed at this stage leaving only muons to pass on into the surrounding muon chambers.

To correctly measure the hadronic energy, the hadron calorimeter information must be used in combination with that from the preceding electromagnetic calorimeter. This is necessary due to the likelihood of hadronic occurring in the 2.2 interaction lengths of material that exist in front of the iron yoke.

The barrel region (HB) contains 9 layers of chambers sandwiched between 8 layers of 10 cm thick iron. The barrel ends are the closed off by toroidal endcap regions (HE) which consist of 8 layers of chambers sandwiched between 7 slabs of iron.

The chambers themselves are limited streamer tube devices strung with anode wires 1 cm apart in a gas mixture of isobutane(75%) and argon (25%) that is continually flushed through the system. The signals from the wires themselves are used only for monitoring purposes. The chamber signals result from induced charge collected on pads and strips located on the outer and inner surfaces of the chambers respectively.

The layers of pads are grouped together to form towers that divide up the detector volume into 48 bins in ϕ and 21 bins in θ. The analogue signals from the 8 or so pads in each chamber are then summed to produce an estimate of the energy in hadronic showers.

The strips consist of 0.4cm wide aluminum and run the full length of the chamber, centered above the anode wire positions. They hence run parallel to the beam line in the barrel region and in a plane perpendicular to this in the endcaps. Strip hits thus provide muon tracking information with positional accuracy limited by the 1 cm wire spacing. Typically, the hadronic shower initialized by a normally incident 10 GeV pion produces 25 strip hits and generates a charge of 600 pc.

Complementing the barrel and endcap regions, the pole-tip(HP) extends the coverage of hadron calorimetry from $|\cos\theta| = 0.91$ down to 0.99. The sampling frequency in this region is increased to 10 in an effort to improve the OPAL energy resolution in the forward direction.

The detectors themselves are 0.7 cm thick multi-wire proportional chambers containing a gas mixture of CO_2 (55%) and n-pentane (45%), strung with anode wires at a spacing of 0.2 cm. Again, the chambers have pads on one side (of typical area 500 cm^2) and strips on the other. Corresponding pads from the 10 layers then form towers analogous to the treatment in the rest of the calorimeter.

Muon Detector

The muon detector aims to identify muons in an unambiguous way from a potential hadron background. To make the background manageable, particles incident on the detector have traversed the equivalent of 1.3 m of iron so reducing the probability of a pion not interacting to be less than 0.001.

The barrel region (MB) consists of 110 drift chambers that cover the acceptance $|\cos\theta| < 0.68$ for four layers and $|\cos\theta| < 0.72$ for one or more layers. The chambers range in length between 10.4 m and 6 m in order to fit between the magnet support legs and all have the same cross sectional area of 120 cm $\times$ 9 cm.

Each chamber is split into two adjoining cells each containing an anode signal wire running the full length of the cell, parallel to the beamline. The inner surface of the cells have 0.75 cm cathode strips etched in them to define the drift field and in the regions directly opposite the anode wires and diamond shaped cathode pads and are digitized via an 8-bit FADC.

Spatial position in the ϕ plane is derived using the drift time onto the anode and can be reconstructed to an accuracy of better than 0.15 cm. A rough estimate of the z coordinate is also achieved by using the difference in time and pulse height of the signals arriving at both ends of anode wire. A much better measure of the z coordinate is given by using induced signals on two sets of cathode pads whose diamond shape repeats every 17.1 cm and 171 cm respectively. This results in a z coordinate to 0.2 cm. modulo 17.1 cm or accurate to 3 cm modulo 171 cm.

Each endcap muon detector (ME) consists of two layers of four quadrant chambers (6 m $\times$ 6 m) and two layers of two patch chambers (3 m $\times$ 2.5 m), for angular coverage of $0.67 < |\cos\theta| < 0.985$. Each chamber is an arrangement of two layers of limited streamer tube in the plane perpendicular to the beam line, where one layer has its wires horizontal and the other vertical.

Forward Detectors

The forward detector (FD) consists of an array of devices whose primary objective is to detect low angle Bhabha scattering events as a way of determining the LEP luminosity for the normalization of measured reaction rates from Z^0 decays.

To achieve this, the forward detector is installed in a relatively clean acceptance for particles between 47 and 120 mrad from the interaction point, with the only obstructions being the beam pipe and 2 mm of aluminum from the central detector pressure vessel.

Components of the forward detector are:

Calorimeter The forward calorimeter consists of 35 sampling layers of lead-scintillator sandwich divided into a presampler of 4 radiation lengths and the main calorimeter of 20 radiation lengths.

Tube Chamber There are three layers of proportional tube chambers positioned between the presampler and main sections of the calorimeter. The positioning is known to ± 0.05 cm and they can give the position of a shower centroid to ± 0.3 cm.

Gamma Catcher The gamma catcher is a ring of lead scintillator sandwich sections of 7 radiation lengths thickness. They plug the hole in acceptance between the inner edge of EE and the start of the forward calorimeter.

Far Forward Monitor The far forward monitor counters are small lead-scintillator calorimeter modules, 20 radiation lengths thick, mounted either side of the beampipe 7.85 m from the intersection region. They detect electrons scattered in the range 5 to 10 mrad that are deflected outward by the action of LEP quadrapole.

Silicon Tungsten Detector

The silicon tungsten detector (SW) is a sampling calorimeter designed to detect low angle Bhabha scattering events in order to measure the luminosity There are 2 calorimeters at ± 238.94 cm in z from the interaction point with an angular acceptance of 25 mrad to 59 mrad. Each calorimeter consists of 19 layers of silicon detectors and 18 layers of tungsten. At the front of each calorimeter is a bare layer of silicon to detect preshowering, the next 14 silicon layers are each behind 1 radiation length (3.8mm) of tungsten and the final 4 layers are behind 2 radiation lengths (7.6 mm) of tungsten.

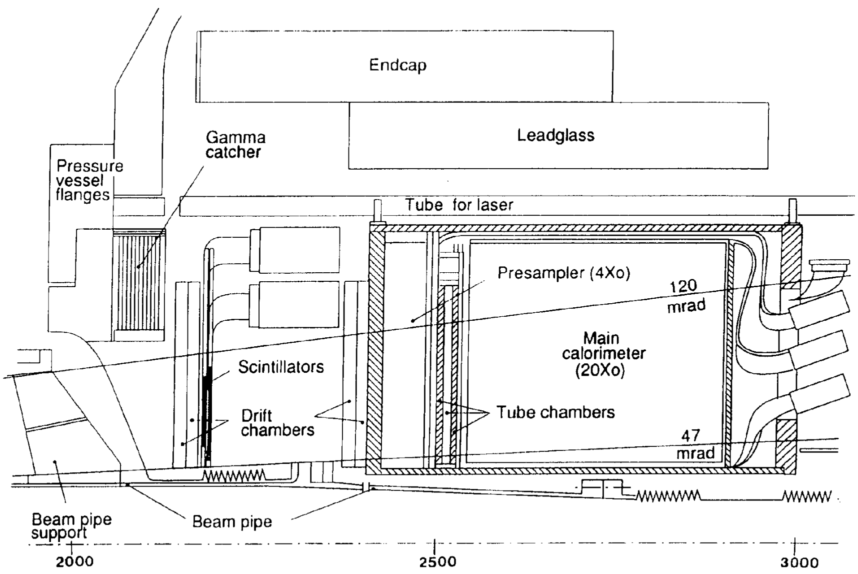

Figure 4.5: The Forward Detector

Each silicon layer consists of 16 wedge shaped silicon detectors. The wedges cover 22.5° in ϕ with an inner radius at 6.2 cm and an outer one at 14.2 cm. The wedges are subdivided into 64 pads (32 in r and 2 in ϕ) giving a total of 38912 channels which are read out individually. Adjacent wedges in a layer are offset by 800 μm in z and positioned in such a way that there is no gap in the active area of the silicon. Consecutive layers in the detector are offset in ϕ by half a wedge (11.25°) so that any cracks between the tungsten half-rings do not line up.

Trigger

Bunch crossings occur every $22.2\mu s$ at LEP. A flexible and programmable trigger system uses fast information from the subdetectors to select crossing with a possible e^+e^- interaction, reducing the 45 kHz bunch crossing rate to an event rate of 1-5Hz which can be handled by the data acquisition system.

The trigger system is designed to provide high efficiency for the various physics reactions, and good rejection of backgrounds arising from cosmic rays, from interactions of the beam particles with the gas inside the beam pipe or the wall of the beam pipe, and from noise. Most of the physics reactions are triggered by several independent conditions imposed on the subdetector signals. This redundancy leads to a high detection efficiency and greatly facilitates the measurements of this efficiency. Detail description of the OPAL trigger system is found in [122].

The 4π range in solid angle covered by the detector is divided into 144 overlapping bins, 6 bins in θ and 24 bins in ϕ. The subdetectors deliver trigger signals matched as closely as possible and are made over only a small region and thus noise is reduced. Besides the $\theta - \phi$ signals, the subdetectors deliver "stand-alone" signals, delivered from total energy sums or track counting.

The trigger signals from the various subdetectors are logically combined in the central trigger logic. $\theta - \phi$ signals are used for hit counting, for the definition of back-to-back hits and to build detector coincidences correlated in space. The following subsections describe trigger signals provided by the tracking system, the time-of-flight system and electromagnetic calorimeter.

Track Trigger The track trigger is a dedicated programmable hardware processor using input from the vertex detector and the jet chamber. Tracks are recognized in the $r-z$ plane if they originate from the interaction region with in an adjustable range in z. Four "rings" (each of 12 adjacent wires) are used, one ring consists of the axial wires of the vertex detector and the other 3 rings are provided by the jet chamber. The radial positions of the rings in the jet chamber can be varied. The z position along the wires is obtained from the measurement of the time difference of propagation of signals to the two ends in the case of the vertex detector, and by charge division in the case of the jet chamber. The values of z/r for wires hit in each of the four rings are filled in four histograms with up to 32 slices in z/r. There are 24 sets of such histograms, one for each $30°\phi$ segment, i.e. a pair of neighboring jet chamber sectors and three adjacent sectors in the vertex detector. The presence of a track is indicated by the track trigger logic if a programmable minimum number of hits is found in corresponding slices of these histograms.

The track trigger accepts tracks within $|\cos\theta| < 0.95$. Tracks which are well contained by the third radial section in the jet chamber, i.e. $|\cos\theta| < 0.82$, are classified as "barrel tracks". The track trigger logic provides 144 $\theta-\phi$ signals and 6 stand alone signals for $\geq 1,2,3$ barrel tracks or $\geq 1,2,3$ tracks in the full detector.

Time-of-Flight Trigger The trigger signals of the time-of-flight system are based on coincidence of the signals from the phototubes at the two ends of the scintillation counters. The counters are combined to form 24 overlapping ϕ sectors of 36° each. There is no segmentation in θ. The 24 ϕ sectors are used to form a signal typically demanding ≥ 6 sectors to have fired. In addition a multiplicity signal is envisaged which requires the number of counters hit to exceed an adjustable threshold between 2 and 5.

Electromagnetic Calorimeter Trigger The trigger signals from the electromagnetic calorimeter are based on analogue sums of groups of ~ 48 lead glass counters. A total of 200 analogue signals from the barrel calorimeter and 24 from each endcap are combined to form overlapping $\theta-\phi$ signals and total energy sums for the barrel and endcaps. Both of total sums and $\theta-\phi$ signals are discriminated at two thresholds. The $\theta-\phi$ signal is used for input to the $\theta-\phi$ matrix. The logical OR of the higher $\theta-\phi$ threshold is used as a stand-alone signal.

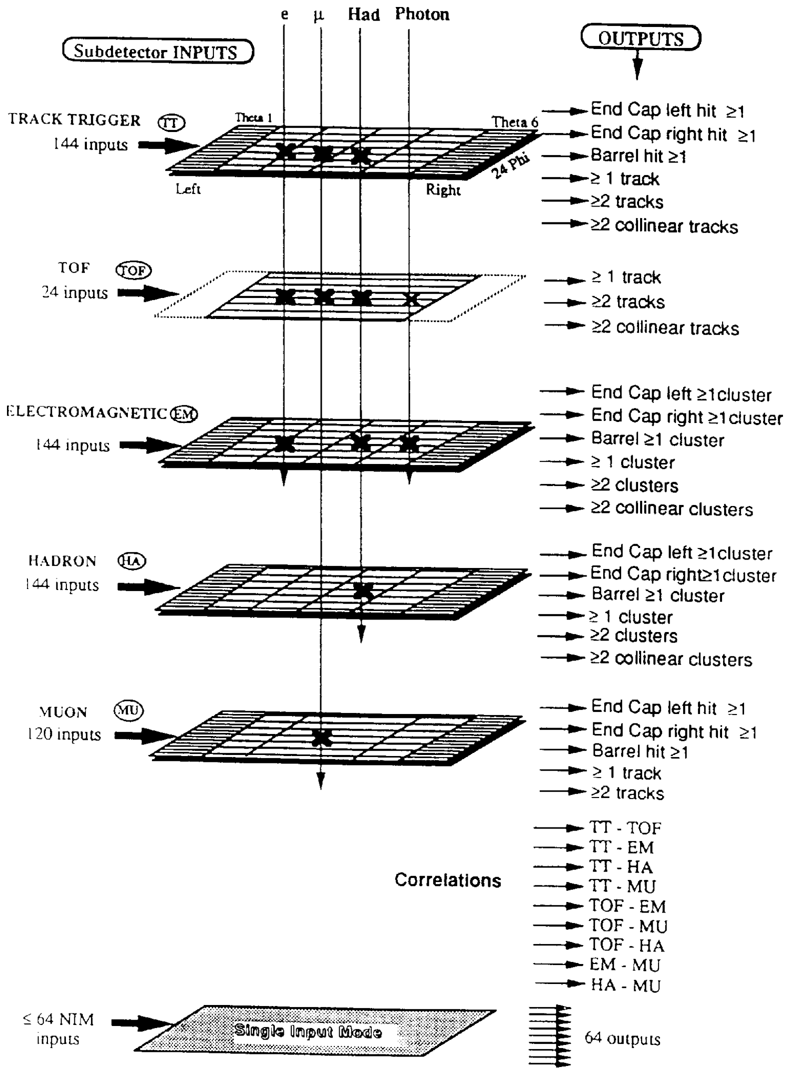

Figure 4.6: The Central Trigger Logic

Chapter 5

Analysis of Radiative Multi-Hadronic Events at LEP1

Measurements of α_s using event shape variables at e^+e^- colliders are usually performed after removing radiative hadronic events. Then, the energy scale of the α_s is set to $2E_{\mathrm{beam}}$(E_{beam} is a beam energy). In this study, radiative hadronic events in data taken at LEP running at $E_{\mathrm{CM}} = 91\mathrm{GeV}$ are used for the measurement of α_s at effective center of mass energies spanning from 24GeV to 78GeV.

Assuming that photons emitted before or immediately after a Z^0 production do not interfere with QCD processes, a measurement of α_s at lower energy scale than Z^0 resonance is possible by using radiative multi-hadronic events.

Most photons emitted before $q\bar{q}$ production (initial state radiation,ISR) escape into beam pipe direction. The rate of initial state radiation is increased at the center-of-mass energy sufficiently lower than M_{Z} or higher than M_{Z}. The measurement of α_s with multi-hadronic events with high energy initial state radiation is realistic for experiments using a high luminosity lower energy collider. Preliminary results of measurements of the total hadronic cross-section with hadronic events with ISR have been presented by the KLOE and BaBar collaboration [123].

At LEP1 isolated high energy photons observed in a detector are mainly photons emitted by the quarks produced by a Z^0 decay (final state radiation,FSR). The measurement of α_s in hadronic events with observed photon has been performed by L3 collaboration [124] and OPAL collaboration [125, 126]. DELPHI collaboration measured $\langle n_{\mathrm{ch}} \rangle$ using such radiative events in [127]. Recently, DELPHI collaboration published a paper on the energy evolution of event shape distribution and their means [128]. It includes the measurement of α_s with radiative hadronic events.

If a photon is emitted before gluon radiations, the mass of the quark system after photon emission is regarded as the energy scale used in the radiation. In the leading log parton shower picture, a virtuality is decreased in each subsequent branching. To emit a hard photon with large angle to quark, it is necessary that the photon is emitted in the early stage of QCD evolution. Using Monte Carlo generator employing the leading log parton shower, the event shape variables for the hadronic system of radiative hadronic events are shown to have same energy dependence with non-radiative hadronic events at the corresponding center-of-mass energy in Section 3.4. The measurement of α_s from event shape variables of the hadronic system with an observed photon at the OPAL experiment is described in this chapter.

Unlike an α_s measurement with non-radiative hadronic events, hadronic events originating in up-type quarks are enhanced because of their electric charge. Since the strong interaction is blind to quark flavor in the Standard Model, the difference is not taken into account in this analysis.

The selection for multi-hadronic events with an isolated high energy photon is described in Section 5.2. The corrections applied to event shape distributions is explained in Section 5.2.5. Selected events are divided into subsamples according to photon energy E_γ. The reduced center-of-mass energy,$\sqrt{s'}$, is defined by:

$$\sqrt{s'} = 2E_{\text{beam}}\sqrt{1 - \frac{E_\gamma}{E_{\text{beam}}}},$$

where E_{beam} is the beam energy. The determination of α_s at various $\sqrt{s'}$ is presented in Section 5.3. Their statistical and systematic uncertainties are explained in Section 5.4.

5.1 Data Set and Monte Carlo Simulation

The data accumulated between 1992 and 1995 at center of mass energies around 91.2GeV is used for this analysis. The corresponding integrated luminosity is $103.27 \pm 0.10\text{pb}^{-1}$. The luminosity is calculated from small angle Bhabha events measured by silicon tungsten The 'off-peak' data which has center-of-mass energies around 89.5GeV and 93GeV is taken also in this period. The luminosity corresponding to the off-peak data is $17.22 \pm 0.03\text{pb}^{-1}$ and $18.41 \pm 0.04\text{pb}^{-1}$, respectively. Since the off peak data is only 14% of the data which has center-of-mass energy in the number of hadronic events, it is not used to avoid complexity of analysis.

Generated events are processed through a full simulation of the OPAL detector [129] which treats in detail the detector geometry and material as well as the effects of detector resolution and efficiency. The simulated events are reconstructed using the same procedures that were used for the OPAL data. Monte Carlo event generators are as follows.

Multi-hadronic Events `JETSET` version 7.4 [48] is used to simulate $e^+e^- \to q\bar{q}$ events, with `HERWIG` version 5.9 [49] and `ARIADNE` version 4.08 [50] used for study of alternative hadronization and parton shower models. `COJETS` [130, 131] uses an incoherent parton shower with independent fragmentation. It was studied in earlier OPAL α_s measurements. However, since the parton shower in this model does not evolve like the other models used in this analysis, it is not appropriate for the multi-parton final state considered in NLLA calculation. `COJETS` is not used in this analysis. Parameters controlling the hadronization of quarks and gluons are tuned to OPAL LEP1 data as described in Ref. [33, 132].

τ Pair Production `KORALZ` version 4.02 [133] is for $e^+e^- \to \tau^+\tau^-$ events. `KORALZ` is a Monte Carlo program mainly for lepton pair production including initial and final state bremsstrahlung corrections up to the $O(\alpha^2)$ and $O(\alpha)$ electroweak corrections.

Two Photon Processes Since the radiative hadronic events with a high energy photon are low multiplicity and strongly boosted, the quark pair production in two-photon processes can be a background process in events with low multiplicity. In order to simulate two-photon processes, the appropriate event generator is chosen considering the decay product and kinematics of the process. Although there are different ways to define the separation between processes, The negative value of the virtuality of the observed electron, $P^2 = -p^2$ and the squared momentum transfer, $Q^2 = 2E_\mathrm{b}E_\mathrm{b}\mathrm{tag}(1-\cos\theta_\mathrm{tag})$, where p is the four-momentum of the observed electron and E_tag and θ_{tag} are energy and polar angle of the observed electron. E_b is the beam energy. `HERWIG` version 5.8 [49] is used to simulate $\gamma\gamma^* \rightarrow$ hadrons. $P^2 > 1.0\mathrm{GeV}^2$ and $Q^2 < 1.0\mathrm{GeV}^2$ are defined. `PHOJET` version 1.05c [134] is used to simulate $\gamma\gamma \rightarrow$ hadrons. $P^2 < 1.0\mathrm{GeV}^2$ and $Q^2 < 1.0\mathrm{GeV}^2$ are defined. The processes $\gamma\gamma^* \rightarrow$ leptons are simulated by `VERMASEREN` version 1.01 [135]. No cut on P^2 and Q^2 is applied for this generator. The processes with $P^2 < 1.0\mathrm{GeV}^2$ and $Q^2 < 1.0\mathrm{GeV}^2$ are simulated by `F2GEN` which was developed based on the `TWOGEN` generator [136].

5.2 Event Selection

The event selection for multi-hadronic events with an isolated high energy photon is divided into multi-hadronic event selection and isolated high energy photon selection. The isolated high energy photon selection is performed with a likelihood ratio method after selection of an isolated electromagnetic cluster. These selections are described in following sections.

5.2.1 Hadronic Event Selection

The standard selection criteria for the OPAL detector are specified for analysis with multi-hadronic events on Z^0 resonance.

The standard multi-hadronic events selection is defined using the information on electromagnetic calorimeter (ECAL) clusters and tracks measured by the central tracking system. Good clusters and good tracks selected by the following criteria are used for the definition. A good cluster in barrel region is required to have an energy of at least 0.1GeV. For endcap region, the energy of the clusters is required to be more than 0.2GeV and shared by at least 2 electromagnetic calorimeter blocks. A good track is required to have at least 20 hits measured in the central tracking system, a distance of closest approach from the nominal interaction point of less than 2cm in $r-\phi$ coordinate and of less than 40cm along the z axis. The z coordinate of vertex is unconstrained in track fitting. The track is required to have a transverse momentum of more than 50MeV/c and a polar angle of larger than 0.995 radian.

Two ratios are defined:

$$R_\mathrm{vis} = \frac{E_\mathrm{shw}}{2 \times E_\mathrm{beam}} \qquad \text{and} \qquad R_\mathrm{bal} = \frac{E_\mathrm{bal}}{E_\mathrm{shw}} \tag{5.1}$$

where E_beam is a beam energy, E_shw and is the sum of ECAL energy. E_bal is defined by $|\sum_i(E^i_\mathrm{cluster}\cos\theta_i)|$, where E^i_cluster is the energy of the ECAL cluster i, θ_i is the polar angle of ECAL cluster i.

Events are selected as multi-hadronic events if an event has at least seven good clusters, at least five good tracks, R_vis of more than 0.10 and R_bal of less than 0.65.

The overall efficiency of the standard multi-hadronic event selection is determined to be $98.6 \pm 0.4\%$ [137]

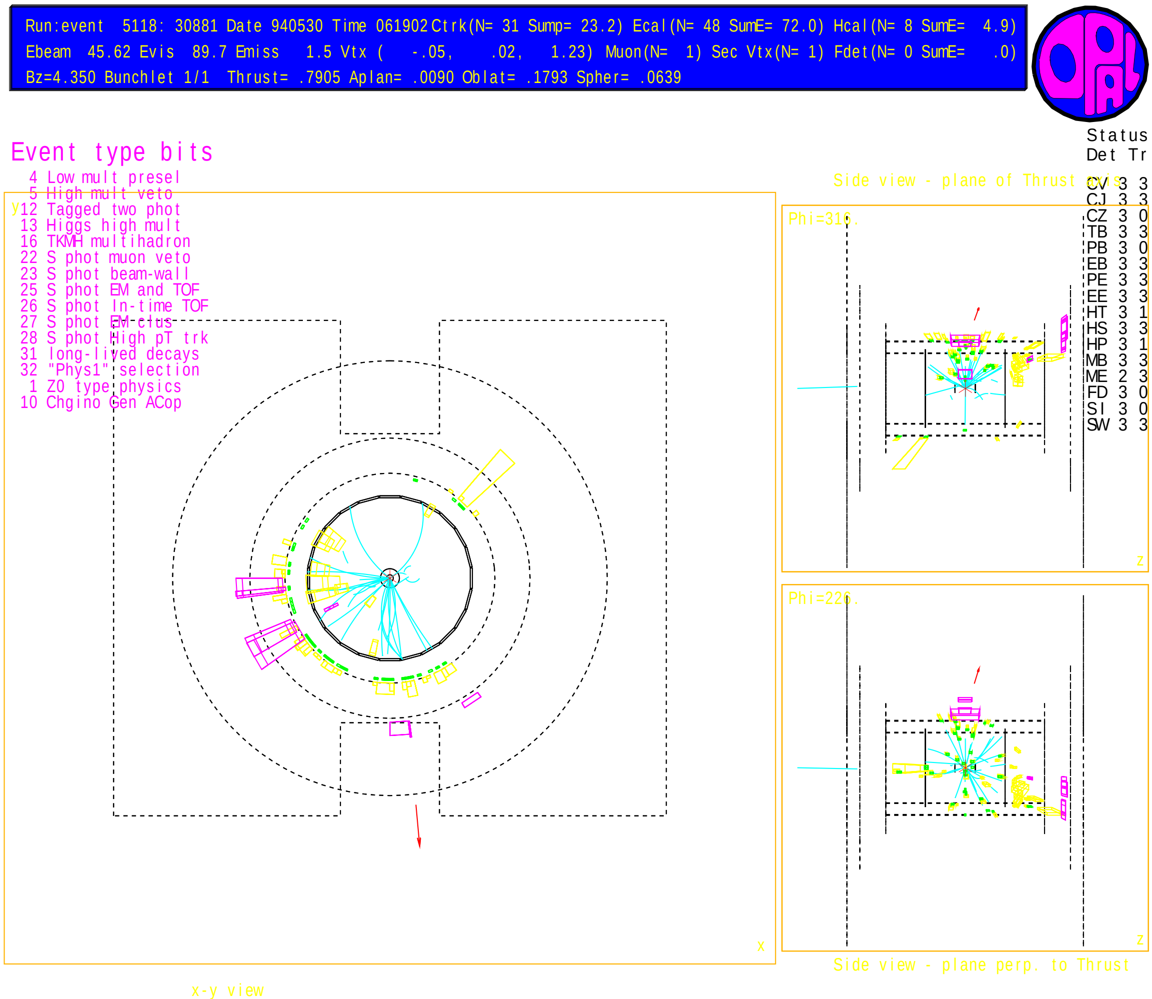

Figure 5.1: A candidate multi-hadronic event with hard isolated photon. A high energy isolated electromagnetic cluster can be seen in the figure. Tracks and electromagnetic clusters are forming two jet and boosted into back-to-back direction to the isolated electromagnetic cluster.

The following tighter criteria on clusters and track quality are required for this selection.

The clusters in the electromagnetic calorimeter are required to have a minimum energy of 100 MeV in the barrel and 250 MeV in the endcap. Tracks are required to have transverse momentum to the beam axis $p_T \geq 150\text{MeV/c}$, at least 40 reconstructed points or half of expected number of hits in the jet chamber, a distance of the point of closest approach to the collision point in the $r-\phi$ plane $d_0 < 2$ cm and in the z direction $z_0 < 25$ cm.

In addition to the standard multi-hadronic events selection, at least five good tracks are required to reduce background from $e^+e^- \to \tau^+\tau^-$ or $\gamma\gamma \to q\bar{q}$ events.

To ensure events are well contained in the OPAL detector, the thrust axis of the event is required to be in polar angle region of less than 0.9 in cosine.

Jets are calculated with tracks and electromagnetic clusters. When tracks associate with an electromagnetic calorimeter cluster, the track momentum measured by central tracking system and the contribution of the track to the cluster energy is doubly counted in the calculation. If a cluster is associated by tracks, the expected energy according to the momentum is subtracted from cluster energy in the calculation. This subtraction is performed by an algorithm called MT described in [138, 139]. In this algorithm, the association of tracks is decided by using the error on measurement of r and ϕ coordinate at the intersection point and region in these coordinate that contains satellite clusters in 90% probability.

The central detector and the electromagnetic calorimeter are required to be fully operational.To ensure that luminosity is well measured, the silicon tungsten detector is required to be fully operational after 1992.

5.2.2 Isolated Electromagnetic Cluster Selection

Isolated photons are selected in these hadronic events as follows. A signal event is defined as an $\mathrm{e^+e^-} \to \mathrm{q\bar{q}}$ event with an initial or final state photon with energy greater than 10 GeV.

Electromagnetic clusters which don't associated with tracks are selected from clusters in multi-hadronic events. Association of tracks are decided by the criteria used in the MT algorithm described in Section 5.2.1.

Electromagnetic clusters with an energy larger than 10 GeV are selected in order to avoid large numbers of photons coming from the decay of mesons. We use electromagnetic clusters in the polar angle region $|\cos\theta_{\mathrm{EC}}| < 0.72$, where there is less material in front of the lead glass than the region with $|\cos\theta|$ larger than the criteria (Figure 5.2a). Besides the amount of material, the non-pointing geometry of endcap electromagnetic calorimeter makes the cluster shape fitting explained in the following section complex. The number of clusters in data which satisfy the criteria on the electromagnetic cluster energy and $|\cos\theta_{\mathrm{EC}}|$ is 1797532. According to the Monte Carlo simulation, 99.3% of these selected clusters come from non-radiative multi-hadronic events.

The candidate clusters are required to be isolated from any jets, and from other clusters and tracks:

- The angle with respect to the axis of any jet, $\alpha^{\mathrm{iso}}_{\mathrm{jet}}$, is required to be larger than 25° (Figure 5.2b). The jets are reconstructed from tracks and electromagnetic clusters, excluding the candidate cluster, using the Durham algorithm with $y_{\mathrm{cut}} = 0.005$.

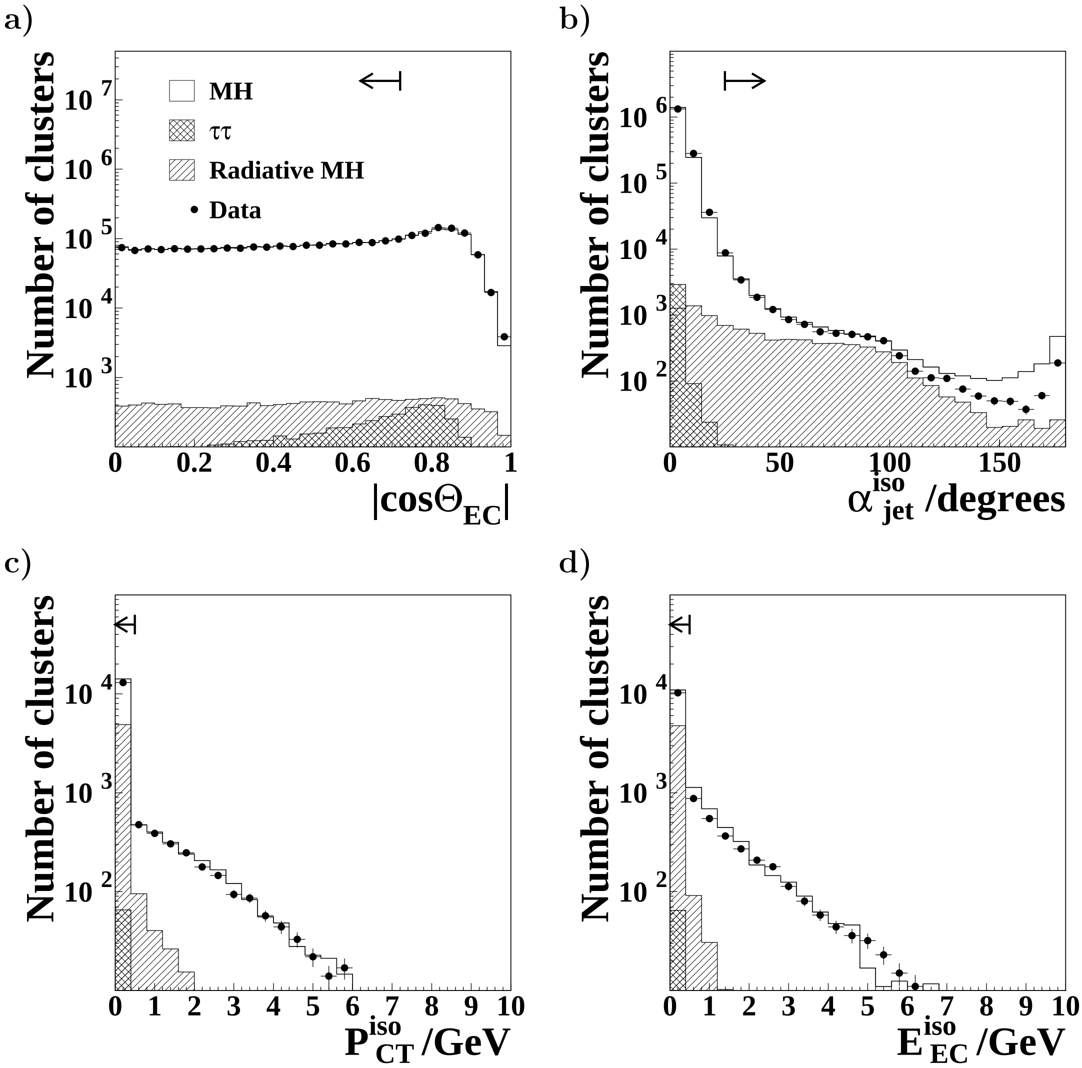

Figure 5.2: Distributions of variable used in isolated electromagnetic cluster selection Histograms by Monte Carlo simulation are normalized with number of events estimated from integrated luminosity and cross-section of the process. Arrows in figures show selected region.

- The sum of the momenta of tracks which, extrapolated to the calorimeter surface, fall inside a 0.2 radian cone around the candidate, $P_{\mathrm{CT}}^{\mathrm{iso}}$, is required to be smaller than 0.5 GeV/c (Figure 5.2c). The total energy deposition in the electromagnetic calorimeter within a cone of 0.2 radian around the candidate, $E_{\mathrm{EC}}^{\mathrm{iso}}$, is also required to be less than 0.5 GeV (Figure 5.2d). There is a discrepancy in the large $\alpha_{\mathrm{jet}}^{\mathrm{iso}}$ region. According to Monte Carlo simulation, two jet events with a quark or gluon transformed into a few hadrons are found. It seems that there are problems in the hadronization simulation in such special condition.

After the isolation cuts, 11265 clusters are retained. Clusters from non-radiative multi-hadronic events are reduced to 52.8%, the background from $\tau^+\tau^-$ events is 0.565% and from two-photon events is 0.010%.

5.2.3 Likelihood Photon Selection

Isolated photon candidates are selected by using a likelihood ratio method with four variables described in the following sections to reduce contamination of clusters from decay of neutral hadrons. The likelihood ratio $\mathcal{L}_{qq\gamma}$ is defined by

$$\mathcal{L}_{\mathrm{q\bar{q}}\gamma} = \frac{L_{\mathrm{q\bar{q}}\gamma}}{L_{\mathrm{q\bar{q}}\gamma} + \sum w_i L_{\mathrm{BG,i}}},$$

where $L_{\mathrm{q\bar{q}}\gamma}$ is the absolute likelihood value for isolated photon, $L_{\mathrm{BG,i}}$ and w_i are the absolute likelihood values for ith background and the weight of the process calculated from cross-section and luminosity. The isolated photon events make a peak around $\mathcal{L}_{\mathrm{q\bar{q}}\gamma} = 1$ and the background processes make a peak around $\mathcal{L}_{\mathrm{q\bar{q}}\gamma} = 0$.

A probability density function obtained for the variables is used as an absolute likelihood. In the calculation of the probability density function, the method called the Projection and Correlation (PC) approximation [140] is employed. In this method, the correlation between variables in a probability density function $\mathcal{P}(\mathbf{x})$ is approximated by the n-dimensional Gaussian. Since each variables x_i are not Gaussian distributed, they are transformed to the Gaussian distributed variable y_i. The approximated probability density function $P(\mathbf{x})$ is defined by the following equation.

$$P(\mathbf{x}) = |V|^{-1/2} \exp(-\frac{1}{2}\mathbf{y}^T(V^{-1} - I)\mathbf{y}) \prod_{i=1}^{n} p_i(x_i).$$

V is the $n \times n$ covariance matrix for y and I is identity matrix. $p_i(x_i)$ is the projection of $\mathcal{P}(\mathbf{x})$ on the x coordinate. The histogram of variable x_i is used as $p_i(x_i)$. (It is called a reference histogram in this analysis.) In this analysis, the reference histogram is obtained by a Monte Carlo simulation.

Since two-photon and $\tau\tau$ background are very small compared to non-radiative hadronic event background, reference histograms are calculated only for signal and non-radiative hadronic event background. Electromagnetic calorimeter clusters are divided into seven subsamples by their energy. Different reference histograms are prepared for each subsamples. Variables used in the likelihood calculation is explained in following subsections.

Cluster Shape Fit Variable

The dominant background for the isolated photon is π^0 decays into two photons. The clusters which come from the two photons are overlapped. It is difficult to distinguish π^0 from the isolated photon by reconstructing π^0 from the two photons. Therefore a variable which represents the shape of the cluster is used for rejecting π^0.

The first variable for the likelihood calculation is cluster shape fit variable, C, defined by

$$C = \frac{1}{N_{block}} \sum_i \frac{(E_{meas,i} - E_{exp,i})^2}{\sigma^2_{meas,i}}, \quad (\sigma_{meas,i} = 0.21 E_{meas,i} + 6.3\sqrt{E_{meas,i}})$$

where N_{block} is the number of blocks which the electromagnetic cluster consists of, $E_{meas,i}$ is the measured energy deposit in the i'th block, $E_{exp,i}$ is the expected energy deposit in the i'th block assuming that the energy is deposited by a single photon and $\sigma_{meas,i}$ is the resolution of energy measured by i'th electromagnetic calorimeter block. The C variable is

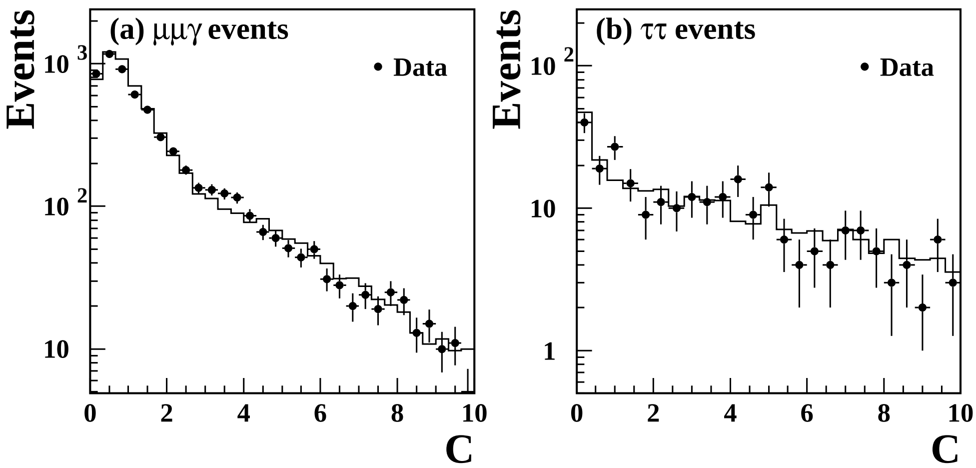

Figure 5.3: C variable distribution of (a) photons obtained from radiative muon pair production events and (b) π^0s obtained from 1-prong decay of τ in $\tau\tau$ pair production events

used for judging whether the cluster is made by single photon or not. The expected energy deposit is obtained by a numerical integration of a shower profile function over lead glass blocks in the cluster. As described in Section 4.2, the electromagnetic calorimeter block in the barrel part nearly points to the interaction region. Although the shower profile function is a function of radius and longitudinal distance from the shower origin, it can be well approximated by the two dimensional integration by neglecting the longitudinal part of the function. The expected energy of i'th block is given by

$$E_{exp,i} = E_0 \times \int_{S_i} f(r) dr d\phi. \tag{5.2}$$

$$f(r) = a \exp(-br) + c \exp(-dr) \qquad \left(\frac{a}{b} + \frac{c}{d} = 1\right) \tag{5.3}$$

S_i is projection of front surface of i'th block to the plane which cross the shower origin and is perpendicular to incident direction. The integration is performed by dividing the region S_i into ring with the origin as center.

Parameter a, b, c and d are obtained by simulation with GEANT program [141].

$$b = 0.6255 - \frac{0.04651}{\sin\theta} + \frac{0.00662}{\sin^2\theta} \tag{5.4}$$

$$a = 0.3110 \times b \tag{5.5}$$

$$d = 3.03480 - \frac{0.11004}{\sin\theta} - \frac{0.24798}{\sin^2\theta} \tag{5.6}$$

$$c = 0.6890 \times d \tag{5.7}$$

The intrinsic energy resolution measured by using an e^- beam without material in front of the calorimeter ($\sigma = 0.21E + 6.3\sqrt{E}$) is used for this analysis.

In order to drop obvious background events before the likelihood calculation, the number of electromagnetic calorimeter blocks is required to be smaller than 10 as a preselection.

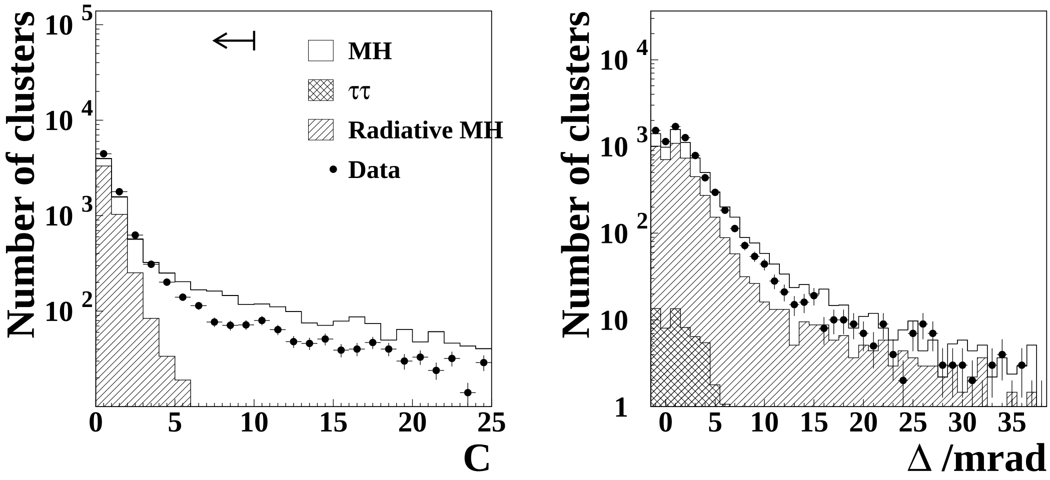

Figure 5.4: Distributions of variable used in the isolated photon likelihood selection.

Check of the Cluster Shape Fit Variable The agreement between data and Monte Carlo is checked simply with photons in radiative muon pair events and π^0 in τ pair events.

For checking the agreement of the C variable between data and Monte Carlo in case of clusters produced by a single photon, events with two muons which have total momentum larger than 7GeV/c are selected from muon pair events which pass the selection criteria described in [142]. If an electromagnetic calorimeter cluster is not associated with tracks and has 3-momentum close to the total 3-momentum of two muons, it is used for the check as a photon. The C variable distribution of the cluster for data is compared with the Monte Carlo distribution for $e^+e^- \rightarrow \mu^+\mu^-(\gamma)$ produced by `KORALZ` (Figure 5.3 (a)). They are in an acceptable agreement.

After selections on the multiplicity of the tracks and the clusters, the shower energy and the visible energy, and the cosmic ray rejection, the identification of τ is performed by a cone based algorithm using both of the tracks and electromagnetic calorimeter clusters. The detailed description of the τ pair selection is found in [142].

First the highest energy particle in the event is selected and a cone with a half opening angle of 35 degrees is defined around it. The particle with the next highest energy particle inside the cone is combined with the first particle. A new cone is defined around the vector sum of momenta of the two particles. This procedure is repeated until no more particles are found inside the cone. If the resulting cone of particles is includes at least one track, it is classified as a τ. The procedure is repeated until all particles are assigned to a cone. If the event has two cones classified as a τ, it is selected as τ-pair events.

For checking the agreement of C variable between data and Monte Carlo, the τ candidates which have one charged track and clusters unassociated with the track are selected. As shown in Figure 5.3 (b), they agree with each other.

Distance between Electromagnetic Cluster and Presampler Cluster

The second new variable is a measure of the distance between the electromagnetic calorimeter cluster and the associated presampler cluster,

$$\Delta = \max(|\Delta\phi|, |\Delta\theta|).$$

$\Delta\phi$ and $\Delta\theta$ are the angular separations between the clusters in azimuthal and polar angle, respectively. The value of Δ tends to to be larger for clusters produced by two overlapping photons, e.g. from a $\pi^0 \to \gamma\gamma$ than for clusters produced by a single photon, because the presampler measures the cluster position at an early stage of development of the electromagnetic shower. The value of Δ is required to be smaller than 50 mrad as preselection. The cut does not apply to clusters with no presampler hit. $\Delta = -1$ is assigned for such clusters in the likelihood selection.

The other variables are $|\cos\theta_{\mathrm{EC}}|$ and $\alpha_{\mathrm{jet}}^{\mathrm{iso}}$ described in Section 5.2.2. The distributions of C and Δ are shown in Figures 5.4. The Monte Carlo distributions in these figures are normalized according to the luminosity obtained from small angle Bhabha events. A disagreement between data and Monte Carlo is seen for C and $\alpha_{\mathrm{jet}}^{\mathrm{iso}}$. As shown in Section 5.2.3, the agreement between data and Monte Carlo for the C distribution is studied with photons in radiative Bhabha events and π^0 and $\pi^{\pm}$ in tau pair events. Therefore, it is related to the difficulty in predicting the rate of isolated neutral hadrons in the Monte Carlo generators, as explained in Section 5.2.4. In this analysis, the rate of isolated neutral hadrons used in the background subtraction is estimated from data.

The likelihood calculation is performed with reference histograms made for seven subsamples chosen to the cluster energy. The cut on the likelihood value is chosen so as to retain about 80% of the signal events. The likelihood distributions for data and Monte Carlo are shown in Figure 5.5.

It can be seen that the likelihood distributions for signal and background events are well separated for each region of electromagnetic cluster energy. The electromagnetic clusters which pass the likelihood selection are regarded as photon candidates.

The effectiveness of each variable is checked by removing one of the likelihood variables in the likelihood calculation. The efficiencies of the selection itself and the purities of signal events after the likelihood selection are shown in Table 5.1. C and $\alpha_{\mathrm{jet}}^{\mathrm{iso}}$ are more effective. Improvement of purity×efficiency is small. But it is better to use $|\cos\theta_{EC}|$ and Δ.

Hadronic events with hard isolated photon candidate are divided into seven subsamples according to the photon energy for further analysis. Table 5.2 shows the mean values of $\sqrt{s'}(= 2E_{beam}\sqrt{1 - E_\gamma/E_{beam}})$, the number of data events and number of background

Variable	Efficiency[%]	Purity[%]	Purity×Efficiency
Default	83.5	94.8	0.792
$\lvert\cos\theta_{\mathrm{EC}}\rvert$	82.5	94.8	0.783
Δ	82.1	95.1	0.781
C	79.6	94.5	0.752
$\alpha_{\mathrm{jet}}^{\mathrm{iso}}$	79.7	96.1	0.765

Table 5.1: Efficiencies and purities of the likelihood selection when one of the likelihood variables is removed. “Default” means the results when all variables are used.

events for each subsample. “Non-rad MH” means a fraction of neutral hadron background estimated by the two independent methods described in the next section. Predictions by `JETSET` are shown also. It is indicated by “MC” in the table. There is a discrepancy in samples with a high cluster energy.

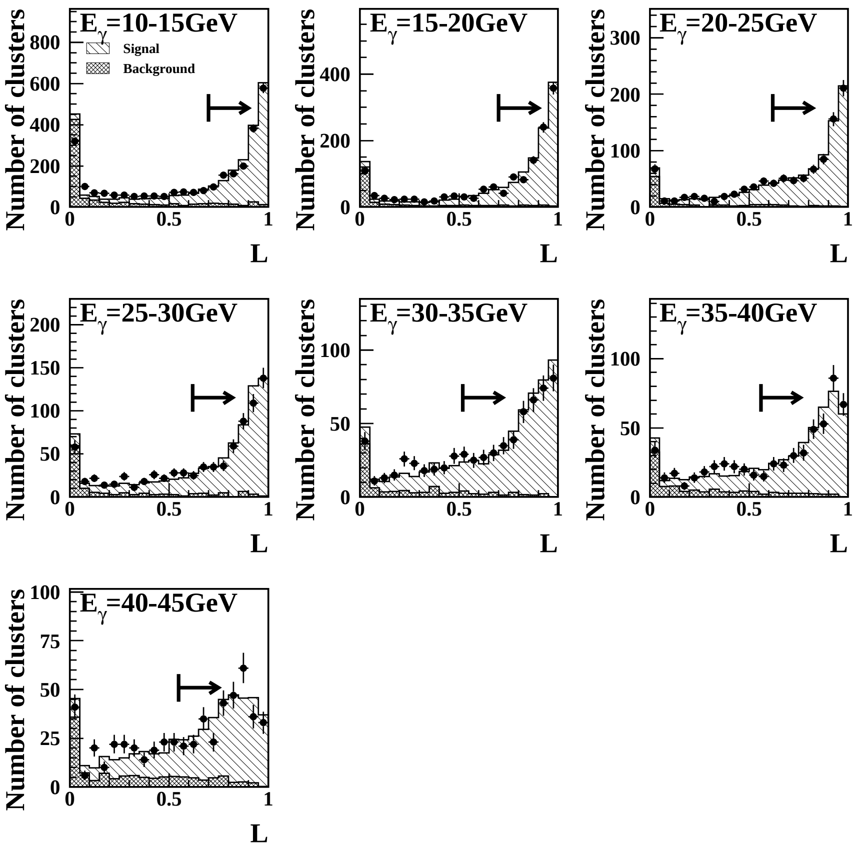

Figure 5.5: Photon likelihood distributions. Monte Carlo distributions are scaled with fraction obtained by fitting described in Section 5.2.4. Arrows show the selected region.

E_γ [GeV]	Events	$\sqrt{s'}_{Mean}$[GeV]	Background [%]			
			Non-rad. MH			$\tau\tau$
			MC	Likelihood	Isolated tracks	
10-15	1560	78.1± 1.7	6.1± 0.6	6.0± 0.7	6.2± 0.9	0.9± 0.2
15-20	954	71.8± 1.9	6.0± 0.8	3.1± 0.5	4.9± 0.8	1.0± 0.3
20-25	697	65.1± 2.0	6.6± 1.0	2.6± 0.6	6.3± 1.1	0.9± 0.4
25-30	513	57.6± 2.3	9.7± 1.4	5.1± 1.1	7.9± 1.4	1.1± 0.5
30-35	453	49.0± 2.6	11.8± 1.6	4.5± 1.1	9.6± 1.6	0.7± 0.4
35-40	376	38.5± 3.5	14.6± 2.0	5.2± 1.2	13.1± 1.9	0.8± 0.5
40-45	290	24.4± 5.3	30.6± 3.2	10.4± 2.3	12.9± 1.7	0.8± 0.5

Table 5.2: Selected number of events and mean value of $\sqrt{s'}$ for each $\sqrt{s'}$ subsample. “Non-rad. MH” means a fraction of neutral hadron background predicted by two different methods described in Section 5.2.4 and predictions by JETSET (It is indicated by “MC”).

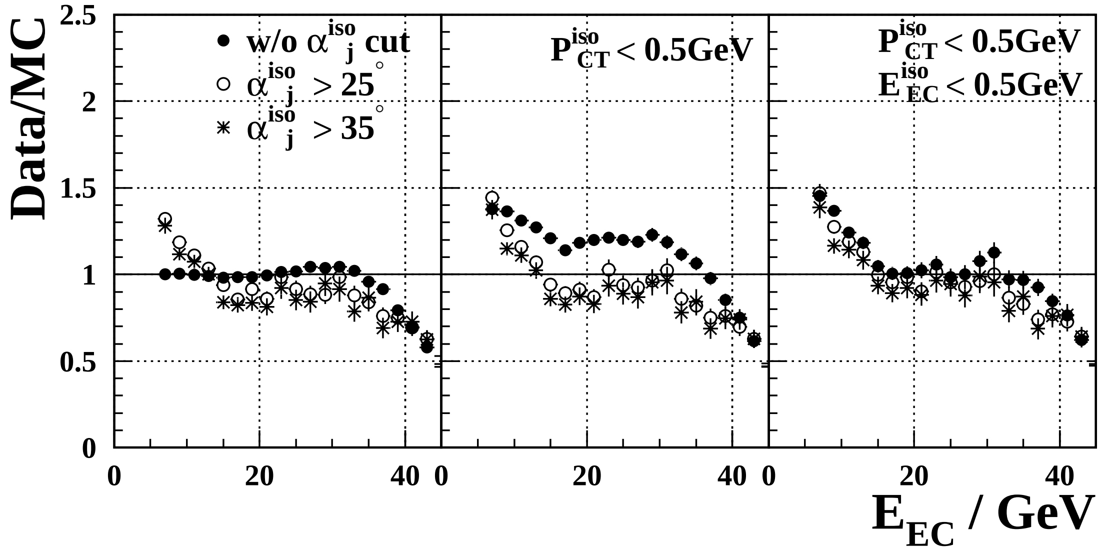

Figure 5.6: Agreement between data and Monte Carlo simulation in the energy of electromagnetic calorimeter clusters. Tighter isolation cut make the agreement worse in the cluster energy.

5.2.4 Background Estimation

Hadronic events and τ pair events with a high energy isolated neutral hadron remain after the isolated electromagnetic cluster selection. According to the Monte Carlo simulation the contribution of two photon processes is less than 0.01% in all subsamples. The contamination of τ pair events is 0.5$\sim$1.0%. In addition to small number of events, since event shape variables for τ pair events are concentrated in the lowest bin of the distribution and outside the fitting range, the effect on the result of fitting is negligible.

As the mentioned in Section 3.3, the Monte Carlo generator fails to reproduce the observed rate of isolated prompt photons. It is found in this analysis also. When the tighter isolation condition is required, the excess of data to Monte Carlo expectation increases as shown in Figure 5.6. The background fraction is evaluated using data based on the two independent method described in the following. The difference in values of α_s obtained by two methods is included in systematic errors.

Estimation with Likelihood Distributions

Fractions of background events from neutral hadrons in the each subsample are estimated by fitting likelihood distributions of signal and background Monte Carlo to data after the isolation cut and preselection. A binned maximum likelihood method is used for the fitting. The fitted distribution C_i is defined as

$$C_i = f_{\rm sig} C_i^{\rm sig} + (1 - f_{\rm sig}) C_i^{\rm bkg}, \tag{5.8}$$

where $C_i^{\rm sig}$ and $C_i^{\rm bkg}$ are the i'th bin contents of signal(radiative multi-hadronic events) and background (non-radiative multi-hadronic events) obtained by Monte Carlo simulations. $f_{\rm sig}$ is the fraction of signal events in all selected events. The result of the fitting is shown in the Table 5.3. The likelihood distribution shown in Figure 5.5 from Monte Carlo is normalized with the number of candidates. Distributions for signal and background are scaled by fractions obtained by the fitting.

The chi-square for samples with $\sqrt{s'} = 78.1\text{GeV}, 71.8\text{GeV}$ and 24.4GeV is substantially larger than other samples. If the lowest bin is not used in the fitting, the reduced chi-square for samples with $\sqrt{s'} = 78.1\text{GeV}$ and 71.8GeV is in 1∼2. For the sample with $\sqrt{s'} = 24.4\text{GeV}$, a few data points contribute most of the chi-square.

Fractions of neutral hadron background estimated by this methods are shown in Table 5.2. Statistical errors for data and Monte Carlo events are shown for method by fitting likelihood.

$\sqrt{s'}$[GeV]	χ^2/d.o.f	f_{sig}[%]
78.1	122.8/18	71.9 ± 2.0
71.8	49.6/18	84.4 ± 2.8
65.1	14.4/18	88.8 ± 3.3
57.6	24.6/18	83.7 ± 3.9
49.0	18.6/18	85.8 ± 4.4
38.5	22.7/18	82.6 ± 4.6
24.4	37.4/18	77.6 ± 5.3

Table 5.3: The results of fitting the likelihood distribution.

Estimation with Charged Hadron Rates

Alternatively we estimate the fraction of background from neutral hadrons after isolation selection by using isospin symmetry.

According to the Monte Carlo information, electromagnetic calorimeter clusters after the isolation cuts originate from the decay of neutral pion (31.6%), neutral kaon (7.0%), neutron(6.3%) and eta meson(3.2%) in addition to initial and final state radiation(45.2%).

When isospin symmetry is assumed to be obeyed in hadron production, rates of neutral pion, neutral kaons and neutron are estimated from rate of charged pions, charged kaons and protons, respectively. The relations between the neutral hadrons and charged hadrons are;

$$N_{\pi^0} = \frac{1}{2}N_{\pi^\pm} \qquad N_{\mathrm{K}^0} = \frac{1}{2}N_{\mathrm{K}^\pm} \qquad N_n = N_p \ . \tag{5.9}$$

As seen in Figure 5.7, a similar discrepancy between data and Monte Carlo is found after the same isolation cuts. The rates of isolated neutral hadrons are estimated from the rates of isolated charged hadrons using these relations.

The isolated $\pi^\pm$, $K^\pm$ and proton rates are obtained from the number of tracks by trusting the composition of these charged particles predicted by Monte Carlo simulation. The fraction of charged pion, charged kaon and proton in all tracks after all isolation cuts ($P_{\text{CT}}^{\text{iso}}$,$E_{\text{EC}}^{\text{iso}}$and $\alpha_{\text{jet}}^{\text{iso}}$) are 43.7%, 38.0% and 11.33%, respectively. The rates of isolated charged hadrons are converted to the rates of isolated π^0, K^0 and neutron using Equation 5.9.

Actually, the isospin symmetry is not satisfied exactly. The sizes of violation of the isospin symmetry could be obtained from the measured production rate for π^0 [143, 144],

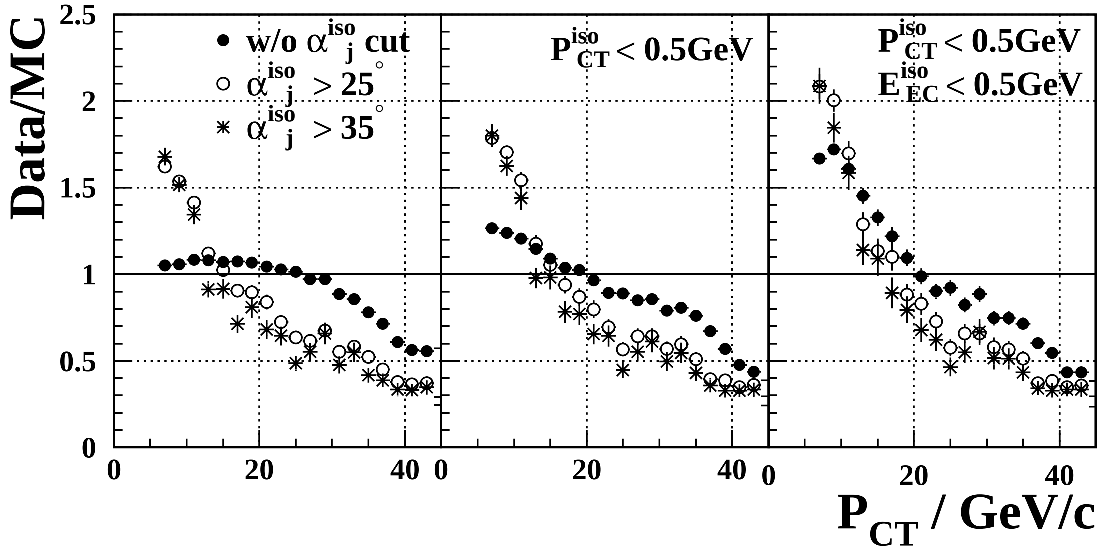

Figure 5.7: Agreement between data and Monte Carlo simulation in the momentum of tracks. Tighter isolation cut make the agreement worse in the track momentum.

$\pi^{\pm}$, $K^{\pm}$, proton [145] and K^0 [143, 146–149] and JETSET and HERWIG tuned with OPAL data [33, 132]. They are shown in the following table.

	Measured	JT7.4	HW6.1
$(N_{\pi^0} - N_{\pi^\pm})/N_{\pi^0}[\%]$	7.93	10.71	10.91
$(N_{K^0} - N_{K^\pm})/N_{K^0}[\%]$	18.22	4.50	5.35
$(N_n - N_p)/N_{n^0}[\%]$	—-	-5.0	-8.93

Table 5.4: Measured value and Monte Carlo prediction of difference of the produc tion rates.

For pions and kaons, the measured values are used for the estimation [1]. The mean of the values for JETSET and HERWIG are used for protons. If the rates estimated from the isolated charged hadron rates are used, the energy distribution of isolated electromagnetic calorimeter clusters after isolation cuts shows a better agreement between data and Monte Carlo prediction (Figure 5.8 a). After the likelihood selection, a excess of data can be seen in the low photon energy region. It is a similar situation as analyses described in Section 3.3.

Fractions of neutral hadron background after all selections estimated by this methods are shown in Table 5.2. Statistical errors and the uncertainty from violation of isospin symmetry are included for the method using isolated tracks.

5.2.5 Event Shape Variables at Detector Level and Hadron Level

The determination of α_s is based on measurements of the event shape variables $(1-T)$, M_H, B_T, B_W, C and y_{23}^D described in Section 2.3.4. In this analysis, event shape variables

[1]In the case of kaons, there is a difference more than three standard deviations between measurement (2.027) and tuned Monte Carlo predictions (2.207 in JETSET 7.4 and 2.262 HERWIG 6.1) in the production rate of K^0

are calculated from tracks and electromagnetic clusters excluding the isolated photon candidate. Contribution of electromagnetic clusters originating from charged particles are removed by the method described in Section 5.2.1.

Since these variables are defined in the center-of-mass frame of the colliding beams, the hadronic system should be boosted back into the center-of-mass frame of the hadrons. The Lorentz boost is determined from the energy and angle of the photon candidate. When the four-momentum of particles in the hadronic system is calculated, electromagnetic clusters are treated as photons with zero mass, and tracks of charged particles are treated as hadrons with the mass of charged pions. The momentum of the system of all hadrons after the boost back is shown in Figure 5.9. The error bar is the RMS of the momentum distribution. The mean value of the momentum is zero for all energy samples in the both case of Data and Monte Carlo. It shows that the hadronic system is correctly boosted back into the center-of-mass system.

Event shape variables for $\sqrt{s'} = 78.1$GeV and 24.4GeV are shown in Figure 5.10 and Figure 5.11. The background distributions are scaled by the fraction of non-radiative hadronic events and τ pair events listed in Table 5.2. τ pair events have a small event shape as expected from the narrow two-jet like topology. The Monte Carlo simulation reproduce the event shape of data for all event shape variables and for both the largest and the smallest $\sqrt{s'}$ samples. The contributions from these background events are removed statistically by subtracting the Monte Carlo distribution. We call it "background subtraction".

The effects of the experimental resolution and acceptance are unfolded using Monte Carlo samples with full detector simulation (detector correction). The unfolding is performed bin-by-bin with correction factors $r_i^{Det} = h_i/d_i$, where h_i represents the value of i'th bin of the event shape distribution of hadrons in Monte Carlo simulation without detector simulation. The "hadrons" are defined as particles with a mean proper lifetime longer than $3 \cdot 10^{-10}$s. d_i represents the value of the i'th bin of the event shape distribution calculated with clusters and tracks obtained from Monte Carlo samples with detector simulation. We refer to the distributions after applying these corrections as data corrected to the "hadron level".

The event shapes for data corrected to the hadron level are shown in Figure 5.12 and Figure 5.13. Figure 5.13 is shown as an example of the smallest statistics samples. The histograms for data corrected to the hadron level are given in Figure 5.5,Figure 5.6, Figure 5.7,Figure 5.8, Figure 5.9 and Figure 5.10. The first error is a statistical error. The second error is a systematic error which is obtained from the difference of bin contents in standard analysis and alternative analyses described in Section 5.4.1.

The event shapes for data at hadron level are compared with the predictions of the Monte Carlo samples with center-of-mass energies set to the mean value of $\sqrt{s'}$ in each subsample. In the production of the Monte Carlo samples, ISR and FSR is switched off and on, respectively. The differences between generators are much smaller than the error for each bin in Figure 5.12. However, the difference between generators can be seen around the peak of M_H,B_T,C and y_{23}^D. The predictions by `HERWIG` deviate from the data distributions. The difference between generators become clearer in this figure. Distributions of `JETSET` and `ARIADNE` are steeper than that of `HERWIG`. `HERWIG` is a little better in agreement with data than `JETSET` and `ARIADNE`. In conclusion, the predictions from event generators are consistent with the data for all the $\sqrt{s'}$ samples.

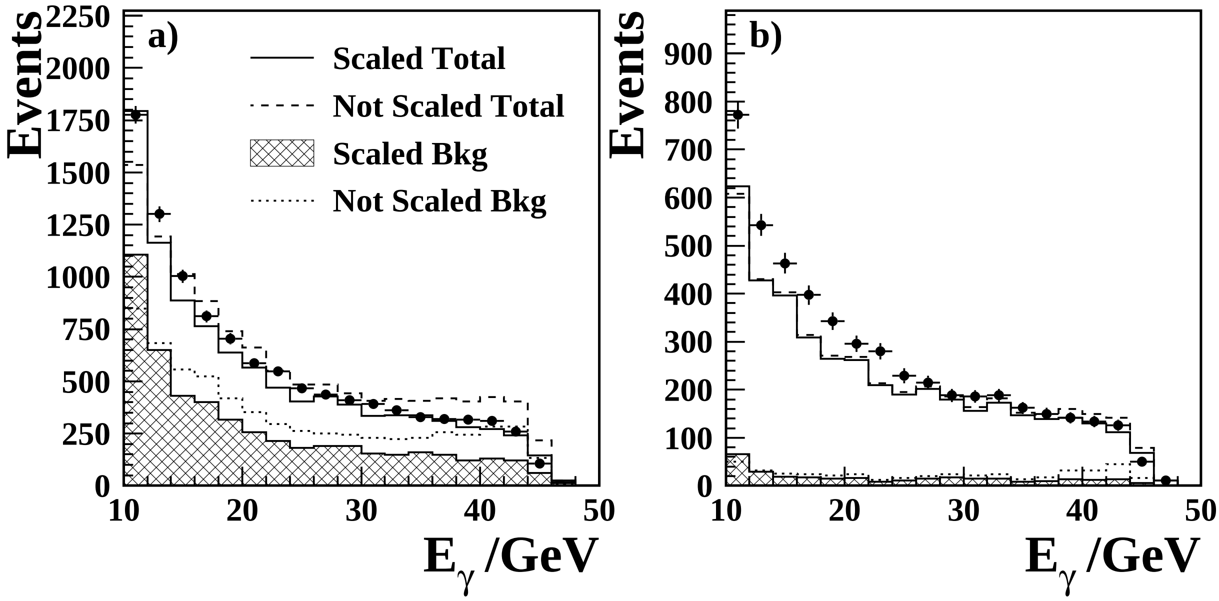

Figure 5.8: The cluster energy after the isolated electromagnetic cluster selection (a)) and after the likelihood selection (b)) The solid (dashed) histogram is a Monte Carlo prediction for all processes when neutral hadron background events are (not) scaled according to the fraction estimated by the rate of isolated charged hadrons. The hatched (dotted) histogram is a Monte Carlo prediction for neutral hadron background events when the neutral hadron background events are (not) scaled.

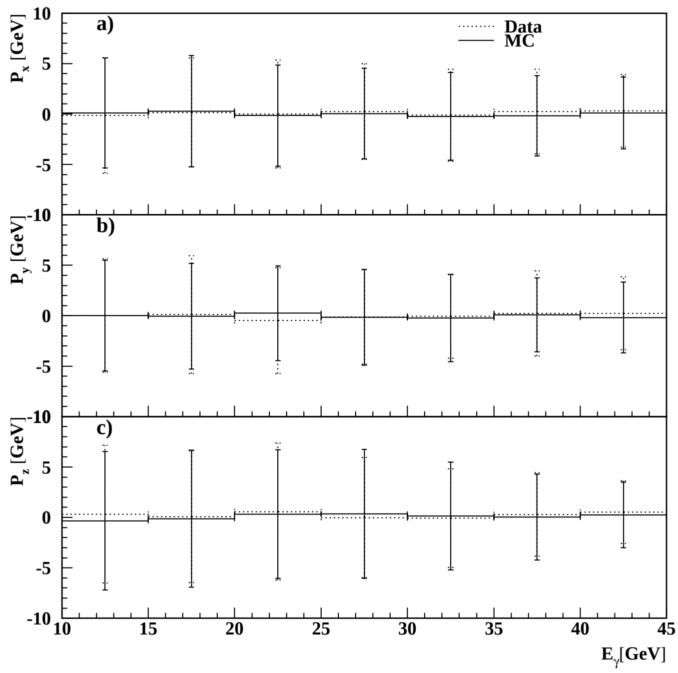

p

Figure 5.9: Momentum of system of all hadrons which are boosted back according to the momentum of the photon.

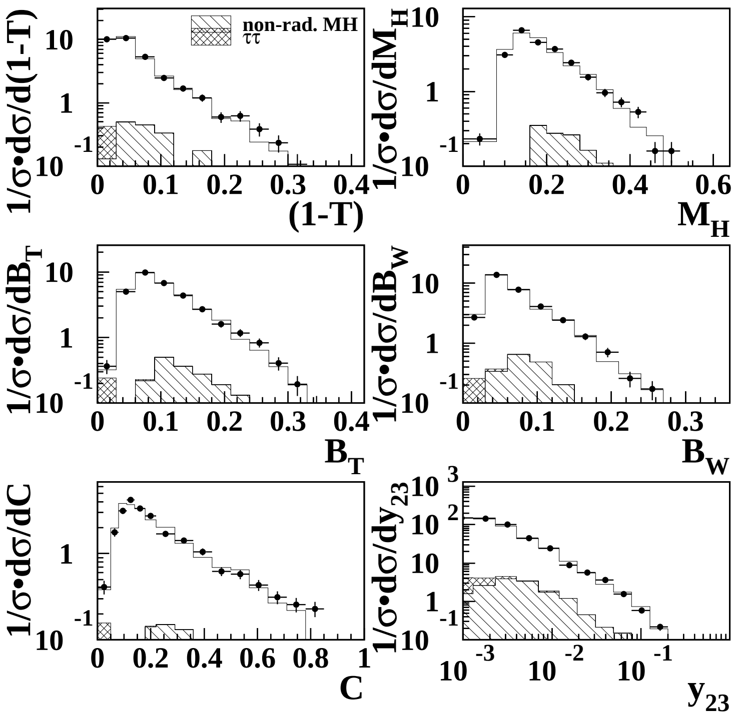

Figure 5.10: Event shape variables at the detector level for $\sqrt{s'} = 78.1$GeV

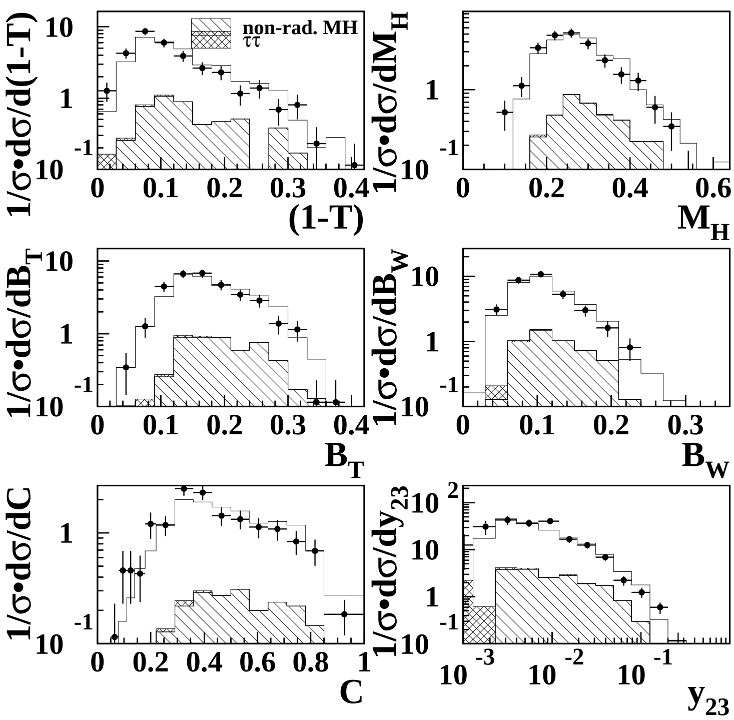

Figure 5.11: Event shape variables at the detector level for $\sqrt{s'} = 24.4$GeV

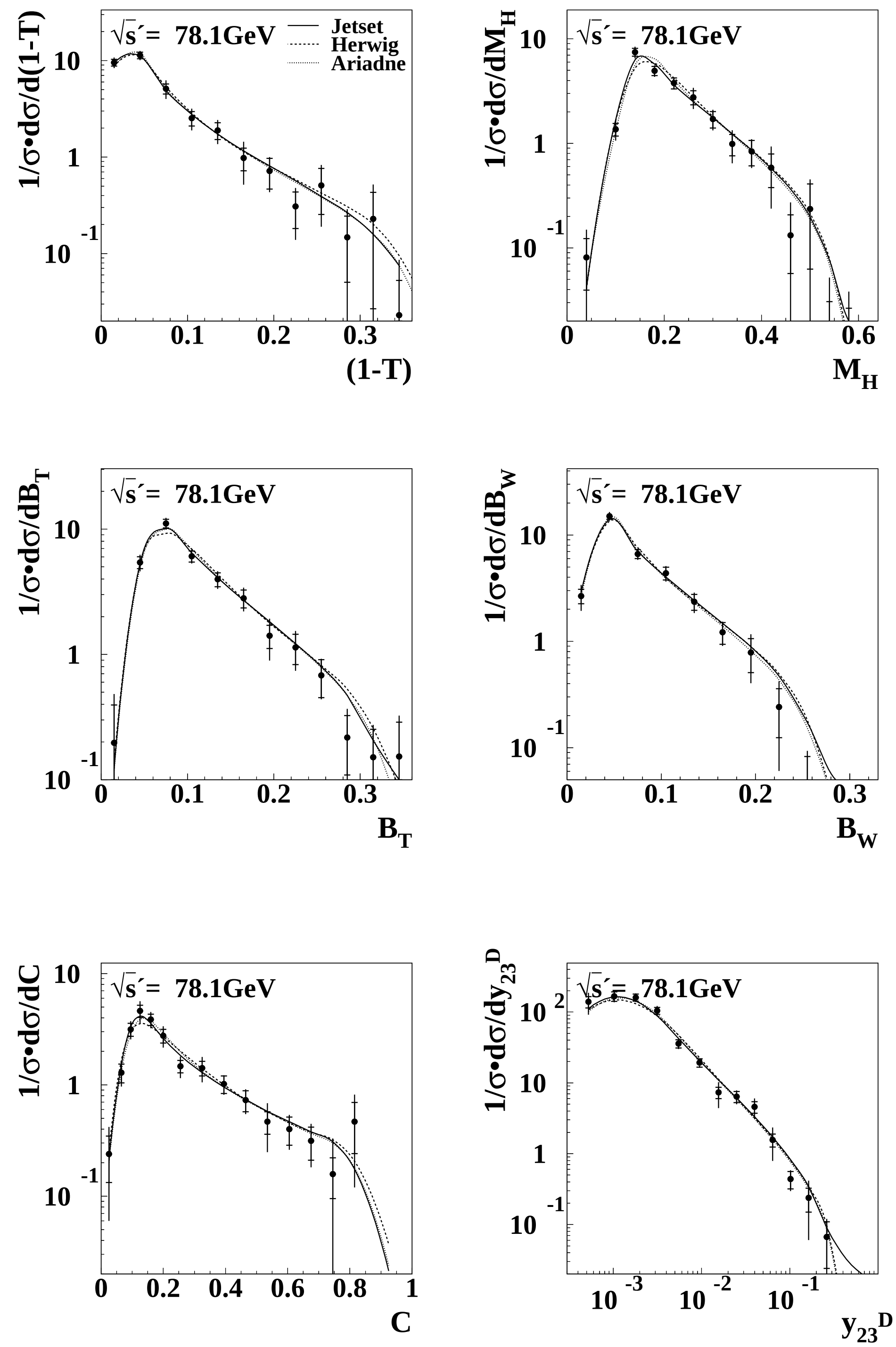

Figure 5.12: Event shape variables at the hadron level for $\sqrt{s'} = 78.1$GeV

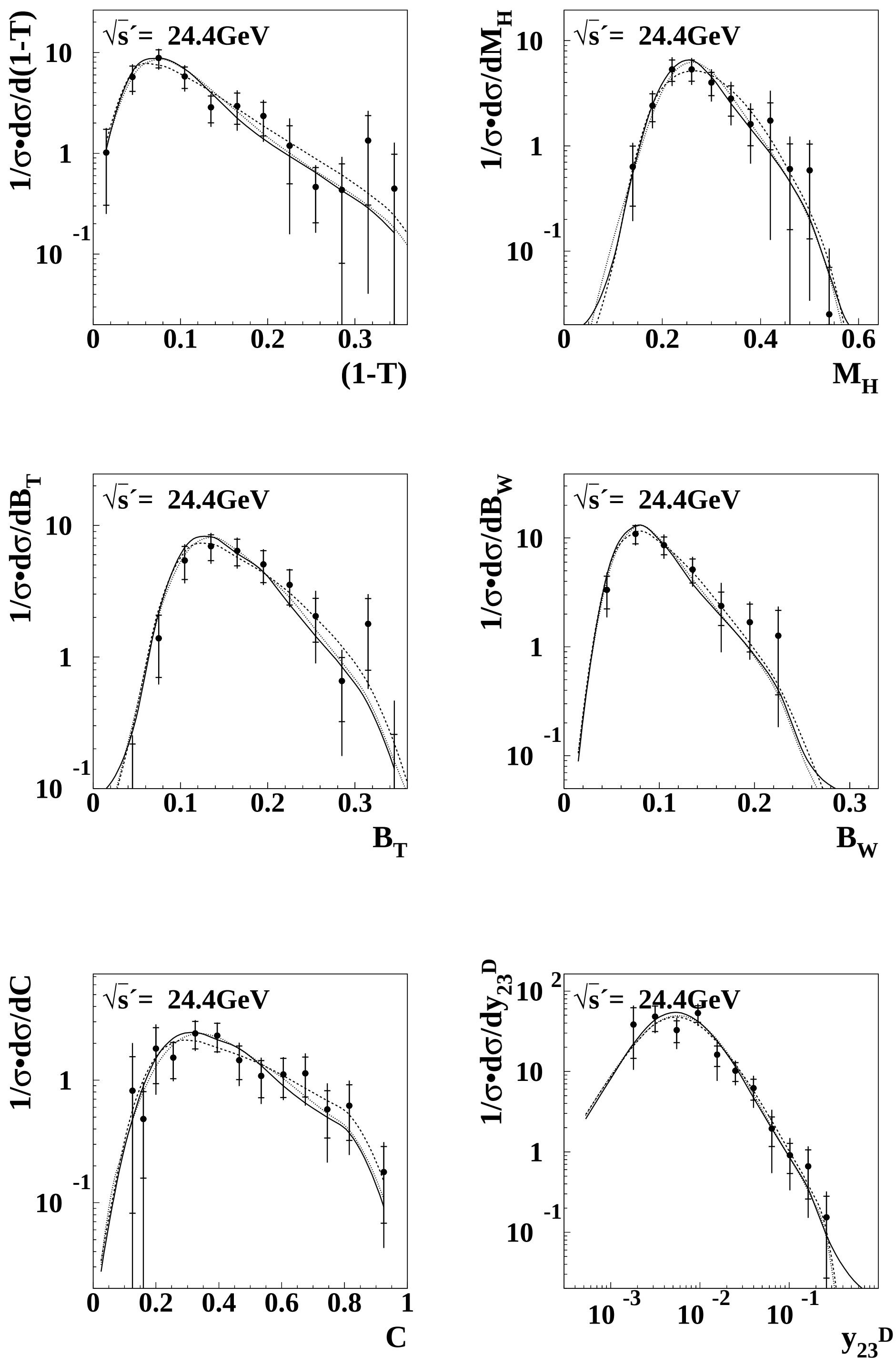

Figure 5.13: Event shape variables at the hadron level for $\sqrt{s'} = 24.4\text{GeV}$

$(1-T)$	$1/\sigma \cdot d\sigma/d(1-T)$			
	78.1GeV	71.8GeV	65.1GeV	57.6GeV
0.00-0.03	9.54 ± 0.77 ± 0.91	6.63 ± 0.77 ± 0.42	7.22 ± 0.96 ± 0.30	5.03 ± 0.91 ± 1.08
0.03-0.06	11.32 ± 0.87 ± 0.91	11.83 ± 1.13 ± 0.79	12.90 ± 1.37 ± 0.81	12.20 ± 1.48 ± 1.24
0.06-0.09	5.11 ± 0.60 ± 0.94	6.06 ± 0.85 ± 0.62	5.12 ± 0.85 ± 0.21	5.66 ± 1.05 ± 0.79
0.09-0.12	2.53 ± 0.43 ± 0.47	3.01 ± 0.56 ± 0.47	2.44 ± 0.58 ± 0.30	2.58 ± 0.66 ± 0.78
0.12-0.15	1.89 ± 0.38 ± 0.37	2.17 ± 0.57 ± 0.35	1.84 ± 0.53 ± 0.42	2.04 ± 0.61 ± 0.29
0.15-0.18	0.98 ± 0.26 ± 0.38	1.43 ± 0.46 ± 0.34	1.50 ± 0.50 ± 0.24	2.45 ± 0.91 ± 0.90
0.18-0.21	0.72 ± 0.25 ± 0.13	0.81 ± 0.29 ± 0.27	0.85 ± 0.38 ± 0.44	2.09 ± 0.98 ± 0.29
0.21-0.24	0.31 ± 0.13 ± 0.11	0.55 ± 0.25 ± 0.43	0.30 ± 0.21 ± 0.16	0.49 ± 0.26 ± 0.13
0.24-0.27	0.51 ± 0.25 ± 0.19	0.43 ± 0.25 ± 0.19	0.65 ± 0.41 ± 0.23	0.22 ± 0.20 ± 0.09
0.27-0.30	0.15 ± 0.10 ± 0.10	0.23 ± 0.15 ± 0.10	0.25 ± 0.16 ± 0.10	0.48 ± 0.39 ± 0.35
0.30-0.33	0.23 ± 0.20 ± 0.21	0.09 ± 0.08 ± 0.03	0.18 ± 0.16 ± 0.13	0.09 ± 0.11 ± 0.15
0.33-0.36	0.02 ± 0.03 ± 0.06	0.05 ± 0.07 ± 0.06	0.10 ± 0.16 ± 0.19	0.00 ± 0.00 ± 0.07
0.36-0.39	0.05 ± 0.07 ± 0.08	0.02 ± 0.05 ± 0.02	0.00 ± 0.00 ± 0.00	0.00 ± 0.00 ± 0.00

$(1-T)$	$1/\sigma \cdot d\sigma/d(1-T)$		
	49.0GeV	38.5GeV	24.4GeV
0.00-0.03	2.60 ± 0.60 ± 0.31	1.69 ± 0.59 ± 0.38	1.02 ± 0.71 ± 0.28
0.03-0.06	12.50 ± 1.69 ± 1.25	10.35 ± 1.69 ± 1.13	5.72 ± 1.60 ± 1.07
0.06-0.09	8.11 ± 1.41 ± 0.75	7.65 ± 1.33 ± 0.75	8.83 ± 1.79 ± 1.05
0.09-0.12	3.13 ± 0.79 ± 0.53	4.54 ± 0.99 ± 0.33	5.78 ± 1.39 ± 0.97
0.12-0.15	2.00 ± 0.57 ± 0.44	2.92 ± 0.93 ± 0.29	2.86 ± 0.85 ± 0.57
0.15-0.18	1.92 ± 0.71 ± 0.66	1.62 ± 0.59 ± 0.33	2.95 ± 1.01 ± 0.78
0.18-0.21	0.59 ± 0.35 ± 0.71	1.23 ± 0.63 ± 0.72	2.34 ± 0.86 ± 0.60
0.21-0.24	0.91 ± 0.48 ± 0.51	1.17 ± 0.61 ± 0.52	1.19 ± 0.69 ± 0.76
0.24-0.27	0.54 ± 0.32 ± 0.03	1.44 ± 0.90 ± 0.23	0.46 ± 0.26 ± 0.15
0.27-0.30	0.40 ± 0.32 ± 0.27	0.42 ± 0.30 ± 0.22	0.43 ± 0.35 ± 0.34
0.30-0.33	0.63 ± 0.85 ± 0.58	0.00 ± 0.00 ± 0.00	1.34 ± 1.03 ± 0.79
0.33-0.36	0.00 ± 0.00 ± 0.00	0.27 ± 0.30 ± 0.20	0.45 ± 0.53 ± 0.64

Table 5.5: Hadron level distributions of $(1-T)$.

M_H	$1/\sigma \cdot d\sigma/dM_H$			
	78.1GeV	71.8GeV	65.1GeV	57.6GeV
0.00-0.08	0.08 ± 0.04 ± 0.05	-0.00 ± 0.01 ± 0.01	0.01 ± 0.01 ± 0.01	0.00 ± 0.00 ± 0.00
0.08-0.12	1.36 ± 0.19 ± 0.24	1.11 ± 0.22 ± 0.16	0.89 ± 0.23 ± 0.23	0.37 ± 0.15 ± 0.14
0.12-0.16	7.47 ± 0.64 ± 0.70	5.30 ± 0.60 ± 0.30	4.73 ± 0.63 ± 0.61	4.36 ± 0.73 ± 1.07
0.16-0.20	4.96 ± 0.50 ± 0.37	6.47 ± 0.80 ± 0.56	7.50 ± 1.00 ± 0.68	6.05 ± 0.90 ± 0.53
0.20-0.24	3.77 ± 0.46 ± 0.17	3.60 ± 0.53 ± 0.36	3.62 ± 0.64 ± 0.49	4.57 ± 0.85 ± 0.76
0.24-0.28	2.76 ± 0.42 ± 0.47	3.04 ± 0.54 ± 0.52	2.49 ± 0.51 ± 0.47	3.48 ± 0.84 ± 0.46
0.28-0.32	1.71 ± 0.31 ± 0.23	1.81 ± 0.39 ± 0.53	2.11 ± 0.54 ± 0.66	1.81 ± 0.52 ± 0.94
0.32-0.36	0.99 ± 0.23 ± 0.26	1.53 ± 0.41 ± 0.16	0.92 ± 0.29 ± 0.23	2.16 ± 0.66 ± 0.64
0.36-0.40	0.84 ± 0.23 ± 0.12	0.90 ± 0.30 ± 0.16	0.91 ± 0.34 ± 0.39	1.01 ± 0.39 ± 0.36
0.40-0.44	0.59 ± 0.21 ± 0.28	0.49 ± 0.18 ± 0.20	1.14 ± 0.58 ± 0.21	0.64 ± 0.35 ± 0.74
0.44-0.48	0.13 ± 0.08 ± 0.12	0.17 ± 0.09 ± 0.09	0.21 ± 0.13 ± 0.15	0.45 ± 0.28 ± 0.26
0.48-0.52	0.24 ± 0.17 ± 0.13	0.20 ± 0.12 ± 0.12	0.34 ± 0.24 ± 0.24	0.09 ± 0.09 ± 0.10
0.52-0.56	0.01 ± 0.02 ± 0.03	0.38 ± 0.48 ± 0.43	0.10 ± 0.12 ± 0.10	0.00 ± 0.00 ± 0.00
0.56-0.60	0.00 ± 0.02 ± 0.03	0.00 ± 0.00 ± 0.00	0.04 ± 0.06 ± 0.07	0.00 ± 0.00 ± 0.00

M_H	$1/\sigma \cdot d\sigma/dM_H$		
	49.0GeV	38.5GeV	24.4GeV
0.08-0.12	0.30 ± 0.13 ± 0.10	0.13 ± 0.12 ± 0.12	0.00 ± 0.00 ± 0.00
0.12-0.16	2.81 ± 0.58 ± 0.45	1.33 ± 0.39 ± 0.36	0.63 ± 0.36 ± 0.24
0.16-0.20	7.05 ± 1.14 ± 0.65	5.70 ± 1.04 ± 0.76	2.41 ± 0.72 ± 0.61
0.20-0.24	5.04 ± 0.96 ± 0.68	5.39 ± 1.01 ± 0.32	5.33 ± 1.23 ± 1.06
0.24-0.28	4.18 ± 0.87 ± 0.54	5.52 ± 1.19 ± 0.44	5.33 ± 1.21 ± 0.93
0.28-0.32	2.15 ± 0.64 ± 0.47	2.53 ± 0.70 ± 0.31	4.00 ± 0.99 ± 0.93
0.32-0.36	1.47 ± 0.49 ± 0.32	2.18 ± 0.70 ± 0.21	2.82 ± 0.90 ± 0.87
0.36-0.40	0.43 ± 0.21 ± 0.17	1.02 ± 0.41 ± 0.26	1.61 ± 0.61 ± 0.71
0.40-0.44	0.85 ± 0.43 ± 0.44	0.72 ± 0.36 ± 0.21	1.74 ± 0.82 ± 1.39
0.44-0.48	0.49 ± 0.34 ± 0.65	0.30 ± 0.22 ± 0.37	0.60 ± 0.44 ± 0.44
0.48-0.52	0.19 ± 0.18 ± 0.11	0.18 ± 0.22 ± 0.17	0.59 ± 0.46 ± 0.31
0.52-0.56	0.06 ± 0.07 ± 0.03	0.00 ± 0.00 ± 0.00	0.03 ± 0.05 ± 0.07

Table 5.6: Hadron level distributions of M_H.

B_T	$1/\sigma \cdot d\sigma/dB_T$			
	78.1GeV	71.8GeV	65.1GeV	57.6GeV
0.00-0.03	0.20 ± 0.20 ± 0.21	0.00 ± 0.05 ± 0.04	0.04 ± 0.13 ± 0.06	0.00 ± 0.00 ± 0.00
0.03-0.06	5.42 ± 0.59 ± 0.58	3.83 ± 0.63 ± 0.37	3.05 ± 0.61 ± 0.37	1.69 ± 0.52 ± 0.40
0.06-0.09	11.10 ± 0.88 ± 0.83	9.23 ± 0.94 ± 0.46	10.86 ± 1.26 ± 0.62	9.30 ± 1.32 ± 0.79
0.09-0.12	6.08 ± 0.63 ± 0.45	7.56 ± 0.93 ± 0.54	7.56 ± 1.03 ± 0.62	8.59 ± 1.26 ± 1.36
0.12-0.15	3.98 ± 0.51 ± 0.39	4.56 ± 0.71 ± 0.55	4.58 ± 0.81 ± 0.69	4.54 ± 0.93 ± 0.74
0.15-0.18	2.80 ± 0.46 ± 0.39	3.18 ± 0.58 ± 0.55	2.36 ± 0.56 ± 0.20	2.69 ± 0.67 ± 0.69
0.18-0.21	1.41 ± 0.30 ± 0.42	1.82 ± 0.45 ± 0.29	1.98 ± 0.56 ± 0.48	2.01 ± 0.61 ± 0.42
0.21-0.24	1.14 ± 0.31 ± 0.25	1.50 ± 0.46 ± 0.23	1.28 ± 0.42 ± 0.21	2.68 ± 0.94 ± 0.50
0.24-0.27	0.68 ± 0.23 ± 0.08	0.80 ± 0.31 ± 0.46	0.69 ± 0.40 ± 0.21	0.55 ± 0.27 ± 0.21
0.27-0.30	0.22 ± 0.11 ± 0.11	0.71 ± 0.33 ± 0.26	0.58 ± 0.29 ± 0.22	0.92 ± 0.51 ± 0.30
0.30-0.33	0.15 ± 0.10 ± 0.07	0.12 ± 0.09 ± 0.07	0.30 ± 0.22 ± 0.12	0.14 ± 0.14 ± 0.26
0.33-0.36	0.15 ± 0.14 ± 0.11	0.00 ± 0.00 ± 0.00	0.04 ± 0.06 ± 0.07	0.23 ± 0.34 ± 0.18

B_T	$1/\sigma \cdot d\sigma/dB_T$		
	49.0GeV	38.5GeV	24.4GeV
0.03-0.06	0.82 ± 0.34 ± 0.33	0.14 ± 0.14 ± 0.11	0.09 ± 0.13 ± 0.10
0.06-0.09	6.68 ± 1.18 ± 0.52	4.48 ± 1.06 ± 0.59	1.39 ± 0.69 ± 0.34
0.09-0.12	8.91 ± 1.38 ± 1.27	7.00 ± 1.24 ± 1.13	5.40 ± 1.52 ± 0.94
0.12-0.15	6.76 ± 1.28 ± 1.07	8.10 ± 1.48 ± 0.93	6.94 ± 1.54 ± 0.98
0.15-0.18	3.46 ± 0.86 ± 0.52	3.69 ± 0.85 ± 0.53	6.40 ± 1.47 ± 0.85
0.18-0.21	2.86 ± 0.79 ± 0.45	4.81 ± 1.36 ± 0.94	5.05 ± 1.38 ± 0.68
0.21-0.24	1.69 ± 0.62 ± 0.32	1.53 ± 0.56 ± 0.53	3.53 ± 1.05 ± 0.46
0.24-0.27	0.54 ± 0.30 ± 0.50	1.56 ± 0.66 ± 0.59	2.04 ± 0.75 ± 0.87
0.27-0.30	1.44 ± 0.76 ± 0.40	1.02 ± 0.56 ± 0.50	0.66 ± 0.33 ± 0.34
0.30-0.33	0.18 ± 0.18 ± 0.06	0.24 ± 0.20 ± 0.04	1.79 ± 0.99 ± 0.70
0.33-0.36	-0.02 ± 0.03 ± 0.05	0.76 ± 1.00 ± 0.40	0.05 ± 0.21 ± 0.36

Table 5.7: Hadron level distributions of B_T.

B_W	$1/\sigma \cdot d\sigma/dB_W$			
	78.1GeV	71.8GeV	65.1GeV	57.6GeV
0.00-0.03	2.67 ± 0.41 ± 0.60	1.58 ± 0.40 ± 0.56	1.20 ± 0.38 ± 0.32	0.92 ± 0.43 ± 0.56
0.03-0.06	15.03 ± 1.01 ± 0.99	13.97 ± 1.21 ± 0.74	15.71 ± 1.53 ± 0.89	13.80 ± 1.63 ± 1.31
0.06-0.09	6.63 ± 0.64 ± 0.48	8.24 ± 0.99 ± 0.49	6.84 ± 0.93 ± 0.54	6.99 ± 1.02 ± 0.58
0.09-0.12	4.37 ± 0.60 ± 0.40	3.47 ± 0.55 ± 0.34	4.41 ± 0.83 ± 0.55	6.07 ± 1.29 ± 0.34
0.12-0.15	2.36 ± 0.40 ± 0.32	2.84 ± 0.61 ± 0.56	2.13 ± 0.54 ± 0.62	1.97 ± 0.54 ± 0.95
0.15-0.18	1.22 ± 0.28 ± 0.14	1.94 ± 0.51 ± 0.23	1.48 ± 0.50 ± 0.18	2.28 ± 0.77 ± 0.46
0.18-0.21	0.78 ± 0.28 ± 0.26	0.55 ± 0.22 ± 0.41	0.97 ± 0.39 ± 0.11	0.55 ± 0.26 ± 0.16
0.21-0.24	0.24 ± 0.12 ± 0.14	0.21 ± 0.11 ± 0.17	0.45 ± 0.29 ± 0.16	0.76 ± 0.54 ± 0.45
0.24-0.27	0.04 ± 0.04 ± 0.03	0.54 ± 0.44 ± 0.23	0.08 ± 0.08 ± 0.03	0.00 ± 0.00 ± 0.20
0.27-0.30	0.00 ± 0.00 ± 0.04	0.00 ± 0.00 ± 0.00	0.05 ± 0.09 ± 0.09	0.00 ± 0.00 ± 0.00

B_W	$1/\sigma \cdot d\sigma/dB_W$		
	49.0GeV	38.5GeV	24.4GeV
0.00-0.03	0.51 ± 0.33 ± 0.20	0.00 ± 0.00 ± 0.06	0.00 ± 0.00 ± 0.00
0.03-0.06	11.88 ± 1.63 ± 0.87	7.93 ± 1.39 ± 0.64	3.34 ± 1.11 ± 0.98
0.06-0.09	9.52 ± 1.40 ± 0.51	11.89 ± 1.79 ± 1.10	10.93 ± 2.09 ± 1.17
0.09-0.12	5.51 ± 1.11 ± 0.31	6.18 ± 1.18 ± 0.77	8.61 ± 1.60 ± 1.47
0.12-0.15	2.51 ± 0.74 ± 0.30	3.81 ± 1.07 ± 0.52	5.14 ± 1.28 ± 0.92
0.15-0.18	1.39 ± 0.47 ± 0.49	2.01 ± 0.73 ± 0.40	2.38 ± 0.81 ± 1.25
0.18-0.21	1.62 ± 0.74 ± 0.91	1.09 ± 0.49 ± 0.42	1.68 ± 0.79 ± 0.48
0.21-0.24	0.35 ± 0.25 ± 0.25	0.41 ± 0.35 ± 0.35	1.27 ± 0.90 ± 0.60
0.24-0.27	0.06 ± 0.07 ± 0.02	0.00 ± 0.00 ± 0.00	-0.02 ± 0.03 ± 0.06

Table 5.8: Hadron level distributions of B_W.

C	$1/\sigma \cdot d\sigma/dC$			
	78.1GeV	71.8GeV	65.1GeV	57.6GeV
0.00-0.05	0.24 ± 0.11 ± 0.14	0.03 ± 0.03 ± 0.05	0.01 ± 0.02 ± 0.02	0.00 ± 0.00 ± 0.00
0.05-0.08	1.29 ± 0.25 ± 0.21	0.88 ± 0.26 ± 0.19	0.96 ± 0.35 ± 0.34	0.58 ± 0.31 ± 0.26
0.08-0.11	3.15 ± 0.42 ± 0.41	2.28 ± 0.45 ± 0.19	2.20 ± 0.50 ± 0.31	0.88 ± 0.31 ± 0.38
0.11-0.14	4.61 ± 0.58 ± 0.85	3.61 ± 0.60 ± 0.69	3.95 ± 0.75 ± 0.43	3.05 ± 0.80 ± 0.78
0.14-0.18	3.87 ± 0.45 ± 0.46	3.74 ± 0.56 ± 0.61	3.32 ± 0.58 ± 0.62	3.65 ± 0.73 ± 0.49
0.18-0.22	2.76 ± 0.39 ± 0.47	2.46 ± 0.40 ± 0.36	3.64 ± 0.66 ± 0.58	3.57 ± 0.73 ± 0.86
0.22-0.29	1.47 ± 0.19 ± 0.26	2.18 ± 0.34 ± 0.36	2.02 ± 0.34 ± 0.22	2.27 ± 0.41 ± 0.29
0.29-0.36	1.42 ± 0.21 ± 0.30	1.45 ± 0.26 ± 0.29	1.67 ± 0.34 ± 0.11	1.28 ± 0.31 ± 0.29
0.36-0.43	1.02 ± 0.18 ± 0.09	0.86 ± 0.18 ± 0.18	0.70 ± 0.19 ± 0.25	1.13 ± 0.32 ± 0.28
0.43-0.50	0.73 ± 0.16 ± 0.10	1.15 ± 0.28 ± 0.12	0.74 ± 0.23 ± 0.13	0.65 ± 0.21 ± 0.18
0.50-0.57	0.47 ± 0.11 ± 0.19	0.58 ± 0.17 ± 0.10	0.58 ± 0.18 ± 0.11	0.82 ± 0.28 ± 0.26
0.57-0.64	0.40 ± 0.11 ± 0.08	0.56 ± 0.17 ± 0.15	0.78 ± 0.28 ± 0.18	0.83 ± 0.33 ± 0.20
0.64-0.71	0.31 ± 0.10 ± 0.08	0.41 ± 0.15 ± 0.19	0.20 ± 0.09 ± 0.10	0.66 ± 0.27 ± 0.08
0.71-0.78	0.16 ± 0.06 ± 0.16	0.41 ± 0.18 ± 0.19	0.24 ± 0.13 ± 0.05	0.27 ± 0.14 ± 0.17
0.78-0.85	0.47 ± 0.23 ± 0.26	0.14 ± 0.07 ± 0.03	0.26 ± 0.14 ± 0.07	0.31 ± 0.18 ± 0.20
0.85-1.00	0.00 ± 0.00 ± 0.01	0.04 ± 0.03 ± 0.01	0.03 ± 0.03 ± 0.02	0.01 ± 0.02 ± 0.02

C	$1/\sigma \cdot d\sigma/dC$		
	49.0GeV	38.5GeV	24.4GeV
0.00-0.05	0.05 ± 0.10 ± 0.09	0.00 ± 0.00 ± 0.00	0.00 ± 0.00 ± 0.00
0.05-0.08	0.28 ± 0.18 ± 0.15	0.00 ± 0.00 ± 0.00	0.00 ± 0.00 ± 0.00
0.08-0.11	0.48 ± 0.23 ± 0.23	0.31 ± 0.25 ± 0.22	0.00 ± 0.00 ± 0.00
0.11-0.14	2.35 ± 0.75 ± 0.27	0.63 ± 0.30 ± 0.17	0.82 ± 0.74 ± 0.94
0.14-0.18	1.91 ± 0.47 ± 0.38	2.19 ± 0.71 ± 0.68	0.48 ± 0.32 ± 0.35
0.18-0.22	3.55 ± 0.80 ± 0.42	1.80 ± 0.53 ± 0.49	1.81 ± 0.87 ± 0.58
0.22-0.29	3.00 ± 0.56 ± 0.18	3.10 ± 0.64 ± 0.58	1.53 ± 0.50 ± 0.22
0.29-0.36	1.97 ± 0.45 ± 0.33	1.63 ± 0.36 ± 0.38	2.41 ± 0.61 ± 0.30
0.36-0.43	1.50 ± 0.41 ± 0.39	2.21 ± 0.52 ± 0.37	2.31 ± 0.61 ± 0.21
0.43-0.50	0.46 ± 0.15 ± 0.10	0.98 ± 0.29 ± 0.16	1.46 ± 0.45 ± 0.34
0.50-0.57	1.06 ± 0.34 ± 0.21	1.15 ± 0.41 ± 0.32	1.08 ± 0.36 ± 0.26
0.57-0.64	0.58 ± 0.23 ± 0.16	0.82 ± 0.31 ± 0.24	1.12 ± 0.39 ± 0.17
0.64-0.71	0.25 ± 0.14 ± 0.18	0.50 ± 0.22 ± 0.21	1.14 ± 0.41 ± 0.32
0.71-0.78	0.52 ± 0.24 ± 0.17	0.38 ± 0.20 ± 0.16	0.58 ± 0.24 ± 0.27
0.78-0.85	0.44 ± 0.24 ± 0.09	0.60 ± 0.28 ± 0.17	0.62 ± 0.30 ± 0.23
0.85-1.00	0.00 ± 0.01 ± 0.02	0.10 ± 0.09 ± 0.05	0.18 ± 0.11 ± 0.08

Table 5.9: Hadron level distributions of C-parameter.

y_{23}^D	$1/\sigma \cdot d\sigma/dy_{23}^D$		
	78.1GeV	71.8GeV	65.1GeV
0.0003-0.0008	139.41 ± 25.55 ± 40.33	66.90 ± 19.11 ± 29.89	90.60 ± 28.11 ± 22.13
0.0008-0.0013	166.68 ± 25.54 ± 15.53	145.55 ± 29.54 ± 24.01	111.20 ± 26.76 ± 52.68
0.0013-0.0023	160.49 ± 18.19 ± 13.25	143.25 ± 22.32 ± 21.03	148.66 ± 25.06 ± 18.60
0.0023-0.0040	104.37 ± 11.64 ± 13.39	80.24 ± 11.73 ± 16.64	87.32 ± 14.48 ± 14.45
0.0040-0.0070	35.86 ± 4.72 ± 3.41	51.59 ± 7.53 ± 6.38	44.85 ± 7.59 ± 5.63
0.0070-0.0120	19.25 ± 2.61 ± 1.22	23.25 ± 3.81 ± 3.29	19.19 ± 3.80 ± 3.65
0.0120-0.0192	7.32 ± 1.34 ± 2.59	10.49 ± 2.08 ± 1.27	15.71 ± 3.61 ± 4.37
0.0192-0.0307	6.41 ± 1.15 ± 0.85	5.24 ± 1.22 ± 1.27	8.18 ± 2.01 ± 0.98
0.0307-0.0491	4.58 ± 0.85 ± 1.19	4.19 ± 0.97 ± 1.00	2.27 ± 0.65 ± 0.33
0.0491-0.0786	1.57 ± 0.33 ± 0.71	1.58 ± 0.40 ± 0.45	1.48 ± 0.46 ± 0.42
0.0786-0.1258	0.44 ± 0.12 ± 0.08	0.74 ± 0.23 ± 0.19	0.87 ± 0.33 ± 0.20
0.1258-0.2013	0.24 ± 0.09 ± 0.15	0.38 ± 0.14 ± 0.09	0.23 ± 0.10 ± 0.11
0.2013-0.3222	0.07 ± 0.04 ± 0.03	0.13 ± 0.09 ± 0.05	0.16 ± 0.12 ± 0.27

y_{23}^D	$1/\sigma \cdot d\sigma/dy_{23}^D$		
	57.6GeV	49.0GeV	38.5GeV
0.0003-0.0008	48.88 ± 24.65 ± 26.54	34.31 ± 20.70 ± 11.68	-0.80 ± 6.97 ± 13.67
0.0008-0.0013	117.96 ± 37.75 ± 33.59	59.79 ± 25.69 ± 22.75	53.00 ± 35.66 ± 30.84
0.0013-0.0023	125.44 ± 27.96 ± 37.22	81.29 ± 21.43 ± 15.40	44.72 ± 16.52 ± 20.11
0.0023-0.0040	83.22 ± 15.33 ± 12.82	67.77 ± 14.20 ± 7.04	52.64 ± 13.49 ± 12.35
0.0040-0.0070	50.60 ± 9.81 ± 13.26	67.76 ± 12.57 ± 2.94	65.64 ± 13.34 ± 8.20
0.0070-0.0120	23.06 ± 4.66 ± 4.19	34.63 ± 7.60 ± 6.89	43.63 ± 8.96 ± 5.01
0.0120-0.0192	12.83 ± 3.41 ± 3.01	16.66 ± 4.46 ± 4.12	17.44 ± 4.20 ± 3.69
0.0192-0.0307	6.98 ± 1.96 ± 0.79	7.34 ± 2.15 ± 1.49	8.52 ± 2.29 ± 2.38
0.0307-0.0491	4.82 ± 1.39 ± 0.44	2.36 ± 0.73 ± 0.60	2.96 ± 1.03 ± 0.46
0.0491-0.0786	1.57 ± 0.55 ± 0.39	1.68 ± 0.55 ± 0.34	2.18 ± 0.73 ± 0.40
0.0786-0.1258	1.06 ± 0.41 ± 0.42	0.84 ± 0.33 ± 0.28	1.11 ± 0.45 ± 0.72
0.1258-0.2013	0.19 ± 0.11 ± 0.13	0.32 ± 0.16 ± 0.26	0.28 ± 0.15 ± 0.07
0.2013-0.3222	0.06 ± 0.05 ± 0.08	0.15 ± 0.12 ± 0.07	0.05 ± 0.08 ± 0.11

y_{23}^D	$1/\sigma \cdot d\sigma/dy_{23}^D$
	24.4GeV
0.0013-0.0023	38.21 ± 23.68 ± 14.45
0.0023-0.0040	48.13 ± 16.78 ± 7.33
0.0040-0.0070	32.68 ± 9.85 ± 9.56
0.0070-0.0120	53.22 ± 12.55 ± 10.79
0.0120-0.0192	16.12 ± 4.61 ± 7.17
0.0192-0.0307	10.19 ± 2.68 ± 2.19
0.0307-0.0491	6.19 ± 1.78 ± 1.99
0.0491-0.0786	1.94 ± 0.78 ± 1.16
0.0786-0.1258	0.91 ± 0.37 ± 0.44
0.1258-0.2013	0.66 ± 0.40 ± 0.31
0.2013-0.3222	0.15 ± 0.13 ± 0.11

Table 5.10: Hadron level distributions of y_{23}^D.

5.3 Measurement of α_s from Event Shape Distributions

The measurement of α_s is performed by fitting perturbative QCD predictions to the event shape distributions corrected to the hadron level for $(1-T)$, M_H [35], B_T and B_W [36]. The $\mathrm{O}(\alpha_s^2)$ and NLLA calculations are combined with the $\ln(R)$ matching scheme.

The effects of hadronization on event shapes must be taken into account in order to perform fitting at the hadron level (hadronization correction). Preserving the normalization in the hadronization correction is not trivial for low $\sqrt{s'}$ samples because of the large hadronization correction. The hadronization correction is applied to the cumulative theoretical calculation to conserve normalization as in our previous analysis at center-of-mass energies of 130 GeV and 136 GeV and above [32, 33, 54]. The event shape distributions from the QCD calculation are obtained from the cumulative theoretical calculation multiplied by a correction factor $R^{Had} = H_i/P_i$, where P_i represents the value of the i'th bin of the cumulative event shape distribution calculated by Monte Carlo simulation without hadronization. `JETSET`, `HERWIG` and `ARIADNE` are used for this hadronization correction and `JETSET` is chosen for the central results. For example, the hadronization correction factors by `JETSET` for differential distributions are shown in Figure 5.14.

The number of events in each bin inside the fitting region is too small to assume that their statistical error is Gaussian. Therefore, the binned maximum likelihood with $\alpha_s(Q)$ treated as a free parameter is employed for the fitting. The likelihood is defined by

$$\ln \mathcal{L} = \sum_{i=1}^{n_b} \left(\frac{d_i}{R_i} + b_i\right) \ln\left(\frac{f_i}{R_i} + b_i\right) - \left(\frac{f_i}{R_i} + b_i\right),$$

where b_i is the i'th bin content of the background distribution with n_b bins, d_i and f_i are the hadron level distributions obtained from data and theoretical distribution. R_i is the detector correction factor including the change of the bin content in the normalization.

The statistical uncertainty is estimated from fit results derived from 100 Monte Carlo subsamples with the same number of events as selected data events. Since there are not enough simulated events to make subsamples, Monte Carlo distributions without the detector simulation are used for the purpose. The shortcoming of this method is that the statistical fluctuation coming from the background events is not included. The statistical fluctuation is assumed to be equivalent to the difference of error of each bin between the detector level and hadron level of data. The error of each bin is scaled according to the difference and the fluctuation is added to the bin content of all subsamples. The impact of the modification to the fitting result is small because bins where the background subtraction and the detector correction are large are excluded from the fitting region as following comments.

The background subtraction, the detector correction and the hadronization corrections are required to be small and uniform in the fitting region. It restricted the fit to regions well described by the perturbative QCD calculation. The size of the each correction is required to be less than 50% in the fitting range. The size of background subtraction and detector correction is small and flat over all region. The range is mainly restricted by the hadronization correction. For $\sqrt{s'} = 25$GeV sample, the size of the hadronization correction is larger in the whole region than that for other $\sqrt{s'}$ samples. It is obvious for C-parameter. Then the fitting ranges for $\sqrt{s'} = 25$GeV is arbitrarily set to wider regions

$\sqrt{s'}$[GeV]	$(1-T)$	M_H	B_T	B_W	C	y_{23}^D
78.1	0.05 - 0.33	0.19 - 0.59	0.09 - 0.38	0.05 - 0.30	0.19 - 0.79	0.0030 - 0.0900
71.8	0.05 - 0.33	0.20 - 0.63	0.10 - 0.39	0.06 - 0.28	0.20 - 0.79	0.0030 - 0.0900
65.1	0.05 - 0.33	0.21 - 0.57	0.11 - 0.38	0.06 - 0.29	0.23 - 0.79	0.0030 - 0.0900
57.6	0.06 - 0.33	0.22 - 0.63	0.12 - 0.37	0.06 - 0.27	0.25 - 0.79	0.0030 - 0.0900
49.0	0.08 - 0.33	0.24 - 0.62	0.14 - 0.39	0.07 - 0.26	0.31 - 0.79	0.0040 - 0.1000
38.5	0.10 - 0.32	0.27 - 0.57	0.17 - 0.40	0.08 - 0.25	0.41 - 0.78	0.0100 - 0.1500
24.4	0.18 - 0.30	0.34 - 0.54	0.28 - 0.39	0.12 - 0.23	0.45 - 0.80	0.0100 - 0.1500

Table 5.11: Region used in fitting.

than that restricted by the correction size. The systematic uncertainty on the choice of the fitting range is included.

The QCD predictions at $\sqrt{s'} = 78$GeV fitted to data after applying the hadronization correction are shown in Figure 5.15. The vertical lines show the fitting region. The lower part of the figure shows the deviation of bin contents in data from the fitted theoretical predictions in standard deviations. The solid line and the dashed line in this part show deviations of $\pm 2\sigma$ and $\pm 1\sigma$. Although some data points have a large deviation, most data points are inside the range of $\pm 2\sigma$.

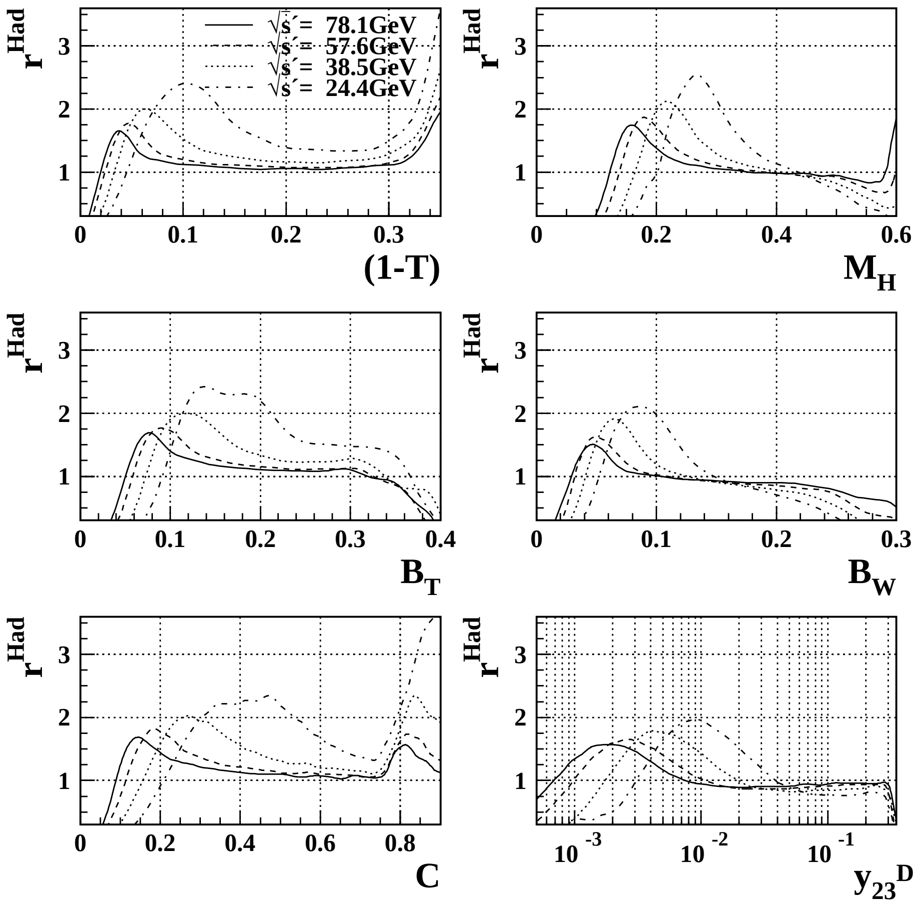

Figure 5.14: The hadronization correction factor for the differential distribution , r^{Had}.

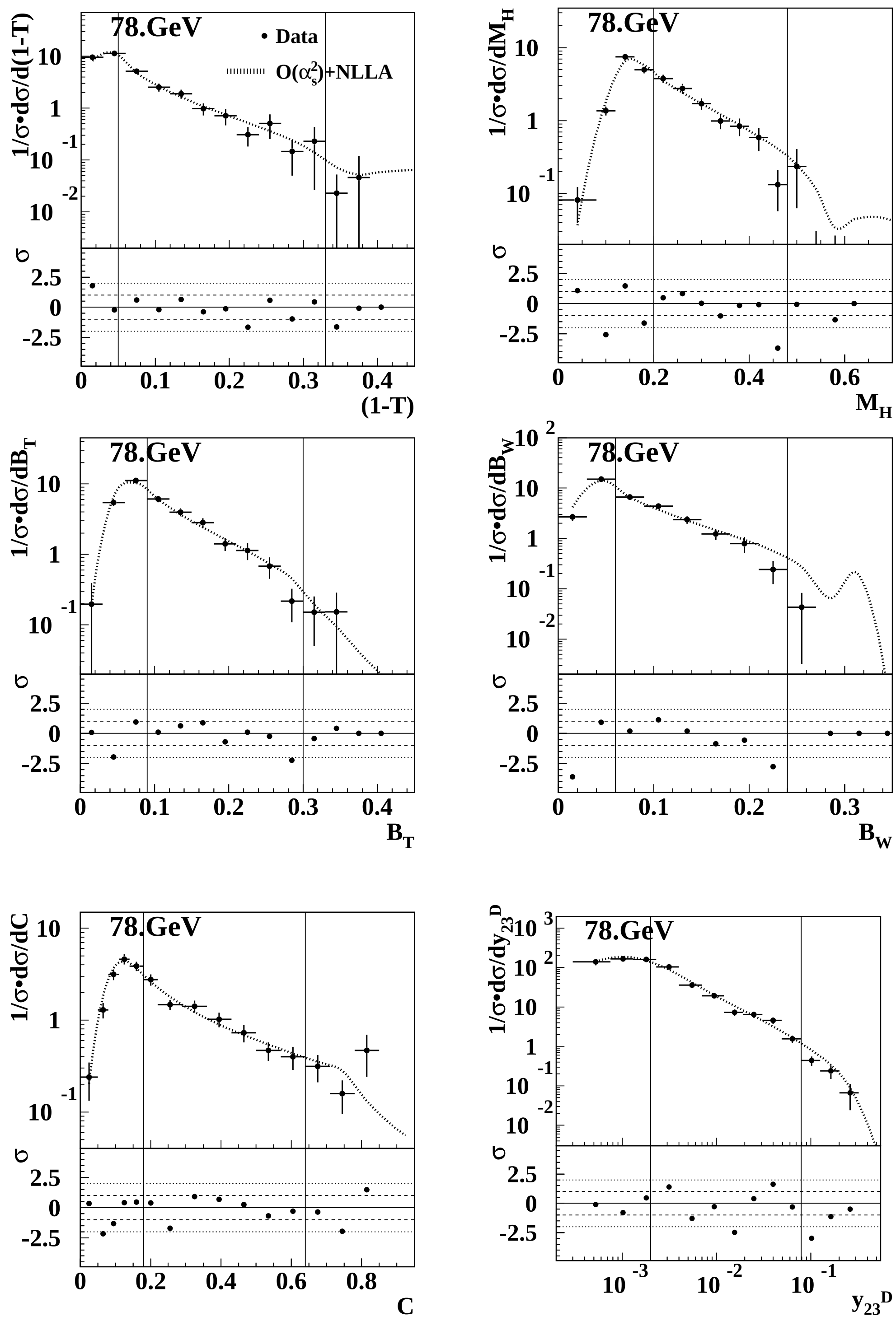

Figure 5.15: The theoretical predictions which are convolved with the hadronization correction and fitted to the hadron level distribution of data.

5.4 Systematic Uncertainties

5.4.1 Experimental Uncertainties

The experimental uncertainty is estimated by adding in quadrature the following contributions.

Track and Cluster Selection As described in Section 5.2.1, the part of the cluster energy doubly counted by track momentum matched to the cluster is subtracted by the method described in [138, 139]. As an extreme case, the analysis using the event shape variables which are calculated without using the subtraction is performed. The difference between the standard result and the result when all clusters and tracks are used is assigned as the experimental systematic uncertainties.

Event Selection The deviation between the standard value and the value obtained by repeating the analysis with tighter selection criteria to eliminate background more securely are studied. Among deviations for selection variables, the largest deviations are assigned as systematic uncertainties. The thrust axis is required to lie in the range $|\cos\theta_T| < 0.7$ or the isolation angle from any jet is required to be larger than $35°$.

The largest deviation between the standard value and the value obtained by repeating the analysis with the background fractions estimated from the rate of isolated charged hadrons described in Section 5.2 is assigned to experimental systematic uncertainties.

ECAL Resolution in C Variable Calculation Difference obtained when using the intrinsic single block energy resolution to calculate the C variable. The effect of material in front of the electromagnetic calorimeter is not included in the resolution. The cluster energy resolution measured by using radiative lepton pair events is $(1.5\pm0.3)\%\oplus(16.0\pm0.3)\%/\sqrt{E}$. Although this includes the effect of material, it is the energy resolution for the cluster, not for a calorimeter block.

The χ^2 distribution obtained in cluster shape fitting of single photon is compared with the expected χ^2 distribution. The distribution is compared for every number of calorimeter blocks , N_{bl}, used in cluster shape fitting. The degree of freedom used in the calculation of χ^2 is set to $(N_{bl}-1)$. The single photon sample is obtained from radiative muon pair events. The χ^2 distributions for typical numbers of calorimeter blocks are shown in Figure 5.16. They show that the intrinsic resolution is preferable to the cluster energy resolution. But χ^2 is larger than the expected χ^2 distribution for the corresponding degrees of freedom.

Calculated χ^2 distribution is fitted to χ^2 obtained in cluster shape fitting with varied resolution, $\sigma/E = A + B/\sqrt{E}$. A normalization factor of the calculated distribution is treated as a free parameter in the fitting. 11 values of parameter A are chosen between 0.2 and 1.5. 21 values of parameter B are chosen between 4.0 and 11.0. optimal values of the parameter B for each A is set to minimize χ^2 of fitting of χ^2 distributions. The optimal values are shown in Figure 5.17. Since Parameter A doesn't change χ^2 distribution so much in the region of $A = 0.2 \sim 1.5$, Optimal values are not calculated. The figure shows that the optimal value of parameter B is depend on the number of calorimeter blocks. Since number of blocks produced by a single photon is from four to nine, the difference between the results using the intrinsic single block energy resolution and block energy resolution resolution with parameter B changed from 6.0 to 8.0 is assigned as a systematic uncertainty.

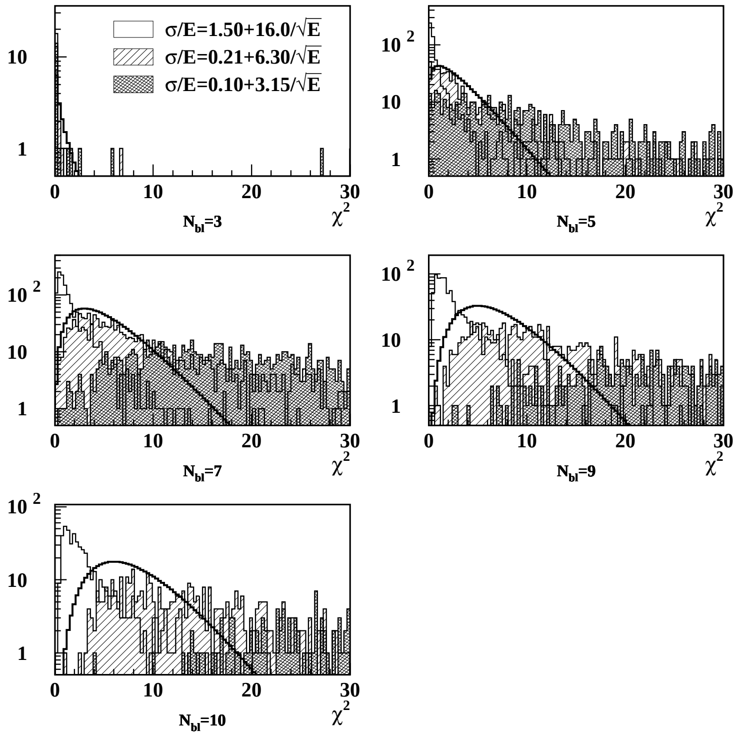

Figure 5.16: Chi-square distribution of cluster shape fit with three sets of ECAL resolution parameters. The solid line shows chi-square for degrees of freedom of $N_{bl} - 1$.

Choice of Fitting Region Although the fitting region is set according to the size of correction to event shape variable, the threshold value on the size is arbitrary. Besides it, the fitting region is set nearly arbitrarily to perform a fitting with enough bins. Therefore, the stability of fit results against the variation of the fitting range is studied. Figure 5.18 shows the deviation of α_s, $\Delta\alpha_s$ in fittings with the varied region from that in fitting with the standard fitting region in Monte Carlo subsamples. The subsamples are same set as that used in the evaluation of statistical uncertainty. The upper and lower limit of the region are shifted independently by ± 1. The dots and the error bar shows the mean value and RMS of $\Delta\alpha_s$.

It is found that there are no samples with a large deviation in the mean value of $\Delta\alpha_s$. The largest error on the mean of $\Delta\alpha_s$ in four cases of the fitting region is assigned as a systematic uncertainty.

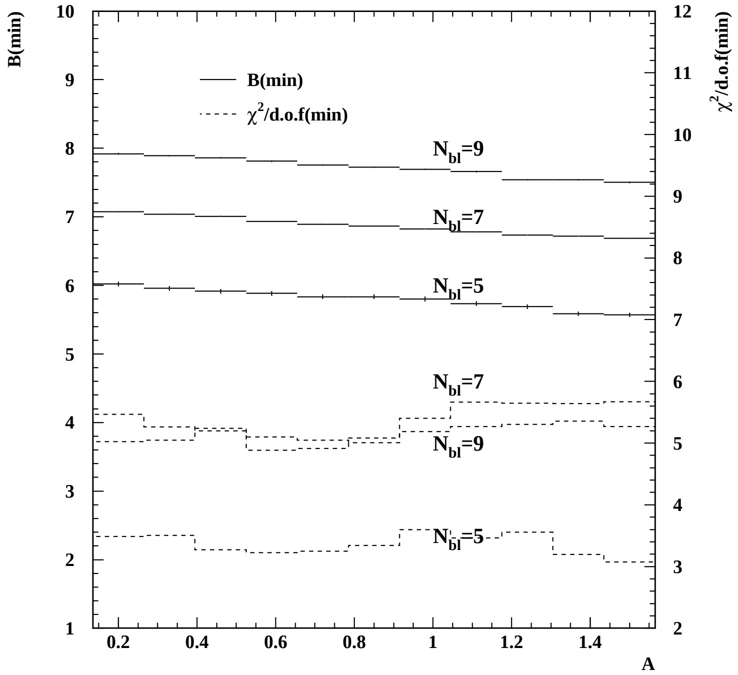

Figure 5.17: Best fit values of the ECAL resolution parameter B in $\sigma/E = A+B/\sqrt{E}$ and chi-square when chi-square distribution of the cluster shape fit is fitted to the chi-square distribution for degrees of freedom of $N_{bl} - 1$.

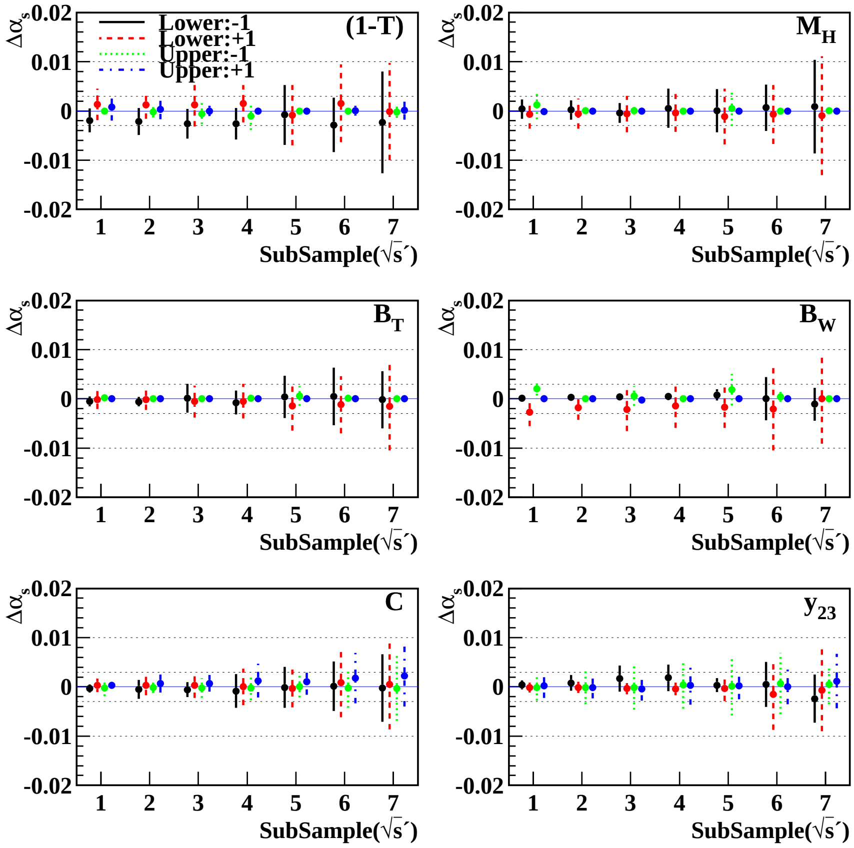

Figure 5.18: Fluctuation of α_s obtained by fittings of subsamples. Error bars show RMS of the α_s distribution.

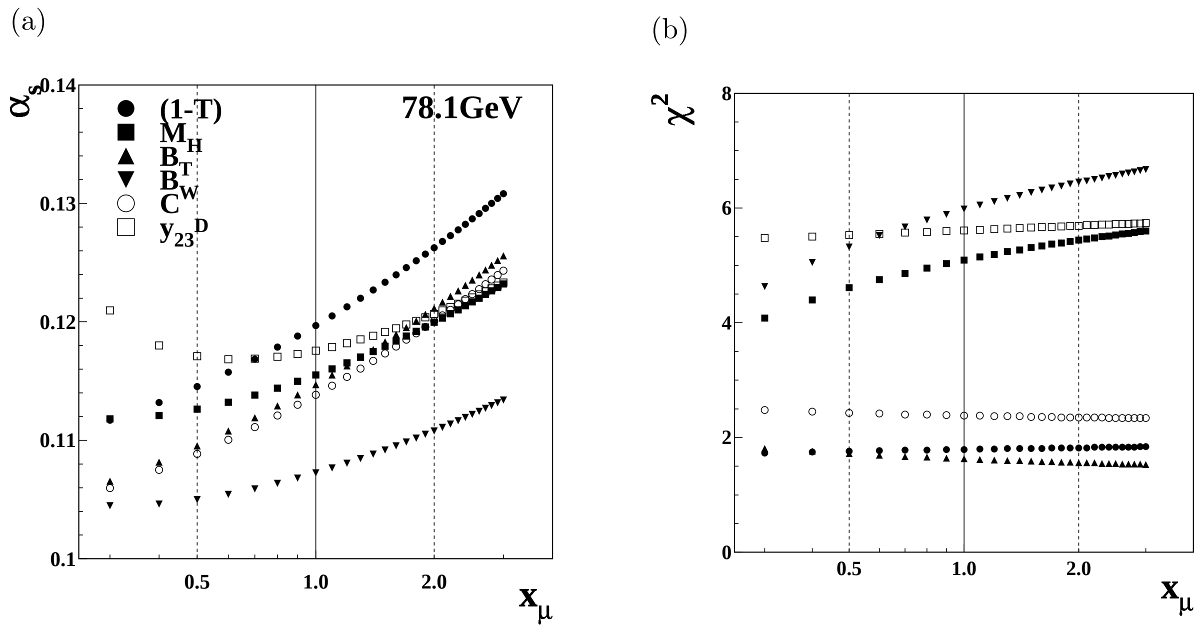

Figure 5.19: α_s and chi-square in fittings of event shape variables with varied x_μ

5.4.2 Hadronization Uncertainties

The uncertainty in the hadronization correction is defined by adding the following in quadrature:

- the largest of the changes in α_s observed when varying the hadronization parameters b and σ_Q by ± 1 standard deviation about their tuned values in `JETSET`;
- the change observed when the parton virtuality cut-off parameter is altered from $Q_0 = 1.9$ GeV to $Q_0 = 4$ GeV in `JETSET`;
- the change observed when only the light quarks u, d, s and c are considered at the parton level in order to estimate potential quark mass effects;
- both differences with respect to the standard result when `HERWIG` or `ARIADNE` are used for the hadronization correction, rather than `JETSET` .

5.4.3 Theoretical Uncertainties

Renormalization Scale The renormalization scale parameter $x_\mu \equiv \mu/Q$ is fixed to 1, where μ is the energy scale at which the theory is renormalized and Q is the energy scale of the reaction. Although the uncertainty on the choice of the value of x_μ gives a large contribution to the systematic uncertainty, the means of quantifying this uncertainty is essentially arbitrary. The scale uncertainty is defined as the variation of α_s when x_μ is changed from 1 to 0.5 and 2.0. As shown in Figure 5.19, the α_s monotonically increases for larger x_μ for all event shape variables except y_{23}^D. In the case of y_{23}^D, the minimum value of α_s is between 0.5 and 1.0. χ^2 is increasing for larger x_μ in case of M_H and B_W. It is flat for other variables. These situation is same for other energy samples.

Matching Scheme The O(α_s^2) and NLLA calculations are combined with the ln(R) matching scheme. The same matching scheme is used in analyses with non-radiative events. This allows a straightforward comparison with their results. The expected variation in $\alpha_s(\sqrt{s'})$ due to using different matching schemes is much smaller than the renormalization scale uncertainty [53], and is not included as an additional theoretical systematic uncertainty.

5.5 Result of Analysis with Radiative Multi-Hadronic Events at LEP1

The fitted values of α_s and their errors for each event shape variable are shown in Tables 5.12 and Table 5.13. Uncertainties coming from tighter selection on $|\cos\theta_T|$ dominantly contribute to the experimental systematic uncertainty. The main contributions to the hadronization uncertainties are due to the choice of the hadronization models, in particular, originating in the difference of hadronization corrections between `HERWIG` and `JETSET`. Since a large difference between `JETSET` and `HERWIG` in hadron level distribution is seen in Figure 5.13, this result is natural. The experimental uncertainty, the hadronization uncertainty and the theoretical uncertainty are comparable in the low and modest $\sqrt{s'}$ sample.

	$(1-T)$	M_H	B_T	B_W	C	y_{23}^D
α_s(78.1GeV)	0.1194	0.1193	0.1144	0.1103	0.1162	0.1225
Statistical Error	± 0.0052	± 0.0047	± 0.0032	± 0.0039	± 0.0045	± 0.0050
Tracks + Clusters	0.0005	-0.0005	-0.0000	-0.0009	0.0002	0.0012
$\lvert cos\theta_T\rvert < 0.7$	0.0096	0.0074	0.0059	0.0063	0.0067	0.0080
$C > 5$	0.0012	0.0001	0.0005	-0.0004	0.0009	0.0006
α_j^{iso}	0.0000	0.0003	0.0027	0.0010	0.0004	-0.0012
Bkg fraction	-0.0001	-0.0001	-0.0001	-0.0001	-0.0001	-0.0000
ECAL Resolution	0.0018	0.0004	0.0004	0.0005	0.0011	-0.0005
Fitting Range	0.0022	0.0005	0.0007	0.0016	0.0005	0.0005
Experimental Syst.	± 0.0101	± 0.0075	± 0.0066	± 0.0066	± 0.0069	± 0.0082
$b-1s.d.$	-0.0005	-0.0006	-0.0004	-0.0002	-0.0006	-0.0004
$b+1s.d.$	0.0004	0.0005	0.0005	0.0002	0.0007	0.0003
$Q_0-1s.d.$	0.0002	-0.0004	0.0006	-0.0003	0.0005	-0.0013
$Q_0+1s.d.$	-0.0002	0.0005	-0.0005	0.0003	-0.0002	0.0010
$\sigma_q-1s.d.$	0.0004	0.0003	0.0005	0.0003	0.0007	0.0007
$\sigma_q+1s.d.$	-0.0005	-0.0000	-0.0005	-0.0003	-0.0007	-0.0005
udsc only	0.0021	-0.0001	0.0056	0.0023	0.0036	0.0065
Herwig 5.9	-0.0053	-0.0046	-0.0064	-0.0042	-0.0082	-0.0078
Ariadne 4.08	0.0000	-0.0015	-0.0017	-0.0001	-0.0023	-0.0033
Total Hadronization.	± 0.0057	± 0.0049	± 0.0087	± 0.0048	± 0.0093	± 0.0108
$x_\mu = 0.5$	-0.0051	-0.0039	-0.0052	-0.0030	-0.0053	-0.0009
$x_\mu = 2.0$	0.0065	0.0054	0.0065	0.0043	0.0067	0.0039
Total error	+ 0.0143 − 0.0137	+ 0.0115 − 0.0108	+ 0.0131 − 0.0125	+ 0.0100 − 0.0095	+ 0.0141 − 0.0136	+ 0.0150 − 0.0145

	$(1-T)$	M_H	B_T	B_W	C	y_{23}^D
α_s(71.8GeV)	0.1336	0.1225	0.1304	0.1161	0.1305	0.1313
Statistical Error	± 0.0062	± 0.0048	± 0.0039	± 0.0054	± 0.0058	± 0.0065
Tracks + Clusters	0.0002	0.0002	-0.0000	0.0001	-0.0005	0.0009
$\lvert cos\theta_T\rvert < 0.7$	0.0028	0.0054	0.0005	0.0008	-0.0024	-0.0005
$C > 5$	0.0003	0.0010	-0.0003	-0.0007	-0.0008	-0.0011
α_j^{iso}	-0.0031	-0.0021	-0.0022	-0.0008	-0.0025	-0.0043
Bkg fraction	0.0000	0.0001	0.0000	0.0001	0.0001	0.0000
ECAL Resolution	0.0015	0.0022	0.0014	0.0023	0.0007	0.0027
Fitting Range	0.0020	0.0007	0.0007	0.0018	0.0004	0.0009
Experimental Syst.	± 0.0049	± 0.0064	± 0.0028	± 0.0032	± 0.0037	± 0.0054
$b-1s.d.$	-0.0006	-0.0005	-0.0005	-0.0001	-0.0006	-0.0004
$b+1s.d.$	0.0005	0.0005	0.0004	0.0002	0.0005	0.0002
$Q_0-1s.d.$	0.0002	-0.0005	0.0007	-0.0003	0.0003	-0.0017
$Q_0+1s.d.$	-0.0004	0.0003	-0.0007	0.0003	-0.0003	0.0011
$\sigma_q-1s.d.$	0.0004	0.0002	0.0005	0.0003	0.0005	0.0004
$\sigma_q+1s.d.$	-0.0005	-0.0002	-0.0005	-0.0003	-0.0005	-0.0006
udsc only	0.0023	-0.0000	0.0061	0.0021	0.0033	0.0060
Herwig 5.9	-0.0063	-0.0049	-0.0072	-0.0041	-0.0084	-0.0088
Ariadne 4.08	-0.0002	-0.0018	-0.0017	-0.0002	-0.0015	-0.0034
Total Hadronization.	± 0.0067	± 0.0053	± 0.0096	± 0.0046	± 0.0092	± 0.0113
$x_\mu = 0.5$	-0.0071	-0.0043	-0.0075	-0.0034	-0.0074	-0.0017
$x_\mu = 2.0$	0.0091	0.0060	0.0094	0.0049	0.0093	0.0049
Total error	+ 0.0138 − 0.0126	+ 0.0113 − 0.0105	+ 0.0143 − 0.0131	+ 0.0092 − 0.0085	+ 0.0147 − 0.0136	+ 0.0150 − 0.0142

	$(1-T)$	M_H	B_T	B_W	C	y_{23}^D
α_s(65.1GeV)	0.1236	0.1208	0.1217	0.1135	0.1242	0.1311
Statistical Error	± 0.0068	± 0.0063	± 0.0058	± 0.0053	± 0.0059	± 0.0133
Tracks + Clusters	-0.0011	0.0019	0.0020	-0.0007	-0.0016	-0.0014
$\lvert cos\theta_T\rvert < 0.7$	0.0043	0.0052	0.0052	0.0018	0.0009	-0.0041
$C > 5$	0.0021	0.0001	0.0002	0.0016	-0.0010	0.0009
α_j^{iso}	0.0022	0.0012	0.0016	0.0022	0.0008	0.0005
Bkg fraction	0.0001	0.0000	0.0000	0.0000	0.0000	0.0000
ECAL Resolution	-0.0002	0.0000	0.0008	0.0007	0.0010	0.0013
Fitting Range	0.0025	0.0010	0.0007	0.0014	0.0006	0.0017
Experimental Syst.	± 0.0059	± 0.0057	± 0.0059	± 0.0037	± 0.0025	± 0.0049
$b-1s.d.$	-0.0007	-0.0006	-0.0005	-0.0003	-0.0008	-0.0002
$b+1s.d.$	0.0005	0.0007	0.0002	0.0003	0.0008	0.0004
$Q_0-1s.d.$	0.0002	-0.0005	0.0005	-0.0004	0.0004	-0.0017
$Q_0+1s.d.$	-0.0003	0.0004	-0.0006	0.0003	-0.0002	0.0015
$\sigma_q-1s.d.$	0.0005	0.0003	0.0004	0.0003	0.0008	0.0007
$\sigma_q+1s.d.$	-0.0007	-0.0003	-0.0005	-0.0004	-0.0009	-0.0005
udsc only	0.0021	0.0001	0.0039	0.0025	0.0034	0.0062
Herwig 5.9	-0.0067	-0.0051	-0.0060	-0.0057	-0.0096	-0.0099
Ariadne 4.08	-0.0007	-0.0025	-0.0007	-0.0009	-0.0027	-0.0040
Total Hadronization.	± 0.0071	± 0.0057	± 0.0072	± 0.0063	± 0.0106	± 0.0125
$x_\mu = 0.5$	-0.0057	-0.0042	-0.0061	-0.0034	-0.0064	-0.0014
$x_\mu = 2.0$	0.0073	0.0058	0.0076	0.0048	0.0081	0.0048
Total error	+ 0.0136 − 0.0128	+ 0.0117 − 0.0111	+ 0.0134 − 0.0126	+ 0.0102 − 0.0096	+ 0.0148 − 0.0140	+ 0.0195 − 0.0190

	$(1-T)$	M_H	B_T	B_W	C	y_{23}^D
α_s(57.6GeV)	0.1378	0.1396	0.1327	0.1194	0.1284	0.1407
Statistical Error	± 0.0085	± 0.0094	± 0.0072	± 0.0064	± 0.0063	± 0.0091
Tracks + Clusters	0.0004	0.0022	-0.0008	0.0005	0.0039	-0.0013
$\lvert cos\theta_T\rvert < 0.7$	0.0065	0.0101	0.0078	0.0054	0.0083	0.0056
$C > 5$	-0.0003	0.0020	0.0013	0.0013	0.0005	0.0009
α_j^{iso}	-0.0010	-0.0052	0.0004	-0.0004	0.0001	-0.0007
Bkg fraction	0.0000	0.0000	0.0000	0.0000	0.0000	0.0000
ECAL Resolution	0.0032	0.0051	0.0035	0.0021	0.0010	-0.0013
Fitting Range	0.0036	0.0006	0.0014	0.0020	0.0011	0.0010
Experimental Syst.	± 0.0082	± 0.0128	± 0.0088	± 0.0063	± 0.0093	± 0.0061
$b-1s.d.$	-0.0009	-0.0004	-0.0005	-0.0003	-0.0010	-0.0006
$b+1s.d.$	0.0006	0.0004	0.0004	0.0004	0.0009	0.0005
$Q_0-1s.d.$	0.0002	-0.0008	0.0006	-0.0005	0.0005	-0.0023
$Q_0+1s.d.$	-0.0005	0.0005	-0.0009	0.0003	-0.0004	0.0016
$\sigma_q-1s.d.$	0.0005	0.0002	0.0005	0.0006	0.0009	0.0006
$\sigma_q+1s.d.$	-0.0009	-0.0002	-0.0005	-0.0004	-0.0010	-0.0007
udsc only	0.0024	-0.0001	0.0042	0.0033	0.0040	0.0063
Herwig 5.9	-0.0076	-0.0039	-0.0072	-0.0066	-0.0101	-0.0113
Ariadne 4.08	-0.0011	-0.0011	-0.0012	-0.0013	-0.0032	-0.0049
Total Hadronization.	± 0.0081	± 0.0041	± 0.0085	± 0.0075	± 0.0114	± 0.0140
$x_\mu = 0.5$	-0.0079	-0.0063	-0.0078	-0.0042	-0.0072	-0.0023
$x_\mu = 2.0$	0.0101	0.0087	0.0098	0.0058	0.0090	0.0063
Total error	+ 0.0175 − 0.0164	+ 0.0186 − 0.0176	+ 0.0172 − 0.0162	+ 0.0130 − 0.0124	+ 0.0183 − 0.0175	+ 0.0189 − 0.0180

Table 5.12: Result of fits for $\sqrt{s'}$ =78.1GeV,71.8GeV,65.1GeV and 57.6GeV

	$(1-T)$	M_H	B_T	B_W	C	y_{23}^D
α_s(49.0GeV)	0.1373	0.1359	0.1413	0.1269	0.1356	0.1440
Statistical Error	± 0.0105	± 0.0098	± 0.0087	± 0.0069	± 0.0089	± 0.0117
Tracks + Clusters	0.0022	0.0007	0.0032	-0.0003	0.0008	-0.0012
$\lvert cos\theta_T \rvert < 0.7$	0.0029	0.0039	0.0004	0.0012	-0.0001	-0.0000
$C > 5$	-0.0010	-0.0038	-0.0017	-0.0001	-0.0049	-0.0018
α_j^{iso}	0.0024	0.0024	0.0007	0.0017	0.0013	0.0046
Bkg fraction	0.0001	0.0000	0.0001	0.0000	0.0000	0.0001
ECAL Resolution	-0.0003	0.0010	-0.0003	0.0009	-0.0000	-0.0005
Fitting Range	0.0027	0.0013	0.0009	0.0016	0.0009	0.0020
Experimental Syst.	± 0.0053	± 0.0062	± 0.0038	± 0.0028	± 0.0052	± 0.0055
$b - 1s.d.$	-0.0005	-0.0009	-0.0006	-0.0005	-0.0009	-0.0008
$b + 1s.d.$	0.0005	0.0008	0.0003	0.0005	0.0007	0.0002
$Q_0 - 1s.d.$	0.0003	-0.0006	0.0006	-0.0003	0.0005	-0.0019
$Q_0 + 1s.d.$	-0.0005	0.0005	-0.0012	0.0004	-0.0005	0.0017
$\sigma_q - 1s.d.$	0.0005	0.0005	0.0004	0.0007	0.0007	0.0007
$\sigma_q + 1s.d.$	-0.0006	-0.0006	-0.0008	-0.0007	-0.0009	-0.0006
udsc only	0.0023	0.0002	0.0039	0.0050	0.0038	0.0060
Herwig 5.9	-0.0083	-0.0090	-0.0080	-0.0083	-0.0123	-0.0114
Ariadne 4.08	-0.0009	-0.0041	-0.0011	-0.0024	-0.0039	-0.0056
Total Hadronization.	± 0.0087	± 0.0099	± 0.0091	± 0.0101	± 0.0135	± 0.0142
$x_\mu = 0.5$	-0.0076	-0.0058	-0.0092	-0.0054	-0.0081	-0.0008
$x_\mu = 2.0$	0.0097	0.0081	0.0117	0.0072	0.0102	0.0056
Total error	+ 0.0176 − 0.0165	+ 0.0173 − 0.0163	+ 0.0176 − 0.0160	+ 0.0144 − 0.0136	+ 0.0198 − 0.0188	+ 0.0201 − 0.0193

	$(1-T)$	M_H	B_T	B_W	C	y_{23}^D
α_s(38.5GeV)	0.1474	0.1374	0.1451	0.1415	0.1421	0.1496
Statistical Error	± 0.0125	± 0.0112	± 0.0088	± 0.0113	± 0.0113	± 0.0101
Tracks + Clusters	0.0024	0.0019	0.0006	0.0001	0.0049	-0.0010
$\lvert cos\theta_T \rvert < 0.7$	0.0026	0.0059	0.0034	0.0061	0.0050	0.0022
$C > 5$	0.0042	0.0038	0.0018	0.0037	0.0052	0.0040
α_j^{iso}	0.0005	-0.0007	-0.0004	0.0043	0.0014	0.0026
Bkg fraction	0.0003	0.0003	0.0002	0.0002	0.0003	0.0004
ECAL Resolution	0.0019	0.0025	0.0003	0.0035	0.0039	0.0055
Fitting Range	0.0033	0.0009	0.0008	0.0013	0.0023	0.0008
Experimental Syst.	± 0.0067	± 0.0077	± 0.0040	± 0.0092	± 0.0099	± 0.0077
$b - 1s.d.$	-0.0009	-0.0007	-0.0007	-0.0004	-0.0007	-0.0005
$b + 1s.d.$	0.0009	0.0006	0.0006	0.0005	0.0005	0.0004
$Q_0 - 1s.d.$	0.0006	-0.0008	0.0011	-0.0008	0.0007	-0.0021
$Q_0 + 1s.d.$	-0.0005	0.0008	-0.0014	0.0006	-0.0007	0.0018
$\sigma_q - 1s.d.$	0.0013	0.0003	0.0008	0.0006	0.0010	0.0005
$\sigma_q + 1s.d.$	-0.0009	-0.0002	-0.0008	-0.0004	-0.0007	-0.0006
udsc only	0.0042	0.0001	0.0060	0.0036	0.0038	0.0064
Herwig 5.9	-0.0150	-0.0096	-0.0105	-0.0107	-0.0125	-0.0127
Ariadne 4.08	-0.0042	-0.0036	-0.0028	-0.0025	-0.0030	-0.0055
Total Hadronization.	± 0.0162	± 0.0103	± 0.0125	± 0.0116	± 0.0135	± 0.0154
$x_\mu = 0.5$	-0.0093	-0.0055	-0.0097	-0.0072	-0.0089	-0.0012
$x_\mu = 2.0$	0.0120	0.0079	0.0124	0.0097	0.0114	0.0063
Total error	+ 0.0247 − 0.0235	+ 0.0188 − 0.0179	+ 0.0201 − 0.0186	+ 0.0210 − 0.0199	+ 0.0232 − 0.0221	+ 0.0210 − 0.0200

	$(1-T)$	M_H	B_T	B_W	C	y_{23}^D
α_s(24.4GeV)	0.1569	0.1524	0.1552	0.1433	0.1406	0.1612
Statistical Error	± 0.0252	± 0.0117	± 0.0115	± 0.0101	± 0.0112	± 0.0181
Tracks + Clusters	0.0038	0.0015	0.0060	-0.0021	0.0080	-0.0074
$\lvert cos\theta_T \rvert < 0.7$	0.0001	0.0008	-0.0027	0.0027	0.0013	-0.0008
$C > 5$	0.0037	-0.0001	-0.0036	-0.0022	-0.0010	-0.0084
α_j^{iso}	0.0110	0.0056	0.0003	0.0023	0.0060	0.0005
Bkg fraction	0.0023	0.0017	0.0018	0.0015	0.0020	0.0031
ECAL Resolution	-0.0035	-0.0053	-0.0039	-0.0013	-0.0025	-0.0057
Fitting Range	0.0035	0.0027	0.0018	0.0017	0.0020	0.0018
Experimental Syst.	± 0.0134	± 0.0085	± 0.0088	± 0.0054	± 0.0109	± 0.0131
$b - 1s.d.$	-0.0007	-0.0014	-0.0007	-0.0013	-0.0012	-0.0013
$b + 1s.d.$	0.0015	0.0017	0.0009	0.0011	0.0012	0.0006
$Q_0 - 1s.d.$	0.0010	-0.0010	0.0023	-0.0009	0.0010	-0.0039
$Q_0 + 1s.d.$	-0.0008	0.0004	-0.0029	0.0000	-0.0010	0.0015
$\sigma_q - 1s.d.$	0.0014	0.0010	0.0011	0.0017	0.0012	0.0011
$\sigma_q + 1s.d.$	-0.0010	-0.0009	-0.0010	-0.0018	-0.0013	-0.0016
udsc only	0.0075	0.0053	0.0140	0.0159	0.0150	0.0168
Herwig 5.9	-0.0212	-0.0080	-0.0134	-0.0126	-0.0103	-0.0193
Ariadne 4.08	-0.0082	-0.0056	-0.0040	-0.0045	-0.0050	-0.0114
Total Hadronization.	± 0.0240	± 0.0113	± 0.0200	± 0.0209	± 0.0190	± 0.0283
$x_\mu = 0.5$	-0.0104	-0.0085	-0.0116	-0.0082	-0.0088	-0.0024
$x_\mu = 2.0$	0.0137	0.0115	0.0151	0.0108	0.0112	0.0084
Total error	+ 0.0397 − 0.0387	+ 0.0216 − 0.0202	+ 0.0289 − 0.0273	+ 0.0262 − 0.0252	+ 0.0270 − 0.0261	+ 0.0371 − 0.0362

Table 5.13: Result of fittings for $\sqrt{s'}$ =49.0GeV,38.5GeV and 24.4GeV.

Chapter 6

Analysis of Multi-hadronic Events at LEP2

The strong coupling constant at the highest energy e^+e^- reactions is obtained by using multi-hadronic events in LEP2 data. The values have an important role as lever arm for the accurate measurement on Z^0 pole to know energy scale dependence. In addition to processes at LEP1, four fermion processes including pair production processes W^+W^- and Z^0Z^0 are opened up at LEP2 (Figure 6.1). Although these four fermion processes are very important to obtain the W mass, width and couplings as key parameters of standard model, they can be dominant backgrounds to measurements of the strong coupling constant with multi-hadronic events. The measurement of α_s with data taken in 1998, 1999 and 2000 is explained in this chapter.

6.1 Data and Monte Carlo

The data set that is used in this analysis is divided into six samples at $\sqrt{s} \approx$ 189, 192, 196, 200, 202 and 206 GeV. Data samples are referred to by these center of mass energies. The integrated luminosity and luminosity averaged center of mass energy are listed in Table 6.1. The luminosity is obtained from measurement of small angle Bhabha scattering cross-section by a Silicon-Tungsten electromagnetic calorimeter.

Monte Carlo event samples are generated at each center of mass energy including a full simulation of the OPAL detector. Events for multi-hadronic events (refer to $e^+e^- \rightarrow (Z^0/\gamma)^* \rightarrow q\bar{q}$) were generated by `KK2f` v4 [150] and `PYTHIA` 6.125 [151]. Photon radiation is calculated in QED up to second order, including all interference effects in `KK2f`. Electroweak corrections are included in first order with higher order extensions. Hadronization and fragmentation of final quarks and gluons are done by `JETSET`. 4-fermion events ($e^+e^- \rightarrow$4-fermion) are generated by `grc4f` v2.1 [152]. They include all four-fermion final states through all possible electroweak four-fermion processes. Parton shower, fragmentation and decay are treated by `JETSET` 7.4. `PYTHIA`, `HERWIG` and `PHOJET` are used to generate hadronic two-photon process. Events of the process $e^+e^- \rightarrow \tau\tau$ are generated by using `KORALZ`. Monte Carlo event generators used for hadronization correction are `JETSET`, `HERWIG` and `ARIADNE`. The parameters of these generators are same as for the analysis of radiative multi-hadronic events with LEP1 data.

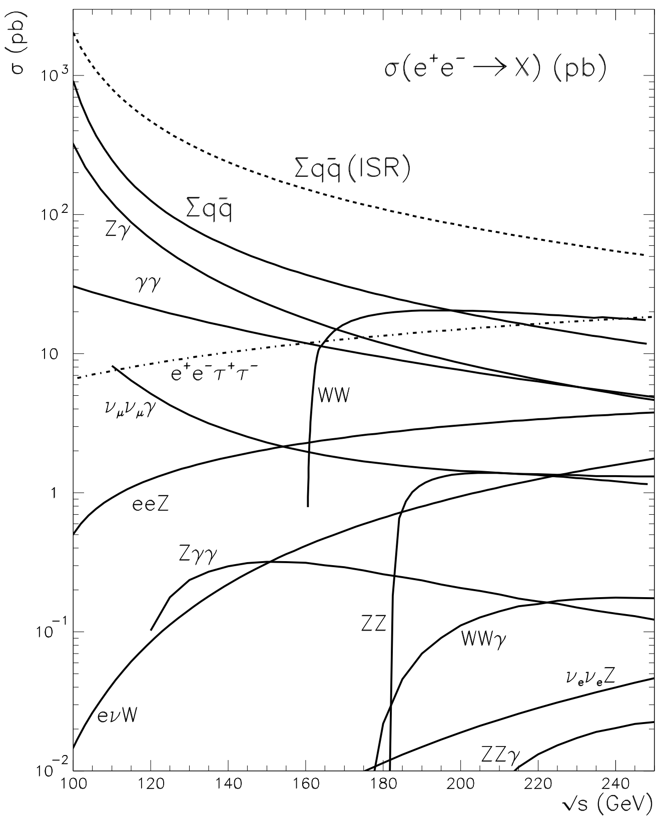

Figure 6.1: Cross-sections for some typical standard model process

	189GeV	192GeV	196GeV	200GeV	202GeV	206GeV
$\int \mathcal{L}dt$ [pb^{-1}]	182.09	29.16	72.60	75.18	38.37	220.85
$\langle E_{\mathrm{beam}} \rangle$ [GeV]	94.3	95.8	97.8	99.8	100.8	103.0

Table 6.1: The luminosity and luminosity weighted mean beam energy are given for data samples at 189, 192, 196, 200, 202 and 206GeV.

6.2 Event Selection

The event selection of non-radiative multi-hadronic events consists of standard hadronic event selection, preselection, ISR event rejection and four-fermion events rejection. They are explained in the following sections.

6.2.1 Hadronic Event Selection

Hadronic events are selected by similar selection criteria to the criteria at LEP 1. The requirement on the balance of total energy in the direction of beam pipe axis, E_{bal}, is loosened to avoid losing hadronic events with initial state radiation which increases at LEP2 beam energy. Events are selected if they satisfy all of

$$R_{\mathrm{vis}} = 0.14, \tag{6.1}$$

$$|R_{\mathrm{bal}}| \leq 0.75, \tag{6.2}$$

$$N_{\mathrm{shw}} \geq 7 \text{ good clusters}, \tag{6.3}$$

$$N_{\mathrm{chg}} \geq 5 \text{ good tracks}, \tag{6.4}$$

where definitions of variables, a good cluster and a good track are the same as the LEP1 analysis described in Section 5.2.1. The efficiency of selecting non-radiative hadronic events is essentially unchanged with respect to lower center-of-mass energies and is approximately 98% [53].

6.2.2 Preselection

τ decays into one or three charged particles with branching ratio 99.8%. As shown in Figure 6.2 (a), the number of tracks for background coming from $\mathrm{e^+e^-} \to \tau^+\tau^-$ events is smaller than six or seven. The number of tracks for $\gamma\gamma \to \mathrm{q\bar{q}}$ events is smaller than $\mathrm{e^+e^-} \to \mathrm{q\bar{q}}$ events because the energy of reaction is reduced. To reject the background from these source, at least seven good tracks are required. The cosine of the polar angle of the thrust axis, $|\cos\theta_T|$, is required to be smaller than 0.9 to ensure the events are well contained in the OPAL detector. Since hadrons in $\gamma\gamma \to \mathrm{q\bar{q}}$ events are boosted into the beam pipe direction and are not be fully contained, this selection reduces the background from such events also.

6.2.3 ISR Event Rejection

The effective center-of-mass energy $\sqrt{s'}$ of the observed hadronic system is determined in order to reduce radiative hadronic events. The $\sqrt{s'}$ is obtained by kinematic fitting assuming from zero to two photons. If an electromagnetic calorimeter cluster passes the following criteria, it is identified as an isolated photon.

(a) (b)

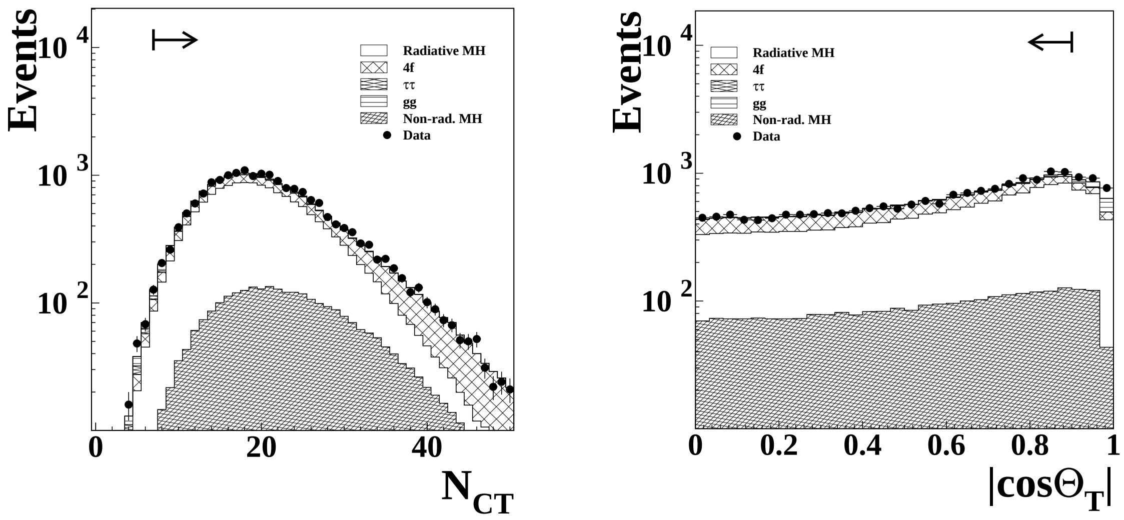

Figure 6.2: (a) The number of tracks (b) The absolute value of cosine of polar angle

1. Number of electromagnetic calorimeter blocks is required to be less than 15, 25, 35 and 20 for good part of barrel ($|\cos\theta| < 0.7$), not so good part of barrel ($|\cos\theta| > 0.7$), overlap region of barrel and endcap and endcap ,respectively.

2. Number of electromagnetic calorimeter blocks with 90% of cluster energy is required to be less than 3, 4, 5 for good part of barrel ($|\cos\theta| < 0.7$), not so good part of barrel ($|\cos\theta| > 0.7$) and overlap or endcap region,respectively.

3. Sum of electromagnetic cluster energy in the isolation cone with angle of 0.2 radian is required to be smaller than 1GeV.

4. Energy of associated hadron calorimeter cluster in the region $|\cos\theta| < 0.955$ is required to be less than 4GeV.

If isolated photons are found, tracks and clusters except the photon clusters are formed into jets using Durham algorithm with a value for the resolution parameter $y_{cut} = 0.02$. Additional photons are assumed to escape into beam pipe direction and give missing energy to the event. Events are categorized into seven cases which are defined in Table 6.2 by number of the observed photons and the escaping photons. The kinematic fitting is performed with jets, an observed photon and missing photons. The most likely of the seven cases is used as the probability of the kinematic fitting. The result of the categorization is shown in the Figure 6.3 a). Prediction of the categorization by Monte Carlo is able to reproduce the data.

Category	1	2	3	4	5	6	7	8
Observed Photon	0	0	1		0	1	2	> 2
Escaping Photon	0	1	0		2	1	0	

Table 6.2: Category of ISR event type. The event which has number of observed and escaping photons more than two in total is categorized into Category 8.

$\sqrt{s} - \sqrt{s'} < 10\text{GeV}$ is required to reject large radiative events. The $\sqrt{s'}$ distribution is shown in Figure 6.3 (b). The $\sqrt{s'}$ distribution of simulated events with $\sqrt{s} - \sqrt{s'_{\text{true}}} < 1\text{GeV}$ is shown shaded.

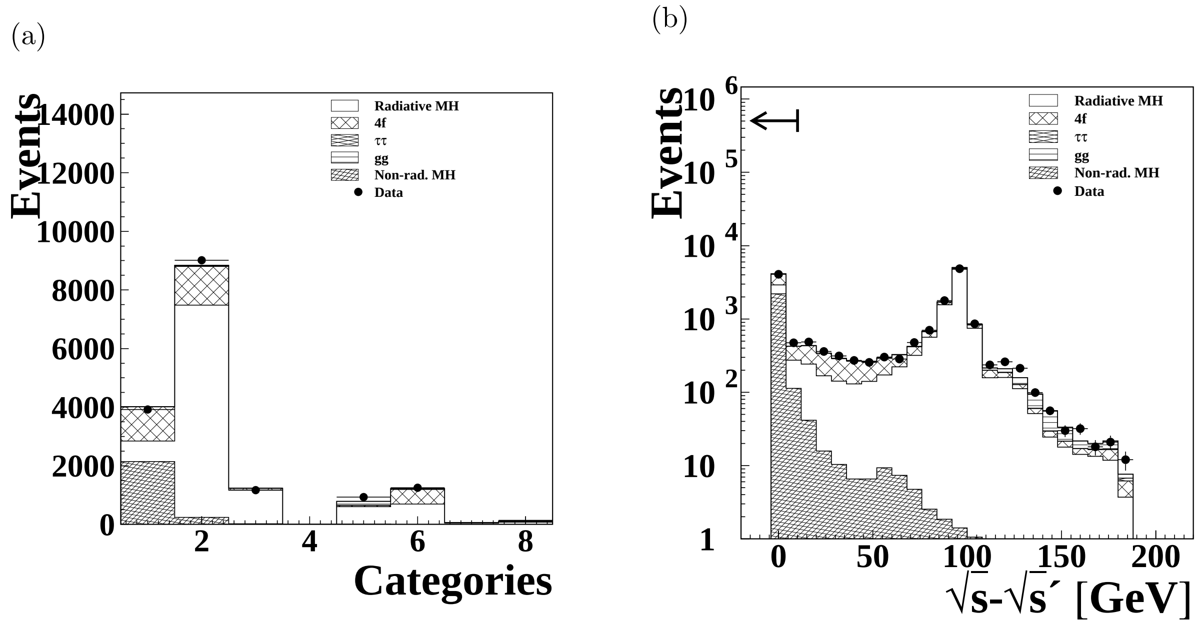

Figure 6.3: (a) The category of ISR event type. (b) The effective center-of-mass energy reconstructed from the kinematic fitting.

6.2.4 Four Fermion Events Rejection

q$\bar{\text{q}}$q$\bar{\text{q}}$ and q$\bar{\text{q}}$gg Matrix Elements

A QCD event weight is employed to reject background from four-fermion processes. The QCD event weight W_{QCD} is defined with QCD matrix elements $|\mathcal{M}(p_1, p_2, p_3, p_4)|^2$ for $\text{e}^+\text{e}^- \to \text{q}\bar{\text{q}}\text{q}\bar{\text{q}}$ and $\text{q}\bar{\text{q}}\text{gg}$ processes by:

$$W_{\text{QCD}} = \max_{\{p_1, p_2, p_3, p_4\}} \log(|\mathcal{M}(p_1, p_2, p_3, p_4)|^2) \tag{6.5}$$

while p_i is the momenta of jets reconstructed by Durham algorithm. The event are forced into four jets. Since jets originating from quarks and gluons are not distinguished, calculations of the matrix elements are performed for all permutations of the jets. The `EVENT2` [153] program is used to calculate the matrix elements. Note that the definition of the event weight W_{QCD} contains kinematic information only and is independent of the value of α_s.

The W_{QCD} distribution is shown in Figure 6.4(a). It shows that multi-hadronic events and events from four fermion processes are separated. The events with W_{QCD} larger than -0.5 are selected.

qqlν Likelihood

The qqlν likelihood is used to reject four-fermion processes with leptons in the final state. The qqlν likelihood and the qqqq likelihood described in the next section are developed for analyses with W pair production. To maintain a high efficiency for $W^+W^- \rightarrow \mathrm{qql}\nu$ events, clear topological signatures are used instead of explicit lepton identification and lepton isolation requirements. The detailed description of the qqlν Likelihood is in [154–156]. The likelihood is described briefly in this section.

The qqlν likelihood is composed of six selections running in parallel. These six selections are optimized for the following decay chains: $\mathrm{W} \rightarrow \mathrm{e}\nu_\mathrm{e}$,$\mathrm{W} \rightarrow \mu\nu_\mu$,$\mathrm{W} \rightarrow \tau\nu_\tau \rightarrow \mathrm{e}\nu_\mathrm{e}\nu_\tau\nu_\tau$, $\mathrm{W} \rightarrow \tau\nu_\tau \rightarrow \mu\nu_\mu\nu_\tau\nu_\tau$, $\mathrm{W} \rightarrow \tau\nu_\tau \rightarrow \mathrm{hn}\pi^0\nu_\tau$, $\mathrm{W} \rightarrow \tau\nu_\tau \rightarrow 3\mathrm{hn}\pi^0\nu_\tau$. At first, the tracks most consistent with each of the six decay chains are identified with variables on the energy and momentum of the track, isolation from clusters and tracks, numbers of hits in the hadron calorimeter and the muon chamber and so on. A single absolute likelihood is obtained by multiplying the probabilities for each variable that the track in question is the lepton in the decay chain. The track with the highest likelihood is taken to be the best candidate for the decay chain.

All tracks and clusters not associated with the tracks identified as the best lepton candidate are forced into two jets using the Durham algorithm. The jet energy/angles are then corrected using the GCE [157] algorithm. Finally, the lepton candidate is added back using the lepton energy E_lept instead of track momenta and cluster energies identified as the best lepton candidate.

After applying preselection cuts, a relative likelihood is calculated. The same variables as the preselection cuts are used in the calculation. They are described in [154,155]. The likelihood $L_{\mathrm{q\bar{q}l}\nu}$ for each decay chain are calculated by multiplying the probabilities for each variable that the events in question originated from the decay chain. The likelihood $L_{\mathrm{q\bar{q}}}$ for Z^0/γ events is calculated also. The relative likelihood $\mathcal{L}_{\mathrm{q\bar{q}l}\nu}$ for each decay chain is calculated as:

$$\mathcal{L}_{\mathrm{q\bar{q}l}\nu} = \frac{L_{\mathrm{q\bar{q}l}\nu}}{L_{\mathrm{q\bar{q}l}\nu} + f \times L_{\mathrm{q\bar{q}}}} \tag{6.6}$$

where the normalization factor, f, is the ratio of preselected background (only $\mathrm{q\bar{q}}$) to signal cross-sections, both obtained from Monte Carlo. The qqlν likelihood used in this analysis is the highest likelihood among the six relative likelihoods.

The $\mathcal{L}_{\mathrm{q\bar{q}l}\nu}$ distributions for data and Monte Carlo are shown in the Figure 6.4(b). Almost all signal events are concentrated around $\mathcal{L}_{\mathrm{q\bar{q}l}\nu} = 0$. Then, events with $\mathcal{L}_{\mathrm{q\bar{q}l}\nu}$ larger than 0.5 are rejected.

qqqq Likelihood

To reject background coming from $\mathrm{e}^+\mathrm{e}^- \rightarrow \mathrm{q\bar{q}q\bar{q}}$ processes further, the qqqq likelihood is used. The qqqq likelihood is obtained from following four variables.

1. $\log_{10}(W_{420})$, the tree level QCD matrix element squared for 4-jet configuration. It is numerically obtained by `EVENT2` [153], using the matrix elements calculated by R.K.Ellis, D.A.Ross and A.E.Terrano [158].

2. $\log_{10}(W_\mathrm{exe})$, the matrix element computed by `EXCALIBUR` [159] for the CC03 process $\mathrm{WW} \rightarrow \mathrm{q\bar{q}q\bar{q}}$. Calculation of the matrix element is performed for all jet pairings. The largest value of the matrix elements is used in likelihood.

3. $\log_{10}(y_{45})$, the value of the jet resolution parameter at which the event is reclassified from a four jet to a five jet event by the Durham algorithm.

(a) (b)

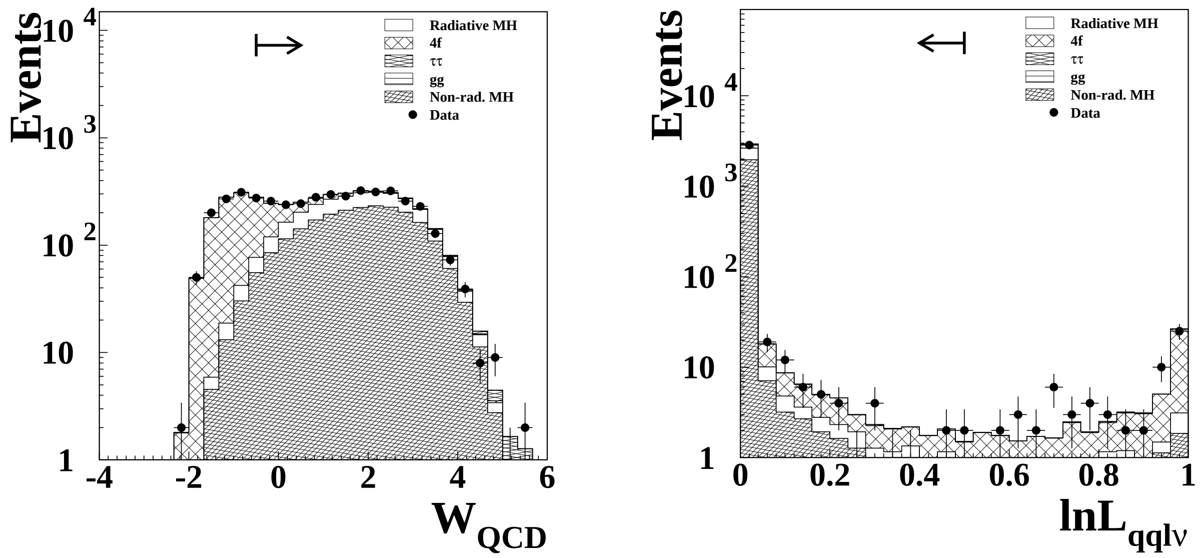

Figure 6.4: (a) $\mathbf{q\bar{q}q\bar{q}}$ and $\mathbf{q\bar{q}gg}$ Matrix Elements (b)qqlν Likelihood

4. Sphericity of the event, $S = 3/2\min(\sum \vec{p_i}^2 / \sum \vec{p}^2)$, where $\sum \vec{p_i}^2$ the sum of the transverse momentum orthogonal to the beam direction. Two jet events consistent with $Z^0 \to q\bar{q}$ topology tend to peak at low values of sphericity.

The likelihood value is calculated using the projection and correlation approximation [140]. The correlation between the four variables is taken into account by the method. The detailed documentation of qqqq likelihood is described in [154, 155]. The qqqq likelihood distributions for data and simulated data are shown in Figure 6.5. It is required to be smaller than 0.25.

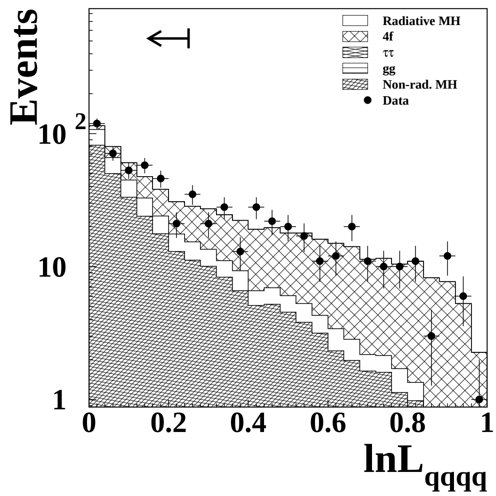

Figure 6.5: qqqq likelihood distribution.

6.2.5 Summary of Event Selection

A summary of the event selection processes is given in Table 6.3. The fractions of each physics process are estimated from Monte Carlo study. Estimated number of selected events agree with the measured number of events within the statistical error for all center-of-mass energies. After all selections, 94% of data events come from $e^+e^- \to q\bar{q}$ process. According to the definition of radiative events given in Section 6.2.3, radiative $e^+e^- \to q\bar{q}$ process is the dominant background and 25% of data events. Four-fermion process background is effectively reduced by selections using $q\bar{q}q\bar{q}$ and $q\bar{q}gg$ matrix elements and qqqq likelihood. The contamination is only about 5%. Background events coming from $e^+e^- \to \tau\tau$ process and two-photon process ($\gamma\gamma \to q\bar{q}$) are 0.2% and less than 6.5×10^{-3}%, respectively. The two processes have negligible effect for further analysis.

189 GeV	Data	MC	Purity [%]	Background [%]			
				qq	4f	$\tau\tau$	$\gamma\gamma$
No cut	21059	20379.7	13.3	80.0	17.1	0.2	2.8
L2MH	19256	18773.7	14.5	79.1	18.1	0.2	2.6
N_{ch}	19118	18647.9	14.5	79.2	18.1	0.1	2.5
$\lvert\cos\theta_T\rvert$	16499	16259.8	14.9	79.4	19.3	0.1	1.2
$\sqrt{s'}$	4410	4436.0	51.5	70.0	29.8	0.2	0.0
$\log W_{QCD}$	3434	3471.5	63.7	86.6	13.2	0.2	0.0
$L_{ql\nu}$	3297	3341.6	65.9	89.5	10.3	0.2	0.0
L_{qqqq}	3015	3058.9	69.9	94.8	4.9	0.2	0.0

200 GeV	Data	MC	Purity [%]	Background [%]			
				qq	4f	$\tau\tau$	$\gamma\gamma$
No cut	7545	7385.7	12.8	76.6	20.5	0.2	2.7
L2MH	6555	6397.3	14.7	74.2	22.9	0.2	2.6
N_{ch}	6505	6357.3	14.8	74.3	22.9	0.1	2.6
$\lvert\cos\theta_T\rvert$	5454	5466.6	15.4	74.3	24.3	0.1	1.3
$\sqrt{s'}$	1590	1632.7	48.4	66.4	33.4	0.1	0.0
$\log W_{QCD}$	1188	1221.8	62.1	85.2	14.6	0.2	0.0
$L_{ql\nu}$	1123	1171.8	64.5	88.4	11.5	0.2	0.0
L_{qqqq}	1030	1060.8	68.9	94.4	5.4	0.2	0.0

192 GeV	Data	MC	Purity [%]	Background [%]			
				qq	4f	$\tau\tau$	$\gamma\gamma$
No cut	3264	3137.2	13.2	78.8	18.2	0.2	2.8
L2MH	2950	2850.2	14.5	77.5	19.6	0.2	2.7
N_{ch}	2926	2832.4	14.5	77.6	19.6	0.1	2.7
$\lvert\cos\theta_T\rvert$	2544	2463.9	14.9	77.8	20.8	0.1	1.3
$\sqrt{s'}$	715	686.3	50.5	68.8	31.0	0.1	0.0
$\log W_{QCD}$	568	528.7	63.3	86.2	13.6	0.2	0.0
$L_{ql\nu}$	550	508.6	65.5	89.1	10.7	0.2	0.0
L_{qqqq}	513	465.9	69.5	94.5	5.3	0.2	0.0

202 GeV	Data	MC	Purity [%]	Background [%]			
				qq	4f	$\tau\tau$	$\gamma\gamma$
No cut	3777	3767.2	12.8	76.6	20.5	0.2	2.7
L2MH	3235	3263.1	14.7	74.2	22.9	0.2	2.7
N_{ch}	3209	3242.7	14.8	74.3	22.9	0.1	2.6
$\lvert\cos\theta_T\rvert$	2718	2788.3	15.4	74.3	24.3	0.1	1.3
$\sqrt{s'}$	820	832.9	48.4	66.4	33.4	0.1	0.0
$\log W_{QCD}$	606	623.2	62.1	85.2	14.6	0.2	0.0
$L_{ql\nu}$	584	597.7	64.5	88.4	11.5	0.2	0.0
L_{qqqq}	516	541.1	68.9	94.4	5.4	0.2	0.0

196 GeV	Data	MC	Purity [%]	Background [%]			
				qq	4f	$\tau\tau$	$\gamma\gamma$
No cut	8040	7478.9	13.0	77.5	19.3	0.2	2.9
L2MH	7130	6648.9	14.6	75.7	21.2	0.2	2.9
N_{ch}	7086	6607.2	14.7	75.8	21.2	0.1	2.9
$\lvert\cos\theta_T\rvert$	6061	5711.0	15.2	75.9	22.6	0.1	1.4
$\sqrt{s'}$	1721	1648.3	49.4	67.5	32.3	0.2	0.0
$\log W_{QCD}$	1281	1247.8	62.8	85.8	13.9	0.2	0.0
$L_{ql\nu}$	1228	1195.5	65.1	89.0	10.8	0.2	0.0
L_{qqqq}	1116	1086.5	69.5	94.8	4.9	0.2	0.0

205 GeV	Data	MC	Purity [%]	Background [%]			
				qq	4f	$\tau\tau$	$\gamma\gamma$
No cut	20730	21108.7	12.3	73.9	19.9	0.2	6.0
L2MH	17081	17624.9	14.7	70.6	23.2	0.2	6.0
N_{ch}	16956	17495.0	14.8	70.8	23.3	0.1	5.8
$\lvert\cos\theta_T\rvert$	14215	14656.3	15.7	71.9	25.3	0.1	2.6
$\sqrt{s'}$	4409	4543.5	47.7	65.2	34.6	0.1	0.1
$\log W_{QCD}$	3229	3343.9	62.0	84.7	15.0	0.2	0.1
$L_{ql\nu}$	3066	3185.7	64.5	88.1	11.6	0.2	0.1
L_{qqqq}	2776	2878.8	69.1	94.3	5.4	0.2	0.1

Table 6.3: Results of non-radiative multi-hadronic event selection.

6.3 Measurement of α_s from Event Shape distributions

Since the procedures after correcting data distributions to hadron level are similar to analysis with radiative hadronic events at LEP1, they are briefly explained here.

Event shape variables of selected data events are corrected to "hadron level" by same method described in Section 5.2.5. For example, hadron level distributions for 189GeV are shown in Figure 6.7. The internal error bar shows the statistical error and the outer error bar shows a sum of the statistical error and the experimental and hadronization uncertainties. All predictions of `JETSET`, `HERWIG` and `ARIADNE` are show very good agreement with the corrected distributions. The bin contents and their errors are shown in Table 6.5, Table 6.6, Table 6.7, Table 6.8, Table 6.9 and Table 6.10.

After correcting the distribution of data to hadron level, fitting perturbative QCD prediction is fittied to the distribution. In setting upper and lower bounds for the fitting, a maximum size of background subtraction, detector correction and hadronization correction are around 10%. In contrast to the analysis with radiative hadronic events at LEP1, these correction factors don't have large difference between different energy samples (Figure 6.6). Therefore, a common fitting range for all energy samples is used in the LEP2 analysis. The fitting ranges are shown in Table 6.4.

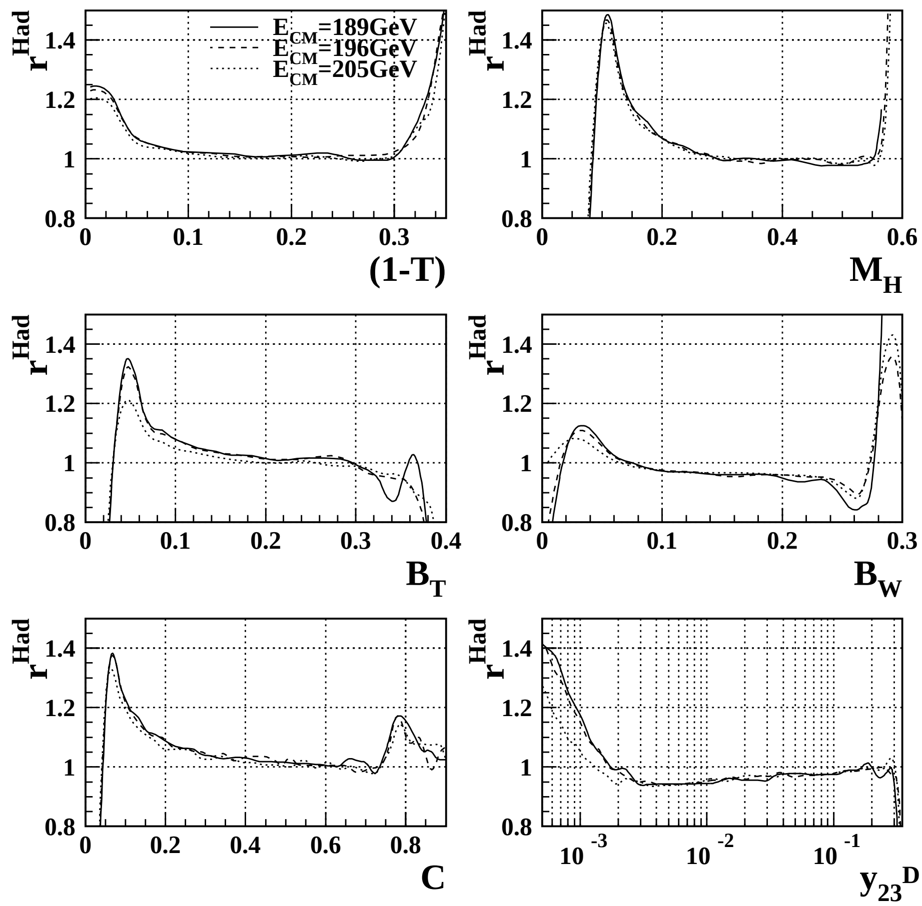

Figure 6.6: The hadronization correction factor for the differential distribution , r^{Had}.

	$(1-T)$	M_H	B_T	B_W	C	y_{23}^D
Lower Limit	0.05	0.17	0.05	0.075	0.20	0.003
Upper Limit	0.30	0.45	0.20	0.250	0.60	0.080

Table 6.4: The lower and upper limit of the fitting range.

The fitting procedure is almost same as the analysis of LEP1 data (Section 5.2.5). The $O(\alpha_s^2)$ and NLLA calculations are combined with the $\ln(R)$ matching scheme. The effects of hadronization on event shapes must be taken into account in order to perform fitting at the hadron level (hadronization correction). The hadronization correction is applied to the cumulative theoretical calculation. Since each bin of a event shape distribution in the analysis of LEP2 data has enough number of events to assume its error as Gaussian error, usual χ^2 method is used.

For example, the fitted theoretical distribution is displayed with the hadron level distribution at 189GeV in Figure 6.8. The vertical lines show the fitting region. The lower part of the figure shows the deviation of bin contents in data from fitted theoretical prediction in standard deviations. Fitted theoretical distributions agree with data distributions in a sufficiently wider range than the fitting range. Therefore, it seems that α_s obtained by the fitting doesn't strongly depend on the fitting range.

6.4 Systematic Uncertainties

The hadronization and theoretical uncertainties are estimated by the same procedure as the analysis with radiative multi-hadronic events at LEP1 described in Section 5.4. Since there are different source for the experimental systematic uncertainties, they are described in this section.

The experimental uncertainty is estimated by adding in quadrature the following contributions.

Track and Cluster Selection As described in Section 5.2.1, a part of cluster energy doubly counted by track momentum matched to the cluster is subtracted by the method described in [138, 139]. In order to treat any inconsistencies caused by the difference of response of the tracking or the calorimeter, three differences are formed for the standard result, the result when all clusters and tracks are used, the result obtained using only tracks. The largest difference is assigned as the experimental systematic uncertainty.

Event Selection The inhomogeneity of the response of the detector in the endcap region was allowed for by restricting the analysis to the barrel region of the detector, requiring the thrust axis of accepted events to lie within the range $|\cos\theta_T| < 0.7$. The corresponding systematic error is the deviation of the results from those of the standard analysis.

The uncertainties associated with the subtraction of four-fermion background is studied by varying the position of cut values on W_{QCD},$\ln L_{\mathrm{ql}\nu}$ and $\ln L_{\mathrm{qqqq}\nu}$. which are changed to 0.0 and -0.5, 0.25 and 0.75, 0.10 and 0.40, respectively.

Estimation of Effective Center-of-Mass Energy Uncertainties arising from the non-radiative events are estimated by repeating the analysis using a different technique to determine the value of $\sqrt{s'}$. This technique differs from the standard $\sqrt{s'}$ algorithm in that in this case the kinematic fit assumes always one unobserved photon close to the beam direction for each event. The difference relative to the standard result is taken as the systematic error.

The selection efficiency and purity are evaluated using Monte Carlo simulation by `KK2f`. It contains QED exponentiated matrix elements for the initial state radiation up to $O(\alpha^3)$. Since similar results are obtained from the simulation by `PYTHIA`, no additional systematic uncertainty is assigned.

6.5 Result of Analysis with Multi-Hadronic Events at LEP2

All results of fitting are listed in Table 6.11, Table 6.12 and Table 6.13. The total hadronization uncertainty is about 0.001. Almost all hadronization uncertainty comes from hadronization model uncertainties. Scale uncertainty is $0.005 \sim 0.006$ at all center-of-mass energies. It is the largest systematic error for the sample at $E_{\mathrm{CM}} = 189\mathrm{GeV}$. Total experimental uncertainty is $0.002 \sim 0.020$ and seems to correlate with the statistical uncertainty. The total experimental uncertainty is the largest largest systematic error for samples at all center-of-mass energies except 189GeV. Although the experimental uncertainties have large statistical fluctuations in the case of samples with small numbers of events, the uncertainties on qqqq likelihood, track selection and $|\cos\theta_T|$ cut.

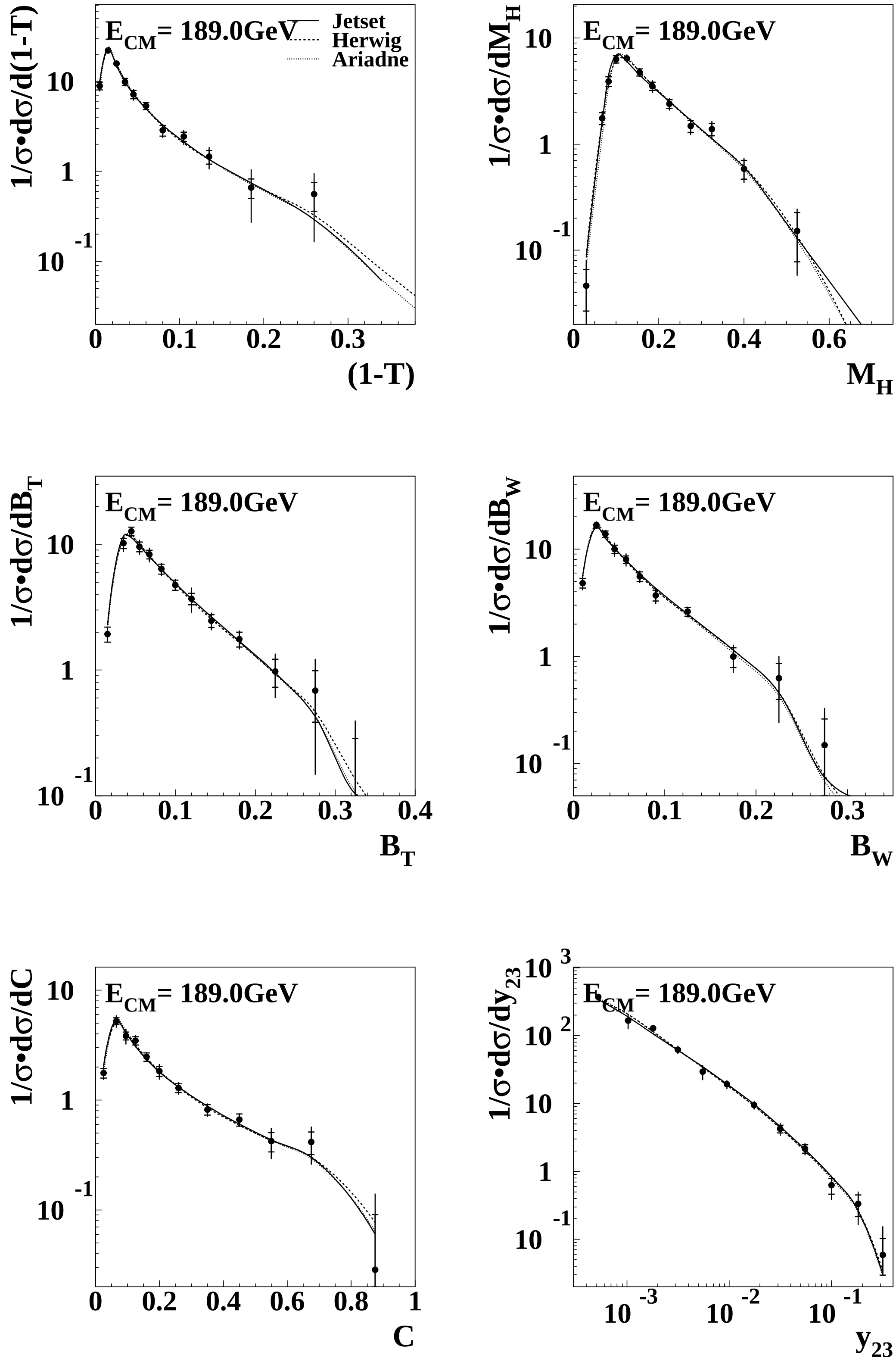

Figure 6.7: Hadron level distribution at $\sqrt{s} = 189\text{GeV}$.

$(1-T)$	$1/\sigma \cdot d\sigma/d(1-T)$					
	189.0GeV	192.0GeV	196.0GeV	200.0GeV	202.0GeV	205.0GeV
0.00-0.01	8.89 ± 0.85 ± 0.79	10.15 ± 2.05 ± 2.23	8.19 ± 1.35 ± 0.94	9.36 ± 1.49 ± 1.20	11.66 ± 2.32 ± 3.05	11.37 ± 1.04 ± 0.83
0.01-0.02	21.99 ± 1.34 ± 0.98	23.34 ± 3.08 ± 3.10	22.88 ± 2.16 ± 1.44	22.72 ± 2.27 ± 0.95	20.71 ± 3.21 ± 2.12	23.78 ± 1.50 ± 1.29
0.02-0.03	15.68 ± 1.09 ± 0.96	13.09 ± 2.32 ± 3.06	15.18 ± 1.70 ± 1.43	13.91 ± 1.76 ± 0.79	16.52 ± 2.69 ± 3.32	15.86 ± 1.21 ± 2.90
0.03-0.04	9.85 ± 0.88 ± 0.59	10.05 ± 2.01 ± 2.78	10.28 ± 1.41 ± 2.22	7.94 ± 1.42 ± 2.20	6.50 ± 1.97 ± 0.77	9.85 ± 0.97 ± 1.38
0.04-0.05	7.15 ± 0.77 ± 0.70	7.52 ± 1.79 ± 1.53	6.93 ± 1.22 ± 1.94	8.37 ± 1.35 ± 2.28	5.67 ± 1.76 ± 2.34	7.33 ± 0.84 ± 1.33
0.05-0.07	5.32 ± 0.48 ± 0.27	5.25 ± 1.08 ± 0.98	4.99 ± 0.75 ± 2.07	4.24 ± 0.74 ± 0.61	4.89 ± 1.12 ± 1.22	5.60 ± 0.54 ± 0.32
0.07-0.09	2.85 ± 0.39 ± 0.33	3.21 ± 0.91 ± 0.75	2.20 ± 0.56 ± 1.59	2.59 ± 0.66 ± 1.81	2.87 ± 0.98 ± 1.86	2.86 ± 0.41 ± 0.50
0.09-0.12	2.43 ± 0.28 ± 0.36	2.11 ± 0.60 ± 0.53	2.43 ± 0.46 ± 0.22	2.25 ± 0.47 ± 0.73	2.74 ± 0.73 ± 0.84	2.25 ± 0.32 ± 0.37
0.12-0.15	1.45 ± 0.25 ± 0.32	1.41 ± 0.58 ± 0.21	1.39 ± 0.41 ± 0.31	1.11 ± 0.41 ± 1.18	1.66 ± 0.65 ± 0.78	1.24 ± 0.29 ± 0.44
0.15-0.22	0.66 ± 0.16 ± 0.36	0.72 ± 0.36 ± 0.41	0.73 ± 0.28 ± 0.37	1.20 ± 0.35 ± 0.68	1.03 ± 0.50 ± 0.38	0.64 ± 0.22 ± 0.32
0.22-0.30	0.56 ± 0.20 ± 0.34	0.33 ± 0.47 ± 0.81	0.79 ± 0.35 ± 0.90	0.52 ± 0.35 ± 0.48	0.60 ± 0.53 ± 0.94	0.10 ± 0.24 ± 0.26
0.30-0.38	-0.08 ± 0.10 ± 0.14	0.08 ± 0.39 ± 0.56	-0.09 ± 0.28 ± 0.64	0.18 ± 0.34 ± 0.60	-0.22 ± 0.31 ± 1.12	-0.11 ± 0.08 ± 0.12

Table 6.5: Hadron level distribution for $(1-T)$.

M_H	$1/\sigma \cdot d\sigma/dM_H$					
	189.0GeV	192.0GeV	196.0GeV	200.0GeV	202.0GeV	205.0GeV
0.00-0.06	0.05 ± 0.02 ± 0.03	0.09 ± 0.05 ± 0.04	0.04 ± 0.03 ± 0.03	0.04 ± 0.04 ± 0.05	0.09 ± 0.06 ± 0.01	0.12 ± 0.03 ± 0.04
0.06-0.07	1.75 ± 0.23 ± 0.20	1.62 ± 0.50 ± 0.54	1.63 ± 0.36 ± 0.19	1.99 ± 0.41 ± 0.19	2.18 ± 0.61 ± 1.24	2.76 ± 0.32 ± 0.88
0.07-0.09	3.90 ± 0.41 ± 0.31	4.55 ± 0.97 ± 1.43	4.30 ± 0.70 ± 1.02	5.63 ± 0.82 ± 1.73	5.94 ± 1.19 ± 2.39	4.69 ± 0.51 ± 0.90
0.09-0.11	6.31 ± 0.51 ± 0.39	7.31 ± 1.23 ± 1.09	6.57 ± 0.83 ± 1.13	6.26 ± 0.88 ± 0.37	6.04 ± 1.24 ± 0.67	6.40 ± 0.56 ± 0.59
0.11-0.14	6.45 ± 0.42 ± 0.38	4.94 ± 0.87 ± 1.34	6.16 ± 0.64 ± 1.08	5.09 ± 0.66 ± 1.18	5.00 ± 0.94 ± 0.78	5.92 ± 0.44 ± 0.45
0.14-0.17	4.76 ± 0.37 ± 0.30	4.87 ± 0.82 ± 0.76	4.58 ± 0.57 ± 1.15	5.07 ± 0.65 ± 1.27	4.70 ± 0.90 ± 0.73	4.99 ± 0.41 ± 0.46
0.17-0.20	3.52 ± 0.32 ± 0.38	4.48 ± 0.79 ± 1.09	3.19 ± 0.49 ± 0.43	3.27 ± 0.55 ± 0.42	3.39 ± 0.79 ± 0.83	3.76 ± 0.36 ± 0.22
0.20-0.25	2.40 ± 0.22 ± 0.24	1.91 ± 0.48 ± 0.53	2.17 ± 0.34 ± 0.28	2.18 ± 0.36 ± 0.54	1.24 ± 0.46 ± 1.54	2.50 ± 0.24 ± 0.27
0.25-0.30	1.48 ± 0.19 ± 0.18	1.94 ± 0.44 ± 0.30	1.62 ± 0.31 ± 0.55	1.32 ± 0.32 ± 0.64	2.37 ± 0.53 ± 0.62	1.41 ± 0.21 ± 0.28
0.30-0.35	1.38 ± 0.18 ± 0.20	0.62 ± 0.35 ± 0.54	1.15 ± 0.28 ± 0.48	1.34 ± 0.33 ± 0.25	1.62 ± 0.49 ± 0.78	1.15 ± 0.21 ± 0.27
0.35-0.45	0.58 ± 0.12 ± 0.10	0.56 ± 0.27 ± 0.33	0.69 ± 0.20 ± 0.20	0.80 ± 0.24 ± 0.25	0.64 ± 0.33 ± 0.73	0.57 ± 0.15 ± 0.19
0.45-0.60	0.15 ± 0.07 ± 0.06	0.32 ± 0.22 ± 0.46	0.29 ± 0.16 ± 0.24	0.22 ± 0.15 ± 0.14	0.22 ± 0.21 ± 0.33	0.02 ± 0.08 ± 0.11

Table 6.6: Hadron level distribution for M_H.

B_T	$1/\sigma \cdot d\sigma/dB_T$					
	189.0GeV	192.0GeV	196.0GeV	200.0GeV	202.0GeV	205.0GeV
0.00-0.03	1.93 ± 0.26 ± 0.09	2.61 ± 0.63 ± 0.41	1.89 ± 0.42 ± 0.66	2.27 ± 0.48 ± 0.47	2.47 ± 0.69 ± 0.58	3.27 ± 0.34 ± 0.22
0.03-0.04	10.19 ± 0.95 ± 1.16	10.31 ± 2.18 ± 4.22	10.41 ± 1.54 ± 2.66	12.00 ± 1.72 ± 2.74	11.08 ± 2.36 ± 1.53	13.12 ± 1.16 ± 1.29
0.04-0.05	12.67 ± 0.99 ± 0.50	11.62 ± 2.14 ± 1.79	11.87 ± 1.52 ± 3.25	11.65 ± 1.64 ± 2.30	9.50 ± 2.17 ± 1.07	10.10 ± 0.98 ± 1.95
0.05-0.06	9.57 ± 0.86 ± 1.00	10.72 ± 1.93 ± 1.25	12.83 ± 1.49 ± 2.43	9.42 ± 1.45 ± 1.30	9.27 ± 2.02 ± 1.82	10.20 ± 0.96 ± 1.73
0.06-0.07	8.30 ± 0.65 ± 0.91	9.02 ± 1.51 ± 1.95	7.36 ± 0.99 ± 1.08	7.58 ± 1.08 ± 1.19	8.59 ± 1.57 ± 1.71	7.95 ± 0.71 ± 0.89
0.07-0.09	6.37 ± 0.58 ± 0.50	4.63 ± 1.16 ± 2.49	5.83 ± 0.88 ± 0.90	5.89 ± 0.95 ± 1.33	4.01 ± 1.20 ± 2.04	6.69 ± 0.64 ± 1.15
0.09-0.11	4.75 ± 0.44 ± 0.28	4.42 ± 0.97 ± 1.09	4.36 ± 0.68 ± 0.37	4.81 ± 0.76 ± 0.29	5.29 ± 1.10 ± 1.56	5.29 ± 0.50 ± 0.63
0.11-0.13	3.69 ± 0.38 ± 0.74	2.90 ± 0.81 ± 1.10	2.62 ± 0.58 ± 0.45	3.06 ± 0.66 ± 0.78	2.30 ± 0.87 ± 1.55	3.49 ± 0.43 ± 0.90
0.13-0.16	2.46 ± 0.29 ± 0.27	2.65 ± 0.64 ± 0.77	2.85 ± 0.47 ± 0.28	2.08 ± 0.48 ± 1.12	2.73 ± 0.72 ± 0.90	2.63 ± 0.31 ± 0.23
0.16-0.20	1.76 ± 0.24 ± 0.19	1.39 ± 0.52 ± 0.83	1.66 ± 0.39 ± 0.33	2.16 ± 0.45 ± 0.82	2.77 ± 0.66 ± 0.61	1.58 ± 0.28 ± 0.48
0.20-0.25	0.97 ± 0.24 ± 0.28	1.38 ± 0.58 ± 0.72	0.95 ± 0.42 ± 0.52	1.44 ± 0.53 ± 0.74	0.54 ± 0.67 ± 1.13	0.79 ± 0.34 ± 0.74
0.25-0.30	0.69 ± 0.30 ± 0.45	0.56 ± 0.71 ± 1.34	1.48 ± 0.63 ± 1.31	0.48 ± 0.52 ± 1.03	1.06 ± 0.82 ± 1.38	-0.04 ± 0.37 ± 0.16
0.30-0.35	0.03 ± 0.25 ± 0.26	0.23 ± 0.66 ± 0.97	-0.37 ± 0.34 ± 0.90	-0.06 ± 0.52 ± 0.83	0.28 ± 0.89 ± 1.05	-0.15 ± 0.27 ± 0.72

Table 6.7: Hadron level distribution for B_T.

B_W	$1/\sigma \cdot d\sigma/dB_W$					
	189.0GeV	192.0GeV	196.0GeV	200.0GeV	202.0GeV	205.0GeV
0.00-0.02	4.83 ± 0.49 ± 0.51	6.74 ± 1.27 ± 0.90	5.06 ± 0.81 ± 0.59	5.73 ± 0.90 ± 0.69	6.32 ± 1.32 ± 0.99	7.16 ± 0.62 ± 0.28
0.02-0.03	16.84 ± 1.14 ± 0.87	14.77 ± 2.42 ± 3.35	15.42 ± 1.71 ± 2.30	16.90 ± 1.94 ± 1.07	15.82 ± 2.69 ± 2.82	16.31 ± 1.21 ± 0.81
0.03-0.04	13.81 ± 1.00 ± 0.80	16.09 ± 2.41 ± 3.14	14.40 ± 1.62 ± 1.34	12.94 ± 1.67 ± 0.90	9.87 ± 2.20 ± 3.12	12.52 ± 1.07 ± 1.28
0.04-0.05	10.00 ± 0.89 ± 1.25	9.29 ± 1.90 ± 2.17	10.14 ± 1.42 ± 1.50	9.08 ± 1.49 ± 1.20	11.83 ± 2.28 ± 2.72	10.02 ± 0.97 ± 1.05
0.05-0.07	8.00 ± 0.65 ± 0.89	7.81 ± 1.49 ± 0.59	6.59 ± 0.97 ± 1.25	7.20 ± 1.05 ± 1.14	8.32 ± 1.56 ± 1.36	8.88 ± 0.73 ± 0.51
0.07-0.08	5.57 ± 0.57 ± 0.46	5.23 ± 1.26 ± 1.12	5.95 ± 0.90 ± 0.66	5.86 ± 0.99 ± 0.69	2.23 ± 1.15 ± 1.43	5.60 ± 0.63 ± 1.02
0.08-0.10	3.71 ± 0.42 ± 0.48	3.59 ± 0.95 ± 0.96	4.80 ± 0.76 ± 1.24	3.82 ± 0.76 ± 0.89	4.00 ± 1.10 ± 1.15	4.09 ± 0.48 ± 0.38
0.10-0.15	2.61 ± 0.25 ± 0.17	2.19 ± 0.52 ± 0.33	1.83 ± 0.36 ± 0.34	2.10 ± 0.41 ± 0.72	3.06 ± 0.64 ± 0.73	2.28 ± 0.27 ± 0.35
0.15-0.20	0.99 ± 0.21 ± 0.21	0.82 ± 0.46 ± 0.60	1.33 ± 0.37 ± 0.25	1.58 ± 0.42 ± 0.79	1.48 ± 0.58 ± 1.13	0.96 ± 0.26 ± 0.37
0.20-0.25	0.63 ± 0.23 ± 0.31	0.91 ± 0.63 ± 0.85	1.06 ± 0.48 ± 0.88	0.61 ± 0.42 ± 0.89	0.36 ± 0.57 ± 0.65	0.11 ± 0.29 ± 0.40
0.25-0.30	0.15 ± 0.11 ± 0.14	0.01 ± 0.21 ± 0.30	0.09 ± 0.19 ± 0.47	0.19 ± 0.25 ± 0.37	0.31 ± 0.40 ± 0.49	0.02 ± 0.09 ± 0.09

Table 6.8: Hadron level distribution for B_W.

C	$1/\sigma \cdot d\sigma/dC$					
	189.0GeV	192.0GeV	196.0GeV	200.0GeV	202.0GeV	205.0GeV
0.00-0.05	1.76 ± 0.18 ± 0.16	1.89 ± 0.42 ± 0.35	1.67 ± 0.28 ± 0.27	2.03 ± 0.33 ± 0.24	2.40 ± 0.49 ± 0.68	2.51 ± 0.22 ± 0.22
0.05-0.08	5.23 ± 0.38 ± 0.55	5.45 ± 0.86 ± 1.18	5.45 ± 0.60 ± 0.87	5.79 ± 0.66 ± 0.71	5.44 ± 0.91 ± 1.09	5.36 ± 0.41 ± 0.45
0.08-0.11	3.84 ± 0.31 ± 0.55	3.99 ± 0.72 ± 0.79	4.06 ± 0.50 ± 0.55	3.57 ± 0.53 ± 0.50	2.56 ± 0.68 ± 0.78	3.91 ± 0.34 ± 0.34
0.11-0.14	3.47 ± 0.30 ± 0.35	3.25 ± 0.64 ± 0.83	3.09 ± 0.44 ± 0.51	2.71 ± 0.47 ± 0.23	3.80 ± 0.72 ± 1.14	2.96 ± 0.30 ± 0.30
0.14-0.18	2.47 ± 0.22 ± 0.09	2.18 ± 0.47 ± 0.38	2.29 ± 0.34 ± 0.74	2.47 ± 0.38 ± 0.34	1.80 ± 0.49 ± 0.38	2.56 ± 0.24 ± 0.25
0.18-0.22	1.83 ± 0.19 ± 0.22	1.69 ± 0.42 ± 0.38	1.78 ± 0.30 ± 0.45	1.92 ± 0.33 ± 0.66	1.10 ± 0.41 ± 0.55	1.77 ± 0.21 ± 0.25
0.22-0.30	1.29 ± 0.12 ± 0.13	1.22 ± 0.26 ± 0.38	1.12 ± 0.18 ± 0.27	1.16 ± 0.19 ± 0.28	1.37 ± 0.29 ± 0.57	1.40 ± 0.13 ± 0.20
0.30-0.40	0.82 ± 0.09 ± 0.07	0.84 ± 0.20 ± 0.28	0.96 ± 0.15 ± 0.16	0.78 ± 0.16 ± 0.20	0.69 ± 0.22 ± 0.61	0.84 ± 0.10 ± 0.08
0.40-0.50	0.66 ± 0.08 ± 0.04	0.69 ± 0.19 ± 0.17	0.48 ± 0.13 ± 0.16	0.63 ± 0.15 ± 0.15	0.83 ± 0.22 ± 0.28	0.63 ± 0.10 ± 0.07
0.50-0.60	0.42 ± 0.08 ± 0.10	0.31 ± 0.18 ± 0.27	0.42 ± 0.14 ± 0.12	0.61 ± 0.17 ± 0.26	0.84 ± 0.26 ± 0.53	0.36 ± 0.10 ± 0.13
0.60-0.75	0.42 ± 0.10 ± 0.12	0.60 ± 0.25 ± 0.27	0.45 ± 0.17 ± 0.30	0.41 ± 0.19 ± 0.12	0.22 ± 0.25 ± 0.67	0.16 ± 0.13 ± 0.21
0.75-1.00	0.03 ± 0.06 ± 0.09	-0.00 ± 0.14 ± 0.20	0.13 ± 0.13 ± 0.26	0.02 ± 0.14 ± 0.09	0.12 ± 0.22 ± 0.58	0.07 ± 0.08 ± 0.08

Table 6.9: Hadron level distribution for C-parameter.

y_{23}^D	$1/\sigma \cdot d\sigma/dy_{23}^D$					
	189.0GeV	192.0GeV	196.0GeV	200.0GeV	202.0GeV	205.0GeV
0.0003-0.0008	372.54 ± 26.72 ± 11.08	322.08 ± 59.27 ± 76.02	350.08 ± 40.78 ± 33.41	389.33 ± 46.61 ± 69.22	359.58 ± 64.48 ± 397.36	29.59 ± 44.71 ± 0.00
0.0008-0.0013	166.66 ± 15.93 ± 39.37	224.87 ± 40.90 ± 63.00	200.59 ± 26.58 ± 28.90	182.94 ± 28.20 ± 18.20	204.88 ± 41.42 ± 75.25	185.62 ± 18.25 ± 8.99
0.0013-0.0023	127.74 ± 9.97 ± 11.75	129.90 ± 22.83 ± 21.13	117.76 ± 15.27 ± 18.91	102.00 ± 15.51 ± 14.88	95.54 ± 21.64 ± 24.05	111.66 ± 10.72 ± 14.71
0.0023-0.0040	62.10 ± 5.56 ± 6.71	77.22 ± 13.93 ± 14.67	55.90 ± 8.51 ± 15.01	61.21 ± 9.27 ± 12.65	72.99 ± 13.89 ± 15.74	69.51 ± 6.39 ± 7.46
0.0040-0.0070	29.41 ± 2.96 ± 6.70	29.28 ± 7.05 ± 5.76	33.41 ± 4.81 ± 9.74	34.04 ± 5.39 ± 6.16	23.02 ± 6.95 ± 11.69	33.96 ± 3.53 ± 3.42
0.0070-0.0120	19.17 ± 1.90 ± 2.03	18.99 ± 4.35 ± 4.55	20.21 ± 3.03 ± 2.16	14.43 ± 3.03 ± 4.39	13.23 ± 4.24 ± 3.66	20.89 ± 2.16 ± 2.10
0.0120-0.0230	9.48 ± 0.93 ± 0.92	8.48 ± 2.13 ± 1.95	6.88 ± 1.38 ± 1.76	10.57 ± 1.70 ± 2.33	6.69 ± 2.17 ± 5.13	8.79 ± 1.04 ± 2.59
0.0230-0.0400	4.23 ± 0.56 ± 0.72	4.13 ± 1.26 ± 1.01	3.95 ± 0.86 ± 0.67	2.74 ± 0.86 ± 1.78	5.15 ± 1.41 ± 1.48	4.40 ± 0.63 ± 1.12
0.0400-0.0700	2.16 ± 0.31 ± 0.30	1.69 ± 0.71 ± 1.09	1.54 ± 0.47 ± 0.28	2.71 ± 0.60 ± 0.91	2.27 ± 0.81 ± 0.77	2.10 ± 0.36 ± 0.53
0.0700-0.1300	0.63 ± 0.16 ± 0.18	1.00 ± 0.42 ± 0.70	0.98 ± 0.30 ± 0.32	0.93 ± 0.32 ± 0.43	1.37 ± 0.50 ± 0.67	0.80 ± 0.23 ± 0.27
0.1300-0.2350	0.33 ± 0.12 ± 0.13	0.20 ± 0.28 ± 0.37	0.58 ± 0.22 ± 0.64	0.32 ± 0.21 ± 0.46	0.47 ± 0.33 ± 0.53	-0.00 ± 0.14 ± 0.16
0.2350-0.4000	0.06 ± 0.04 ± 0.09	-0.05 ± 0.06 ± 0.07	0.06 ± 0.09 ± 0.18	0.06 ± 0.13 ± 0.14	0.06 ± 0.19 ± 0.24	0.01 ± 0.04 ± 0.07

Table 6.10: Hadron level distribution for y_{23}^D.

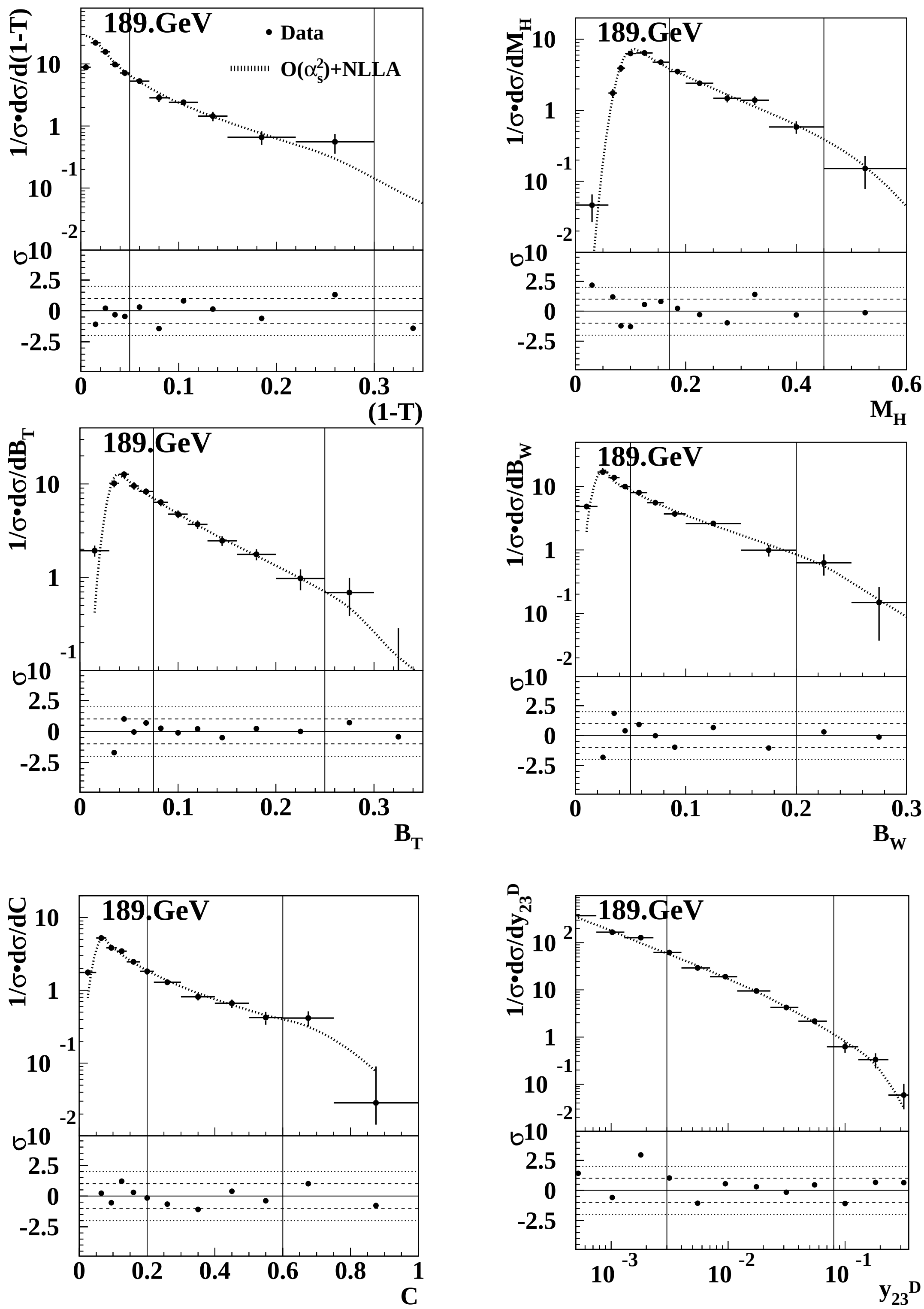

Figure 6.8: The theoretical predictions which are convolved with the hadronization correction and fitted to the hadron level distribution of data.

	$(1-T)$	M_H	B_T	B_W	C	y_{23}^D
α_s(189GeV)	0.1134	0.1058	0.1107	0.1025	0.1083	0.1154
Statistical Error	± 0.0038	± 0.0029	± 0.0030	± 0.0025	± 0.0035	± 0.0033
Tracks + Clusters	0.0001	-0.0009	-0.0001	0.0003	0.0015	0.0004
TracksOnly	0.0006	-0.0003	-0.0018	-0.0018	-0.0008	-0.0017
$\lvert cos\theta_T\rvert < 0.7$	-0.0000	-0.0009	0.0022	0.0005	0.0009	0.0029
$\sqrt{s'}$	-0.0010	-0.0004	0.0004	0.0002	0.0005	0.0012
$\ln W_{QCD} > 0.0$	-0.0000	-0.0005	-0.0006	-0.0003	-0.0005	-0.0004
$\ln W_{QCD} > -0.8$	0.0001	-0.0000	0.0005	0.0001	0.0003	-0.0001
$\ln L_{qql\nu} > 0.25$	-0.0000	-0.0002	-0.0003	-0.0003	0.0000	-0.0002
$\ln L_{qql\nu} > 0.75$	-0.0002	0.0002	-0.0002	0.0000	-0.0000	0.0003
$\ln L_{qqqq} > 0.10$	-0.0012	-0.0003	-0.0001	-0.0001	0.0011	-0.0001
$\ln L_{qqqq} > 0.40$	-0.0005	-0.0005	0.0003	-0.0002	-0.0014	-0.0005
Experimental Syst.	± 0.0017	± 0.0015	± 0.0030	± 0.0022	± 0.0030	± 0.0038
$b - 1s.d.$	-0.0000	-0.0001	-0.0001	-0.0001	-0.0002	0.0001
$b + 1s.d.$	0.0001	0.0004	0.0002	0.0001	0.0001	-0.0001
$Q_0 - 1s.d.$	0.0001	-0.0002	0.0003	-0.0001	0.0001	-0.0003
$Q_0 + 1s.d.$	-0.0001	0.0003	-0.0002	0.0000	-0.0001	0.0002
$\sigma_q - 1s.d.$	0.0003	0.0001	0.0003	0.0001	0.0003	-0.0000
$\sigma_q + 1s.d.$	-0.0002	0.0000	-0.0002	-0.0001	-0.0002	-0.0001
udsc only	0.0004	-0.0000	0.0014	0.0005	0.0006	0.0005
Herwig5.9	-0.0002	0.0006	-0.0015	0.0000	-0.0009	-0.0006
Ariadne4.08	0.0011	0.0007	0.0003	0.0008	0.0008	0.0005
Total Hadronization.	± 0.0013	± 0.0011	± 0.0021	± 0.0010	± 0.0014	± 0.0010
$x_\mu = 0.5$	-0.0046	-0.0029	-0.0048	-0.0026	-0.0043	-0.0007
$x_\mu = 2.0$	0.0058	0.0040	0.0059	0.0036	0.0054	0.0032
Total error	+ 0.0072 − 0.0063	+ 0.0053 − 0.0045	+ 0.0075 − 0.0067	+ 0.0050 − 0.0044	+ 0.0072 − 0.0065	+ 0.0061 − 0.0052

	$(1-T)$	M_H	B_T	B_W	C	y_{23}^D
α_s(192GeV)	0.1121	0.1051	0.1035	0.0966	0.1074	0.1153
Statistical Error	± 0.0087	± 0.0076	± 0.0076	± 0.0058	± 0.0091	± 0.0087
Tracks + Clusters	0.0005	-0.0001	-0.0007	0.0006	-0.0005	0.0000
TracksOnly	-0.0008	-0.0011	0.0020	0.0018	-0.0053	0.0020
$\lvert cos\theta_T\rvert < 0.7$	-0.0034	0.0016	-0.0051	-0.0022	-0.0046	-0.0040
$\sqrt{s'}$	-0.0013	-0.0008	-0.0012	-0.0005	-0.0013	-0.0001
$\ln W_{QCD} > 0.0$	0.0025	-0.0003	0.0015	0.0005	0.0028	0.0016
$\ln W_{QCD} > -0.8$	0.0003	0.0006	0.0009	-0.0001	0.0003	0.0004
$\ln L_{qql\nu} > 0.25$	0.0001	0.0001	-0.0000	0.0000	-0.0001	-0.0002
$\ln L_{qql\nu} > 0.75$	0.0009	0.0005	0.0010	0.0006	0.0012	0.0007
$\ln L_{qqqq} > 0.10$	-0.0060	-0.0052	-0.0046	-0.0032	-0.0051	-0.0008
$\ln L_{qqqq} > 0.40$	0.0018	0.0023	0.0034	0.0017	0.0054	0.0021
Experimental Syst.	± 0.0077	± 0.0056	± 0.0077	± 0.0044	± 0.0094	± 0.0052
$b - 1s.d.$	-0.0006	-0.0004	-0.0016	-0.0007	-0.0007	-0.0009
$b + 1s.d.$	0.0001	0.0001	0.0002	0.0001	0.0002	-0.0003
$Q_0 - 1s.d.$	0.0002	-0.0004	0.0003	-0.0001	0.0002	-0.0004
$Q_0 + 1s.d.$	-0.0001	0.0001	-0.0002	0.0001	-0.0001	0.0003
$\sigma_q - 1s.d.$	-0.0002	0.0001	-0.0011	-0.0005	-0.0003	-0.0008
$\sigma_q + 1s.d.$	-0.0003	-0.0001	-0.0002	-0.0001	-0.0001	-0.0002
udsc only	0.0000	0.0000	0.0000	0.0000	0.0000	0.0000
Herwig5.9	-0.0006	0.0002	-0.0027	-0.0005	-0.0013	-0.0021
Ariadne4.08	0.0012	0.0005	0.0003	0.0008	0.0008	0.0002
Total Hadronization.	± 0.0015	± 0.0008	± 0.0032	± 0.0012	± 0.0017	± 0.0023
$x_\mu = 0.5$	-0.0044	-0.0026	-0.0040	-0.0020	-0.0043	-0.0004
$x_\mu = 2.0$	0.0056	0.0038	0.0049	0.0029	0.0054	0.0029
Total error	+ 0.0130 − 0.0125	+ 0.0102 − 0.0098	+ 0.0123 − 0.0120	+ 0.0079 − 0.0076	+ 0.0143 − 0.0139	+ 0.0108 − 0.0104

Table 6.11: Result of fits for $\sqrt{s}$ =189GeV (Upper) and 192GeV (Lower)

	$(1-T)$	M_H	B_T	B_W	C	y_{23}^D
α_s(196GeV)	0.1089	0.1017	0.1052	0.0997	0.1042	0.1079
Statistical Error	± 0.0064	± 0.0046	± 0.0054	± 0.0043	± 0.0059	± 0.0057
Tracks + Clusters	-0.0012	0.0002	-0.0002	0.0002	-0.0027	0.0048
TracksOnly	-0.0044	-0.0004	0.0014	0.0007	-0.0003	0.0069
$\lvert cos\theta_T \rvert < 0.7$	0.0050	0.0006	-0.0004	-0.0003	-0.0014	-0.0059
$\sqrt{s'}$	0.0003	0.0003	-0.0008	0.0006	0.0001	0.0022
$\ln W_{QCD} > 0.0$	-0.0030	-0.0007	0.0000	-0.0010	-0.0014	0.0013
$\ln W_{QCD} > -0.8$	0.0002	-0.0001	0.0006	0.0007	0.0009	0.0000
$\ln L_{ql\nu} > 0.25$	-0.0000	0.0002	-0.0003	-0.0001	-0.0003	-0.0003
$\ln L_{ql\nu} > 0.75$	-0.0010	-0.0001	-0.0013	-0.0003	-0.0005	-0.0004
$\ln L_{qqqq} > 0.10$	-0.0045	-0.0050	-0.0008	-0.0036	0.0018	-0.0011
$\ln L_{qqqq} > 0.40$	-0.0026	-0.0018	-0.0016	-0.0012	-0.0008	-0.0008
Experimental Syst.	± 0.0086	± 0.0051	± 0.0028	± 0.0039	± 0.0038	± 0.0095
$b - 1s.d.$	0.0003	-0.0002	0.0013	0.0005	0.0005	0.0005
$b + 1s.d.$	0.0003	0.0001	0.0002	0.0000	0.0002	-0.0001
$Q_0 - 1s.d.$	0.0005	-0.0003	0.0016	0.0004	0.0007	0.0003
$Q_0 + 1s.d.$	-0.0000	0.0003	-0.0002	0.0001	-0.0001	0.0003
$\sigma_q - 1s.d.$	0.0003	0.0001	0.0002	0.0001	0.0004	-0.0001
$\sigma_q + 1s.d.$	0.0002	-0.0001	0.0011	0.0003	0.0003	0.0005
udsc only	0.0004	-0.0001	0.0014	0.0005	0.0006	0.0005
Herwig5.9	-0.0001	0.0008	-0.0015	0.0000	-0.0008	-0.0006
Ariadne4.08	0.0013	0.0007	0.0003	0.0008	0.0009	0.0006
Total Hadronization.	± 0.0015	± 0.0011	± 0.0029	± 0.0011	± 0.0016	± 0.0011
$x_\mu = 0.5$	-0.0041	-0.0026	-0.0042	-0.0024	-0.0039	-0.0004
$x_\mu = 2.0$	0.0052	0.0036	0.0051	0.0034	0.0048	0.0024
Total error	+ 0.0120 − 0.0116	+ 0.0079 − 0.0075	+ 0.0085 − 0.0079	+ 0.0068 − 0.0064	+ 0.0087 − 0.0082	+ 0.0114 − 0.0111

	$(1-T)$	M_H	B_T	B_W	C	y_{23}^D
α_s(200GeV)	0.1056	0.1019	0.1094	0.1008	0.1047	0.1136
Statistical Error	± 0.0059	± 0.0057	± 0.0067	± 0.0047	± 0.0067	± 0.0062
Tracks + Clusters	0.0021	0.0013	-0.0026	-0.0008	0.0006	0.0015
TracksOnly	0.0106	0.0058	0.0009	0.0012	0.0054	-0.0016
$\lvert cos\theta_T \rvert < 0.7$	0.0042	0.0039	0.0042	0.0020	0.0020	0.0023
$\sqrt{s'}$	-0.0011	-0.0002	-0.0027	-0.0011	-0.0013	0.0015
$\ln W_{QCD} > 0.0$	-0.0026	-0.0015	-0.0029	-0.0010	-0.0015	-0.0004
$\ln W_{QCD} > -0.8$	0.0019	0.0009	0.0021	0.0008	-0.0012	0.0016
$\ln L_{ql\nu} > 0.25$	0.0003	-0.0001	-0.0003	-0.0001	-0.0000	-0.0002
$\ln L_{ql\nu} > 0.75$	0.0002	0.0001	-0.0004	-0.0005	-0.0015	-0.0018
$\ln L_{qqqq} > 0.10$	-0.0010	-0.0027	-0.0017	-0.0036	-0.0014	-0.0024
$\ln L_{qqqq} > 0.40$	0.0008	-0.0006	0.0010	0.0000	0.0000	0.0005
Experimental Syst.	± 0.0118	± 0.0076	± 0.0070	± 0.0048	± 0.0064	± 0.0053
$b - 1s.d.$	-0.0001	-0.0001	-0.0001	0.0000	-0.0001	0.0001
$b + 1s.d.$	0.0006	0.0001	0.0015	0.0005	0.0009	0.0003
$Q_0 - 1s.d.$	0.0003	-0.0003	0.0002	-0.0001	0.0002	-0.0000
$Q_0 + 1s.d.$	-0.0000	0.0003	-0.0001	0.0001	0.0000	0.0004
$\sigma_q - 1s.d.$	0.0005	-0.0000	0.0015	0.0006	0.0009	0.0005
$\sigma_q + 1s.d.$	0.0002	-0.0001	0.0011	0.0004	0.0004	0.0004
udsc only	0.0004	-0.0000	0.0013	0.0005	0.0006	0.0004
Herwig5.9	-0.0000	0.0008	-0.0013	0.0001	-0.0010	-0.0006
Ariadne4.08	0.0016	0.0007	0.0016	0.0013	0.0015	0.0011
Total Hadronization.	± 0.0018	± 0.0012	± 0.0029	± 0.0015	± 0.0021	± 0.0015
$x_\mu = 0.5$	-0.0038	-0.0027	-0.0047	-0.0025	-0.0039	-0.0006
$x_\mu = 2.0$	0.0048	0.0037	0.0058	0.0035	0.0049	0.0030
Total error	+ 0.0141 − 0.0138	+ 0.0103 − 0.0099	+ 0.0117 − 0.0112	+ 0.0077 − 0.0073	+ 0.0107 − 0.0103	+ 0.0088 − 0.0083

Table 6.12: Result of fits for $\sqrt{s}$ =196GeV (Upper) and 200GeV (Lower)

	$(1-T)$	M_H	B_T	B_W	C	y_{23}^D
α_s(202GeV)	0.1186	0.1073	0.1123	0.1036	0.1063	0.1073
Statistical Error	± 0.0088	± 0.0079	± 0.0070	± 0.0063	± 0.0093	± 0.0088
Tracks + Clusters	-0.0043	-0.0023	-0.0001	-0.0027	-0.0005	0.0013
TracksOnly	-0.0047	0.0056	0.0011	0.0017	0.0045	0.0145
$\lvert cos\theta_T\rvert < 0.7$	-0.0017	-0.0014	-0.0001	0.0022	-0.0037	-0.0018
$\sqrt{s'}$	-0.0040	-0.0040	0.0003	-0.0013	-0.0014	0.0005
$\ln W_{QCD} > 0.0$	-0.0035	0.0008	-0.0012	0.0008	0.0067	0.0028
$\ln W_{QCD} > -0.8$	0.0000	-0.0008	0.0007	-0.0007	0.0002	0.0008
$\ln L_{ql\nu} > 0.25$	-0.0001	0.0001	-0.0001	0.0001	-0.0005	-0.0006
$\ln L_{qql\nu} > 0.75$	-0.0002	-0.0002	0.0001	-0.0001	0.0001	0.0001
$\ln L_{qqqq} > 0.10$	0.0048	0.0048	0.0041	0.0011	0.0165	0.0045
$\ln L_{qqqq} > 0.40$	-0.0005	-0.0015	-0.0009	-0.0022	-0.0013	-0.0022
Experimental Syst.	± 0.0087	± 0.0102	± 0.0045	± 0.0056	± 0.0189	± 0.0156
$b - 1s.d.$	-0.0001	-0.0002	-0.0001	-0.0002	-0.0000	-0.0000
$b + 1s.d.$	-0.0002	0.0000	-0.0009	-0.0005	-0.0003	-0.0008
$Q_0 - 1s.d.$	-0.0002	-0.0003	-0.0008	-0.0006	-0.0003	-0.0008
$Q_0 + 1s.d.$	-0.0001	0.0001	-0.0001	0.0000	-0.0000	0.0008
$\sigma_q - 1s.d.$	-0.0001	-0.0001	-0.0008	-0.0004	-0.0003	-0.0004
$\sigma_q + 1s.d.$	-0.0005	-0.0001	-0.0012	-0.0005	-0.0007	-0.0005
udsc only	0.0000	0.0000	0.0000	0.0000	0.0000	0.0000
Herwig5.9	-0.0003	0.0008	-0.0019	-0.0004	-0.0009	-0.0019
Ariadne4.08	0.0011	0.0005	0.0004	0.0006	0.0009	0.0007
Total Hadronization.	± 0.0012	± 0.0010	± 0.0024	± 0.0011	± 0.0015	± 0.0023
$x_\mu = 0.5$	-0.0054	-0.0034	-0.0052	-0.0030	-0.0043	-0.0004
$x_\mu = 2.0$	0.0068	0.0045	0.0063	0.0040	0.0053	0.0024
Total error	+ 0.0142 − 0.0136	+ 0.0137 − 0.0134	+ 0.0108 − 0.0101	+ 0.0094 − 0.0090	+ 0.0218 − 0.0216	+ 0.0182 − 0.0181

	$(1-T)$	M_H	B_T	B_W	C	y_{23}^D
α_s(205GeV)	0.1117	0.1058	0.1143	0.1043	0.1109	0.1204
Statistical Error	± 0.0043	± 0.0042	± 0.0038	± 0.0030	± 0.0049	± 0.0037
Tracks + Clusters	-0.0009	-0.0001	-0.0013	-0.0002	0.0009	0.0009
TracksOnly	0.0006	0.0016	-0.0008	-0.0003	0.0013	0.0002
$\lvert cos\theta_T\rvert < 0.7$	-0.0023	-0.0017	-0.0009	0.0003	-0.0037	-0.0021
$\sqrt{s'}$	-0.0013	-0.0014	-0.0012	-0.0014	-0.0013	-0.0002
$\ln W_{QCD} > 0.0$	0.0003	-0.0009	0.0013	-0.0006	0.0025	-0.0012
$\ln W_{QCD} > -0.8$	0.0001	0.0004	-0.0002	0.0002	-0.0006	0.0000
$\ln L_{qql\nu} > 0.25$	0.0001	-0.0001	0.0001	0.0001	0.0001	0.0001
$\ln L_{qql\nu} > 0.75$	-0.0003	0.0001	-0.0003	-0.0001	-0.0001	-0.0002
$\ln L_{qqqq} > 0.10$	0.0009	-0.0016	0.0019	-0.0006	-0.0017	-0.0002
$\ln L_{qqqq} > 0.40$	0.0001	0.0009	0.0002	0.0009	0.0014	0.0021
Experimental Syst.	± 0.0032	± 0.0034	± 0.0030	± 0.0018	± 0.0051	± 0.0034
$b - 1s.d.$	-0.0002	-0.0002	-0.0002	-0.0000	-0.0002	0.0002
$b + 1s.d.$	0.0002	0.0002	0.0002	0.0000	0.0001	-0.0000
$Q_0 - 1s.d.$	0.0001	-0.0002	0.0002	-0.0001	0.0001	-0.0000
$Q_0 + 1s.d.$	-0.0001	0.0002	-0.0002	0.0000	-0.0002	0.0005
$\sigma_q - 1s.d.$	0.0002	0.0001	0.0003	0.0001	0.0001	0.0003
$\sigma_q + 1s.d.$	-0.0003	-0.0001	-0.0002	-0.0001	-0.0003	0.0002
udsc only	0.0000	0.0000	0.0000	0.0000	0.0000	0.0000
Herwig5.9	-0.0006	0.0006	-0.0026	-0.0004	-0.0013	-0.0007
Ariadne4.08	0.0013	0.0007	0.0002	0.0007	0.0007	0.0008
Total Hadronization.	± 0.0014	± 0.0010	± 0.0026	± 0.0008	± 0.0015	± 0.0012
$x_\mu = 0.5$	-0.0044	-0.0029	-0.0052	-0.0027	-0.0047	-0.0006
$x_\mu = 2.0$	0.0055	0.0040	0.0064	0.0038	0.0059	0.0035
Total error	+ 0.0078 − 0.0071	+ 0.0068 − 0.0062	+ 0.0085 − 0.0076	+ 0.0052 − 0.0045	+ 0.0093 − 0.0087	+ 0.0062 − 0.0052

Table 6.13: Result of fits for $\sqrt{s}$ =202GeV (Upper) and 205GeV (Lower)

Chapter 7

Combination of Result of LEP1 and LEP2 Analysis

In this section, the combination of the results which are obtained in the LEP1 radiative hadronic event analysis and LEP2 analysis are presente.

At first, the values of α_s for all event shape variables are combined into one value for each energy sample. Since theoretical calculations have not been completed yet, QCD fits for each variable gives different estimations in principle. To get the best estimation of α_s, the results for all event shape variables are combined by the method described in Section 7.1. The combination is shown by solid downward arrows in Figure 7.1.

The energy dependence of α_s is compared with the solution of the renormalization group equation. Fitting the solution to α_s gives $\Lambda^{(5)}_{\overline{MS}}$, which is the fundamental constant of QCD and determines the energy dependence of the evolution of α_s. $\alpha_s(M_{\rm Z})$ can be obtained from the $\Lambda^{(5)}_{\overline{MS}}$. This procedure is shown by the right arrow written in the two dot-dashed line in Figure 7.1. This procedure is described in Section 7.2.

In order to look at the difference between event shape variables, the results from all energy samples are combined into one value for each variable. When the results are compared with results from other measurements, it is convenient to set the energy scale to $M_{\rm Z}$. Therefore, the values of α_s are evolved to the energy scale of $M_{\rm Z}$(the dashed right-arrow) before the combination for the energy sample (the dotted right-arrow). This

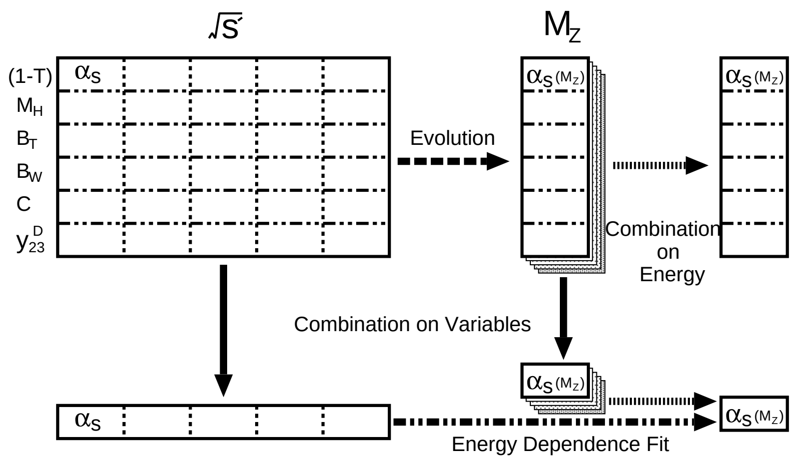

Figure 7.1: Procedure of the combination.

procedure is described in Section 7.3.

Finally, the values of α_s evolved to the energy scale of M_Z are combined for all variables and all energy samples. It is shown by the solid downward arrow and the dotted right-arrow. It should produce a similar value to that by fitting of the energy dependence.

7.1 Combination for All Variables

In order to account for the correlation between errors on α_s for each variable, values of α_s in fitting of the six event shape variables are combined into one value, $\hat{\alpha_s}$, by minimizing

$$\chi^2 = \sum_{i=1}^{6} \sum_{j=1}^{6} (\hat{\alpha_s} - \alpha_s^{(i)})(V^{-1})_{ij}(\hat{\alpha_s} - \alpha_s^{(j)}) \tag{7.1}$$

with respect to $\hat{\alpha_s}$, where V is the covariance matrix of the six individual measurements. The covariance matrix consists of covariance matrices for the statistical fluctuation, the experimental and hadronization systematic uncertainty.

The minimization is straightforward and leads to the following analytical formulas for $\overline{\alpha_s}$:

$$\overline{\alpha_s} = \frac{\sum_{i,j}(\alpha_s^{(i)} + \alpha_s^{(j)})(V)_{ij}}{2\sum_{i,j}(V_{ij})} \tag{7.2}$$

and its error $\Delta\overline{\alpha_s}$, where $W = \sum_{i,j}(V^{-1})_{i,j}$:

$$\Delta\overline{\alpha_s} = \frac{1}{W}\left(\sum_{l,k}\left(\sum_i (V^{-1})_{li}\right)\left(\sum_i (V^{-1}_{ki})\right) V_{l,k}\right)^{\frac{1}{2}} \tag{7.3}$$

The covariance matrix between the i'th and j'th variable for statistical fluctuations is the expected value of $(\alpha_s^{(i)} - \overline{\alpha_s})(\alpha_s^{(j)} - \overline{\alpha_s})$ for 100 Monte Carlo subsamples with the same number of events as selected data events. For the systematic uncertainties, the covariance matrix is obtained by

$$V_{ij} = \sum_{n=1}^{N_{\text{effect}}} (\alpha_s^{(i,n)} - \alpha_s^{(i,\text{standard})})(\alpha_s^{(j,n)} - \alpha_s^{(j,\text{standard})}), \tag{7.4}$$

where n counts the N_{effect} effects considered in the systematic uncertainty. $\alpha_s^{(i,n)}$ denotes the α_s values obtained from the i'th variable when considering the n'th effect. $\alpha_s^{(i,\text{standard})}$ denotes the value obtained from i'th variable in the standard analysis.

Since the correlation of the renormalization scale uncertainty between different variables and different energy samples is not well known, the renormalization scale uncertainty is accounted for by repeating the standard analysis and the analyses with the modifications considered in Section 5.4, but x_μ is changed to 0.5 and 2.0.

The result of the combination is shown in Table 7.1, Table 7.6, Table 7.2 and Table 7.7. Table 7.6 and Table 7.7 show results on the α_s evolved to the energy scale of M_Z.

The chi-square of combination in $\sqrt{s'} = 78.1$GeV of LEP1 analysis is larger relative to the number of degrees of freedom. It is caused by missing scale uncertainty in the chi-square calculation. When the scale uncertainty is included in the calculation, the chi-square reduces to 6.061. The large contributions to the chi-square without the scale uncertainty comes from y_{23}^D, and $(1-T)$. The increasing of x_μ makes the chi-square slightly smaller.

The combined values are close to the smallest value among α_s for all event shape variables. It seems to caused by that the full correlation between event shape variables is assumed in the definition of covariance matrix by Equation 7.4. Combined values for all variables when each systematic effects is not considered in the combination are shown in Figure 7.2, Figure 7.3, Figure 7.4 and Figure 7.5. "All Expt"("All Hadr") in the figures means a combined value when all experimental effects (hadronization effects) are not considered. The figures shows that the systematic uncertainty when `HERWIG` is used for hadroniztion corrections make the combined values smaller. At $\sqrt{s'}$ =78.1GeV and 57.6GeV, the systematic uncertainty when the tighter criteria on $|\cos\theta_T|$ is used make the combined value smaller, also.

$\sqrt{s'}$ [GeV]	78.1	71.8	65.1	57.6	49.0	38.5	24.4
$x_\mu = 1.0$							
$\alpha_s(\sqrt{s'})$	0.1090	0.1166	0.1157	0.1211	0.1323	0.1405	0.1473
χ^2/d.o.f	4.00/5	7.00/5	3.45/5	8.07/5	2.73/5	0.77/5	1.40/5
Total Error	0.0084	0.0071	0.0085	0.0114	0.0109	0.0143	0.0165
Stat. Error	0.0047	0.0048	0.0047	0.0061	0.0066	0.0081	0.0109
Expt. Error	0.0060	0.0033	0.0041	0.0073	0.0032	0.0057	0.0064
Hadr. Error	0.0035	0.0041	0.0058	0.0063	0.0080	0.0103	0.0107
$x_\mu = 0.5$							
$\alpha_s(\sqrt{s'})$	0.1041	0.1121	0.1118	0.1154	0.1242	0.1308	0.1365
χ^2/d.o.f	5.82/5	6.00/5	4.24/5	9.69/5	3.74/5	1.60/5	1.96/5
Total Error	0.0073	0.0060	0.0075	0.0098	0.0092	0.0119	0.0131
Stat. Error	0.0041	0.0042	0.0040	0.0051	0.0057	0.0071	0.0089
Expt. Error	0.0051	0.0025	0.0036	0.0064	0.0029	0.0049	0.0051
Hadr. Error	0.0032	0.0034	0.0053	0.0054	0.0066	0.0082	0.0081
$x_\mu = 2.0$							
$\alpha_s(\sqrt{s'})$	0.1139	0.1214	0.1207	0.1268	0.1409	0.1506	0.1596
χ^2/d.o.f	3.31/5	7.72/5	3.49/5	7.21/5	2.44/5	0.69/5	1.21/5
Total Error	0.0097	0.0085	0.0098	0.0134	0.0129	0.0171	0.0208
Stat. Error	0.0053	0.0056	0.0056	0.0074	0.0078	0.0098	0.0135
Expt. Error	0.0070	0.0043	0.0049	0.0084	0.0037	0.0068	0.0080
Hadr. Error	0.0040	0.0047	0.0065	0.0073	0.0096	0.0123	0.0137

Table 7.1: Combined values for all variables in each energy sample in LEP1 analysis.

$\sqrt{s'}$ [GeV]	188.6	191.6	195.5	199.5	201.6	205.9
$x_\mu = 1.0$						
$\alpha_s(\sqrt{s'})$	0.1074	0.1028	0.1032	0.1052	0.1086	0.1095
χ^2/d.o.f	11.53/5	5.37/5	2.47/5	3.19/5	1.85/5	11.87/5
Total Error	0.0024	0.0065	0.0043	0.0059	0.0065	0.0031
Stat. Error	0.0020	0.0051	0.0032	0.0039	0.0051	0.0024
Expt. Error	0.0011	0.0039	0.0026	0.0041	0.0037	0.0017
Hadr. Error	0.0009	0.0010	0.0013	0.0014	0.0016	0.0010
$x_\mu = 0.5$						
$\alpha_s(\sqrt{s'})$	0.1041	0.1005	0.1001	0.1025	0.1046	0.1061
χ^2/d.o.f	14.37/5	6.76/5	2.80/5	4.01/5	2.10/5	16.64/5
Total Error	0.0022	0.0060	0.0039	0.0054	0.0057	0.0028
Stat. Error	0.0018	0.0046	0.0029	0.0035	0.0045	0.0021
Expt. Error	0.0009	0.0038	0.0023	0.0038	0.0032	0.0015
Hadr. Error	0.0008	0.0009	0.0012	0.0014	0.0015	0.0010
$x_\mu = 2.0$						
$\alpha_s(\sqrt{s'})$	0.1116	0.1059	0.1072	0.1088	0.1134	0.1138
χ^2/d.o.f	11.00/5	4.69/5	2.41/5	2.85/5	1.83/5	9.90/5
Total Error	0.0027	0.0072	0.0049	0.0065	0.0074	0.0035
Stat. Error	0.0022	0.0057	0.0037	0.0044	0.0058	0.0027
Expt. Error	0.0012	0.0043	0.0029	0.0045	0.0042	0.0020
Hadr. Error	0.0010	0.0011	0.0014	0.0015	0.0018	0.0012

Table 7.2: Combined values for all variables in each energy sample in LEP2 analysis.

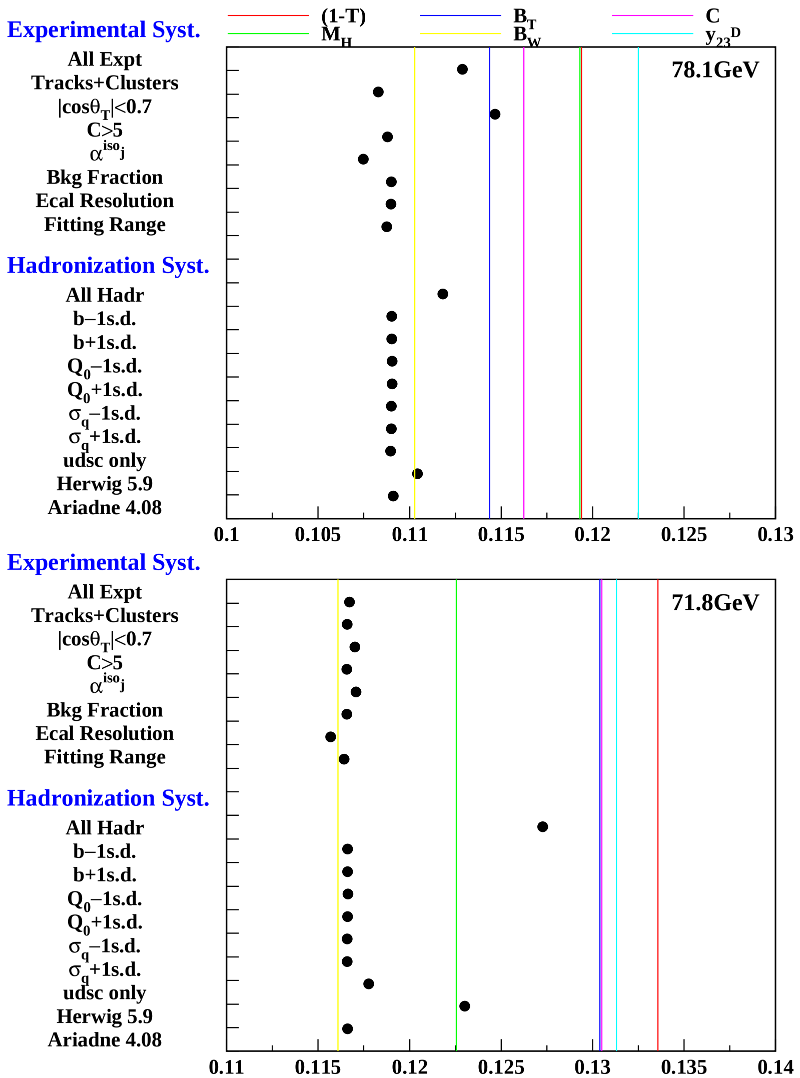

Figure 7.2: Combined values for all variables when each systematic effects is not considered in the combination. $\sqrt{s'}$ =78.1GeV and 71.8GeV

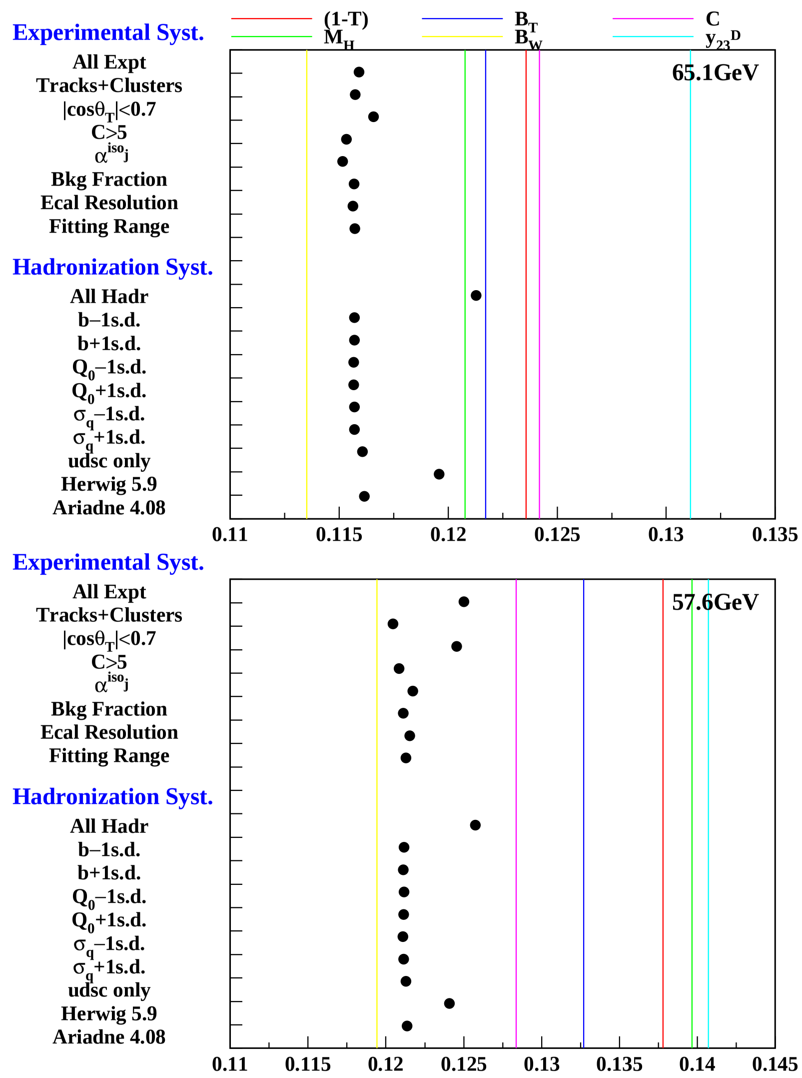

Figure 7.3: Combined values for all variables when each systematic effects is not considered in the combination. $\sqrt{s'}$ =65.1GeV and 57.6GeV

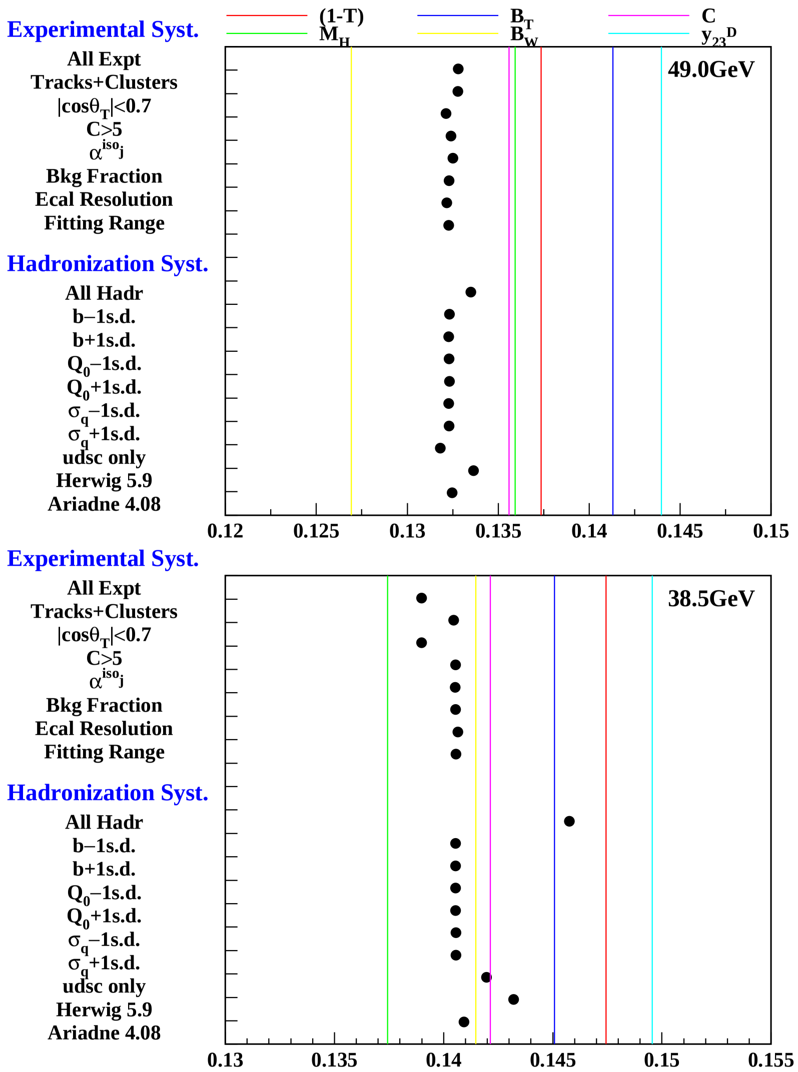

Figure 7.4: Combined values for all variables when each systematic effects is not considered in the combination. $\sqrt{s'}$ =49.0GeV and 38.5GeV

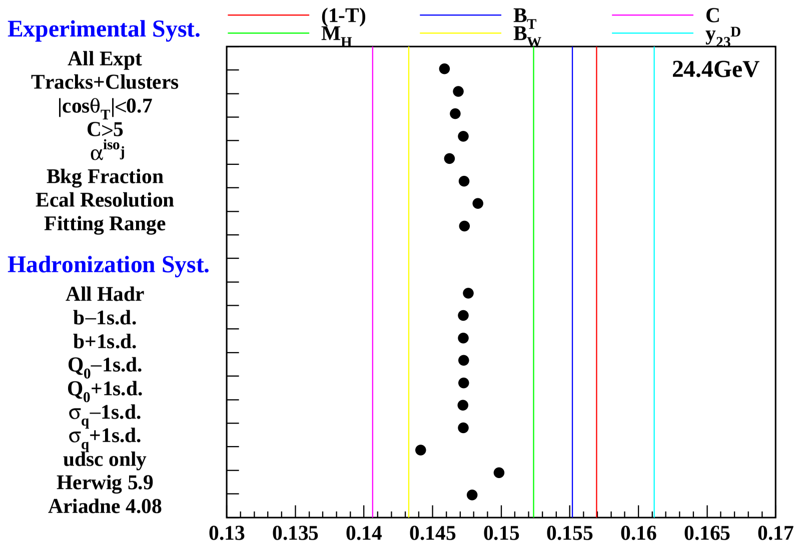

Figure 7.5: Combined values for all variables when each systematic effects is not considered in the combination. $\sqrt{s'}$ =24.4GeV

7.2 Energy Dependence of α_s

Values of α_s for each event shape variable and for combined values of the variables (Table 7.1 and Table 7.1) are fitted to the solution of the renormalization group equation at NNLO described in Equation 2.26. The fundamental constant $\Lambda^{(5)}_{\overline{MS}}$ is treated as a free parameter in the fit. The covariance matrix for the different energy samples is constructed with the following assumptions.

There is no statistical correlation between errors in the different energy samples. For experimental uncertainty and hadronization uncertainty, the "minimum overlap" correlation is assumed for errors in different energy samples. The minimum overlap assumption means that the covariance matrix

$$V_{ij} = \min(\sigma_i^2, \sigma_j^2), \tag{7.5}$$

is used instead of $\sigma_i \times \sigma_j$, where σ_i is the error on the result from i'th energy sample. The LEP QCD working group is using this assumption for the combination of results from all LEP experiments. According to the report by the LEP QCD working group [160], The reason to use the assumption is that fully-correlated errors make the result unstable.

The fitting is performed with the covariance matrix for covariance matrices for the statistical error, the experimental uncertainty and the hadronization uncertainty. The theoretical uncertainties of $\Lambda^{(5)}_{\overline{MS}}$ are obtained by repeating the fitting with α_s and the covariance matrix for $x_\mu = 0.5$ and $x_\mu = 2.0$. The theoretical uncertainty is assigned as an asymmetric error.

The values of $\Lambda^{(5)}_{\overline{MS}}$ from fitting the energy dependence and the corresponding α_s values are shown in Table 7.3, Table 7.4 and Table 7.5, which are for the fitting with results from only LEP1 analysis, only LEP2 analysis, and LEP1 and LEP2 analysis, respectively. (The fitted energy dependences corresponding to each result are shown in Figure 7.7,Figure 7.9 and Figure 7.11. The fitted energy dependences for individual event shape variables are shown in Figure 7.6, Figure 7.8 and Figure 7.10)

The value of $\Lambda^{(5)}_{\overline{MS}}$ derived from the values of α_s combining the event shape variables is

$$\Lambda^{(5)}_{\overline{MS}} = 0.2242 \pm 0.031(\text{stat.} + \text{expt.} + \text{hadr.})^{+0.072}_{-0.048}(\text{scale.})\ \text{GeV}\ \ (\chi^2/\text{d.o.f} = 8.3/12). \tag{7.6}$$

This value and its total errors correspond to $\alpha_s(M_Z) = 0.119^{+0.0058}_{-0.0050}$ in NNLO. The QCD prediction of α_s with $\Lambda^{(5)}_{\overline{MS}}$ obtained by the fitting is shown in Figure 7.11. The subsample with $\sqrt{s'} = 38.5$ GeV dominantly contributes to the χ^2 value in these fittings. The total errors on combined $\Lambda^{(5)}_{\overline{MS}}$ in fitting for LEP1 and LEP2 analyses are slightly reduced comparing to that in fitting only for LEP2 analysis.

The α_s converted from $\Lambda^{(5)}_{\overline{MS}}$ for LEP1 analysis is slightly lower than that for only LEP2 analysis or LEP1 and LEP2 analysis. The difference seems to be due to the difference of energy dependence of B_W and C between LEP1 and LEP2 analysis and the stronger correlation between variables.

	$(1-T)$	M_H	B_T	B_W	C	y_{23}^D	Combined
$\Lambda_{\overline{MS}}^{(5)}$[GeV]	0.2785	0.2133	0.2802	0.1363	0.2362	0.3094	0.1474
Stat.+Expt.+Hadr.	0.1155	0.0895	0.1158	0.0531	0.1182	0.1742	0.0512
χ^2/d.o.f	2.5/6	1.4/6	4.5/6	1.6/6	2.5/6	0.9/6	2.7/6
Total Error	-0.1369	-0.1002	-0.1394	-0.0594	-0.1358	-0.1750	-0.0632
	0.1639	0.1158	0.1657	0.0696	0.1562	0.1875	0.0728
$\alpha_s(M_Z)$	0.1234	0.1184	0.1235	0.1109	0.1203	0.1255	0.1121
Total Error	0.0102	0.0087	0.0103	0.0072	0.0107	0.0106	0.0071
	-0.0112	-0.0099	-0.0113	-0.0080	-0.0130	-0.0148	-0.0078

Table 7.3: Result of fitting of energy dependence for LEP1 radiative events.

	$(1-T)$	M_H	B_T	B_W	C	y_{23}^D	Combined
$\Lambda_{\overline{MS}}^{(5)}$[GeV]	0.3251	0.1990	0.2862	0.1693	0.2372	0.4319	0.2309
Stat.+Expt.+Hadr.	0.0721	0.0428	0.0767	0.0350	0.0698	0.1050	0.0323
χ^2/d.o.f	1.2/6	0.7/6	2.9/6	1.8/6	1.0/6	2.4/6	3.5/6
Total Error	-0.1089	-0.0571	-0.1086	-0.0459	-0.0932	-0.1058	-0.0572
	0.1477	0.0755	0.1435	0.0609	0.1194	0.1338	0.0791
$\alpha_s(M_Z)$	0.1265	0.1172	0.1239	0.1144	0.1204	0.1326	0.1199
Total Error	0.0084	0.0061	0.0089	0.0055	0.0084	0.0066	0.0058
	-0.0075	-0.0055	-0.0083	-0.0049	-0.0081	-0.0061	-0.0049

Table 7.4: Result of fitting of energy dependence for LEP2 data.

	$(1-T)$	M_H	B_T	B_W	C	y_{23}^D	Combined
$\Lambda_{\overline{MS}}^{(5)}$[GeV]	0.3198	0.2041	0.2977	0.1672	0.2380	0.4279	0.2242
Stat.+Expt.+Hadr.	0.0678	0.0424	0.0750	0.0335	0.0644	0.1017	0.0309
χ^2/d.o.f	3.8/11	2.1/11	7.7/11	3.5/11	3.7/11	3.1/11	8.3/11
Total Error	-0.1056	-0.0580	-0.1092	-0.0450	-0.0897	-0.1025	-0.0569
	0.1447	0.0773	0.1444	0.0606	0.1168	0.1315	0.0780
$\alpha_s(M_Z)$	0.1262	0.1176	0.1247	0.1142	0.1204	0.1324	0.1193
Total Error	0.0083	0.0061	0.0087	0.0055	0.0082	0.0065	0.0058
	-0.0074	-0.0054	-0.0081	-0.0048	-0.0078	-0.0059	-0.0050

Table 7.5: Result of fitting of energy dependence for LEP1 radiative events and LEP2 data.

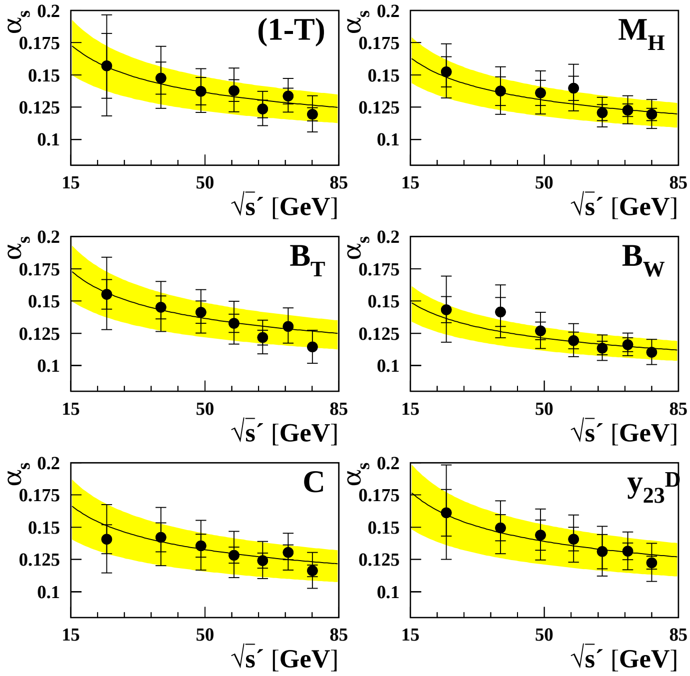

Figure 7.6: Energy dependence of α_s obtained by the analysis with LEP1 radiative events.

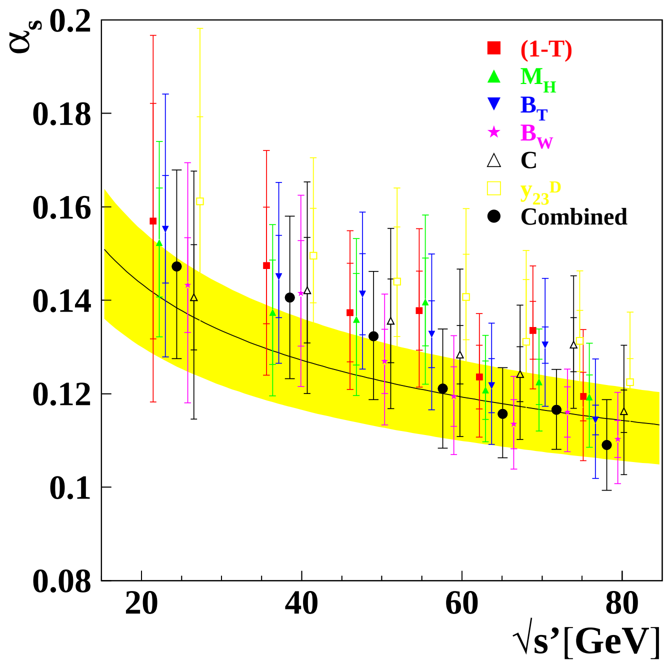

Figure 7.7: Energy dependence of α_s obtained by the analysis with LEP1 radiative events. The values of α_s which are combined for all event shape variables are shown.

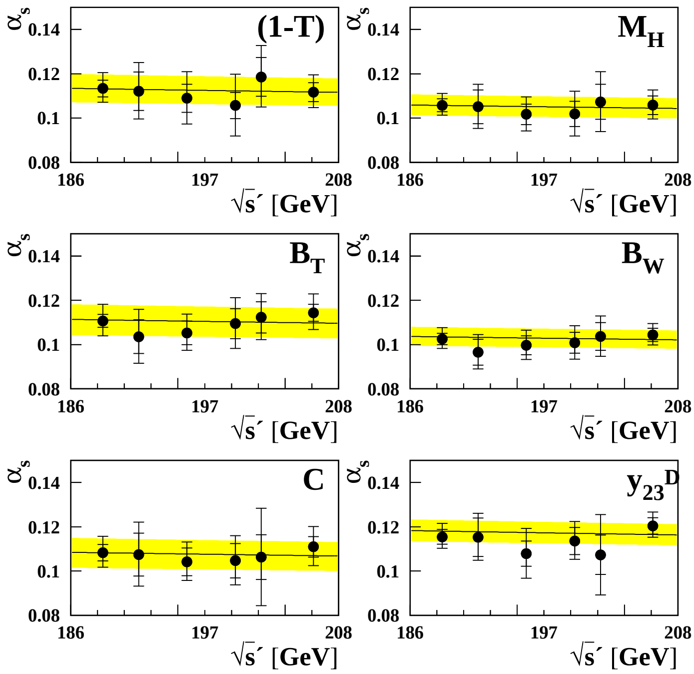

Figure 7.8: Energy dependence of α_s obtained by the analysis with LEP2 non-radiative events.

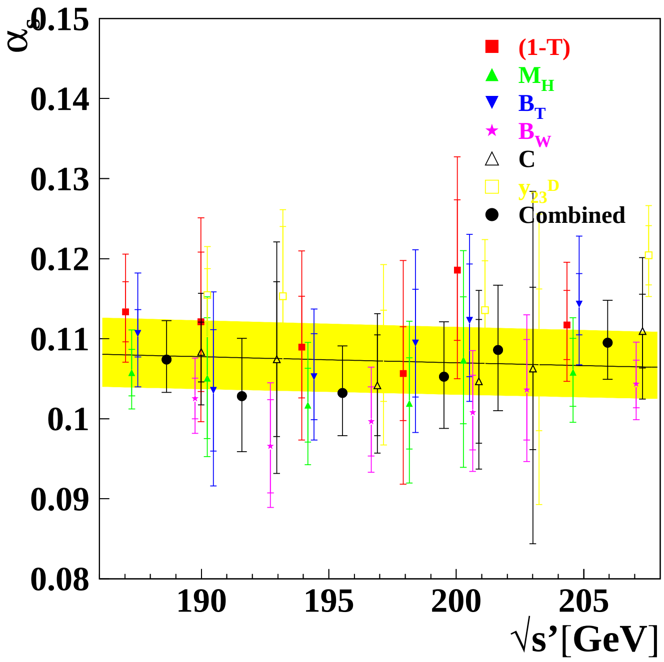

Figure 7.9: Energy dependence of α_s obtained by the analysis with LEP2 non-radiative events. The values of α_s which are combined for all event shape variables are shown.

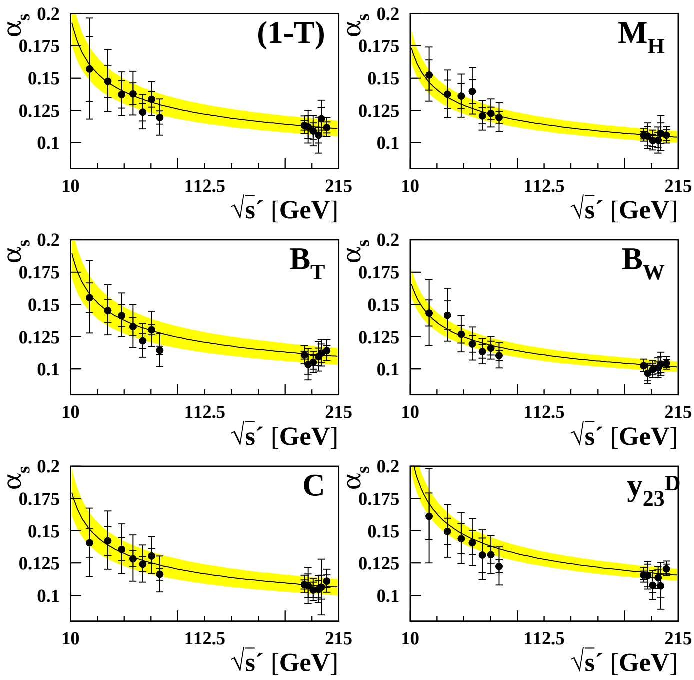

Figure 7.10: Energy dependence of α_s obtained by the analysis with LEP1 radiative events and LEP2 non-radiative events.

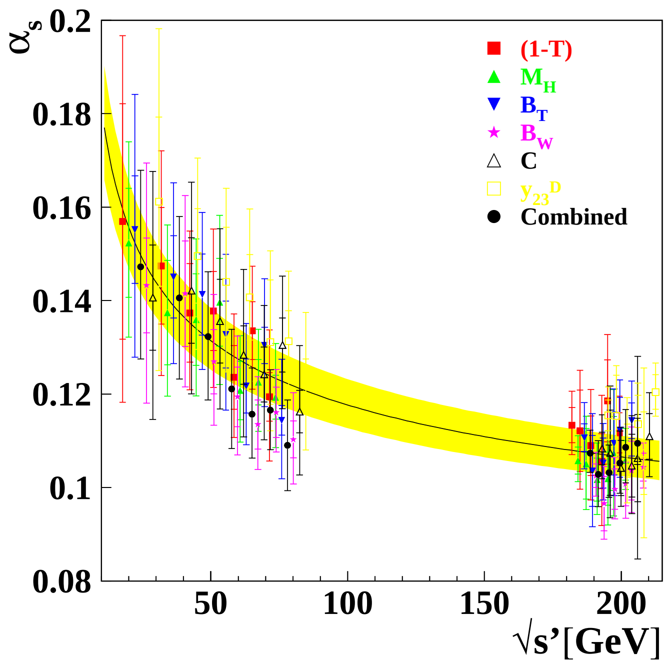

Figure 7.11: Energy dependence of α_s obtained by the analysis with LEP1 radiative events and LEP2 non-radiative events. The values of α_s which are combined for all event shape variables are shown.

7.3 Combination of α_s

All values of α_s are propagated to the energy scale of M_{Z} using Equation 2.20 for the evolution of α_s. The values of $\alpha_s(M_{\mathrm{Z}})$ and their statistical and systematic uncertainties are listed in Table 7.6 and Table 7.7. The combination is carried out using the covariance matrix, which is constructed from the uncertainties on the assumption described in Section 7.2. The α_s which is combined for all variables and all energy subsamples are obtained by applying same procedures for the values of $\alpha_s(M_{\mathrm{Z}})$ combined for all variables.

The combined value, $\hat{\alpha_s}$, and its error $\Delta\hat{\alpha_s}$ is simply calculated with the weights w_i obtained by the method of least squares with the covariance matrix V_{ij}.

$$\hat{\alpha_s} = \sum_i w_i \alpha_s^{(i)}, \qquad \Delta\hat{\alpha_s} = \sum_{i,j} w_i V_{ij} w_j. \tag{7.7}$$

where w_i is the weight of the i'th result and is defined by

$$w_i = \frac{\sum_j (V^{-1})_{ij}}{\sum_{kl} (V^{-1})_{kl}}. \tag{7.8}$$

The statistical error, the experimental and the hadronization uncertainty for the combined value are calculated by replacing the covariance matrix which is used in the Equations 7.7 by the covariance matrix for each uncertainty.

The combined values are shown in Table 7.8, Table 7.9 and Table 7.10. Previous results using non-radiative events and the world average value of α_s from the PDG are shown for comparison in Figure 7.12, Figure 7.13 and Figure 7.14. These other values are consistent with each other and in good agreement with the present result. As pointed out in the analysis with non-radiative events at LEP1 [53] and LEP2 [32, 33, 54], the α_s value obtained by fitting B_W is lower than for the other three variables [1].

The combined value of $\alpha_s(M_{\mathrm{Z}})$ for all energy samples and all event shape variables is

$$\alpha_s(M_{\mathrm{Z}}) = 0.1193 \pm 0.0017(\mathrm{stat.})^{+0.0055}_{-0.0046}(\mathrm{syst.}). \tag{7.9}$$

The systematic uncertainty has contributions from experimental effects (± 0.0015), hadronization effects (± 0.0012) and variations of renormalization scale ($+0.0052, -0.0042$). This value is consistent with the result from the analysis using non-radiative events in LEP1 data, $\alpha_s(M_{\mathrm{Z}}) = 0.120 \pm 0.006$. More event shape variables have been fitted for the non-radiative events. When the variables are restricted to the same set (i.e. $(1-T)$,M_H,B_T and y_{23}^D) used in the present analysis, the combined value evaluated from the non-radiative events by the procedure described in Section 7.1 is $\alpha_s(M_{\mathrm{Z}}) = 0.1155^{+0.0071}_{-0.0060}$.

[1] The B_T and B_W calculation by Catani, Turnock and Webber [37] is used in our previous measurements [32, 33, 53, 54]. The calculation by Dokshitzer, Lucenti, Marchesini and Salam [36] treats the quark recoil properly and is used in this analysis. The comparison with our previous results is not trivial because a different calculation is used in this analysis.

$\sqrt{s'}$ [GeV]	78.1	71.8	65.1	57.6	49.0	38.5	24.4
$x_\mu = 1.0$							
$\alpha_s(M_Z)$	0.1068	0.1127	0.1104	0.1141	0.1201	0.1218	0.1184
χ^2/d.o.f	4.03/5	7.05/5	3.53/5	8.19/5	2.71/5	0.77/5	1.35/5
Total Error	0.0080	0.0066	0.0077	0.0099	0.0089	0.0107	0.0106
Stat. Error	0.0044	0.0045	0.0042	0.0052	0.0053	0.0060	0.0069
Expt. Error	0.0057	0.0031	0.0037	0.0064	0.0026	0.0042	0.0040
Hadr. Error	0.0034	0.0038	0.0053	0.0055	0.0066	0.0078	0.0069
$x_\mu = 0.5$							
$\alpha_s(M_Z)$	0.1022	0.1085	0.1070	0.1090	0.1134	0.1146	0.1115
χ^2/d.o.f	5.86/5	6.04/5	4.28/5	9.85/5	3.76/5	1.64/5	1.94/5
Total Error	0.0070	0.0056	0.0068	0.0086	0.0076	0.0091	0.0087
Stat. Error	0.0039	0.0039	0.0035	0.0044	0.0047	0.0053	0.0058
Expt. Error	0.0050	0.0023	0.0033	0.0056	0.0024	0.0037	0.0034
Hadr. Error	0.0030	0.0032	0.0048	0.0048	0.0055	0.0064	0.0054
$x_\mu = 2.0$							
$\alpha_s(M_Z)$	0.1115	0.1173	0.1149	0.1192	0.1271	0.1292	0.1261
χ^2/d.o.f	3.34/5	7.81/5	3.57/5	7.36/5	2.42/5	0.68/5	1.15/5
Total Error	0.0092	0.0078	0.0088	0.0115	0.0104	0.0126	0.0128
Stat. Error	0.0051	0.0051	0.0050	0.0062	0.0062	0.0071	0.0083
Expt. Error	0.0067	0.0040	0.0044	0.0073	0.0030	0.0048	0.0048
Hadr. Error	0.0038	0.0044	0.0059	0.0063	0.0078	0.0092	0.0084

Table 7.6: Combined values for all variables in each energy samples. α_s is evolved to the energy scale of M_Z

$\sqrt{s'}$ [GeV]	188.6	191.6	195.5	199.5	201.6	205.9
$x_\mu = 1.0$						
$\alpha_s(M_Z)$	0.1191	0.1134	0.1146	0.1172	0.1218	0.1232
χ^2/d.o.f	11.41/5	5.22/5	2.41/5	3.12/5	1.85/5	11.70/5
Total Error	0.0030	0.0081	0.0054	0.0074	0.0082	0.0040
Stat. Error	0.0024	0.0063	0.0040	0.0050	0.0064	0.0030
Expt. Error	0.0013	0.0049	0.0032	0.0052	0.0047	0.0022
Hadr. Error	0.0011	0.0012	0.0016	0.0018	0.0021	0.0013
$x_\mu = 0.5$						
$\alpha_s(M_Z)$	0.1150	0.1104	0.1107	0.1138	0.1168	0.1189
χ^2/d.o.f	14.05/5	6.56/5	2.73/5	3.90/5	2.09/5	16.25/5
Total Error	0.0027	0.0074	0.0048	0.0067	0.0072	0.0035
Stat. Error	0.0022	0.0057	0.0036	0.0044	0.0056	0.0027
Expt. Error	0.0012	0.0046	0.0028	0.0048	0.0041	0.0019
Hadr. Error	0.0010	0.0011	0.0015	0.0017	0.0018	0.0012
$x_\mu = 2.0$						
$\alpha_s(M_Z)$	0.1243	0.1171	0.1195	0.1216	0.1279	0.1287
χ^2/d.o.f	10.92/5	4.55/5	2.35/5	2.78/5	1.83/5	9.78/5
Total Error	0.0034	0.0091	0.0062	0.0083	0.0095	0.0046
Stat. Error	0.0028	0.0072	0.0046	0.0057	0.0074	0.0035
Expt. Error	0.0015	0.0053	0.0037	0.0058	0.0055	0.0025
Hadr. Error	0.0013	0.0013	0.0018	0.0019	0.0023	0.0015

Table 7.7: Combined values for all variables in each energy samples. α_s is evolved to the energy scale of M_Z

	$(1-T)$	M_H	B_T	B_W	C	y_{23}^D	Combined
$\alpha_s(M_Z)$	0.1232	0.1185	0.1227	0.1103	0.1207	0.1250	0.1119
χ^2/dof	2.45/6	1.53/6	4.77/6	1.83/6	2.56/6	0.98/6	3.02/6
Stat. Error	0.0030	0.0025	0.0030	0.0027	0.0031	0.0031	0.0026
Expt. Error	0.0048	0.0055	0.0032	0.0030	0.0030	0.0050	0.0032
Hadr. Error	0.0061	0.0048	0.0070	0.0046	0.0087	0.0105	0.0038
Stat.+Expt.+Hadr.	0.0083	0.0077	0.0083	0.0062	0.0097	0.0121	0.0056
$x_\mu = 0.5$	-0.0057	-0.0040	-0.0061	-0.0032	-0.0058	-0.0011	-0.0044
$x_\mu = 2.0$	0.0072	0.0055	0.0075	0.0046	0.0072	0.0041	0.0050

Table 7.8: Combined value of α_s for all $\sqrt{s'}$ samples in the analysis with LEP1 radiative events.

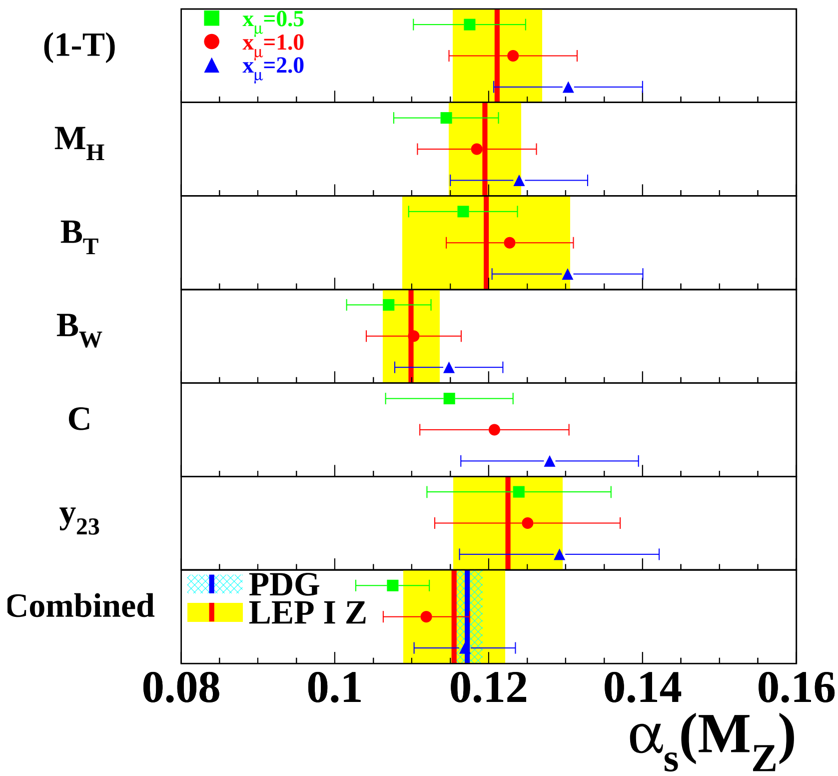

Figure 7.12: Combined value of α_s for all $\sqrt{s'}$ samples in the analysis with LEP1 radiative events.

	$(1-T)$	M_H	B_T	B_W	C	y_{23}^D	Combined
$\alpha_s(M_Z)$	0.1265	0.1172	0.1239	0.1144	0.1204	0.1325	0.1196
χ^2/dof	1.24/5	0.67/5	2.89/5	1.74/5	1.01/5	2.43/5	3.38/5
Stat. Error	0.0034	0.0028	0.0026	0.0021	0.0033	0.0029	0.0017
Expt. Error	0.0026	0.0023	0.0037	0.0025	0.0040	0.0046	0.0015
Hadr. Error	0.0016	0.0013	0.0028	0.0011	0.0018	0.0013	0.0012
Stat.+Expt.+Hadr.	0.0046	0.0038	0.0053	0.0035	0.0055	0.0056	0.0026
$x_\mu = 0.5$	-0.0057	-0.0036	-0.0059	-0.0031	-0.0053	-0.0006	-0.0041
$x_\mu = 2.0$	0.0073	0.0050	0.0074	0.0045	0.0067	0.0041	0.0052

Table 7.9: Combined value of α_s for all E_{CM} samples in the analysis with LEP2 non-radiative events.

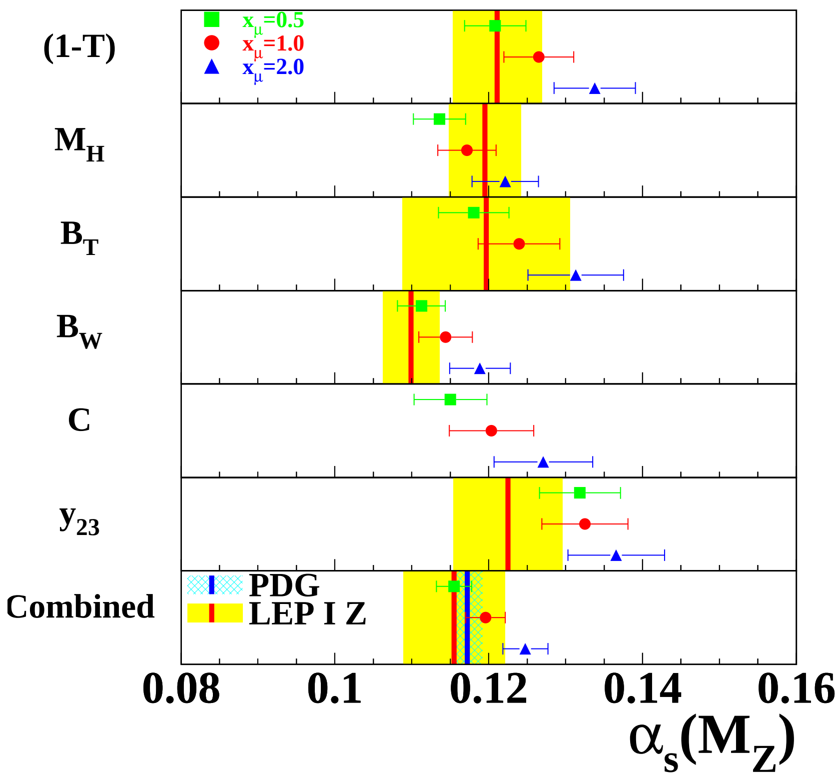

Figure 7.13: Combined value of α_s for all E_{CM} samples in the analysis with LEP2 non-radiative events.

	$(1-T)$	M_H	B_T	B_W	C	y_{23}^D	Combined
$\alpha_s(M_Z)$	0.1264	0.1172	0.1256	0.1140	0.1210	0.1323	0.1193
χ^2/dof	4.12/12	2.74/12	8.35/12	3.83/12	4.18/12	3.39/12	8.48/12
Stat. Error	0.0031	0.0027	0.0024	0.0020	0.0030	0.0027	0.0017
Expt. Error	0.0026	0.0023	0.0033	0.0025	0.0032	0.0046	0.0015
Hadr. Error	0.0018	0.0013	0.0030	0.0012	0.0021	0.0015	0.0012
Stat.+Expt.+Hadr.	0.0044	0.0038	0.0051	0.0034	0.0049	0.0055	0.0026
$x_\mu = 0.5$	-0.0057	-0.0036	-0.0060	-0.0032	-0.0055	-0.0006	-0.0042
$x_\mu = 2.0$	0.0073	0.0050	0.0075	0.0046	0.0068	0.0040	0.0052

Table 7.10: Combined value of α_s for all E_{CM} samples in the analysis with LEP1 radiative events and the analysis with LEP2 non-radiative events.

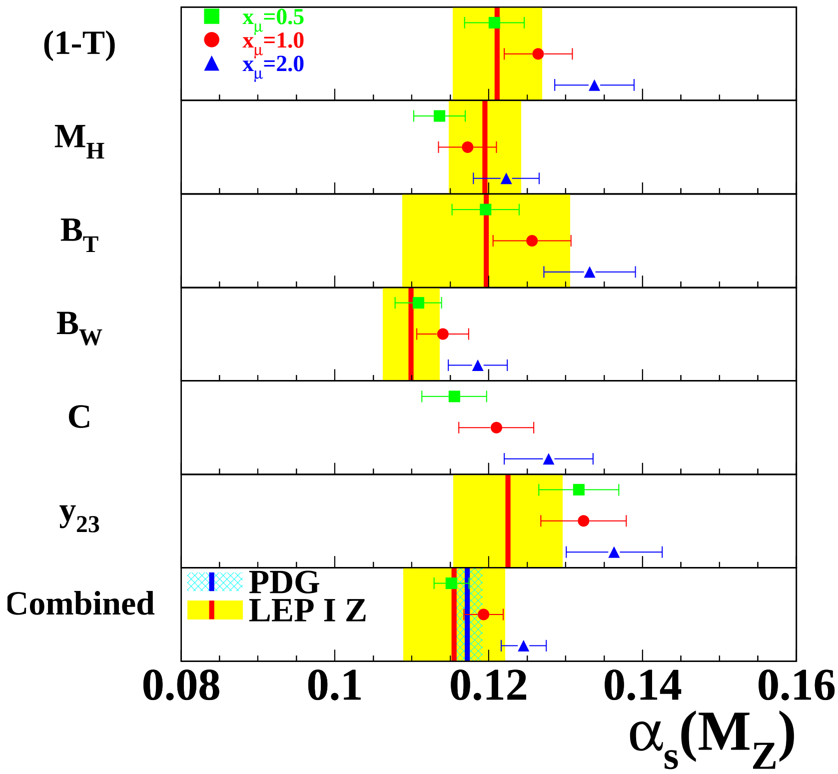

Figure 7.14: Combined value of α_s for all E_{CM} samples in the analysis with LEP1 radiative events and the analysis with LEP2 non-radiative events.

Chapter 8

Discussion

As mentioned in Section 2.3.3, α_s is determined by various method and compared by converting to $\alpha_s(M_{\mathrm{Z}})$. The values of $\alpha_s(M_{\mathrm{Z}})$ obtained from the analysis described in Section 5 and Section 6 are compared with results from similar analyses using event shape variables of radiative multi-hadronic events in Section 8.1. In Section 8.2, the result obtained from this study is compared with the results obtained from the other α_s measurements using event shape variables.

8.1 Comparison with α_s Measurements with Radiative multi-hadronic events

8.1.1 α_s Measurement by Fitting of Event Shape Variables

α_s measurement with radiative events has been performed by L3 Collaboration [124]. They determine α_s for four event shape variables, $(1-T)$,M_H,B_T,B_W using 3.6 million hadronic events. In the L3 analysis, the isolated electromagnetic calorimeter clusters with energy larger than 5GeV are selected from multi-hadronic events. In addition to the isolation cuts, a cut on the shower shape discriminator is applied to the isolated clusters. The isolation cuts include a cut on the energy deposit in the local isolation cone around the cluster, and a cut on the angle of the nearest jet. The shower shape discrimination is based on an artificial neural network and is used to distinguish multi-photon showers from single-photon showers in the electromagnetic calorimeter. Therefore, event selection is similar with this analysis. Numbers of selected events and background fractions are shown in Table 8.1. The results from multiple energy samples are merged according to the range of $\sqrt{s'}$ used in the L3 analysis. The background fraction is average weighted by a number of selected events. Although the number of selected events in this analysis is equal or smaller than that in the L3 analysis, the backgrounds are much smaller than the L3 analysis.

	$\sqrt{s'}$ [GeV]	Statistics	Background [%]		
			MH	$\tau\tau$	$\gamma\gamma$
L3	41.4(30-50)	1247	29.3	2.0	0.2
OPAL	49.0,38.5,24.4	1119	17.1	0.7	0.0
L3	55.3(50-60)	1047	19.2	2.6	0.2
OPAL	57.6	512	10.2	1.1	0.0
L3	65.4(60-70)	1575	11.6	2.3	0.1
OPAL	65.1	696	7.8	1.1	0.0
L3	75.7(70-80)	2938	9.0	1.7	0.0
OPAL	78.1,71.8	2524	7.4	1.1	0.1

Table 8.1: Results of event selection. Results from this analysis are shown for comparison.

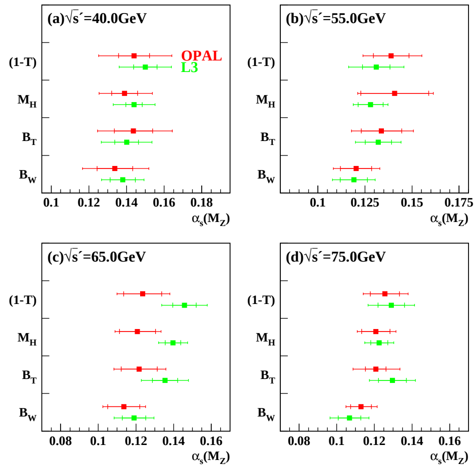

Figure 8.1: $\alpha_s(M_Z)$ in this analysis and L3 analysis.

The values of α_s in this analysis and the L3 analysis are shown in Figure 8.1. The values of α_s in this analysis are evolved to the energy scale shown in the column "Reference" in Table 8.1 and combined with the procedure in Section 7.3. Since results for each variable are shown only for $\sqrt{s'} = 50 - 60$GeV and $\sqrt{s'} = 84 - 66$GeV in [124], the results in the internal note [161] are compared. Though deviations can be seen in the $\sqrt{s'} = 65$GeV sample, results from L3 analysis and this study are consistent within their errors for all energy samples. The total errors of results from this analysis is comparable with those from the L3 analysis for all energy samples except the sample with $\sqrt{s'} = 40$GeV. The difference in total error for the sample comes from the experimental and hadronization uncertainty.

α_s Measurement using Power Corrections Recently, the DELPHI collaboration reports a study of the energy evolution of event shape distributions and their means [128]. In addition to non-radiative multi-hadronic events, radiative multi-hadronic events with a observed high energy photon are used for extracting α_s. The radiative events are divided into three subsamples corresponding to a mean center-of-mass energy of 76,66 and 45GeV. Numbers of selected events and purity in the radiative multi-hadronic events selection are listed in Table 8.2.

E_{CM} [GeV]	N_{sel}	Purity [%]
76.3	1212	87.6
66.0	1099	91.3
45.2	650	84.2

Table 8.2: Mean center of mass energy and number of selected events and purity in the analysis with radiative hadronic events by DELPHI.

They extract α_s from differential distributions and mean values of hadron level event shape variables for multiple energy samples by using the power correction model instead of the hadronization correction factor. In event shape distributions, the effect of the power corrections shifts the perturbative spectra to larger values.

$$\frac{1}{\sigma}\frac{d\sigma^{corrected}(x)}{dx} = \frac{1}{\sigma}\frac{d\sigma^{pert}(x-\delta x)}{dx} \quad , \delta x = a_x \mathcal{P} \tag{8.1}$$

with

$$\mathcal{P} = \frac{4C_F}{\pi^2}\mathcal{M}\frac{\mu_I}{Q}\left[\alpha_0(\mu_I) - \alpha_s(Q) - \frac{\beta_0}{2\pi}\left(\ln\frac{Q}{\mu_I} + \frac{K}{\beta_0} + 1\right)\alpha_s^2(Q)\right], \tag{8.2}$$

where

$$\mathcal{M} = 1 + \frac{2.437C_A - 0.052n_f}{\beta_0}, K = C_A\left(\frac{67}{18} - \frac{\pi^2}{6}\right) - \frac{5}{9}n_f. \tag{8.3}$$

a_x is an observable dependent constant and given in [162–166]. α_0 is a non-perturbative parameter accounting for the contributions to the event shape below an infrared matching scale μ_I.

Fits of event shape variables are performed with $\alpha_s(M_\mathrm{Z})$ and α_0 as free parameters. for $(1-T)$, M_H, B_T and B_W and C at the center-of-mass energies between 45GeV and 202 GeV. They obtain weighted and an unweighted mean of the values of $\alpha_s(M_\mathrm{Z})$ and α_0 for these variables. In case of the extraction from differential event shape distribution, the unweighed mean values are

$$\alpha_s(M_\mathrm{Z}) = 0.1110 \pm 0.0055 \pm 0.0007 - 0.0008 \text{ and } \alpha_0 = 0.559 \pm 0.073 \pm 0.009 + 0.013,$$

where the first error on each measurement is statistical uncertainty and the second error is systematic uncertainty. The third error is the difference between the $\ln R$ matching scheme and the R matching scheme.

L3 collaboration performs unweighted mean of values of α_s obtained by using the power correction model [29]. Results for $(1-T)$,M_H, B_T, B_W and C are included in the mean. The center-of-mass energies of data are between 30GeV and 189 GeV. They are

$$\alpha_s(M_\mathrm{Z}) = 0.1110 \pm 0.0045 \pm 0.0034 \text{ and } \alpha_0 = 0.537 \pm 0.070 \pm 0.021,$$

where the first error on each measurement is experimental (it is corresponds to statistical error and experimental uncertainty in this analysis). The second error is theoretical, which is estimated by varying the renormalization scale factor between 0.5 and 2.0 (± 0.0033 for $\alpha_s(M_\mathrm{Z})$,± 0.021 for α_0) and varying μ_I between 1GeV and 3GeV(0.0010 for $\alpha_s(M_\mathrm{Z})$).

In the case of this analysis, the fitting of the energy dependence of the unweighted mean of $\alpha_s(M_\mathrm{Z})$ for the same variables as L3 and DELPHI gives $\Lambda^{(5)}_{\overline{MS}} = 0.2026^{+0.0857}_{-0.0592}$, where the errors includes the statistical, experimental, hadronization and renormalization scale uncertainties. The fit gives $\chi^2 = 11.5$ for 13 degrees of freedom. The value of $\Lambda^{(5)}_{\overline{MS}}$ is converted to

$$\alpha_s(M_\mathrm{Z}) = 0.1167^{+0.0055}_{-0.0044}.$$

Although the $\alpha_s(M_\mathrm{Z})$ is larger than results from L3 and DELPHI, it is consistent with these results. The total error of $\alpha_s(M_\mathrm{Z})$ in this analysis is comparable with the these results.

8.2 Comparison with measurements of α_s by event shape variables

The PDG world averages are shown with values of α_s used in their combinations. The results from analyses which include α_s measurements using radiative events are shown also.

The α_s values which are obtained from analyses using radiative hadronic events are lower than the α_s values which are obtained from analyses using only non-radiative hadronic events. The results for the α_s measurements using radiative events are close to the PDG average for all measurements.

In case of OPAL analysis, α_s for the radiative events at LEP1 smaller than the combined value with α_s for the non-radiative events at LEP2(Section 7.3). The situation is similar in the values of α_s for each variables.

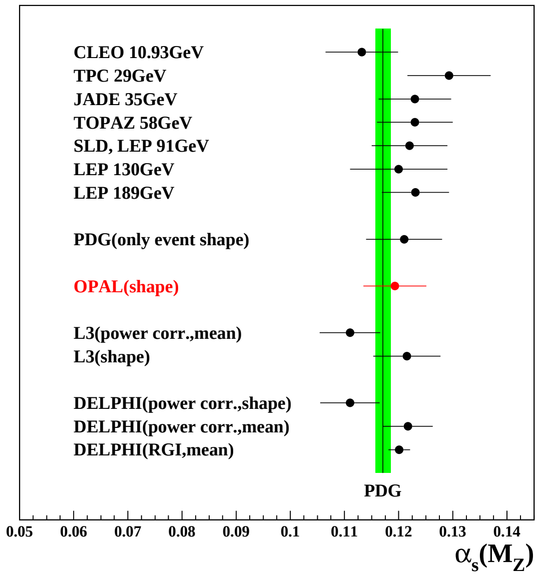

Figure 8.2: $\alpha_s(M_{\mathrm{Z}})$ in this study, PDG world average and other analyses used in the average.

	$\alpha_s(E_{\mathrm{CM}})$	$\alpha_s(M_{\mathrm{Z}})$
CLEO 10.93GeV [167]	0.164 ± 0.004(expt.) ± 0.014(theo.)	0.1132 ± 0.0067
TPC 29GeV [10, 11]	0.160 ± 0.012	0.1293 ± 0.0077
JADE 35GeV [12, 13]	$0.145^{+0.012}_{-0.007}$	0.1230 ± 0.0067
TOPAZ 58GeV [14]	0.132 ± 0.008	0.123 ± 0.007
LEP/SLD 91GeV		0.122 ± 0.007
[15, 16], [17, 18], [19], [20, 21], [22–24]		
LEP 130GeV [25, 26]	0.114 ± 0.008	0.120 ± 0.009
LEP 189GeV	0.1104 ± 0.005	0.1231 ± 0.0062
[27], [28], [29], [30–33], [34]		
PDG [59]		
Event shape		0.121 ± 0.007
All measuremnts		0.1171 ± 0.0014
OPAL		0.1193 ± 0.0058
L3 [29]		
Power correction, Mean		0.1110 ± 0.0056
Shape		0.1215 ± 0.0062
DELPHI [127]		
Power correction, Shape		0.1110 ± 0.0055
Power correction, Mean		0.1217 ± 0.0046
RGI, Mean		0.1201 ± 0.0020

Table 8.3: $\alpha_s(M_{\mathrm{Z}})$ in this study, PDG world average and other analyses used in the average.

Chapter 9

Conclusions

The strong coupling constant α_s is determined at an effective center-of-mass energy, $\sqrt{s'}$, ranging from 20 GeV to 80 GeV and from 189 GeV to 205 GeV with the OPAL detector at LEP.

α_s at $\sqrt{s'}$ ranging from 20 GeV to 80 GeV is determined by using multi-hadronic events with a hard isolated photon at center-of-mass energy around 91GeV. The date is collected in the term of LEP1 during the running year from 1992 to 1995.

Assuming that photons emitted before or immediately after the Z^0 production do not interfere with QCD processes, a measurement of α_s at the reduced center-of-mass energy, $\sqrt{s'}$, is possible by using radiative multi-hadronic events (i.e. $e^+e^- \rightarrow q\bar{q}\gamma$ events). The mean values of the event shape variables used in this measurement are shown to have the same energy dependence in Monte Carlo simulations with parton shower algorithms based on the leading logarithm approximation.

The hard isolated photon is selected from isolated electromagnetic calorimeter (ECAL) clusters in multi-hadronic events by the likelihood ratio which uses the cluster shape fit variable and the angle to jets. 4843 radiative multi-hadronic events are selected in total. The selected events are divided into seven subsamples by the cluster energy. For each subsample, six event shape variables are calculated with the ECAL cluster energy and track momentum after boosting back into the center-of-mass system of the hadrons. The selected events still include 2$\sim$15% of backround events which are caused by identifying two photons which are decay products of the neutral pion as a prompt photon. The contribution of such background events in event shape variables are statistically subtracted from data. The effects of acceptance and resolution of the OPAL detector to event shape distribution are corrected by using Monte Carlo simulation.

α_s at $\sqrt{s'}$ ranging from 189 GeV to 205 GeV is determined by using non-radiative hadronic events at center-of-mass energy between 189GeV and 209GeV. The data is collected in the term of LEP2 during the running year from 1996 to 2000. In order to measure α_s at an energy scale of the center-of-mass energy, the difference between the center-of-mass energy and the effective center-of-mass energy which obtained by the kinematic fit of jets and photons is required to be smaller than 10GeV. To reduce the contribution of four fermion processes, the selection based on the matrix element of four jets QCD processes and the likelihoods for four fermion processes are performed. 8966 non-radiative multi-hadronic events are selected in total. The subtraction of backgrounds and the correction of the detector effects are applied to the event shape distributions for each center-of-mass energy by the same procedures as the analysis of LEP1 radiative hadronic events.

In order to determine the α_s, the event shape distributions by $\mathcal{O}(\alpha_s^2)$ + NLLA QCD calculation are fitted to the corrected data distributions. Since the calculation is done with partons, the correction of hadronization effect is applied to the theoretical prediction before the fitting. The result of the fitting are shown with the statistical error and the systematic uncertainties including the experimental uncertainties, hadronization model uncertainties and renormalization scale uncertainty.

The constant $\Lambda^{(5)}_{\overline{MS}}$ is determined by fitting the solution of the renormalization group equation at NNLO to α_s determined at various effective center-of-mass energies. The energy dependence of the combined α_s for all variables gives

$$\Lambda^{(5)}_{\overline{MS}} = 0.2242 \pm 0.031(\text{stat.} + \text{expt.} + \text{hadr.})^{+0.072}_{-0.048}(\text{scale.})\ \text{GeV}.$$

The α_s for each event shape variables and combined value for all event shape variables are combined for all effective center-of-mass energy subsamples. The combined values for all variables are consistent with α_s obtained from non-radiative hadronic events at LEP1. The combined value of α_s for all energy samples and event shape variables is

$$\alpha_s(M_\text{Z}) = 0.1193 \pm 0.0017(\text{stat.})^{+0.0055}_{-0.0046}(\text{syst.}). \tag{9.1}$$

It is consistent with the result from non-radiative hadronic events at LEP1 and the PDG world average.

This study includes the first α_s measurement using radiative hadronic events presented by OPAL collaboration. α_s is measured in wide energy range by this method. The values of α_s measured in same conditions (selections, systematic uncertainties ...) can be used for study of the energy dependence of α_s. The measurement of α_s at the center of mass energies 189GeV to 205GeV is the measurement at highest energy e^+e^- collisions. The values have an important role as lever arm for the accurate measurement on Z^0 pole to know energy scale dependence.

References

[1] K. Ackerstaff *et al.*, Eur. Phys. J. **C2**, 39 (1998).

[2] P. Abreu *et al.*, Z. Phys. **C69**, 1 (1995).

[3] O. Adriani *et al.*, Phys. Lett. **B292**, 472 (1992).

[4] C.-N. Yang and R. L. Mills, Phys. Rev. **96**, 191 (1954).

[5] G. 't Hooft, Nucl. Phys. **B254**, 11 (1985).

[6] D. J. Gross and F. Wilczek, Phys. Rev. Lett. **30**, 1343 (1973).

[7] H. D. Politzer, Phys. Rev. Lett. **30**, 1346 (1973).

[8] J. D. Bjorken, Phys. Rev. **179**, 1547 (1969).

[9] L. Gibbons *et al.*, , cLNS-95-1323.

[10] SLAC-PUB-6518.

[11] D. A. Bauer *et al.*, , contributed to Int. Conf. on High Energy Physics, Glasgow, Scotland, Jul 20-27, 1994.

[12] P. A. Movilla Fernandez *et al.*, Eur. Phys. J. **C1**, 461 (1998).

[13] O. Biebel, P. A. Movilla Fernandez, and S. Bethke, Phys. Lett. **B459**, 326 (1999).

[14] Y. Ohnishi *et al.*, Phys. Lett. **B313**, 475 (1993).

[15] K. Abe *et al.*, Phys. Rev. Lett. **71**, 2528 (1993).

[16] K. Abe *et al.*, Phys. Rev. **D51**, 962 (1995).

[17] P. D. Acton *et al.*, Z. Phys. **C55**, 1 (1992).

[18] P. D. Acton *et al.*, Z. Phys. **C58**, 405 (1993).

[19] O. Adriani *et al.*, Phys. Lett. **B284**, 471 (1992).

[20] D. Decamp *et al.*, Phys. Lett. **B255**, 623 (1991).

[21] D. Decamp *et al.*, Phys. Lett. **B257**, 479 (1991).

[22] P. Abreu *et al.*, Z. Phys. **C59**, 21 (1993).

[23] P. Abreu *et al.*, Phys. Lett. **B456**, 322 (1999).

[24] M. Acciarri *et al.*, Phys. Lett. **B404**, 390 (1997).

[25] D. Buskulic *et al.*, Z. Phys. **C73**, 409 (1997).

[26] P. Abreu *et al.*, Z. Phys. **C73**, 229 (1997).

[27] CERN-99-303(1999).

[28] P. Abreu *et al.*, Eur. Phys. J. **C14**, 557 (2000).

[29] M. Acciarri *et al.*, Phys. Lett. **B489**, 65 (2000).

[30] QCD Analyses Using Jets in e+e- Annihilation at Energies between 35 GeV and 189 GeV, OPAL Physics Note, PN403, July 1999.

[31] M. Acciarri *et al.*, Phys. Lett. **B371**, 137 (1996).

[32] G. Alexander *et al.*, Z. Phys. **C72**, 191 (1996).

[33] K. Ackerstaff *et al.*, Z. Phys. **C75**, 193 (1997).

[34] QCD studies with e+e- annihilation data from 130 to 183 GeV, the ALEPH Collaboration, ALEPH 98-025(1998).

[35] S. Catani, L. Trentadue, G. Turnock, and B. R. Webber, Nucl. Phys. **B407**, 3 (1993).

[36] Y. L. Dokshitzer, A. Lucenti, G. Marchesini, and G. P. Salam, JHEP **01**, 011 (1998).

[37] S. Catani, G. Turnock, and B. R. Webber, Phys. Lett. **B295**, 269 (1992).

[38] J. C. Collins and D. E. Soper, Nucl. Phys. **B193**, 381 (1981).

[39] J. C. Collins and D. E. Soper, Nucl. Phys. **B197**, 446 (1982).

[40] J. C. Collins and D. E. Soper, Nucl. Phys. **B284**, 253 (1987).

[41] J. Kodaira and L. Trentadue, Phys. Lett. **B112**, 66 (1982).

[42] R. Fiore, A. Quartarolo, and L. Trentadue, Phys. Lett. **B294**, 431 (1992).

[43] G. Kramer and H. Spiesberger, Z. Phys. **C73**, 495 (1997).

[44] G. Dissertori and M. Schmelling, Phys. Lett. **B361**, 167 (1995).

[45] S. Catani *et al.*, Phys. Lett. **B269**, 432 (1991).

[46] S. Catani, Y. L. Dokshitzer, F. Fiorani, and B. R. Webber, Nucl. Phys. **B377**, 445 (1992).

[47] G. Altarelli and G. Parisi, Nucl. Phys. **B126**, 298 (1977).

[48] T. Sjostrand, Comput. Phys. Commun. **82**, 74 (1994).

[49] G. Marchesini *et al.*, Comput. Phys. Commun. **67**, 465 (1992).

[50] L. Lonnblad, Comput. Phys. Commun. **71**, 15 (1992).

[51] R. Odorico, Comput. Phys. Commun. **72**, 238 (1992).

[52] B. Van Eijk, , iN *MADISON 1985, PROCEEDINGS, NEW PARTICLES 1985* 268-275.

[53] P. D. Acton *et al.*, Z. Phys. **C59**, 1 (1993).

[54] G. Abbiendi *et al.*, Eur. Phys. J. **C16**, 185 (2000).

[55] X. Artru and G. Mennessier, Nucl. Phys. **B70**, 93 (1974).

[56] B. Andersson, G. Gustafson, and T. Sjostrand, Phys. Scripta **32**, 574 (1985).

[57] G. C. Fox and S. Wolfram, Nucl. Phys. **B168**, 285 (1980).

[58] R. D. Field and S. Wolfram, Nucl. Phys. **B213**, 65 (1983).

[59] K. Hagiwara *et al.*, Phys. Rev. **D66**, 010001 (2002).

[60] S. Bethke, Nucl. Phys. Proc. Suppl. **121**, 74 (2003).

[61] R. Ammar *et al.*, Phys. Rev. **D57**, 1350 (1998).

[62] B. A. Kniehl, G. Kramer, and B. Potter, Phys. Rev. Lett. **85**, 5288 (2000).

[63] L. Bourhis, M. Fontannaz, J. P. Guillet, and M. Werlen, Eur. Phys. J. **C19**, 89 (2001).

[64] J. H. Kim *et al.*, Phys. Rev. Lett. **81**, 3595 (1998).

[65] D. Allasia *et al.*, Z. Phys. **C28**, 321 (1985).

[66] K. Varvell *et al.*, Z. Phys. **C36**, 1 (1987).

[67] V. V. Ammosov *et al.*, Z. Phys. **C30**, 175 (1986).

[68] P. C. Bosetti *et al.*, Nucl. Phys. **B142**, 1 (1978).

[69] A. Airapetian *et al.*, Phys. Lett. **B442**, 484 (1998).

[70] K. Ackerstaff *et al.*, Phys. Lett. **B464**, 123 (1999).

[71] P. L. Anthony *et al.*, Phys. Lett. **B463**, 339 (1999).

[72] P. L. Anthony *et al.*, Phys. Lett. **B493**, 19 (2000).

[73] J. Blumlein and H. Bottcher, AIP Conf. Proc. **602**, 94 (2001).

[74] R. Barate *et al.*, Eur. Phys. J. **C4**, 409 (1998).

[75] K. Ackerstaff *et al.*, Eur. Phys. J. **C7**, 571 (1999).

[76] C. T. H. Davies *et al.*, Phys. Rev. **D56**, 2755 (1997).

[77] A. Spitz *et al.*, Phys. Rev. **D60**, 074502 (1999).

[78] A. X. El-Khadra, G. Hockney, A. S. Kronfeld, and P. B. Mackenzie, Phys. Rev. Lett. **69**, 729 (1992).

[79] A. X. El-Khadra, (1996).

[80] P. Boucaud *et al.*, JHEP **01**, 046 (2002).

[81] S. Booth *et al.*, Phys. Lett. **B519**, 229 (2001).

[82] M. Jamin and A. Pich, Nucl. Phys. **B507**, 334 (1997).

[83] J. R. Ellis and M. Karliner, Phys. Lett. **B341**, 397 (1995).

[84] D. Adams *et al.*, Phys. Lett. **B329**, 399 (1994).

[85] K. Abe *et al.*, Phys. Rev. Lett. **74**, 346 (1995).

[86] A. L. Kataev, G. Parente, and A. V. Sidorov, Nucl. Phys. **B573**, 405 (2000).

[87] J. Santiago and F. J. Yndurain, Nucl. Phys. **B563**, 45 (1999).

[88] A. A. Penin and A. A. Pivovarov, Phys. Lett. **B435**, 413 (1998).

[89] The LEP Electroweak Working Group, CERN-EP/2000-016.

[90] G. Parisi, Phys. Lett. **B74**, 65 (1978).

[91] J. F. Donoghue, F. E. Low, and S.-Y. Pi, Phys. Rev. **D20**, 2759 (1979).

[92] S. Bethke, Z. Kunszt, D. E. Soper, and W. J. Stirling, Nucl. Phys. **B370**, 310 (1992).

[93] N. Brown and W. J. Stirling, Z. Phys. **C53**, 629 (1992).

[94] S. Catani, L. Trentadue, G. Turnock, and B. R. Webber, Preprint CERN-TH-6640-92 (1992).

[95] S. Catani and B. R. Webber, Phys. Lett. **B427**, 377 (1998).

[96] B. R. Webber, Proc. 'QCD - 20 Years later', Achen (1992), CERN-TH-6706-92 (1992).

[97] K. Koller, T. F. Walsh, and P. M. Zerwas, Zeit. Phys. **C2**, 197 (1979).

[98] E. Laermann, T. F. Walsh, I. Schmitt, and P. M. Zerwas, Nucl. Phys. **B207**, 205 (1982).

[99] G. Kramer and B. Lampe, Phys. Lett. **B269**, 401 (1991).

[100] G. Kramer and B. Lampe, Fortschr. Phys. **37**, 161 (1989).

[101] H. Baer, J. Ohnemus, and J. F. Owens, Phys. Rev. **D42**, 61 (1990).

[102] P. Aurenche, R. Baier, and M. Fontannaz, Phys. Rev. **D42**, 1440 (1990).

[103] E. L. Berger and J.-w. Qiu, Phys. Rev. **D44**, 2002 (1991).

[104] E. W. N. Glover and W. J. Stirling, Phys. Lett. **B295**, 128 (1992).

[105] Z. Kunszt and Z. Trocsanyi, Nucl. Phys. **B394**, 139 (1993).

[106] L. E. Gordon and W. Vogelsang, Phys. Rev. **D50**, 1901 (1994).

[107] E. W. N. Glover and A. G. Morgan, Z. Phys. **C62**, 311 (1994).

[108] A. Gehrmann-De Ridder and E. W. N. Glover, Nucl. Phys. **B517**, 269 (1998).

[109] S. Frixione, Phys. Lett. **B429**, 369 (1998).

[110] M. H. Seymour, , presented at Workshop on Photon Radiation From Quarks, Annecy, France, Dec 2-3, 1991.

[111] T. Sjostrand, , in *Annecy 1991, Proceedings, Photon radiation from quarks* 89-96 and CERN Geneva - TH. 6369 (92/01,rec.Apr.) 14 p.

[112] L. Lonnblad, , prepared for 10th Workshop on Photon-photon Collisions (PHOTON '95), Sheffield, England, 8-13 Apr 1995.

[113] e. . Cartwright, S., , geneva, Switzerland: CERN (1992) 234 p. and CERN Geneva - CERN 92-04 (92/07,rec.Jul.) 234 p.

[114] E. Witten, Nucl. Phys. **B120**, 189 (1977).

[115] C. H. Llewellyn Smith, Phys. Lett. **B79**, 83 (1978).

[116] D. Buskulic *et al.*, Z. Phys. **C69**, 365 (1996).

[117] D. Buskulic *et al.*, Z. Phys. **C57**, 17 (1993).

[118] D. P. Kirby, , uMI-96-11517.

[119] O. Rind, , uMI-98-40636.

[120] I. G. Knowles *et al.*, (1995).

[121] K. Ahmet *et al.*, Nucl. Instrum. Meth. **A305**, 275 (1991).

[122] M. Arignon *et al.*, Nucl. Instrum. Meth. **A313**, 103 (1992).

[123] A. G. Denig, (2002).

[124] M. Acciarri *et al.*, Phys. Lett. **B411**, 339 (1997).

[125] Measurement of α_s in Radiative Hadronic Events, OPAL Physiscs Note PN519 April, 2003.

[126] O. collaboration, , presented at 2003 Meeting of the American Physical Society, Division of Particles and Fields (DPF 2003), Philadelphia, Pennsylvania, 5-8 April 2003.

[127] P. Abreu *et al.*, Z. Phys. **C70**, 179 (1996).

[128] J. Abdallah *et al.*, Eur. Phys. J. **C29**, 285 (2003).

[129] J. Allison *et al.*, Nucl. Instrum. Meth. **A317**, 47 (1992).

[130] R. Odorico, Comput. Phys. Commun. **32**, 139 (1984).

[131] R. Odorico, Comput. Phys. Commun. **59**, 527 (1990).

[132] G. Alexander *et al.*, Z. Phys. **C69**, 543 (1996).

[133] S. Jadach, B. F. L. Ward, and Z. Was, Comput. Phys. Commun. **79**, 503 (1994).

[134] L. Lonnblad *et al.*, (1995).

[135] J. A. M. Vermaseren, Nucl. Phys. **B229**, 347 (1983).

[136] A. Buijs, W. G. J. Langeveld, M. H. Lehto, and D. J. Miller, Comput. Phys. Commun. **79**, 523 (1994).

[137] G. Alexander *et al.*, Z. Phys. **C52**, 175 (1991).

[138] T. Omori, S. Asai, I. Nakamura, and S. Yamashita, A Matching Algorithm: MT Package, OPAL Technical Note TN381 July, 1996.

[139] S. Mihara and S. Yamashita, a new algorithm to calculate energy flow based on MT package, OPAL Technical Note TN575 November, 1998.

[140] D. Karlen, Computers in Physics, **12** (1998) 380.

[141] *CERN Program Library Long Writeup W5013, GEANT - Detector Description and Simulation Tool 1993.*

[142] G. Abbiendi *et al.*, Eur. Phys. J. **C19**, 587 (2001).

[143] M. Acciarri *et al.*, Phys. Lett. **B328**, 223 (1994).

[144] W. Adam *et al.*, Z. Phys. **C69**, 561 (1996).

[145] R. Akers *et al.*, Z. Phys. **C63**, 181 (1994).

[146] D. Buskulic *et al.*, Z. Phys. **C64**, 361 (1994).

[147] P. Abreu *et al.*, Phys. Lett. **B275**, 231 (1992).

[148] P. Abreu *et al.*, Z. Phys. **C65**, 587 (1995).

[149] G. Alexander *et al.*, Phys. Lett. **B264**, 467 (1991).

[150] S. Jadach, B. F. L. Ward, and Z. Was, Comput. Phys. Commun. **130**, 260 (2000).

[151] T. Sjostrand, L. Lonnblad, and S. Mrenna, (2001).

[152] J. Fujimoto *et al.*, Comput. Phys. Commun. **100**, 128 (1997).

[153] S. Catani and M. H. Seymour, Phys. Lett. **B378**, 287 (1996).

[154] K. Ackerstaff *et al.*, Eur. Phys. J. **C1**, 395 (1998).

[155] G. Abbiendi *et al.*, Eur. Phys. J. **C8**, 191 (1999).

[156] M.A. Thomson, The OPAL $W^+W^- \rightarrow q\bar{q}l\nu_l$ Event Selection, OPAL Technical Note TN635 November, 2000.

[157] M. Z. Akrawy *et al.*, Phys. Lett. **B253**, 511 (1991).

[158] R. K. Ellis, D. A. Ross, and A. E. Terrano, Nucl. Phys. **B178**, 421 (1981).

[159] F. A. Berends, R. Pittau, and R. Kleiss, Comput. Phys. Commun. **85**, 437 (1995).

[160] The LEP QCD Working Group, Preliminary Combination of $alpha_s$ Values Derived from Event Shape Variables at LEP, OPAL Technical Note TN689 May 2001.

[161] Study of Hadronic Events and Test of QCD at Reduced Centre of Mass Energies from Z Decays, L3 Note #2084 May 15, 1997.

[162] Y. L. Dokshitzer and B. R. Webber, Phys. Lett. **B352**, 451 (1995).

[163] Y. L. Dokshitzer, A. Lucenti, G. Marchesini, and G. P. Salam, JHEP **05**, 003 (1998).

[164] Y. L. Dokshitzer, G. Marchesini, and G. P. Salam, Eur. Phys. J. direct **C1**, 3 (1999).

[165] Y. L. Dokshitzer, (1999).

[166] B. R. Webber, (1995).

[167] CLNS 95-1323(1995).

Acknowledgment

At first, I would like to thank Prof. Tomio Kobayashi, for his appropriate advice and continuous encouragement during six years of my research.

I would like to thank T. Kawamoto, for his many helpful advices on this analysis. I enjoyed to talk about the analysis with him. I would like to thank S. Asai, for teaching me when I started analyses at CERN.

I would like to thank my colleagues in ICEPP: K. Ozone, K. Yamamoto, H. Nanjo, H. Nishiguchi, Y. Kataoka, K. Shibuya, H. Nomoto, Y. Hane, Y. Hisamatsu, Y. Fujii. I refreshed by dinners and the BBQ parties with them.

I would like to thank staffs in ICEPP: M. Ishino, S. Komamiya, T. Mashimo, T. Saeki, H. Sakamoto, J. Tanaka, I. Ueda, S. Yamashita, for useful comments for this analysis and my presentations at meetings. I would like to thank secretaries in ICEPP: E. Bandai, C. Ito, R. Ono, I. Tsukamoto.

I would like to thank my colleagues in OPAL collaboration, especially S. Kluth and P. Wells for useful advice as an OPAL QCD group convener and a physics coordinator. I would like to thank the secretariat in OPAL collaboration, H. Dawn.

Finally I thank my father Akira Toya, my mother Aiko Toya, my brother Junji Toya, for their encouragement.

Daisuke Toya